I C M A R' 98

HTПM

Novosibirsk, Russia

Proceedings

Part II

9

REPORT DOCUMENTATION PAGE

Form Approved OMB No. 0704-0188

1. AGENCY USE ONLY (Leave blank)	2. REPORT DATE 1998	3. REPORT TYPE AND DATES COVERED Conference Proceedings

4. TITLE AND SUBTITLE

International Conference on the Methods of Aerophysical Research 98 "ICMAR 98"

5. FUNDING NUMBERS

F61775-98-WE002

6. AUTHOR(S)

Conference Committee

7. PERFORMING ORGANIZATION NAME(S) AND ADDRESS(ES)

Institute of Theoretical and Applied Mechanics
Novosibirsk 630090
Russia

8. PERFORMING ORGANIZATION REPORT NUMBER

N/A

9. SPONSORING/MONITORING AGENCY NAME(S) AND ADDRESS(ES)

EOARD
PSC 802 BOX 14
FPO 09499-0200

10. SPONSORING/MONITORING AGENCY REPORT NUMBER

CSP 98-1025

11. SUPPLEMENTARY NOTES

This is volume two. Volume one of the proceedings was sent earlier.

12a. DISTRIBUTION/AVAILABILITY STATEMENT

Approved for public release; distribution is unlimited.

12b. DISTRIBUTION CODE

A

13. ABSTRACT (Maximum 200 words)

The Final Proceedings for International Conference on Methods of Aerophysical Research (ICMAR'98), 29 June 1998 - 3 July 1998

This is an interdisciplinary conference. Topics include: Problems of Modeling at sub/trans/super/hypersonic velocities; Methods of flow diagnostics; Instrumentation for aerophysical experiments; Verification of CFD models and methods.

14. SUBJECT TERMS

Aerodynamics, Flow Diagnostics, Computational Fluid Dynamics

15. NUMBER OF PAGES

229

16. PRICE CODE

N/A

17. SECURITY CLASSIFICATION OF REPORT UNCLASSIFIED	18. SECURITY CLASSIFICATION OF THIS PAGE UNCLASSIFIED	19. SECURITY CLASSIFICATION OF ABSTRACT UNCLASSIFIED	20. LIMITATION OF ABSTRACT UL

NSN 7540-01-280-5500

Standard Form 298 (Rev. 2-89)
Prescribed by ANSI Std. 239-18
298-102

RUSSIAN ACADEMY OF SCIENCES   SIBERIAN DIVISION
RUSSIAN NATIONAL COMMITTEE
ON THEORETICAL AND APPLIED MECHANICS
INSTITUTE OF THEORETICAL AND APPLIED MECHANICS
INTERNATIONAL CENTER OF AEROPHYSICAL RESEARCH

INTERNATIONAL CONFERENCE
ON THE METHODS OF AEROPHYSICAL RESEARCH

29 June – 3 July , 1998, Novosibirsk, Russia

Proceedings
Part II

Novosibirsk
1998

THE MEASUREMENT OF THERMAL RADIATION OF C_{60} CLUSTERS IN A FLOW

A.A. Agarkov, A.A. Vostrikov, D.Yu. Dubov, V.A. Galichin, S.V. Drozdov
Institute of Thermophysics SB RAS,
630090, Novosibirsk, Russia

INTRODUCTION

The blowing out of a gas flow from a surface is one of the possible methods to change the aerodynamic characteristics of the aircrafts and to decrease the heat flux to their walls [1]. During this process, the restructuring of supersonic jet occurs. This leads to the formation of a detachment flow and a significant decrease in the resistance of streamlined body. An active restructuring of the incident supersonic jet is observed when the fine particles are in this jet [2]. The efficiency of the two-phase flow injection depends on a size of these particles and their distribution near the surface of streamlined body. Thus, the use of monodispersive particles and the possibility to measure their spatial distribution in the supersonic jet near the streamlined body are of a particular importance. For example, in [2] authors used aluminium (Al_2O_3) particles with a size from 50 to 100 μm, but their distribution was not measured.

To improve the aerodynamic characteristics of supersonic streamline of the bodies by means of blowing out from them of a gas with particles, we suggest to use the carbon C_{60} particles which are called fullerene [3]. In the condensed state these fullerenes are called fullerites. While heating the fullerite of C_{60}, it evaporates with the formation of vapor of C_{60} molecules. The unique property of fullerene for the development of aerophysical research methods is as follows. Molecules of C_{60} have a great mass and they are resistant to dissociation. The dissociation of gaseous C_{60} becomes notable only at the temperature $T > 3000$ K [4]. It does not break into fragments during collision with a surface even for the kinetic energy of 200 eV [5]. The spatial distribution of gaseous molecules of C_{60} can be easily measured with the help of standard electrical-physical and optical methods. Our investigations with crossed beams of C_{60}^- and electrons show that particles of C_{60} have a large cross-sections for the electron capture with the formation of stable ions of C_{60}^- [6] and for the molecule ionization yielding ions of C_{60}^+ [7]. Due to the high number and density of internal degrees of freedom, C_{60} excitation is accompanied by rapid heating of molecule. The heating of these molecules is not depending on the excitation method. For instance, the C_{60} molecule is efficiently heated by an electron impact and by the collision with a surface [8, 9]. The use of C_{60} fullerene for the aerodynamic investigations allows one to trace the streamlines pattern for the transition from the atomic particles injection to the injection of heavy particles.

In the current paper we studied the radiation properties of the gaseous C_{60} molecule excited by an electron impact, in terms of C_{60} using as a main or probe component for the aerodynamic investigations. The revealed thermal radiation of C_{60} described by Plank's law for radiation of absolute black body, and the effect of electron's thermal emission during the C_{60} heating, gives us an opportunity to measure the spatial distribution of C_{60} molecules during the body streamline in a supersonic gas flow.

EXPERIMENTAL TECHNIQUE

In short, molecular beam experimental arrangement was the following. The C_{60} vapor was allowed to effuse out of a cylinder oven containing a fullerene sample. The sample temperature, T_0, was 800 K. The electron beam from an oxide-coated cathode was collimated
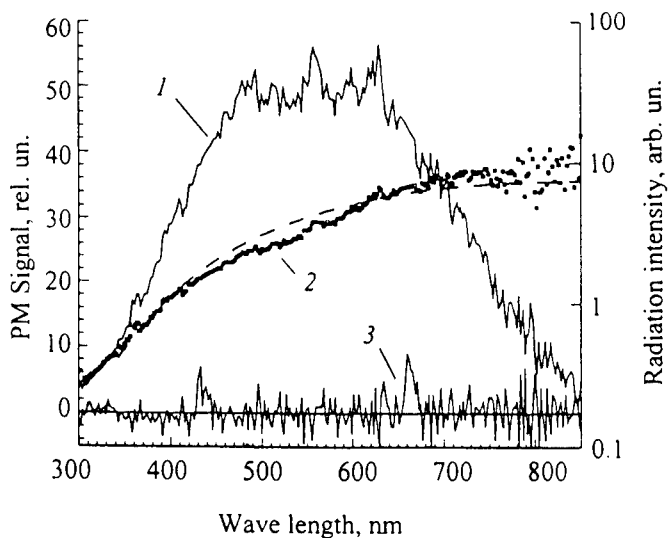
Fig. 1

For comparison Fig. 1 presents also the black body radiation spectrum with temperature T = 3341 K (dashed curve). Notice that the C_{60} radiation spectrum agrees well with the black body radiation.
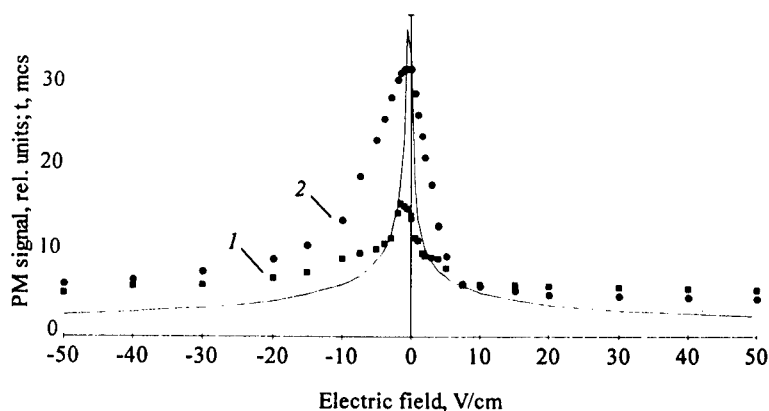
Fig. 2

Figure 2 (curve 1,2) shows the intensity of total radiation depending on the strength and polarity of electric field ξ between plates. These curves were obtained at E_e = 40 (curve 1) and 65 eV (curve 2). Here is also shown the residence time, t, of C_{60}^+ ion in the detection region versus ξ (solid line). This time has been calculated for the ion formed at the centre of the electron beam with the vector of initial thermal velocity of C_{60} directed at the angle of 40^0 to the optical system axis. In Fig.2 one can see that the ions contribute mainly to the radiation intensity.

4

by a set of diaphragms and crossed at right angles with the fullerene beam. In the course of our experiments the electron energy ranges from 0 to 100 eV and the electron current was not larger than 100 μA. The radiation from the beams crossing region was collected in a direction normal to the electron beam; the angle with the molecular beam direction was about 40^0. With the short-focal lens the radiation was focused onto the input slit of a MUM grating monochromator (the working wavelength range was 200 - 800 nm, inverse dispersion 3.2 nm/mm) and after spectral decomposition it was recorded with a photomultiplier (PM). The system of the radiation registration and the electron beam collimation of the longitudinal magnetic field precluded the cathodoluminescence. The electron beam was modulated by applying a negative potential to one of the diaphragms, and the signal from PM was measured in a lock-in mode. In this scheme was recorded the background gas radiation. At the registration of background gas radiation the output of effusion source (beam of C_{60}) was closed by electromagnetic shutter. Each of experimental point was measured at open and closed shutter. The C_{60} radiation was recorded as a difference between total and background signals.

In order to separate the contribution to the radiation from neutral $C_{60}*$ and C_{60}^+, we applied electric field to the two plates placed along the axes of molecular and electron beam. The distance between the plates was 10 mm and they were equidistant from the electron beam. The residence time of ions in the observation region was reduced with increasing voltage. Our system parameters were checked in the measurements of electron-induced radiation of N_2^+ $(B_2\Sigma^+)$ ion and N_2 $(C^3\Pi_u)$ molecule depending on the electron energy E_e. For this purpose the C_{60} beam was closed by shutter and the vacuum chamber was filled of nitrogen to pressure $2 \cdot 10^{-6}$ Torr.

RESULTS

In Fig.1 the result of C_{60} electron-induced radiation measurement was shown for E_e = 66 eV. The radiation spectrum (curve 2) was obtained as the difference of the total PM signal (curve 1) and the radiation of the background gas (curve 3), normalized to the total spectral sensitivity of the detecting system. One can see the spectrum from a beam of fullerene has quasicontinuous character (within the spectral resolution).

In view of the large number of radiating modes, the form of the spectrum is determined rather by internal temperature of molecule than by a structure of the vibrational levels. Therefore it is of interest to compare this spectrum with the Planck spectrum of radiation of a black body with some temperature T. The rate of photon emission from a heated ball in the recorded wavelength region, $[\lambda, \lambda + \Delta\lambda]$, K_λ, is

$$K_\lambda = 2\pi c S \Delta\lambda \varepsilon(\lambda,T) / \lambda^4[\exp(hc/\lambda kT) - 1], \tag{1}$$

here $S = 4\pi d^2$ is the surface area, d is the diameter of the C_{60} ball, $\varepsilon(\lambda,T)$ is the emissivity (i.e. the blackness coefficient of a body). Assuming that at $d << \lambda$ this coefficient should be $\leq d/\lambda$ [10], we shall set $\varepsilon = d/\lambda$, i.e., the dependence of $\varepsilon(T)$ can be neglected. It gives us for our spectral region (where the photon energy is much greater than kT)

$$K_\lambda(\lambda,T) \sim \lambda^{-5} \exp(-hc/\lambda kT), \tag{2}$$

i.e., the radiation depends very strongly on temperature.

5

The total intensity of electron-induced radiation as a function of electron energy, $I(E_e)$, is shown in Fig.3 (curves 1-3). Here curve 1 was measured at extracting field $\xi = 12$ V/cm, i.e. it corresponds to the radiation of the neutral molecules C_{60}^*. Curve 2 corresponds to the total radiation of C_{60}^+ and C_{60}^* ($\xi = 0$ V/cm). Curve 3 is the intensity radiation of C_{60}^+ and C_{60}^* for $\lambda = 540$ nm.

In Fig.3 the temperature of radiating particles depending on the electron energy is also given. This dependence was received from measurements of $I(E_e)$ for different wavelengths (from 450 to 700 nm) and least-squares-fitting of the data according to the formula (2). The corresponding internal energy of radiating particle has been calculated with the help of the thermal capacity data for neutral molecules C_{60} [9].

In Fig.3 one can see that initially the dependence $T(E_e)$ increases proportionally with E_e, but at $E_e = 50$ eV it reaches the limiting value, $T = 3000 \pm 100$ K. The existence of the limiting value T is explained by the competition between the radiative cooling of electron-heated particle and other cooling processes, such as the fragmentation, thermionic emission [11,12] and dissociative ionization [13].
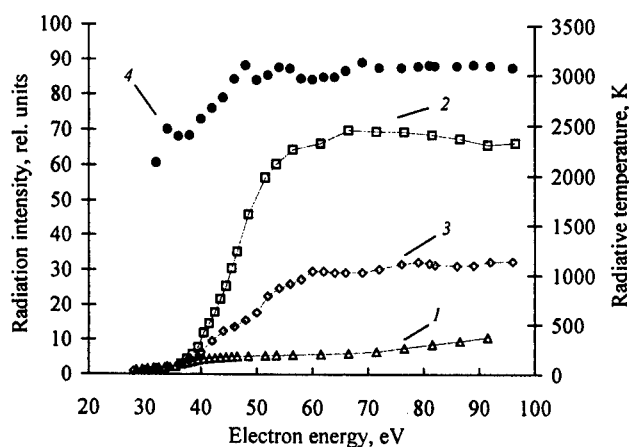
Fig. 3

The results of performed investigations showed that the density of fullerene particle C_{60} may be register uncontactly by optical methods in broad wavelength range at very low partial density (10^{10} molecule/cm^3). The maximum value of C_{60} radiation intensity was reached at the electron energy E_e=60 eV and remained essentially constant with further increasing of the electron energy. Considering also the experience of electron beam using for density measurements in hypersonic boundary layer [14] it may be concluded that the fullerene particles in gas phase may be exploited as sample particle or basic components in aerodynamical studies of particle blowing effect on aerodynamical and thermal characteristics.

REFERENCES

1. Baev V.K., Garanin A.F., Tretiakov P.K. About the interaction of hydrogen jet with the contrary supersonic flow // Fizicheskaia gidrodinamika/ AN SSSR - 1976. - № 6. - P. 50-52.
2. Gridnev N.P., Katsnelson S.S., Fomin V.M., Fomichev V.P. Experimental and theoretical investigation of improvement the aerodynamical characteristics of supersonic flow around a body by blowing-out from body the gas jet with particles // Sib. Fiz.-Tekh.Zhurnal.- 1991. - № 4. - P. 36 - 39.
3. Eletskii A.V., Smirnov B.M. Fullerenes and the structures of carbon // Usp. Fiz. Nauk - 1995. - Vol. 165, № 9. - P. 977 - 1009.
4. Kim S.G., Tomanek D. Melting the fullerenes: A molecular dynamics study // Phys. Rev. Lett. – 1994. – Vol. 72. – P. 2418.
5. Beck R.D., St.John P., Alvarez M.M., Diederich F., Whetten R.L. Resilience of all-carbon molecules C_{60}, C_{70}, and C_{84}: A surface scattering time-of-flight investigation // J. Phys. Chem. – 1991. – Vol. 95. - P. 8402.
6. Vostrikov A.A., Dubov D.Yu., Agarkov A.A. Electron attachment cross section for fullerene in a beam // Tech. Phys. Lett. - 1995. - Vol. 21, № 7. - P. 517 - 518.
7. Vostrikov A.A., Dubov D.Yu., Agarkov A.A. Direct and delayed ionization of C_{60} clusters by electron impact // Tech. Phys. Lett. - 1995. - Vol. 21, № 9. - C. 715 - 716.
8. Vostrikov A.A., Dubov D.Yu., Agarkov A.A. Electron-induced radiation from C_{60} fullerene in the gas phase // JETP Lett. - 1996. - Vol. 63, № 12. - P. 963 - 967.
9. Kolodney E., Tsipinyuk B., and Budrevich A. The thermal stability and fragmentation of C_{60} molecule up to 2000 K on the milliseconds time scale // J. Chem. Phys. - 1995. – Vol. 102. – P. 9263.
10. Landau L.D., Lifshitz E.M. Electrodynamics of continuous media.- Moscow: Nauka, 1982, P. 445.
11. Hansen K., Campbell E.E.B. Radiative cooling of fullerenes // J. Chem. Phys. – 1996. - Vol. 104. - P. 5012.
12. Hansen K., Echt O. Thermionic emission and fragmentation of C_{60} // Phys. Rev. Lett. – 1997. – Vol. 78. - P. 2337 – 2343.
13. Foltin M., Lezius M., Scheier P., and Mark T.D. On the unimolecular fragmentation of C_{60}^{+} fullerene ions: The comparison of measured and calculated breakdown patterns // J. Chem. Phys. – 1993. – Vol. 98. - P. 9624 - 9634.
14. Maslov A.A., Mironov S.G., Shiplyuk A.N. An experimental study of pulsation's in hypersonic shock layer on a plate // Zhurnal Prikl. Mekh. Tekh. Fiz. - 1996. - Vol. 37, № 6. - P. 51 - 60.

INVESTIGATION OF PRESSURE PULSE PROPAGATION IN SATURATED POROUS SAMPLE AND THEIR EFFECT ON PHASE PERMEABILITY

A.T. Akhmetov, A.A. Gubaidullin, O.Yu. Kuchugurina, D.N. Dudko

Tyumen Branch of Institute of Theoretical and Applied Mechanics SB RAS,
Taymirskaya St.74, Tyumen, 625000 Russia

INTRODUCTION

During shock wave propagation from liquid to saturated porous medium, complex wave configuration may form in the medium. At that wave action on the process of multiphase filtration may have effect on permeabilities of phases. To determine the effect, the experiments on vertical shock tube were carried out. Air-saturated core with isolated lateral sides was placed on the bottom of the tube. Liquid was filtered through sample from top to bottom at pressure difference of 10 kPa. On transition to a steady filtration, liquid was loaded by pulse shock action, and it caused short-time (5-10 minutes) increase of flow rate to 20-30 %. To clear the mechanism of wave action, the experiments with transparent plane micromodel of porous medium were made with use of analogous method. It was established that jammed gas bubbles are displaced from restrictions of porous medium at a moment of shock action; therefore rate flow increases as long as new bubbles fill the restrictions.

It should be pointed that practical interest for these problems gave rise to a number of papers on application of vibroaction in oil recovery [1] and use of effect of shock waves on bottom zone of well [2].

Numerical research of process of pressure pulse propagation from liquid to saturated porous medium was carried out. The features of wave passage through interface and wave propagation in porous medium.

MATHEMATICAL MODEL

The closed set of equations governing plane one-dimensional motion of saturated porous medium is in the form [3, 4]:

$$\frac{\partial_1 \rho_1}{\partial t} + \rho_1 \frac{\partial v_1}{\partial x} = 0, \qquad \frac{\partial_1 \rho_2}{\partial t} + \rho_2 \frac{\partial v_2}{\partial x} = 0,$$

$$\rho_1 \frac{d_1 v_1}{d t} = -\alpha_1 \frac{\partial p_1}{\partial x} - F, \qquad \rho_2 \frac{d_2 v_2}{dt} = -\alpha_2 \frac{\partial p_1}{\partial x} + \frac{\partial \sigma_{2*}}{\partial x} + F,$$

$$t_{20} \left(\frac{d_2 \sigma_{2*}}{dt} - E_{*f} \frac{d_2 \varepsilon_2}{dt} \right) + \left(\sigma_{2*} - E_{*e}\, \varepsilon_2 \right) = 0,$$

$$\frac{d_2 \varepsilon_2}{dt} = \frac{\partial v_2}{\partial x}, \qquad \left(\frac{d_i}{dt} = \frac{\partial}{\partial t} + v_i \frac{\partial}{\partial x} \right)$$

$$p_1 - p_{10} = C_1^2 \left(\rho_1^0 - \rho_{10}^0 \right), \qquad p_2 - p_{20} = C_2^2 \left(\rho_2^0 - \rho_{20}^0 \right), \qquad \sigma_{2*} = \alpha_2 \left(p_1 - p_2 \right)$$

$$\rho_1 = \alpha_1 \rho_1^0, \qquad \rho_2 = \alpha_2 \rho_2^0, \qquad \alpha_1 + \alpha_2 = 1$$

$$F = F_\mu + F_m, \qquad E_{*f} = \rho_{20}\, D^2_{*f}, \qquad E_{*e} = \rho_{20}\, D^2_{*e},$$

$$F_\mu = \eta_\mu\, a_2^{-2}\, \alpha_1\, \alpha_2\, \mu_1 \left(v_1 - v_2\right), \qquad F_m = \frac{1}{2}\eta_m\, \alpha_1\, \alpha_2\, \rho_1^0 \left(\frac{d_1\, v_1}{d\, t} - \frac{d_2\, v_2}{d\, t}\right).$$

Here $\alpha_i, \rho_i, \rho_i^0, v_i$ are volume fraction, effective and true densities and velocity of i-phase. Subscripts $i = 1, 2$ refers to parameters of liquid and solid phase; p_l is pressure of liquid, σ_{2*}, ε_{2*} are longitudinal stress and strain; D_{f*}, D_{e*} are longitudinal dynamic and static sound speeds; E_{f*}, E_{e*} are dynamic and static elastic moduli. Force of phase interaction F is a sum of force of viscous friction F_μ and associated mass force F_m, η_μ and η_m are coefficients of viscous and inertial phase interaction, μ_1 is dynamic viscosity of liquid, a_2 is radius of grains of skeleton of porous medium.

In numerical experiments the procedure based on differential scheme of through count [4] has been used. The conditions of continuity of stress and velocity are to be valid at the interface "liquid - saturated porous medium". It follows from the analysis that the procedure ensures validity of the conditions at the interface. It should be noted that no special algorithm has been used for interface because interface has no time to spread during such short-time processes.

RESULTS OF NUMERICAL MODELING

Propagation of step-type and pulse compression waves from liquid to liquid-saturated porous medium and their evolution in the medium was studied. The numerical results showed that on entering the more dense medium, perturbation increases and develops a two-wave appearence, that is, the passed wave is a sum of fast (deformational) and slow (filtrational) waves. In the fast mode velocities of liquid and skeleton are close together and have the same directions, velocity of liquid is some greater that that of solid. In the slow mode velocities of phases are opposite in sign; at that liquid has positive velocity and is compressed while skeleton has negative velocity and is rarefied. Slow wave damps strongly, fast wave damps less intensively. Total stress is of one-wave structure because in slow mode liquid is compressed and skeleton is rarefied with the same amplitudes, hence there is no total stress in slow wave.

To estimate effect of phase interaction on the processes, calculations without account for interaction forces (at $F=0$) were made. As follows from the calculations, interaction forces result in considerable deceleration and attenuation of slow wave. Attenuation of fast wave is determined by intergranular friction in skeleton. Without account for interphase forces and intergranular friction both fast and slow waves propagate without dispersion and dissipation, that is, they hold their form. The latter is in agreement with the results of analysis of dispersion relation. Note that decrease of longitudinal dynamic sound speed D_{*f} results in decrease of acoustic rigidity of porous medium and decrease of amplitude of slow waves, at that in fast wave amplitude in skeleton decreases but in liquid increases. Increase of porosity results in decrease of speed and amplitude of fast wave as well as increase of speed and decrease of amplitude of slow wave. Steepness of waves does not vary. When intensity of incident wave growing, intensity of fast wave relative to intensity of incident wave does not vary practically, and that of slow wave non-monotonously varies (first incsreases and then decreases). Steepness of slow wave decreases.
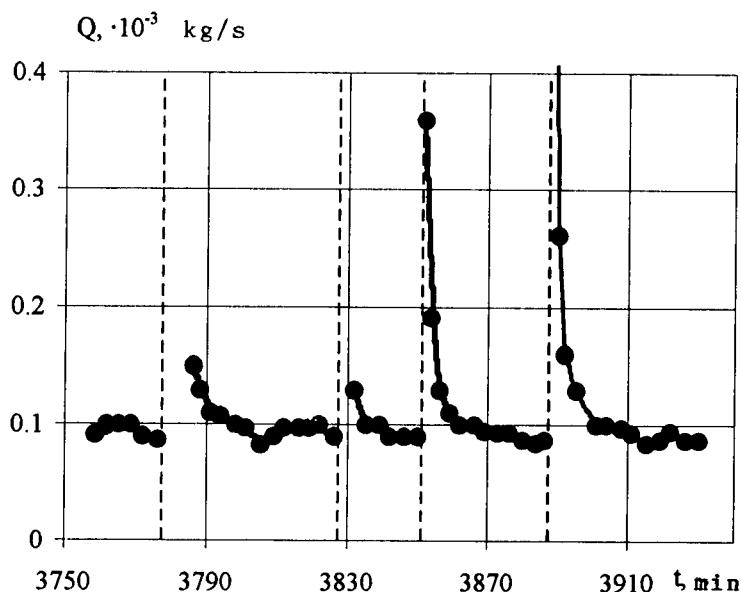
Fig.1. Flow rate of water filtering through core at constant pressure difference
of 10 kPa. Moments of shock action are showed with dashed lines

EXPERIMENTAL RESULTS

Experimental investigations were carried out on shock tube with a provision for measurement of core porosity and on plane transparent micromodel of porous structure which allows generation of pulse action on saturating phase.

Vertical shock tube consisted of sections with inner diameter of 90 mm, there were one starting and two registering piezoelectric transducers in the measuring section. Pressure proliles were recorded by two-beam oscillograph, the signal of oscillograph was worked with use of computer. Real core (27 mm in diameter and 37 mm in length) of oil-saturated rocks was used as working porous sample. It was fixed at the lower part of measuring section. Lateral sides were isolated with resin, fitrational flow was upward or downward vertically directed according to the given conditions.

In the experiments core was dried beforehand under vacuum, then was saturated with air and placed at the bottom of shock tube. Then tube was carefully filled with water up to a height of 1 m above core surface, and so process of liquid filtration through gas-saturated core was initiated.

To make pulse effect, the rod of a cylindrical pistone was struck. After a shock a pistone turned back to its initial position near surface of liquid and stayed there in stressed state. Pulse propagated in liquid downwards and its parameters were recorded by piezoelectric transducers in the registering section. The pulse had the shape of bell, 0.5 MPa in amplitude and 3 ms in duration. After shock action flow rate through core was increased but it returned to its initial value in 5-10 minutes (see fig.1).

The curves in fig.1 were constructed by V.L. Nedochyotov by the way of working of experimental data with the method of trend-interpolation.
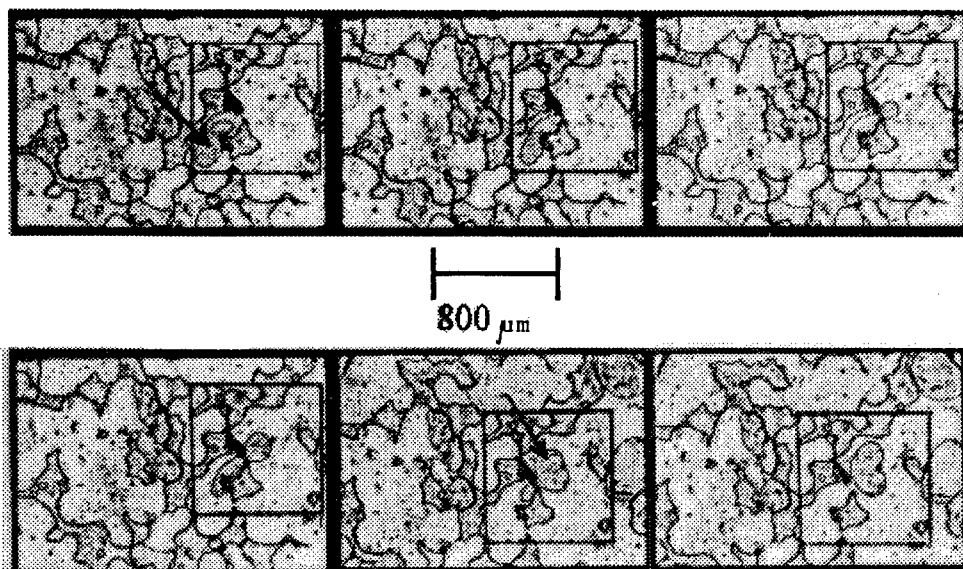
10

Fig.2. Influence of pressure waves on motion of remained gas bubbles through restrictions of pores

To gain greater insight into why phase permeability increases for some time during shock action, the experiments on plane micromodel of porous structure were performed. The porous model was made with photolithography method, it represented pore structure of real core with pore channels of 23 μm in depth, from 6 to100 μm in width. Pulses were initiated by shocks upon elastic tube which conducted water to the model. Motion of water in pores was registered with use of microscope.

The scheme of experiment was analogous to the previous one: water was filtered through porous sample saturated with air. Remained air bubbles collected before restrictions of pore channels and stayed there in spite of great pressure difference. In a situation shown in fig.2, pressure gradient is 2 MPa/m, air bubble is flowed around by liquid, but capillary force between bubble and solid and force of surface tension allowed it to stay in rest. Series of pulses in liquid phase pushed bubble through restriction. After the first pulse it displaced by 5 μm.

The above illustration of influence of shock pulses on mobility of remained gas bubbles allows an understanding of the short-time increasing of phase permeability of core after series of shock actions. During shock action remained gas phase is pushed through restrictions and so hydraulic resistence to motion of carrying phase decreases. Then phase permeability returned to its previous value as bubbles.

CONCLUSION

When pressure wave propagating from liquid to liquid-saturated porous medium, it amplifies and devides into two waves, that are fast and slow modes. In the fast mode both liquid and skeleton are copressed, their velocities are close together and have the same directions. In the slow mode velocities of phases are opposite in sign; at that liquid has positive

11

velocity and is compressed while skeleton has negative velocity and is rarefied. Amplitude of fast wave is greater than that of slow wave. Slow wave damps strongly because of interaction forces between phases. Increase of porosity results in decrease of speed and amplitude of fast wave as well as increase of speed and decrease of amplitude of slow wave. Steepness of waves does not vary. When intensity of incident wave growing, intensity of fast wave relative to intensity of incident wave does not vary practically, and that of slow wave non-monotonously varies (first incsreases and then decreases). Steepness of slow wave decreases.

The experimental investigations on action of pressure pulses on water-and-air-saturated core allowed to find the effect of short-time increase of phase permeability after the pulse action and to explain it qualitatively by illistration of motion of the remained gas phase in pores of micromodel at pressure pulse action.

REFERENCES

1. Kuchumov R.Ya. Application of vibroaction method in oil recovery. Ufa: Bashk. Kn. Izd., 1988.
2. Popov A.A. Shock action on bottom zone of well. - Moscow: Nedra, 1990.
3. Nigmatulin R.I. Dynamics of Multiphase Media. - Hemisphere Publ. Corp.: New York, 1991.
4. Gubaidullin A.A., Urmancheyev S.F. Numerical Modelling of Compression Wave Passage from Liquid to Liquid - Saturated Rorous Media // Trans. of TIMMS. - Tyumen, 1992. - No3. - P.16-21.

AEROACOUSTIC RESONANCE AND COUPLED PHENOMENA IN FLOWS WITH COHERENT STRUCTURES

S.P. Bardakhanov, O.V. Belay
Institute of Theoretical and Applied Mechanics
Siberian Division of Russian Academy of Sciences
Novosibirsk, RUSSIA, 630090

The boundary layer has been a subject of investigation since the beginning of the XXth century because it does constitute in significant extent forces affecting a body placed to a stream of liquid or gas. Conditions in which the boundary layer detaches the surface of the body can change the drag catastrophically - from extremely small value in a flow without separation over an airfoil to quite large one when global separation occurs. If flowed body is bluff, then, with the Reynolds number getting great enough, unsteady flow regime set in. The flow pattern is constituted in this case by interaction between vortical disturbances of boundary layer and acoustical disturbances of external flow. Vortical-acoustical interaction consists of the receptivity of the boundary layer (and, in particular, of the separation region) [1] and of the sound generation by separating boundary layer. To comprehend the mechanism of this interaction, it is necessary to study the wake flow past the body, where disturbances develop introduced by sound in the separation region.

Turbulent wake behind bluff bodies contains large-scale regular structures resulting from interaction between vortical disturbances of the boundary layer and external flow, when the boundary layer separates from the trailing edge of the body. These structures, which can be called as «coherent», shed alternately from one side and from the other, forming an almost periodical sequence. The general flow pattern for the semicircular trailing edge is presented in figure 1.
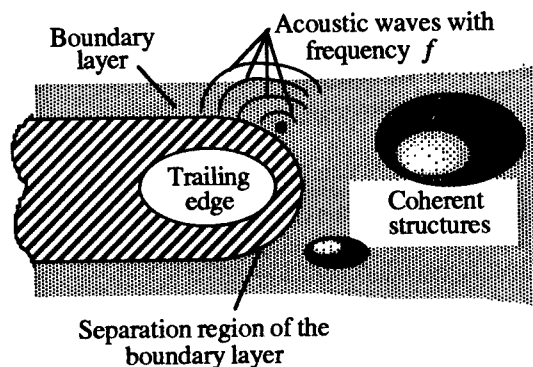

Figure 1. Flow pattern near the trailing edge.

The interaction of the vortical disturbances with the disturbances of the external flow can lead in favorable conditions to appearance of the aeroacoustic resonance [2]. The objective of this work was the study of the possibilities of flow control in resonance regime. Both «passive» (through changes of geometrical parameters) and «active» (by applying external disturbances) kinds of control are considered. The delimitation on «active» and «passive» methods is conventional to a significant extent - our study deals with the cases where the sound generator is the flow itself, but this sound can be considered as external in some sense, with the different parts of flow generating sound «almost independently».

Experimental setup

The experiments were carried out in the subsonic closed-circuit wind tunnel MT-324 with a closed working section of square cross-section, 0.2 x 0.2 m with the length 0.8 m at the Institute of Theoretical and Applied Mechanics of Siberian Division of Russian Academy of Sciences. Following experimental models were used: rectangular flat plate 200 mm length and 8 mm thick; rectangular flat plate 300 mm length, 40 mm thick; «sliding» plate 150 mm length (in downstream direction), 10 mm thick angled by 60°; and «crosses» - the models constructed from rectangular flat plates joined by their side edges. Three kinds of «crosses» were tested.

The first kind below referred to as «model 1» consisted of three rectangular plates 8 mm thick joined by their side edges on a single axis so, that angles between plates were all 120°. Two models of this type were tested: 15 (model 1a) and 30 cm (model 1b) length (in downstream direction).

The second kind of experimental models - «model 2», it consisted of a plate 20 cm wide (referred to as «horizontal») and another plate joined to the axis of symmetry of the first one so, that the latter could be rotated around the hint. The model of this type 15 cm length is below referred to as «model 2a», 30 cm length - «model 2b».

The second kind - «model 3» - was assembled from a plate 20 cm wide (referred to as «horizontal») and two plates of the same length (referred to as «vertical») joined to the «horizontal» plate's axis of symmetry, the one of the two was mounted below, and the other - above. The angles between «horizontal» and «vertical» plates were 90°. The model length was 15 cm.

The leading and trailing edges of all the models were rounded. The models were installed parallel to the flow. The scheme of the experimental setup is presented in figure 2.
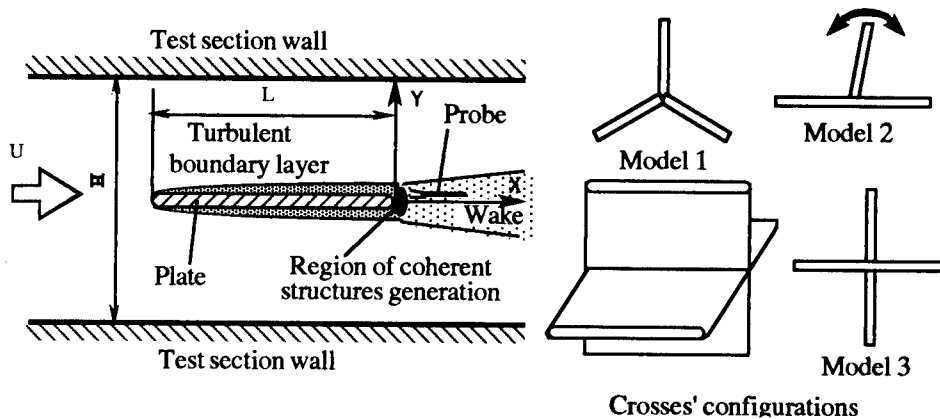

Figure 2. Scheme of experimental setup.

Mean flow speed U was measured using pitot static probe. Measurements were done in flow speed range from 5 to 45 m/s. Streamwise components of mean velocity and velocity fluctuations were measured by means of constant-temperature hot-wire anemometer with a single-wire probe. The signal of the hot-wire anemometer was passed through analog-digital converter to a personal computer, where it was then processed in digital form. In particular, narrow-band (4 Hz) spectral analysis was done.

A microphone was used for qualitative observation of sound pressure level, sound wave spectral analysis and as a reference when synchronized hot-wire readings were done.

Results

Two plates.

When loudspeaker is used to introduce a disturbance into the boundary layer, the amplitude and direction of propagation of incident sound wave depend on location and orientation of the loudspeaker as well on its amplitude-frequency characteristic. If channel flow is considered, resonant properties of the channel are important too. It leads to non uniform sound field, which also depends on sound frequency. The factors enumerated result in practical unpredictability of sound velocity magnitude and direction in the region where sound transforms to boundary layer disturbance. By the reasons mentioned above, a question appears to be interesting about effectiveness of aeroacoustic resonance as an origin of disturbances of boundary layer on a body, that is not involved in resonance generation. An effort was made to introduce a disturbance with the frequency quite different from the natural one to the wake behind the plate 40 mm thick (it is below referred to as «thick»). Resonant sound generated by additional («thin») plate 8 mm thick was used as an origin of the disturbance. The «thin» plate was installed between the «thick» plate and test section wall. It was shown by means of phase measurements in the wake behind the «thick» plate, that there was no sound transformation to disturbance of the wake.

«Crosses»

Model 1a was installed in square test section of the wind tunnel. This model did not present clearly heard resonance. Model 1b when installed in square channel generated louder sound. Mounting it in the round test section (the round insertable unit was set into square test section) resulted in greater sound level and allowed to observe dependence of resonant oscillations from orientation of the model (when it was being turned around its longitudinal axis). As it was found, the plates of the model equally contributed in resonant sound generation with some orientations chosen (it damaged the resonance when pivot of half-span length was placed in the region of coherent structures shedding on the trailing edge of any plate). When the other orientations were chosen the only two of plates were important. Not only trailing edges but also the regions near the leading edges of the models had significance for generation of the resonance observed. Beating was heard in resonant sound at some flow speed.

Model 2a was installed in square test section and like model 1a did not generate intensive sound. Shortening to 15 cm (model 2b) and then setting the round insertable unit led to the increase of sound intensity. When upper cover of the test section was removed, the additional growth in sound level was observed (the insertable unit was shorter than the test section, and with the cover removed the flow was rebuilt). Unlike model 1 resonance could be broken by the pivot placed in separation region only at the «horizontal» plate.

Model 3 was installed in square channel and generated loud sound. Beating was heard in the sound, it is shown schematically in figure 3. The model modifications (removal of one of the «vertical» plates, the changes of the angles between the plates) did not result in decrease of sound level.

«Sliding» plate

An aeroacoustic resonance was observed in tests with the «sliding» plate. This resonance showed some features distinguishing it from an «ordinary» two-dimensional one on a square plate. The «shelf» on "frequency-flow velocity" plot has a marked slope, i.e., the resonant frequency gradually increases with overall change being about 30 Hz. Wake velocity fluctuation spectra make this resonance similar to a two-dimensional one with hysteresis occurred.

An attempt was done to «visualize» wake behind the model. To do this, velocity field was measured in the wake by means of hot-wire anemometer. Phase locked ensemble average of ten realizations of the signal was made for each location of measurements using microphone signal as a reference. Mean values of ten were calculated for each measuring location (realization readings were initiated by reference microphone signal). Mean velocities and streamwise
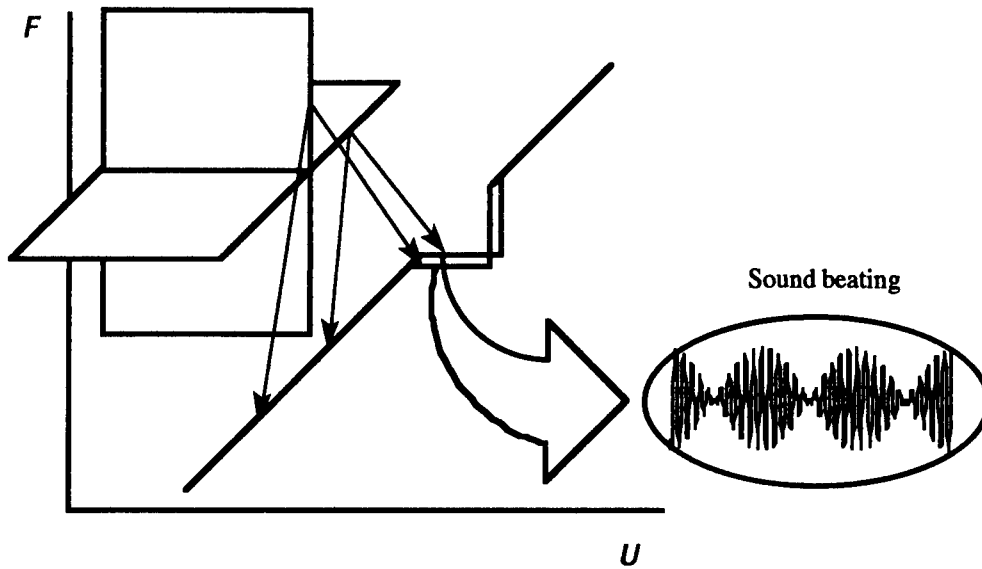
Figure 3. Dominant frequency of the wake behind model 3 versus flow speed (schematic illustration of sound beating).

velocity fluctuations were calculated from those «mean realizations». Local values of velocity fluctuations gotten in some instant (the same for all measuring region) formed streamwise fluctuation «field». Then the transversal fluctuations «field» was calculated by means of continuity equation, and then - the field of fluctuation amplitudes. Isocontours of this field are presented in figure 4. One can see at the figure that the isocontours are grouped into several formations spaced almost periodically. The formations correspond to vortices forming almost periodical street.
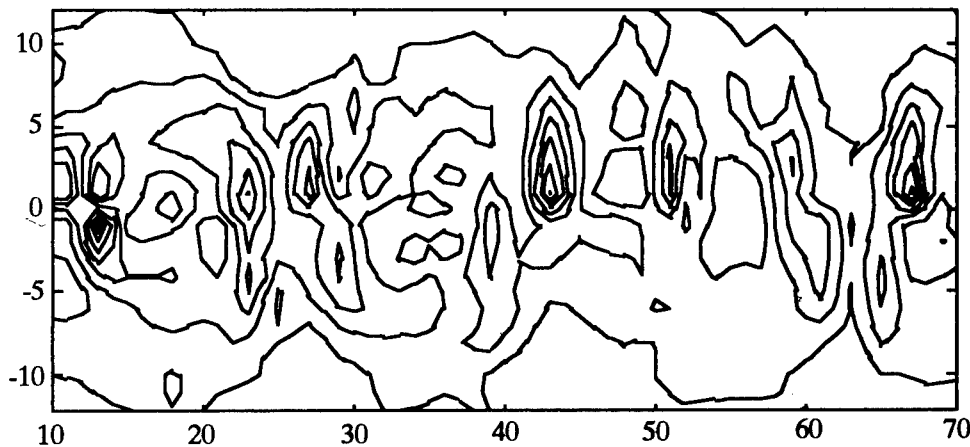

Figure 4. Isocontours of velocity fluctuation amplitudes in wake behind «sliding» plate.

Conclusions

It was shown in the paper for all considered configurations the existense of resonant sound amplification regimes conditioned by coherent structures generation.

There was no possiblility to introduce a disturbance into the wake behind the «thick» plate using resonant sound generated by the other (thin) plate, when the resonant sound frequency was quite different from the natural wake frequency of the «thick» plate.

Separation region modification either on leading or trailing edges can break the process of sound-wake synchronization. As a result the resonance can be removed.

For the "crosses" sound beating was observed in some flow speed range witnessing that several resonances are generated at the same flow speed. Each of these is generated by one of the plate forming the model.

Essential influence of the factors described above on the trailing edge region and on the flow as a whole confirms the importance of the conditions in the separation region for control of the integral flow characteristics.

References

1. S.P. Bardakhanov, V.V. Kozlov. Onset and development of coherent structures in turbulent shear flows// Perspectives in Turbulence Studies: Proc. of Int. Symp./ Eds. H.-U.Meier, P.Bradshaw. Berlin: Springer-Verlag, 1987. P. 154-187.

2. R. Parker. Resonance Effects in Wake Shedding from Parallel Plates: Some Experimental Observations// *J. of Sound and Vibration*. 1966. Vol. 4, No. 1. P. 62-72.

THE STABILITY OF DISPERSED FLOWS CLOSED TO PLANE PARALLEL ONES

E. V. Belkina, E. B. Isakov, V. Ya. Rudyak

Novosibirsk State University of Civil Engineering
630008, Novosibirsk, Russia

INTRODUCTION

Present work continues the investigations series related to a dispersed flows stability [1-6]. The plane Poiseuille and Couette flows, wake and jet had been studied early within the frame of linear theory. Of course, our investigation can not be complete without a boundary layer consideration.

Dispersed boundary layer has a relatively complex structure because of its non-parallelism. In addition this structure depend on number of conditions such as initial distribution of dispersed phase and so it can be various. Two different approach to this problem are possible. The first one is to study some typical configurations of dispersed flow and after that to pick out general features. The second way is to investigate the most general boundary layer at once. We had selected the last approach.

THE FIRST STAGE: PARALLEL APPROXIMATION

Let us consider two-phase flow near a flat plate. We shall assume that a carrier fluid is viscous and non-compressible, hard particles of dispersed phase do not interact one with other. The interphase force supposed to be a proportional to a difference between the phases velocities. The detailed description of such a media model can be found in [1,2,6]. It was shown there that both phases have the same velocity profile $U(y)$ in steady parallel flow. We use the Blasius profile and model Polhausen profile and obtain the similar results. Also two-phase flow can be characterized by the mass density profile of dispersed phase $f(y)$ and two similarity parameters: the Reynolds number Re and the dimensionless media relaxation time S. Estimations show that for real flows mass concentration f can reach values up to 1, and relaxation time S has a value between 10^{-2} (coarse particles) and 10^{-8} (fine particles).

Linear stability problem of the flow has the following form

$$(W - c)(\varphi'' - \alpha^2\varphi) - W''\varphi + \frac{d}{dy}(f'J\varphi) = \frac{1}{i\alpha\text{Re}}\left(\frac{d^2}{dy^2} - \alpha^2\right)^2\varphi, \tag{1}$$

$$W(y) = U(y) + fJ(y), \qquad J(y) = \frac{U - c}{1 + i\alpha S\text{Re}(U - c)}, \qquad c = \frac{\omega}{\alpha};$$

$$\varphi(0) = 0; \qquad \varphi'(0) = 0; \qquad \varphi(\infty) \to 0. \tag{2}$$

Here $\varphi\exp[i(\alpha x - \omega t)]$ is the stream function of a small flow disturbance that has wave number α and frequency ω. Relations (2) are ordinal boundary conditions.

This stability problem was solved numerically, using the well-known orthogonalization and differential factorization methods. It was shown, that flow stability essentially depends on the particles distribution in the flow.

BOUNDARY LAYER WITH UNIFORM PARTICLES DISTRIBUTION

The simplest form of dispersed phase distribution is uniform $f = \text{const}$. Neutral stability curves of two-phase boundary layer with low particle density $f = 0.05$ are shown in Fig. 1. Dashed line corresponds to one-phase flow. We can see that all the stability curves are closed one to other. Some distinguishes are seen in the upper branch neighborhood only.
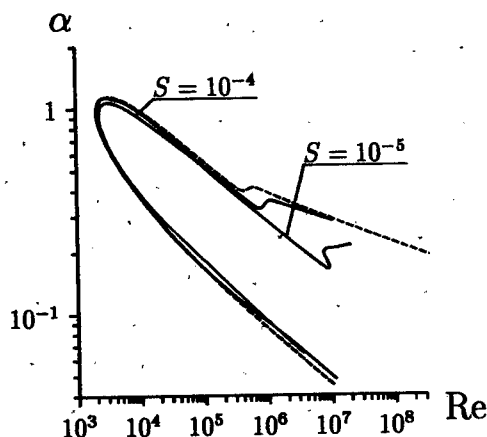

Fig. 1   Boundary layer with low density of dispersed phase ($f = 0.05$)

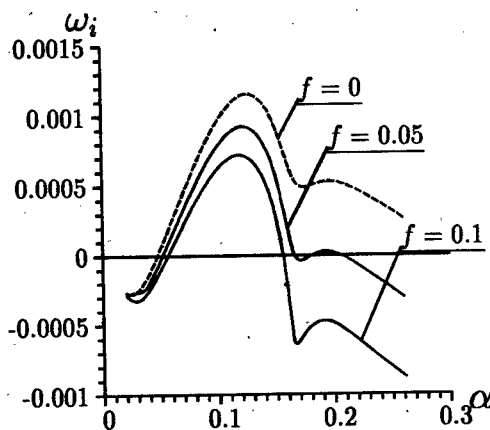Fig. 2   Disturbances growth increments ($\text{Re} = 8.3 \cdot 10^6$, $S = 10^{-5}$)

The main reason of these distinguishes is low disturbances growth increment in this region (Fig. 2). Coarse inertial particles move with average flow velocity and so they dump disturbances. If the particles concentration reaches certain critical value ($f \gtrsim 0.05$) upper branch of neutral curve can change its asymptotics.

Let us now consider boundary layer flow with high mass concentration of the particles ($f = 0.3$). Neutral stability curves of such a flow are shown in Fig. 3. There we can see opposite effect of flow destabilization when particles added. This effect takes a place at low stream velocity and so critical Reynolds number decreases. It can be explained by the change of media density with the particles addition. On the other hand, at high Reynolds number stabilization influence of dispersed phase is great so that the flow instability region changes topology ($S = 10^{-5}$). Two separated instability subregions appear. Within the range between these subregions flow becomes stable with respect to a small 2-D disturbances. Similar effect was early observed in plane Poiseuille flow [2,6]. It is necessary to note, that the flow instability within the described range is determined by 3-D disturbances, that remain growing [4].

Critical Reynolds number of two-phase boundary layer as a function of a particles size (which is proportional to $\sqrt{S}$) is shown in Fig. 4. It is seen, that there is a certain value of media relaxation time S corresponding to a maximum stabilization effects ($f = 0.05$, $f = 0.1$). Curve $f = 0.3$ has the break due to a change of instability region topology.
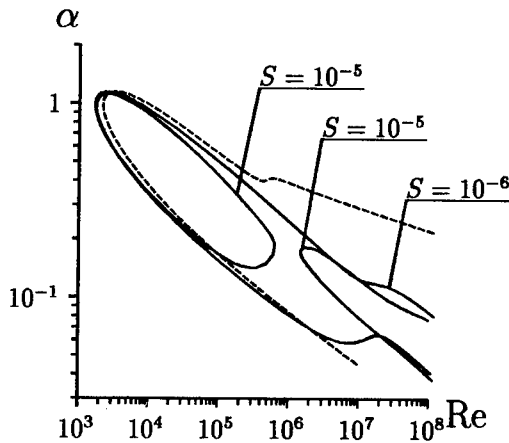
Fig. 3 Change of neutral stability curves topology at high particles density ($f = 0.3$)

Fig. 4 Critical Reynolds number of two-phase flows in boundary layer

NON-UNIFORM DISTRIBUTION OF PARTICLES

Distribution of dispersed phase in plane parallel flow can be arbitrary [2,6]. So the profile of particle density have to be according to a problem physical sense only. To the goals of present work we choose this profile in the following form

$$f(y) = f_0 \exp(-y/L). \tag{3}$$

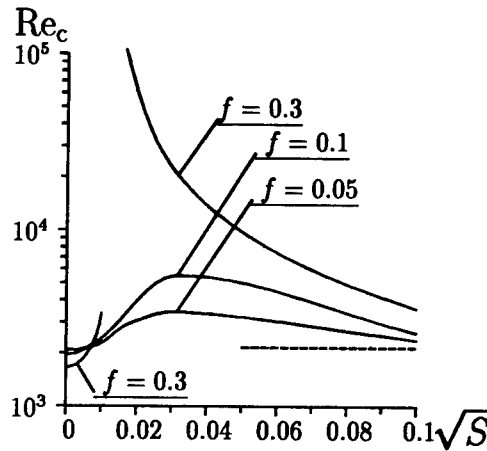Here L is characteristic width of the distribution. Such a distribution can imitate for example the sedimentation process with a satisfactory accuracy.

The neutral stability curves of boundary layer with non-uniform particles distribution (3) are shown in Fig. 5 ($f_0 = 0.3$). Instability region of uniform flow $L \to \infty$ was signified by dotted line. Distribution width L reduces it means that total number of particles decreases too. Therefore the stabilization effect of coarse particles falls down. It is seen that instability regions grow when L reduces.
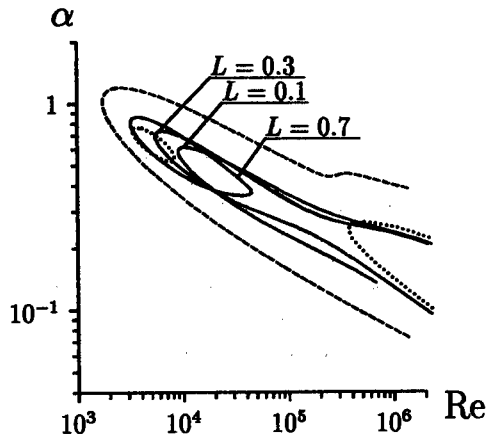

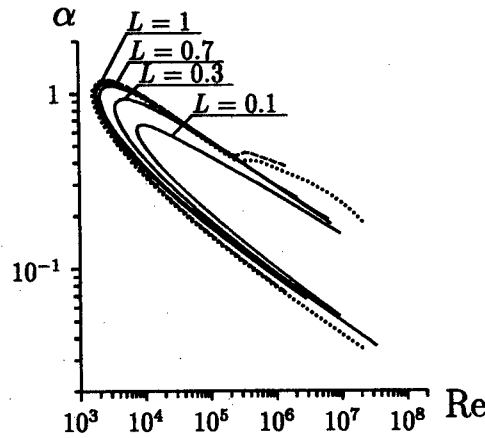Fig. 5   Boundary layer with non-uniform particles distribution, coarse particles ($f_0 = 0.3$, S $= 10^{-4}$)

Fig. 6   Boundary layer with non-uniform particles distribution, fine particles ($f_0 = 0.3$, S $= 10^{-8}$)

On the other hand the fine particles ($S = 10^{-8}$) do not stabilize flow at the Reynolds numbers up to value $Re = 10^7 \div 10^8$ (see Fig. 6). However they effectively change media density profile. So the third term

$$\frac{d}{dy}(f'J\varphi)$$

in Equation (1) become considerable when L decreases. It is seen that significant flow stabilization follows.

STRUCTURE OF STEADY BOUNDARY LAYER FLOW

It was written above the both phases have the same velocity profile in plane parallel flow. Because of non-parallelism of boundary layer this rule does not work in reality. In general sace the carrier and dispersed phases have different velocity profiles $U_f(y)$ and $U_p(y)$, respectively. We calculated these profiles for a small value of the particle mass concentration f and they are shown in Fig. 7. Two-phase boundary layer is not self-similar flow. On the other hand, such flows with different relaxation time values are

similar one to other. So the longitudinal coordinate has the special dimensionless form xSRe.
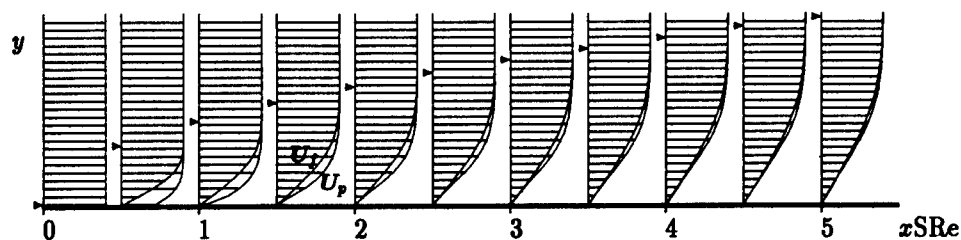

Fig. 7. Carrier and dispersed phase velocity profiles in boundary layer

As we see the velocity profiles are considerably differed within the range of longitudinal coordinate $0 < x$SRe $\lesssim 4$. All the results described above are valid in the flow domain xSRe > 4, i.e. far enough from the plate edge. In the edge neighborhood it is necessary to solve general problem with independent velocity profiles of the phases.

Since the speed of flow reduces near plate, particles density increases (see Fig. 8). Obtained dispersed phase profile can be qualitatively presented by (3).
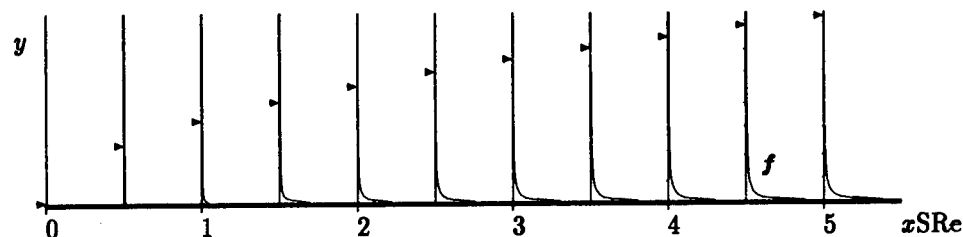
Fig. 8. Dispersed phase mass concentration profile in boundary layer

CONCLUSIONS

It was shown that boundary layer stability characteristics change considerably with hard small particles addition into the flow. Flows with the Blasius and Polhausen velocity profiles had been studied and the same qualitavely results were obtained. Some features are similar to a plane Poiseuille flow studied early. Quantitative characteristics were obtained are valid for remote region of flow. It was also shown, that in the plate

edge neighborhood carrier and dispersed phases have different velocity profiles and so it's necessary to solve generalized problem of stability.

REFERENCES

[1] Isakov E.B., Rudyak V.Ya. Stability of rarefied dusty gas and suspension flows in a plane channel//Fluid Dynamics. — 1995. — Vol. 30, $\mathcal{N}$ 5. — P. 708-712.

[2] Rudyak V.Ya., Isakov E.B., Bord E.G. Heterogeneous media stability. II. Poiseuille flow with suspended particles.-Novosibirsk State Academy of Civil Engineering: Preprint $\mathcal{N}$ 1(6)-95. — Novosibirsk, 1995.

[3] Rudyak V.Ya., Isakov E.B., Bord E.G. Stability of dispersed fluid flows. III. Wake and jet.-Novosibirsk State Academy of Civil Engineering: Preprint $\mathcal{N}$ 1(9)-96. — Novosibirsk, 1996.

[4] Bord E.G., Isakov E.B., Rudyak V.Ya., Surovtseva E.V. Stability of dispersed fluid flows. IV. Couette flow.-Novosibirsk State Academy of Civil Engineering: Preprint $\mathcal{N}$ 1(10)-97. — Novosibirsk, 1997. (In Russian)

[5] Bord E.G., Isakov E.B., Rudyak V.Ya. The stability of laminar flows of dilute dispersed media.//Fluid Dynamics. — 1997. — Vol. 32, $\mathcal{N}$ 4. — P. 495-499.

[6] Rudyak V.Ya., Isakov E.B., Bord E.G. Hydrodynamic stability of the Poiseuille flow of dispersed fluid//J. Aerosol Sci. — 1997. — Vol. 28, $\mathcal{N}$ 1. — P. 53-66.

EXPERIMENTAL INVESTIGATION OF THE SPATIAL FLOW STRUCTURE AT LATE STAGES OF LAMINAR-TURBULENT TRANSITION IN A BOUNDARY LAYER

V.I. Borodulin[1], V.R. Gaponenko[1], Y.S. Kachanov[1], C.B. Lee[2], Q. X. Lian[3]

[1] Institute of Theoretical and Applied Mechanics, Novosibirsk, Russia

[2] Institute of Atmospheric Physics Chinese Academy of sciences, Beijing, PRC

[3] Beijing University of Aeronautics and Astronautics, Beijing, PRC

INTRODUCTION

At present there are many experimental results concerning a generation and development of specific structures in the transitional boundary layer. At nonlinear stages of the transition so-called Λ-structures appear which consist mainly of a Λ-vortex [1] and 3D high-shear layer [2]. Further downstream in a vicinity of the Λ-vortex tip one can observe an appearance of very intensive fluctuations of the streamwise velocity known as 'spikes' [3,4] which represent one more kind of the coherent structures. The 'spikes' were investigated in detail in [5-9] and named as the CS-solitons (coherent structures - solitons). The process of CS-solitons generation corresponds to a multiple reconnection of the Λ-vortex tip [9-12]. Initially this sequence of events was observed only in so-called K-regime of the boundary-layer breakdown. However, it was shown recently in [13] that the same, in fact, processes of the Λ-vortex evolution and 'spikes' generation take place at later nonlinear stages of another known regime of breakdown (the N-regime). It was also found that very similar processes are observed in the developed turbulent boundary layer and it is quite probable that there is a universal mechanism of the turbulence production in the two these flows (see for example [9,14-17]). That is why a study of generation and evolution of the above mentioned structures can be very helpful for understanding both the transitional and the developed turbulent flows. Meanwhile, unfortunately, the existing amount of experimental data is not enough to obtain a complete description of the process. Several very important questions are not answered yet, namely: (i) what are the properties of the coherent structures at very late stages of the transition, (ii) which of them are similar and which are different in the transitional boundary layer and in the developed turbulent flow, (iii) what is the main mechanism of breakdown of the structures and the chaos origin at late stages of the transition, (iv) what is the role of the two kinds of the coherent structures in the process of the flow randomization, and (v) is an interaction between these structures important or not?

To find out some answers to these questions it is necessary to know quantitatively the spatial structure of the flow disturbances. At present this information is available mainly for initial stages of transition and in a plane of symmetry of the structures. The goal of the present investigation was to fulfill some of existing gaps in our knowledge by means of obtaining a quantitative information about the mean and disturbance velocity fields at late stages of the transition process.

EXPERIMENTAL MODEL AND METHODS OF MEASUREMENTS

Experiments were carried out in a low-turbulence wind tunnel T-324 ITAM at a free stream velocity $U_0 = 9.18$ m/s under controlled disturbance conditions. Similar to experiments [11] the perturbations (harmonic in time) were introduced into the flat plate boundary layer by means of a vibrating ribbon combined with a very small (specially shaped) roughness strips pasted onto the plate surface under the ribbon. For convenience of comparison the mean-flow and disturbance parameters have been chosen approximately the same as in the previous studies (for example in [4,11]). Namely the K-regime of transition was realized and studied. The initial disturbance with frequency 81.4 Hz had rather high amplitude and was almost two-dimensional one with the only small local maximum near the spanwise position $z = 0$. Further downstream a formation of Λ-structures and their subsequent development took place in a vicinity of this

position (called usually the 'peak' position). A more detail description of the experimental conditions is presented in [11]. All main measurements were conducted by means of a hot-wire anemometer with a linearizer. A single-wire probe had a wire of 6 μm in diameter and 0.3 mm length of its sensitive element. that provided a very well spatial resolution of the measurements. The probe was mounted on an (x,y,z)-traverse. The following coordinate system was used in the present paper: x is the streamwise coordinate ($x = 0$ at the plate leading edge), y is the normal-to-wall coordinate, z is the spanwise coordinate.

It is not easy to choose a proper method of the data processing for the present case. The matter is that the late stages of transition are very sensitive to the flow and disturbance parameters. For this reason it is practically impossible to obtain a perfect repeatability of disturbance fields (which are periodic in time originally) even within one set of measurement. Moreover. at very late stages of transition the deterministic processes (such as reconnection of the Λ-vortex 'legs') are interfered by a process of flow randomization and a spatial location of the structures is varied from one fundamental period to another. It is very useful to use in this case a kind of conditional sampling technique to obtain the deterministic part of the instantaneous flow field but the result of its application depends significantly on 'a priori' information about the structures studied. In the present investigation we widely used the ensemble averaging technique and measured the streamwise components of the mean velocity field $U(x,y,z)$ and the instantaneous disturbance fields $u'(x,y,z,t)$. The disturbance phases were measured with respect to a clock generator that feed the vibrating ribbon.
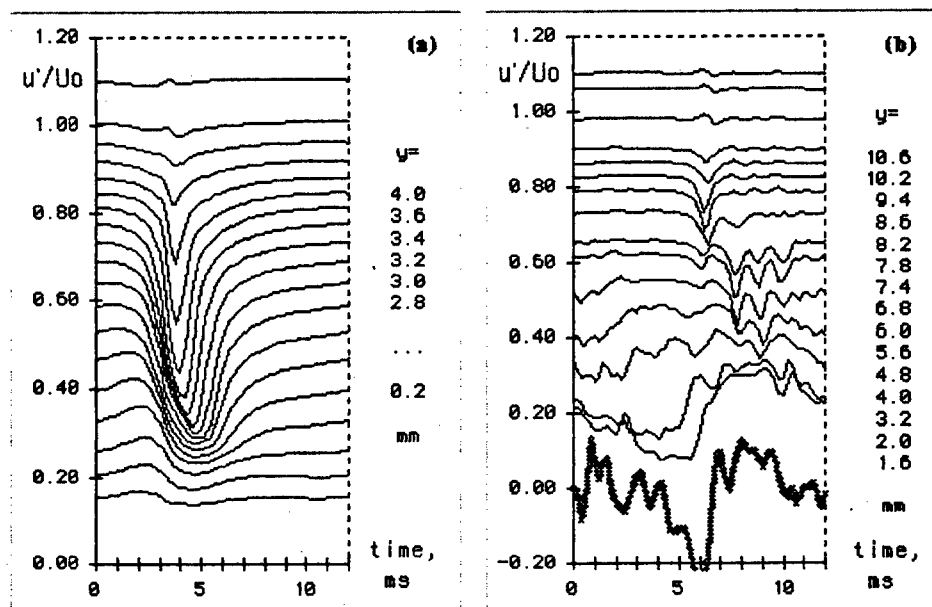

Fig. 1. Ensemble averaged time traces $u'(t)$ recorded in the plane ($z=0$) at different y positions. $x=450$ mm (a), $x=550$ mm (b).

The ensemble averaged data presented in the present paper are very useful for quantitative comparison with calculations despite some details are hidden due to the procedure of averaging. For example non-averaged time traces show that the Λ-vortex tip reconnects many times, but only few reconnections can be seen on the averaged traces due to a very strong spatial (and temporal) localization of the spike and a rather intensive modulation of its phase in time at late stages of transition. To observe the details hidden by averaging the instantaneous not-averaged signals (synchronized with the reference one) were also documented in the most of spatial

25

points. This information is important for investigation of non-periodical perturbations at stages of the flow randomization but it is not discussed in the present short paper. An additional very important data can be obtained by means of a flow visualization which gives a real instantaneous information about the flow field as a whole; despite this information is only qualitative. This method was used in another paper prepared by almost the same authors and published in this volume [18].

RESULTS OF MEASUREMENTS

A set of time-traces $u'(t)$ measured in the peak position at two streamwise coordinates are shown on Fig. 1. Lower traces are obtained in the near-wall region, the upper ones — in the external part of the boundary layer. Fig. 1a corresponds to a 'one spike' stage ($x = 450$ mm). The flow at this stage is very regular (periodic) despite the disturbance amplitudes (the magnitude of the spikes) are very high and exceed 40% of the free-stream velocity. Fig. 1b corresponds to a rather late stage ($x = 550$ mm) where, in contrast, the ensemble averaged perturbations have much lower magnitudes than at the previous stages. The flow in the near-wall region is very irregular at this stage and rather close to the turbulent one. Some irregular motions are visible at $x = 550$ mm even on the ensemble averaged time-traces but they are much more pronounced on a not-averaged time-trace shown at the bottom of Fig. 1b as a bold gray line. This trace was recorded at the same spatial position as the lowest averaged one. A rapid 'jump' of the velocity perturbation from negative to positive values is seen on the two time traces. As it was shown in [11,12] this jump corresponds to the high-shear layer positioned above the Λ-vortex . It is important to note that first four spikes appeared at $x \approx 470$ mm are still observed at $x = 550$ mm in the outer part of the boundary layer (Fig. 1b) demonstrating a very strong conservatism of the CS-solitons (the ring-like vortices) attributed to the spikes.
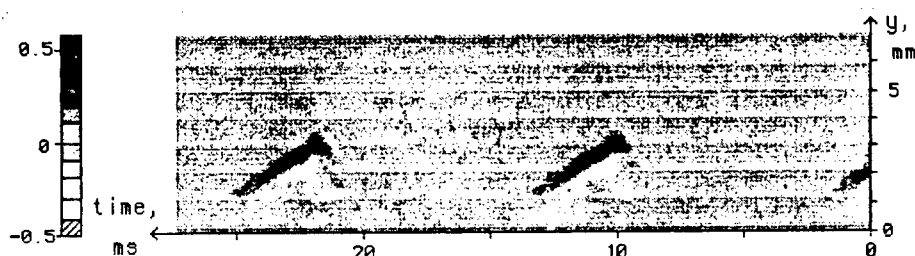

Fig. 2. Contours of instantaneous spanwise vorticity ω_z in (y,t)-plane: $x = 450$ mm, $z = 0$.

Figs 2 to 4 display contours of instantaneous du/dy which coincide in the boundary layer (with a very high accuracy) with the spanwise vorticity ω_z. Fig. 2 contains the data obtained in the peak position for the 'one-spike' stage. It demonstrate a shape of a cross-section of the Λ-shaped 3D high-shear layer (HS-layer) located rather close to the wall and continuously stretching when moving downstream. The first spike on time traces is observed *under* the tip of the HS-layer where the instantaneous flow velocity is low. Meanwhile *above* the HS-layer the instantaneous velocity is high and near the HS-layer tip a small positive spike is seen on the time traces (Fig. 1a). When the hot-wire probe is positioned close to the wall a jump of the instantaneous velocity fluctuation from negative to positive values is observed (Fig. 1b) at the time moment when the HS-layer pass the probe. The ring-like vortices [10,11] start only to form at this early stage of the transition.

The 3D structure of the HS-layer is visually seen in Fig. 3 where the spanwise vorticity fluctuation is shown in the (y,z)-plane at $x = 450$ mm. The sequence of figures from Fig. 3a to Fig. 3d corresponds to displacement along the Λ-structure (or the Λ-shaped HS-layer) in the streamwise direction. It is seen the following: (a) a cross-section of the Λ-structure 'legs', (b)

the 'legs' are converging and moving away from the wall, (c) a cross-section of the Λ-structure near its tip (the 'legs' are merged), (d) the very tip of the Λ-structure.
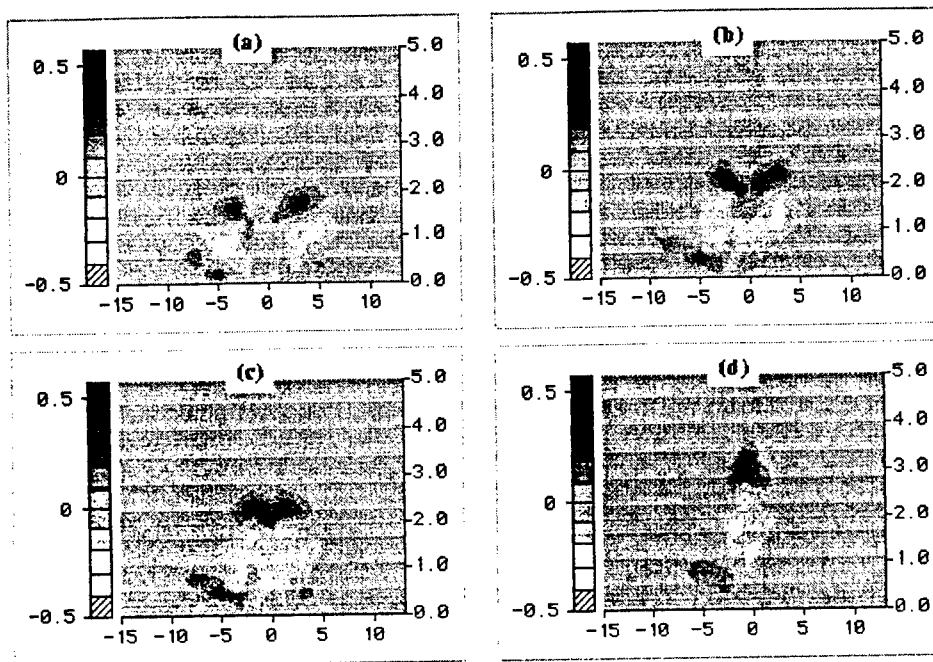

Fig. 3. Contours of spanwise vorticity ω_z in (y,z)-plane for 4 time moments; $x = 450$ mm.

Far downstream (at $x = 550$ mm) the 3D HS-layer (which is located mainly between the 'legs' of Λ-vortex and slightly above them) becomes stretched very much because its near-wall 'tails' move slower than the tip. At this stage the tip of the Λ-vortex reconnects many times and produce a sequence of the CS-solitons (the ring-like vortices) seen in Fig. 1b as a set of spikes. Their cross-sections are observed in Fig. 4c and 4d as couple regions positioned rather far from the wall ($y \approx 4$ to 7 mm) with a positive (upper region) and negative (lower region) spanwise vorticity. Of course, the side parts of the rings are not visible on the pictures of the spanwise vorticity presented in these figures because the vorticity vector is nearly perpendicular to the wall. Fig. 4d corresponds to the first ring-like vortex (attributed to the first spike), while Fig. 4c — to the second one. [Note that there are no any significant perturbations in this region in the other time moments between these two pictures.] One can see that at this stage the ring-like vortices are not connected with the HS-layer (that is seen at $y \approx 1$ mm at the time moments presented in Figs. 4c and 4d) They move ahead of the HS-layer with almost free-stream speed.

Fig. 4b corresponds to the time moment of merging the Λ-structure 'legs'. In the rest of the fundamental period these 'legs' remain split (two black spots in Fig. 4a). They are observed at a distance about 1 or 2 mm from the wall and have orientation almost parallel to each other and to the wall. A comparison of the pictures measured at $x = 450$ (Fig. 3) and 550 (Fig. 4) mm shows that the spanwise vorticity in the Λ-vortex remains almost the same (or becomes even greater) when moving downstream but the thickness of the HS-layer (and a 'diameter' of the Λ-vortex 'legs') gets significantly smaller due to their continuous starching.

Note also, that streamwise vortices similar to the Λ-vortex 'legs' at late stages are typically observed in the developed turbulent flow in the near-wall region.[19,20], as well as in the transitional boundary layers at high levels of the external perturbations (the 'bypass' transition) (see e.g. [21]) and are called very often 'the streaky structures'. The ring-like vortices and

spikes also represent very typical phenomena observed in the outer part of the turbulent boundary layer [22,23]. This similarity testifies to a universality of the mechanisms of turbulence production discussed in the present paper.
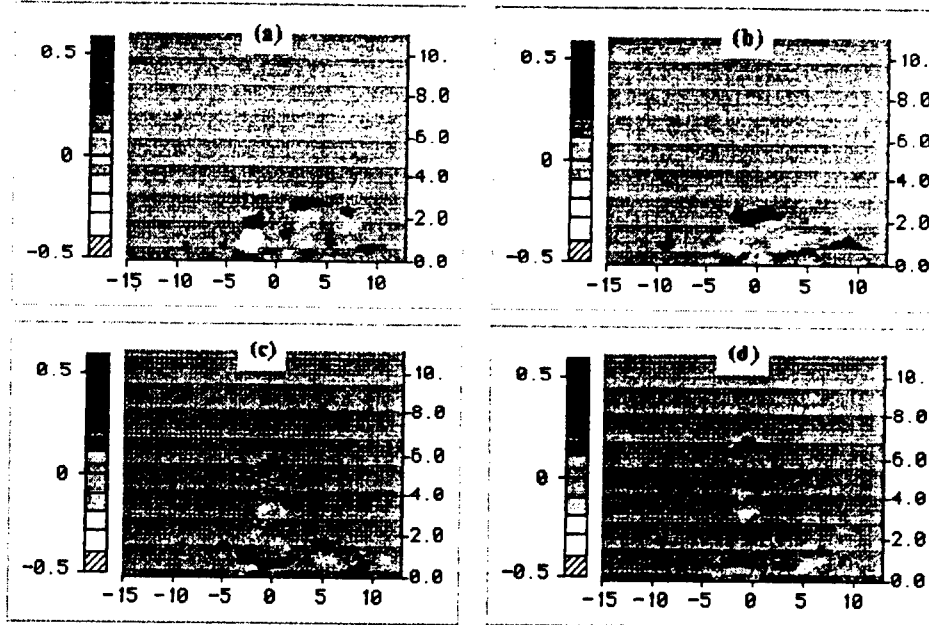

Fig. 4. Contours of spanwise vorticity ω_z in (y,z)-plane for 4 time moments; $x = 550$ mm.

Conclusions

The data obtained in present experiments confirm completely the notions on the evolution of the 3D nonlinear structures in transitional boundary layer and provide an additional information about these phenomena. The present results are in a very good qualitative agreement with direct numerical simulations, in particular with those performed in the Stuttgart's research group (see for instance [10,12]), and can be used for subsequent quantitative comparison and validation of the theory.

This data is very important also for understanding the physical mechanisms of the turbulence production in the developed turbulent near-wall flows.

Although the results discussed above concern mainly the ensemble averaged values, a future processing of the experimental data obtained in the present study will provide new additional information regarding the mechanisms of the flow randomization.

References

1. Hama F.R., Nutant J. Detailed flow-field observations in the transition process in a thick boundary layer // Proc. 1963 Heat Transfer & Fluid Mech. Inst. - Palo Alto, Calif.: Stanford Univ. Press, 1963. P. 77-93.

2. Kovasznay L.S., Komoda H., Vasudeva B.R. 1962. Detailed flow field in transition // Proc. 1963 Heat Transfer & Fluid Mech. Inst. - Palo Alto, Calif.: Stanford Univ. Press, 1963, P. 1-26.
3. Klebanoff P.S., Tidstrom K.D., Sargent L.M. The three-dimensional nature of boundary-layer instability // J. Fluid Mech. - 1962. - Vol. 12. - P.1-34.
4. Kachanov Y.S., Kozlov V.V., Levchenko V.Y., Ramazanov M.P. The nature of K-breakdown of laminar boundary layer // Proc. Siberian Div. USSR Acad. Sci., Ser. Tech. Sci. - 1989. - No 2. - P. 124-158 (in Russian).
5. Borodulin, V.I. & Kachanov, Y.S. Role of the mechanism of local secondary instability in K-breakdown of boundary layer // Izv. Sib. Otd. Akad. Nauk SSSR, Ser. Tekh. Nauk. - 1988. - Vol. 5, No 18. - P. 65-77 (in Russian). (Transl. Soviet J. Appl. Phys. - 1989. - Vol. 3, No 2. - P. 70-81.)
6. Borodulin V.I., Kachanov Y.S. Experimental study of soliton-like coherent structures in boundary layer // Proceedings of Scientific & Methodological Seminar on Ship Hydrodynamics, 19th Session. Vol. 2. - Varna: Bulgarian Ship Hydrodyn. Center, 1990, P. 99-1 - 99-10.
7. Kachanov Y.S., Ryzhov O.S., Smith F.T. Formation of solitons in transitional boundary layers: theory and experiments // J. Fluid Mech. - 1993. - Vol. 251. - P. 273-297.
8. Lee C.B., Lian Q.X. Combined CS-solitons, CS-solitons and wave resonant concept // IUTAM Symp. on Nonlinear Instability and Transition in Three-Dimensional Boundary Layers / P.W. Duck & P. Hall. - Dordrecht: Kluwer, 1995.
9. Kachanov Y.S. Physical mechanisms of laminar-boundary-layer transition // Annu. Rev. Fluid Mech. - 1994. Vol. 26. - P. 411-482.
10. Rist U., Kachanov Y.S. Numerical and experimental investigation of the K-regime of boundary-layer transition // Laminar-Turbulent Transition / R. Kobayashi - Berlin: Springer, 1995, P. 405-412.
11. Borodulin V.I., Kachanov Y.S. Formation and development of coherent structures in transitional boundary layer // Applied Mechanics & Technical Physics. - 1995. - Vol. 36, No 4. - P. 60-97.
12. Rist U., Fasel H. Direct numerical simulation of controlled transition in a flat-plate boundary layer // J. Fluid Mech. - 1995. - Vol. 298. - P. 211-248.
13. Bake S., Kachanov Y.S., Fernholz H.H. Subharmonic K-regime of boundary-layer breakdown // Transitional Boundary Layers in Aeronautics. - Amsterdam: North-Holland, 1996, P. 81-88.
14. Kline S.J., Reynolds W.C., Schraub F.A., Runstadler W.P. The structure of turbulent boundary layer // J. Fluid Mech. - 1967. - Vol. 30. - P. 741-773.
15. Repik, E.U., Sosedko, U.P. Studies of intermittent flow structure in near-wall region of turbulent boundary layer.-Turbulent Flows. Moscow: Nauka Publ., 1974 (in Russian).
16. Blackwelder R.F. Analogies between transitional and turbulent boundary layers // Phys. Fluids. - 1983. - Vol. 26, N 10. - P. 2807-2815.
17. Lian Q.X. A visual study of the coherent structure of the turbulent boundary layer in flow with adverse pressure gradient // J. Fluid Mech. - 1990. - Vol. 215. - P. 101-214.
18. Lee C.B., Lian Q.X., Du X.D., Borodulin V.I., Gaponenko V.R., Kachanov Y.S. Combined study of mechanisms of evolution and breakdown of coherent structures in transitional boundary layer at controlled conditions // Proc. of Int. Conference on Methods of Aerophysical Research. - Novosibirsk: Inst. Theor. & Appl. Mech., 1998. Pt 1, P. 141-146.
19. Kendall J.M. Experimental study of disturbances produced in a pre-transitional laminar boundary layer by week freestream turbulence.-AIAA Paper 85-1695, 1985.
20. Gulyaev A.N., Kozlov V.E., Kuznetsov V.R., Mineev B.I., Sekundov A.N. Interaction of a laminar boundary layer with external turbulence // Fluid Dyn. - 1990. - Vol. 24, N 5. - P. 700-710.
21. Elofsson P.A., Alfredsson P.H. An experimental investigation of oblique transition in a Blasius boundary layer // EUROMECH Colloquium 359. - Stuttgart, Mach 3-6, 1997.
22. Falco R.E. Coherent motions in the outer region of turbulent boundary layer // Phys. Fluids Suppl. - 1977 - Vol. 20, No 10. - P. S124-S132.
23. Thomas A.S.W., Bull M.K. On the role of wall-pressure fluctuations in deterministic motions in the turbulent boundary layer //J. Fluid Mech. - 1983. - Vol. 128. - P. 283-332.

A METHOD OF EXPERIMENTAL DETERMINATION OF THE LINEAR RECEPTIVITY COEFFICIENTS OF A 3D BOUNDARY LAYER SUBJECTED TO MICROSCOPICSURFACE NON-UNIFORMITIES. VERIFICATION OF THEORY

J.D. Crouch[1], V.R. Gaponenko[2], A.V. Ivanov[2], Y.S. Kachanov[2]

[1] Boeing Commercial Airplane Group, Seattle, U.S.A.

[2] Institute of Theoretical and Applied Mechanics, Novosibirsk, Russia.

1. INTRODUCTION

In the modern notion of laminar-turbulent transition in swept-wing boundary layers, localized surface non-uniformities are considered to be among the most important factors influencing the transition location. However, despite the great practical interest in this problem, there are few studies containing quantitative data about the swept-wing boundary-layer receptivity to surface non-uniformities (both stationary and non-stationary). Recently these problems were studied experimentally in [1,2] and theoretically in [3-5]. The main goal of the present paper is to carry out a quantitative comparison of the swept-wing boundary-layer receptivity characteristics obtained in experiments [2] with the theoretical ones based on a linear receptivity theory [4,5].

Previous experience in the experimental investigation of swept-wing boundary-layer receptivity to stationary surface non-uniformities (see [6]) shows the extreme complexity of directly obtaining the linear receptivity coefficients. The difficulties result from a circumstance that even in the best low-turbulence wind-tunnels the free stream has a slow time modulation (frequencies less than 0.1 Hz) of the flow velocity with a magnitude about $0.3 \div 0.5\%$. In the presence of such background modulation, it is almost impossible to extract a weak signal (with an amplitude of about 0.01%) attributed to the zero-frequency instability modes generated by micro-roughness. In previous experiments [6] an attempt was made to increase the amplitude of the steady flow disturbance (in order to make it measurable) by means of increased roughness height. However, this resulted in non-linearity of the receptivity mechanism.

In the experimental part of the present study a new method of obtaining the roughness-receptivity coefficients is developed and used. The method incorporates an investigation of the swept-wing boundary-layer receptivity to localized surface vibrations at several disturbance frequencies (as close to zero frequency as possible) and an extrapolation of the results obtained to the zero frequency of vibrations. A correctness of the limit transition $f \rightarrow 0$ is investigated and substantiated. As a result, the coefficients of the linear receptivity of the 3D boundary layer to localized surface roughness are obtained experimentally for various values of the disturbance spanwise wavenumber. These coefficients are independent of the specific shape of the roughness and can be directly compared with the linear receptivity theory. The theoretical part of the present study is carried out within the linear framework of the swept-wing boundary-layer receptivity to localized surface non-uniformities developed in [4,5]. The calculations are performed for the conditions of the present experiments.

2. METHODS OF STUDY

2.1. Experimental procedure. The experiments were carried out at the Institute of Theoretical and Applied Mechanics (Novosibirsk) in a low-turbulence wind-tunnel T-324 on a model of a swept wing (described in [7]) with the sweep angle $\chi = 25.0°$. The mean flow was produced by the flow over a swept-plate with a pressure gradient induced by a contoured wall bump positioned over the plate on the test-section ceiling.

A special circular surface vibrator was used as a non-stationary surface non-uniformity with known geometry. The vibrator (the source) had a diameter of 20 mm and was mounted flush with the swept-plate wall at a distance $x' = x'_s = 404.2$ mm ($x_s = 466$ mm) from the leading edge, where the x'-axis is directed along the chord of the model and the x-axis — along the tunnel free-stream velocity vector. The design of the source (described in [8]) allowed control of the amplitude and frequency of the vibrations.

The measurements in the flow were performed by means of a hot-wire anemometer. A single-wire probe measured the x-component of both the mean-velocity vector and the vector of the velocity fluctuations. In every spatial point four averaged values were documented: (i) the mean flow velocity, (ii) the r.m.s. value of the total intensity of velocity fluctuations, (iii) the phases, and (iv) the r.m.s. amplitudes of the velocity fluctuations at the frequency of excitation (within an effective frequency band $\Delta f = 0.1$ Hz).

The vibrator generated the wave-trains of the instability waves which were harmonic in time and localized in the spanwise direction. The measurements were performed at 6 different disturbance frequencies: $f = 24.80, 21.43, 17.91, 15.00, 12.00$ and 9.02 Hz. At the position of the source these frequencies correspond to nondimensional frequency parameters $F = 2\pi f \nu/U_{os}^2 = 60.7 \cdot 10^{-6}, 52.4 \cdot 10^{-6}, 43.6 \cdot 10^{-6}, 36.5 \cdot 10^{-6}, 29.5 \cdot 10^{-6}$, and $22.2 \cdot 10^{-6}$ (where U_{os} is the edge velocity at $x = x_s = 466$ mm, $z = 0$, i.e. at the source position).

In the main measurements the spanwise (z'-direction) distributions of the flow velocity fluctuations were measured at 7 chordwise positions downstream the disturbance source (where the z'-axis is parallel to the leading edge of the model). During these measurements the nondimensional distance to the wall was fixed (y/δ_l = const. = 1.0) and corresponded approximately to the maxima of the cross-flow instability-wave amplitudes in their y-profiles (see section 3 below).

2.2. Analysis of experimental data.
The experimental data was analyzed according to a procedure described in [1]. With the help of the Fourier transform the wave-trains were decomposed into the normal cross-flow instability modes inclined at different angles to the flow direction. After that, the initial values of the normal mode amplitudes and phases were 'reconstructed' at the source position by means of an upstream extrapolation of the experimental data. A 2D wavenumber spectrum of the vibrator shape was determined and the 'resonant' spectral modes were selected from it with the help of the dispersion relationship obtained for the cross-flow waves. These 'resonant' modes had the same values of the streamwise wavenumber (at every fixed value of the disturbance frequency and the spanwise wavenumber) as those of the instability modes generated by the vibrations in the flow. As a result, the complex receptivity coefficients were obtained as functions of the spanwise wavenumber for each of six disturbance frequencies studied. Finally, the results were extrapolated to the zero frequency of vibrations and, in this way, the values of the roughness-receptivity coefficients were determined.

2.3. Theoretical analysis.
In the perturbation analysis, the boundary-layer flow is decomposed into a basic-state velocity and a perturbation velocity

$$V(x',y,z',t) = V_0(y,x') + \varepsilon V_\varepsilon(x',y,z',t)$$

The basic-state velocity is given by the Falkner-Skan-Cooke solutions for an undisturbed boundary layer with no spanwise variation. The chordwise (x') edge velocity is given by $U' = (x')^m$, where the value of m is chosen to locally match the experimentally-observed edge conditions. The perturbation velocity is the result of the surface membrane displacement, given by

$$y = \varepsilon H(x',z) \exp(-i\omega t), \quad \text{with } \varepsilon \ll 1.$$

The governing equations for the perturbation velocity are derived according to the quasi-parallel approximation. This approximation locally neglects the chordwise divergence of the boundary layer leading to the Orr-Sommerfeld and Squire equations governing the disturbance. For the stability analysis, these equations are solved with homogeneous boundary conditions. The modal frequency (ω) and spanwise wavenumber (β') are imposed, and the (complex) chordwise wavenumber (α') is solved for as an eigenvalue. In the receptivity analysis, nonhomogeneous boundary conditions are imposed due to the surface membrane. The surface perturbation is modeled by linearized boundary conditions derived from a Taylor expansion in terms of ε — the membrane perturbation amplitude. The $y = 0$ boundary conditions are

$$u_\varepsilon = - \partial u_{o}/\partial y, \quad w_\varepsilon = - \partial w_{o}/\partial y, \quad v_\varepsilon = - i\omega.$$

The receptivity analysis considers the forced disturbance introduced by the surface membrane. The local disturbance velocity (at the source) is given by Fourier integrals in x' and z'. After calculating the velocity components in Fourier space, the physical velocities are determined by integrating over α' and β'. The integration over α' is taken in the complex plane. Focusing on the modes which dominant the solution downstream, the α' integral is given by the residue associated of the most unstable eigenmode for a given frequency and spanwise wavenumber. The modal disturbance amplitude at the source x_0 is then given by

$$B(x'_{o}, \beta', \omega) = \varepsilon K(\alpha'_{CF}, \beta', \omega) \tilde{H}(\alpha'_{CF}, \beta').$$

where ε is a measure of the surface-perturbation amplitude, K is a (complex) response function for a given mode, and $\tilde{H}$ is the Fourier transform of the membrane shape evaluated at the eigenmode wavenumber α'_{CF}.

3. MEAN FLOW STRUCTURE

The structure of the basic flow on the experimental model was studied in detail in [6,7], including the measurements by the X- and W-shaped double-wire probes. In the region of the main measurements ($x = 440 \div 650$ mm) the potential flow velocity U_0 increased downstream and reached at the source position 6.26 m/s. The boundary-layer displacement thickness over the vibrator was $\delta_1 = 1.21$ mm, the local Reynolds number was Re $= U_0\delta_1/\nu = 498$. Shown in Fig. 1 is a comparison of measured and calculated normal-to-wall profiles of the x^*- and z^*-components of the mean-velocity vector in the boundary layer. The coordinate system (x^*,z^*) is local and the x^* - axis is directed along the potential-flow velocity vector. It is seen that there is a good agreement between the basic-flow structure studied in the experiment and in the theory.

Comparison of the eigen-functions of the normal cross-flow instability modes is presented in Fig. 2 for one of the disturbance frequencies and for two different values of the spanwise wavenumber β'. The experimental points are obtained by means of the Fourier decomposition of the corresponding wave-train into the normal oblique modes.
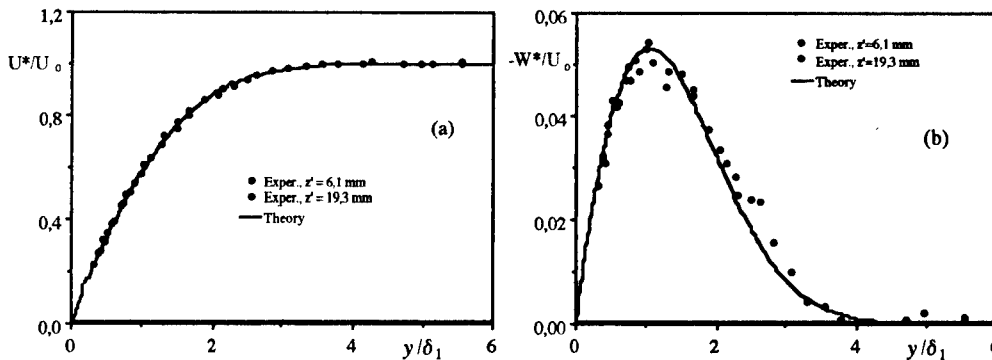

Fig. 1. Comparison of experimental and theoretical profiles of streamwise (a) and spanwise (b) components of the mean-velocity vector.
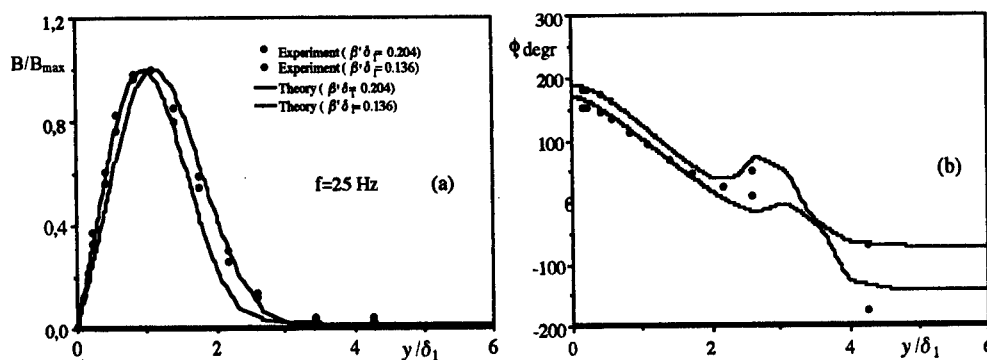
Fig. 2. Comparison of amplitude (*a*) and phase (*b*) parts of eigen functions of normal cross-flow modes.

The figure demonstrates a good agreement of the experimental and theoretical results. Fig. 2*a* shows also that the non-dimensional distance to the wall y/δ_1 = const = 1.0 used during the main receptivity measurements corresponds to an approximate position of the disturbance amplitude maximum in the *y* -profiles.

4. INITIAL SPECTRA OF CROSS-FLOW MODES

The shape of the surface non-uniformity was measured in the experiment and used in the calculations in order to compare the initial spectra of the instability waves generated by it in the boundary layer. In the experiment the values of the magnitude of the non-uniformity were chosen rather low (to avoid non-linearity) and were equal to about 40 to 50 microns.

Shown in Fig. 3 are four initial spanwise-wavenumber spectra of the cross-flow instability waves determined in the experiment and calculated at the source position. These spectra represent the boundary-layer response to the presence of the non-uniformity and characterize the flow receptivity. The results are presented for three different disturbance frequencies (Fig. 3*a*,*b*,*c*) and for the zero frequency, i.e. for the steady surface roughness (Fig. 3). It is seen that the best agreement is observed at the frequency f = 9.02 Hz. At higher frequencies and in a range of low values of the spanwise wavenumber $\beta' \delta_1$ (from 0 to about 0.2) the theory gives somewhat greater values of the initial amplitudes as compared to the experiment.
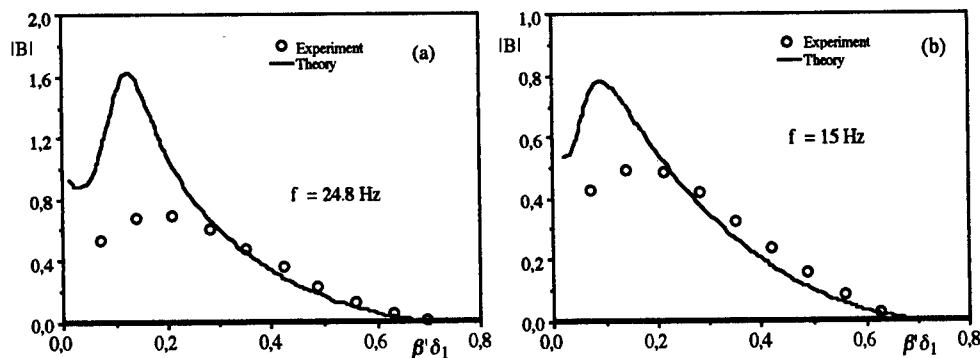

Fig. 3. Initial spanwise-wavenumber spectra of the cross-flow instability modes generated by unsteady (a,b,c) and steady (d) surface non-infirmities.
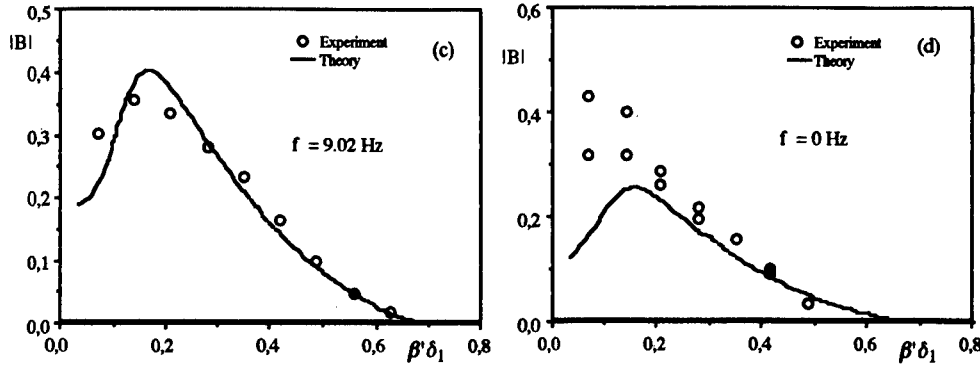
33

Fig.3. End.

For the zero-frequency (i.e. for the surface roughness) the theory, in contrast, predicts somewhat lower initial values of the cross-flow vortices. However, and this is of the most importance, in the range $\beta'\delta_1 \approx 0.3$ to 0.6, which includes the most unstable cross-flow modes (see [9]), an agreement between the theory and the experiment is very good in the whole frequency range studied, including the zero frequency.

6. RECEPTIVITY FUNCTIONS

The magnitude of the receptivity functions obtained in the theory and experiment are presented in Fig. 4 for non-stationary ($f = 9.02$ Hz) and stationary surface non-uniformities. The experimental and theoretical values of the receptivity response functions are seen to be close to each other, especially in the range of the spanwise wavenumber corresponded to the most unstable cross-flow modes. This agreement is rather good taking into account the extreme complexity of the experimental procedure of determining the receptivity coefficients — including an extrapolation of the experimental results to the position of the source and to the zero frequency of the perturbations. The results presented in Fig. 4 are independent of the shape of vibrator.
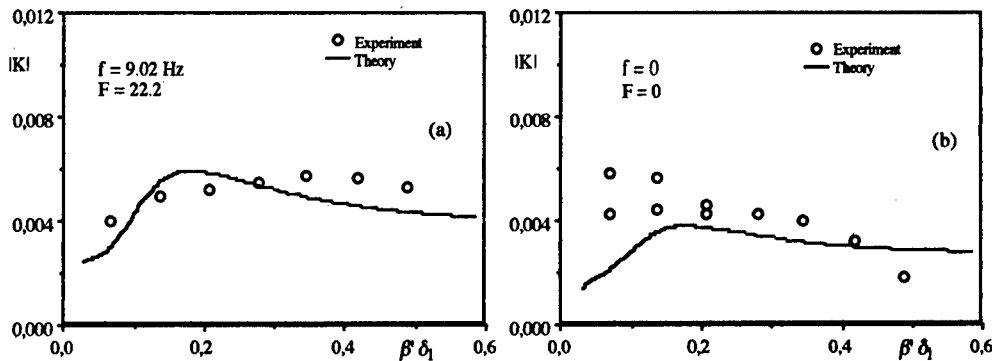

Fig. 4. Receptivity amplitudes obtained for unsteady (a) and steady (b) surface non-uniformities.

Conclusions

The method of experimental determination of the receptivity characteristics of the 3D boundary layer is developed. As a result, the quantitative characteristics of the swept-wing boundary-layer receptivity to localized surface vibrations and non-uniformities are obtained and compared with the theoretical ones. A rather good agreement of the experimental and theoretical receptivity characteristics is found in a range of values of the disturbance spanwise wavenumber and frequency corresponded to the most unstable cross-flow instability modes. This testifies to the correctness of both the theoretical and the experimental approaches and gives possibility to perform quantitative evaluations of the initial amplitudes of the cross-flow instability waves and vortices generated in the swept-wing boundary layer by unsteady and steady surface non-uniformities.

References

1. Gaponenko V.R., Ivanov A.V., Kachanov Y.S. Experimental study of 3D boundary-layer receptivity to surface vibrations //.Nonlinear Instability and Transition in Three-Dimensional Boundary Layers / Eds. P.W. Duck, P. Hall. — Dordrecht: Kluwer, 1996. P. 389-398.
2. Gaponenko V.R., Ivanov A.V., Kachanov Y.S. Experimental study of swept-wing boundary-layer receptivity to stationary and non-stationary surface non-uniformities // IV Siberian Workshop on Stability of Homogeneous and Non-homogeneous Fluid Flow: Abstracts / Ed. V.V. Kozlov. - Novosibirsk: Inst. Theor. and Appl. Mech., 1997, P. 32-34 (in Russian).
3. Fyodorov, A.V.. Generation of the cross-flow instability waves in swept-wing boundary layer // Zhur. Prik. Mekh. i Tekh. Fiz. - 1988. - No 5. - P. 46-52 (in Russian).
4. Crouch J.D. Receptivity of three-dimensional boundary layers.—AIAA Paper No 93-0074, 1993.
5. Crouch J.D. Theoretical studies on the receptivity of boundary layers.—AIAA Pap. No 94-2224, 1994.
6. Kachanov Y.S., Tararykin O.I. The experimental investigation of stability and receptivity of a swept-wing flow // Laminar-Turbulent Transition / Eds. D. Arnal , R. Michel. — Berlin: Springer-Verlag, 1990, P.499-509.
7. Kachanov Y.S., Tararykin O.I., Fyodorov A.V. 1989. Experimental simulation of swept-wing boundary layer in the region of secondary flow formation // Proc. Siberian Div. USSR Acad. Sci., Ser. Tech. Sci. - 1989. - V. 3. - P. 44-53 (in Russian).
8. Ivanov A.V., Kachanov Y.S., Koptsev D.B. Experimental study of generation of instability waves in 3D boundary layer at scattering of an acoustic wave on a vibrator // Thermophysics and Aeromechanics. -1997. - V. 4, No 4. - P. 359-372.
9. Gaponenko V.R., Ivanov A.V., Kachanov Y.S. Experimental study of swept-wing boundary-layer stability to unsteady disturbances // Thermophysics and Aeromechanics. - 1995. - V. 2, No 4. - P. 287-292.

STABILITY CALCULATION OF PRE-SEPARATION BOUNDARY LAYER FLOW AT MODERATE FREE FLOW TURBULENCE

N.D.Dikovskaya, B.Yu.Zanin

Institute of Theoretical and Applied Mechanics SB RAS

630090, Novosibirsk, Russia

INTRODUCTION

Experimental investigations [1] of the laminar-turbulent transition on an airfoil at the moderate turbulence of free stream ($\varepsilon = 0.4\%$) showed that the transition takes place by means of the development of an instability wave packet analogous to one at the low level ($\varepsilon < 0.04\%$). At the same time the frequency characteristics of that wave packet and the growth of the amplitude down stream differ one from the other in those two cases. The objective of the conducted calculation was the determination the reason discovered differences, for that the stability of the experimental mean velocity profiles in boundary layer from [1] was studied by the numerical method.

EXPERIMENTS

The experiments [1] were carried out in the T-324 low-turbulence wind tunnel (ITAM SB RAS) on an airfoil model NACA 63-2-615 (span 1 m, model chord $b=270$ mm, angle of attack $6°$) at the free stream velocity $U_\infty= 8$ m/s. Measurements were performed at two levels of turbulence of the free stream: $\varepsilon \approx 0.04\%$ (regime 1) and $\varepsilon \approx 0.4\%$ (regime 2). The mean velocity $U(y)$ in the boundary layer, the amplitude and the frequency spectra of the pulsation were measured by the hot-wire anemometer DISA.

Fig. 1 shows the experimental results based for calculation, that are (a) the distribution of pressure coefficient gradient dC_p/dX, (here $C_p=2\Delta p/(\rho U_\infty^2)$, p is the static pressure, ρ is density of air) and (b) the profile of longitudinal mean velocity in the boundary layer along model chord. For both of the considered regimes the pressure gradient dC_p/dX is positive in the investigation range $X=x/b=0.26$-0.55, and then the velocity profiles have an inflection point. The exception is the region at $X=0.2$-0.3 for the regime 2, in which the range without a gradient was formed by upon the moderate turbulence of the free stream. For both of those regimes there was the separated bubble in the neighborhood $X=0.55$ with the smaller size of the bubble for the regime 2. The boundary layer for the regime 2 was more thin, and the inflection point was at a shorter distance from the wall, then for the regime 1. Thus, the increasing of the turbulence leads to the change of the mean flow both in the external part of the boundary layer and near the wall, and in this case the relatively stable region was formed in the leading part of the model. For both of the regimes up to $X=0.55$ the boundary layer was laminar. The laminar-turbulent transition takes place by means of the development of the wave packets with the central frequencies equal $f_1=406$ Hz and $f_2=324$ Hz accordingly for the regimes 1 and 2.

CALCULATIONS

The stability of the laminar boundary layer developing under the gradient flow conditions were calculated within the frame of the linear theory of small disturbances growth under the assumption of "local parallelism" for a two-dimensional flow. Two-dimensional

disturbances $[U(y),V(y)]\exp[i(\alpha x - \omega t)]$ were considered which were the oscillations periodic in time with the amplitudes changing streamwise. Here $\alpha = \alpha_r + i\alpha_i$ is the complex eigenvalue to be determined, α_r is the streamwise wave number, $-\alpha_i$ is the spatial growth rate of disturbances (the flow is unstable, while $\alpha_i < 0$), $\omega = 2\pi f$ is the cyclic frequency of the wave. The phase velocity of the wave propagation along the flow is $C_r = \omega/\alpha_r$, $\lambda = 2\pi/\alpha_r$ is the wavelength. The Orr-Sommerfeld equation for the disturbance amplitudes $V(y)$ was solved [2,3]. Before calculating the stability, the experimental mean velocity profiles were smoothed by the polynomials of the powers $n=5$.

Figure 2 shows the results of calculations of the spatial growth rate $-\alpha_i(f)$ in various points from $X=0.26$ to $X=0.55$. Figure 3 presents $(\alpha_i)_m$ (a) and f_m(b) of maximally increasing disturbances against the distance X. For both regimes at $X=0.26$ there are not increasing disturbances in spite of the presence of the adverse pressure gradient for the regime 1.
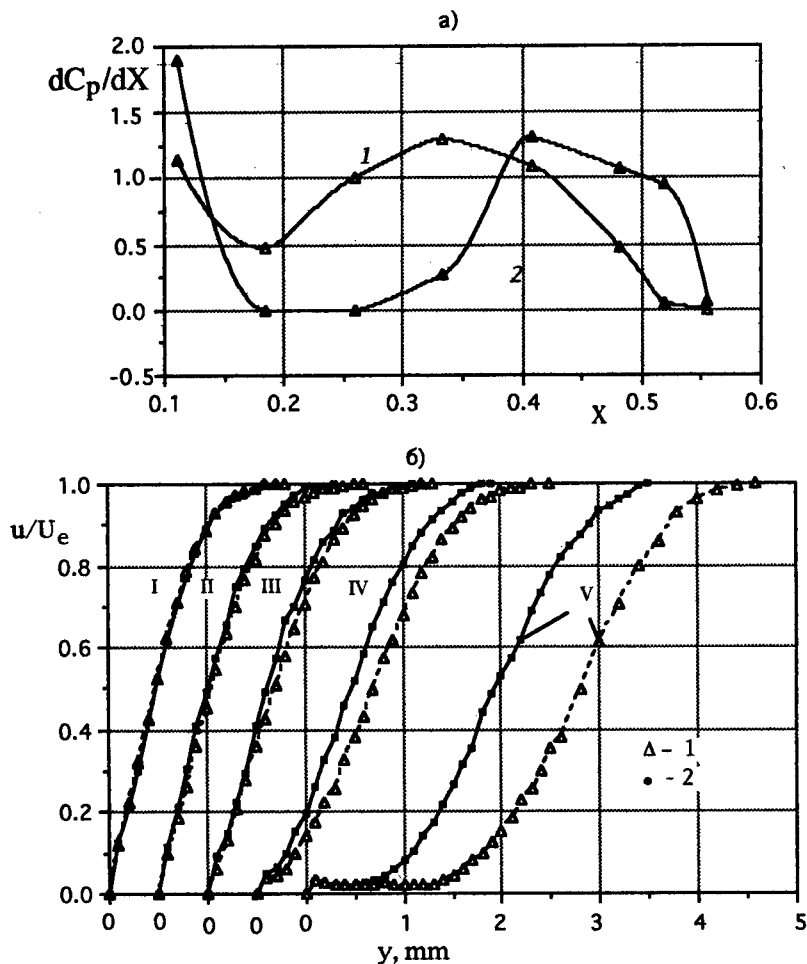

Fig.1. The distribution of pressure coefficient gradient dC_p/dX (a) and the profiles $u/U_e(y)$ of longitudinal mean velocity (b) in the boundary layer along model chord at $X=0.26$(I); 0.33(II); 0.41(III); 0.48(IV); 0.55(V) for the regime 1 (curves 1) and regime 2 (curves 2).

Downstream the unstable disturbances region is located in a frequency diapason f=200-500 Hz, that is typical for the viscous instability. For the first time the unstable disturbances appear in the cross section $(X_0)_1 \approx 0.29$ for the regime 1 and $(X_0)_2 \approx 0.39$ for the regime 2. It means, that the most high turbulence influence is at X=0.33, where the flow is stable for the regime 1, but it is unstable for the regime 2. At X>0.41 (in pre-separated region) the frequency diapason of unstable disturbances is extended, by including both the low and the high frequencies and the growth rate $-\alpha_i$ considerably increases (that is the mechanism of the inviscid instability is presents), in this case the values $(\alpha_i)_m$ for the both regimes are little different.

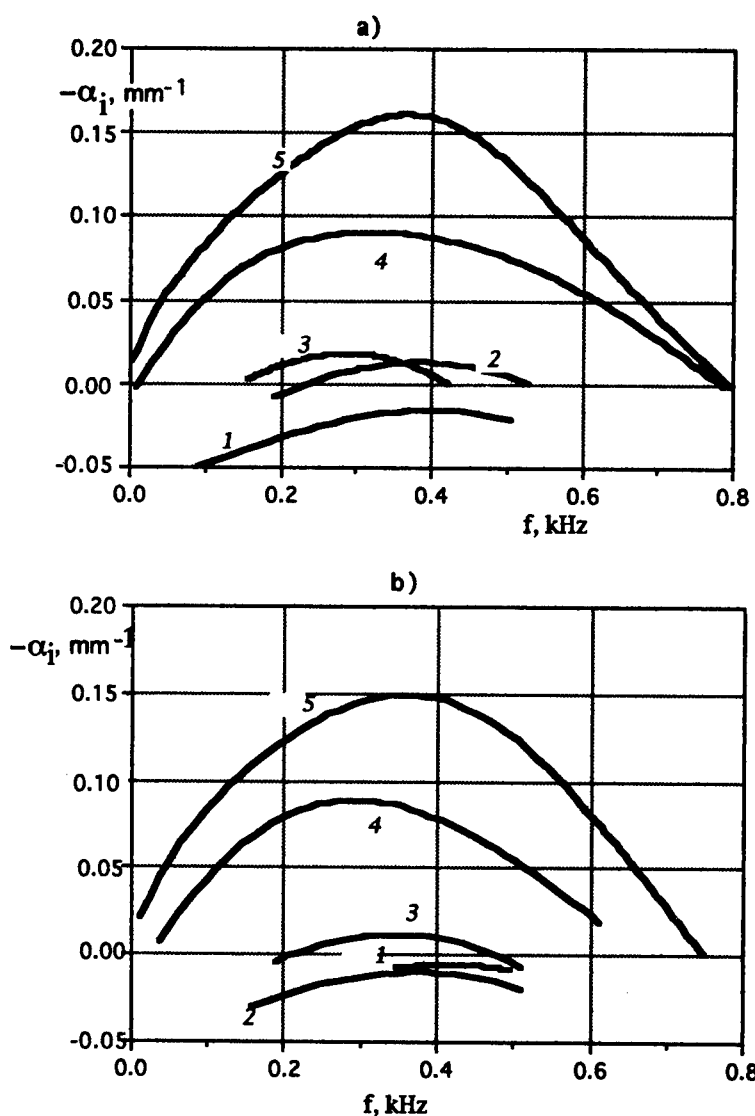The curves $f_m(X)$ (Fig.3,b) have a minimum at the pre-separation regions, and under

Fig. 2 The spatial growth rate $-\alpha_i(f)$ at X=0.26(1), 0.33(2), 0.41(3), 0.48(4), 0.55(5) for the regime 1 (a) and regime 2 (b).
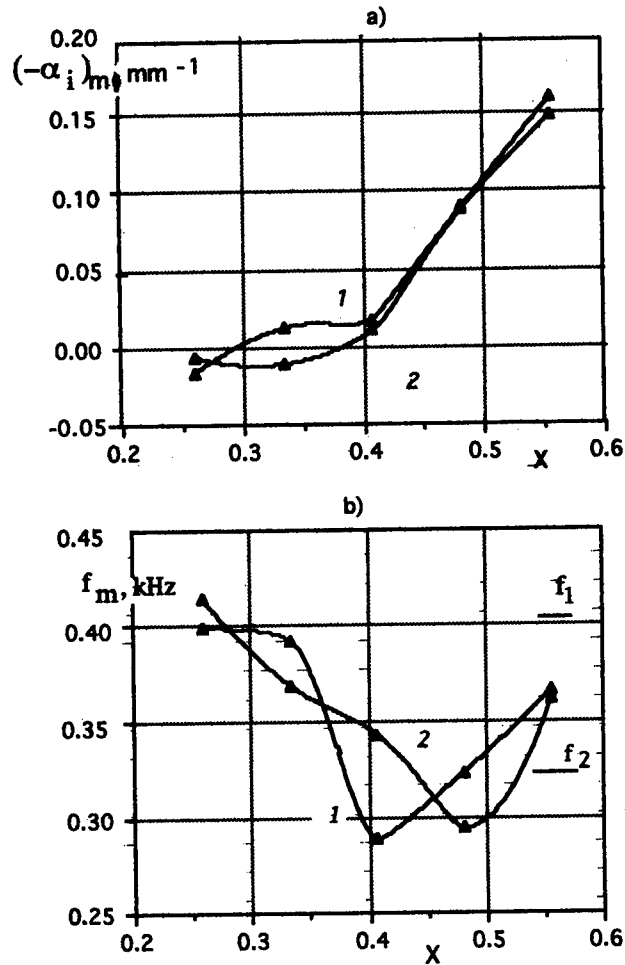
38

Fig.3. The spatial growth rate $(-\alpha_i)_m$ (a) and the frequency f_m (b) of maximally increasing disturbances against the distance X;
$1, f_1$- for the regime 1; $2, f_2$- for the regime 2, f_1 и f_2 - from [1].

the increasing turbulence it displaces downstream at the distance equal approximately the ungradient pressure region. The value of the frequency f_0, corresponding to the cross section of the stability loss X_0, changes from $(f_0)_1$=400 Hz (for the regime 1) to $(f_0)_2$=350 Hz (for the regime 2). For reference, the measured central frequencies of the wave packets f_1=406 Hz (regime 1) and f_2=324 Hz (regime 2) are plotted in Fig.3,b also. From this figure we notice that the calculation results correctly predict the remove of the unstable frequency diapason to the low-frequency region. It appears under the increasing turbulence of the free stream. Besides, for the low turbulence flow the numerical frequency quantitatively agrees with experimental date. A gap between the calculated and observed values is less then 2%. The mistake increases up to 8% for the regime 2.

The phase velocity of disturbances C_r and the velocity of the inflection point u_i are shown in Fig. 4. A line in the shaded region corresponds to the phase velocity $(C_r)_m$ of the

most increasing frequency f_m. For both regimes, as indicated in the picture, the inflection point are displaced from the wall by removing downstream, and velocity u_i increases, remaining less then C_r up to $X=0.4$. At $X \geq 0.45$ the velocity u_i and $(C_r)_m$ are approximately equal.

The wavelengths of the most increasing disturbances λ_1 obtained from the calculation, and λ experimental observed [1] are presented on Fig. 5. The wavelengths λ_δ are realized from the approximate formula $\lambda_\delta = 2\pi\delta$ [1]. This formula connects the boundary layer thickness δ with the unstable wavelength λ_δ. It is evident from the presented curves that λ_1 correlates well with λ_δ on beginning part of the range of disturbance development. That it is nearly up to $X=0.45$ for regime 1 and up to $X=0.50$ for regime 2. Downstream the results are separated. Also it seems the value λ corresponds to λ_1 that is obtained at the cross section near the maximum dC_p/dX, but not near X_0 or near $dC_p/dX=0$.

CONCLUSION

Thus, the calculated characteristics of the streamwise development of disturbances show that the moderate level of turbulence of the free flow increases the boundary layer stability on the airfoil. It makes itself evident in the fact that the region of the beginning of unstable disturbances removes downstream. It can be expected that the frequency decrease and the
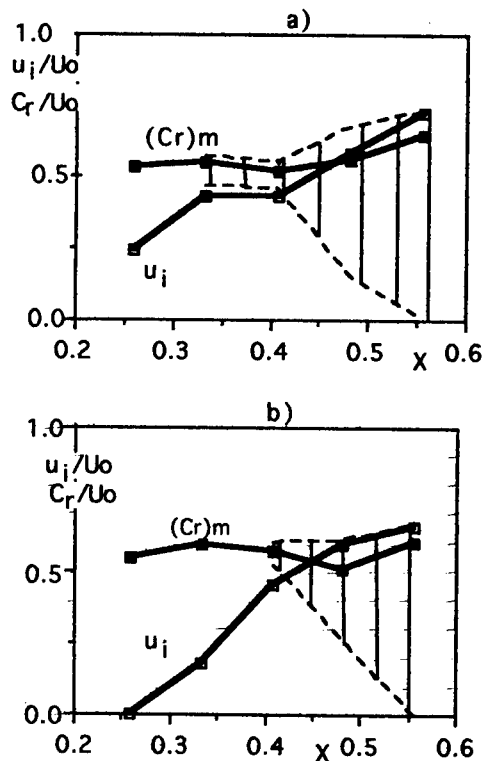

Fig.4. The phase velocity of disturbances C_r and the velocity in the inflection point u_i for the regimes 1 (a) and 2 (b). The shaded regions correspond to the phase velocity $(C_r)_m$ of the most increasing frequencies.
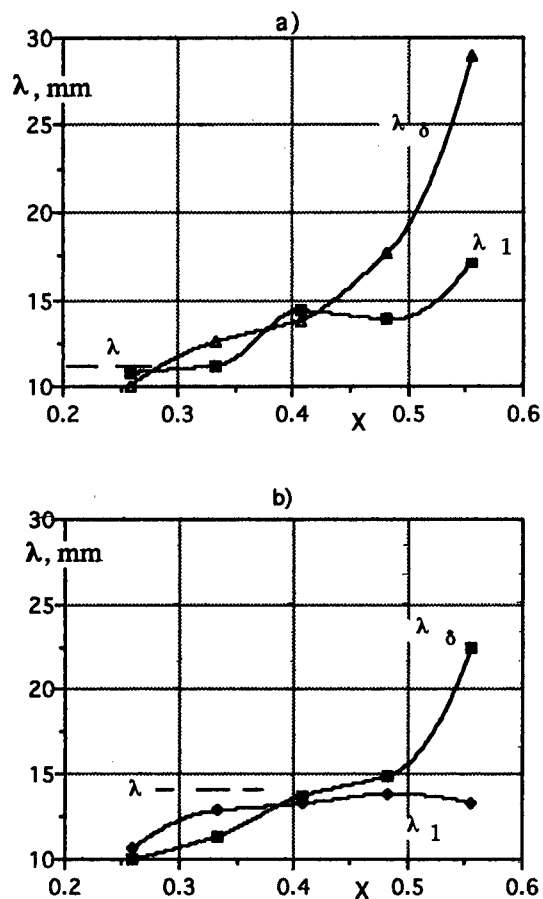
Fig.5. The wavelengths of the most increasing disturbances: λ_1 - obtained from the calculation, λ - experimental observed [1] and the λ_δ - realized from the approximate formula $\lambda_\delta = 2\pi\delta$ [1] for the regimes 1 (a) and 2 (b).

increase of the wavelength of the most growth disturbances are determined, in particular, owing to the boundary layer state changes in near the cross section under the maximum gradient pressure.

REFERENCES
1. Zanin B.Yu. Origin of instability waves in a boundary layer with moderate free-stream turbulence // Fluid Dynamics - 1994. - Vol. 29, № 1. - P. 38-41.
2. Hanifi A. Stability characteristics of the supersonic boundary layer on a yawed cone // Licentiate Thesis, TRITE-MEK. - Technical Report 1993, N 6. - Royal Inst. of Technology - Stockholm, Sweden.
3. Dikovskaya N.D., Zanin B.Yu. Verification of the stability calculation of the boundary layer flow on the wing profile // Int. Conf. on the Methods of Aerophys. Research: Proc. Pt.2. - Novosibirsk, 1996. - P.58-63.

THE STUDY OF SPECIAL GASDYNAMIC FEATURES OF THE FLOW IN A DIAMETER DISK PUMP BY MEANS OF LIQUID CRYSTAL THERMOGRAPHY

V.P. Fomichev, S.V. Khaidarov, V.N. Kovrizhina, S.S. Pravdin, G.M. Zharkova

Institute of Theoretical & Applied Mechanics of SB of RAS,
4/1, Institutskaya Str., 630090, Novosibirsk, RUSSIA

1. INTRODUCTION

A great number of various types of pumps include friction pumps where the moving element transports the fluid under the action of viscous forces. As a result, the mechanical energy of the fluid increases due to the input of external energy. The majority of studies dealing with disk friction pumps consider the Tesla pump construction [1-3].

In the present work, an investigation of a diameter disk pump is performed. In contrast to the Tesla centrifugal pump, the working medium is sucked in from the periphery (Fig. 1). Devices of this kind possess a remarkable peculiarity in addition to merits of the friction pumps: they can be used as flowing reactors (e.g. as absorbing air-conditioners or heat exchangers). Because of this, the effective working body of the device is its important feature. This was exactly the parameter of our interest. Thus, the local heat withdrawal from the disk heated at the axes was examined. The heat withdrawal was determined from the analysis of the temperature distribution over the radius, which was obtained by means of the LC thermography method.

2. EXPERIMENTAL SETUP

The experimental setup (Fig. 1) consisted of body _1_, horizontal rotor _2_, and input-output channels _3_ and _4_, located together on one side of the rotor and separated by partition _5_. The rotor was a pack of aluminium disks _6_ mounted on the shaft with equal gaps _b_ between them with the use of separating rings _7_. When the shaft was rotated, the gas passed from the suction region to the pumping area due to viscous friction in the boundary layers on the disk surfaces. The setup construction allowed for the variation of external D_2 and internal D_1 diameters of the disks, the gap between them, the separating plate height h, and the angular velocity of shaft rotation ω.. An electric heater was located inside the shaft. For the flow visualisation and measurement of the flow parameters between the disks, the front wall of the body was made of acrylic plastic, which allowed one to observe the
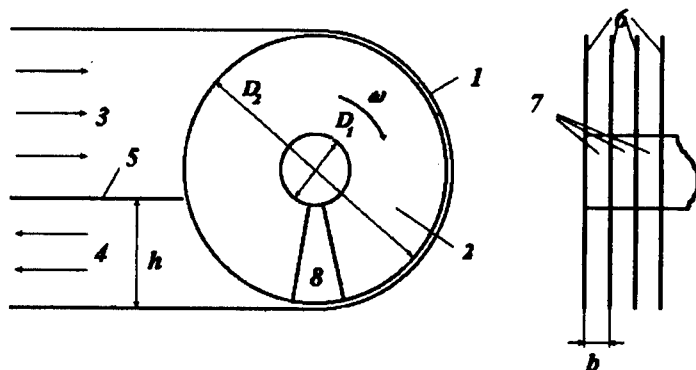

Fig. 1.1 - body; 2 - rotor; 3 - input channel; 4 - output channel;
5 - separating partition; 6 - aluminium disks; 7 - separating rings;
8 - LC indicator

temperature distribution on the next disk where a film with LC indicator *8* was placed. The rotation velocity was measured by a strobotachometer. The temperature distribution over the disk surface was visualised and measured by the LC thermography method.

3. LIQUID CRYSTAL THERMOGRAPHY

The methodical basis for panoramic temperature measurements is formed by thermooptical effects in cholesteric LC, high sensitivity of the helical pitch to temperature variation, and associated changes in the wavelength of selectively reflected light with a minimum sensitivity to mechanical shear. The analysis of LC radiation spectra reveals temperature-invariant parameters: positions of selective reflection extrema in red, green, and blue regions. The registration of the optical response of an LC coating permits the obtaining of the surface temperature distribution with a high spatial resolution, which can be also used to calculate the local heat transfer coefficients. The input of a TV image of the surface examined to a computer and its subsequent digital processing eliminates the effect of subjective factors on the measurement results and increases appreciably their informativeness.

The colour videocamera was used to register the optical response of the liquid crystal. Individual TV frames were captured by a special interface called the frame grabber. An analogue TV signal passed through correction circuits, a decoder dividing it into RGB components, and then to an ADC where it was converted to a digital form and recorded to buffer for further analysis and digital processing.

In true colour image processing, the digital algorithms built on the general principles of colorimetry were used. The measurement process consists of determining the coordinates of a colour point in this or that colorimetric system. A three-dimensional colour space is generally used for that. According to the theory of three-component colour vision, the basic colours of this system are monochromatic radiations with the wavelengths of 760 nm, 546.1 nm, and 435.8 nm (red, green, and blue spectral lines of mercury vapour). This group of three independent basic colours determines the generally accepted colorimetric system RGB. Apart from RGB, some other colorimetric systems are used in practice, they utilize both linear and nonlinear methods for description of colour videoinformation. The choice of the system of colour representation depends on specific purposes [4].

For the quantitative description of colour information, a system of nonlinear coordinates was used, where the colour is expressed in terms of hue, saturation and intensity (HSI). The advantage of such representation, in particular, is that it characterises the colour in terms of its fundamental features related to its natural human perception. The point-by-point transformation from one basis to another is performed by the special formulas

To obtain quantitative information from a digitised videoframe, the calibration temperature dependence on hue T(H) was used. Thin-film coatings on the basis of polymer-encapsulated cholesteric LC with different selective reflection bandwidths (2.9, 2.2, 1.6 °C) were used as thermoindicators.

A copper disk 40 mm in diameter was used for calibration, the coating being applied to its polished surface. The disk was installed inside body *1* (Fig.1) for calibration. The disk temperature was controlled by a water thermostat. This procedure was performed under light conditions and geometry of the experiment. The study of the calibration curve for different image positions on the disk (the influence of angular dependence of selective reflection of the LC) showed that the experimental data obtained in the LC test region are well reproduced for given conditions and thermoindicator.

4. EXPERIMENTAL TECHNIQUE AND RESULTS

4.1 Description of technique and measurements of angle-averaged temperature distribution on the disk

Let us consider a stationary problem of heat propagation over the disk under the conditions of possible heat withdrawal from its surface: the parameters at each point are constant in the stationary coordinate system.

Let us firstly show that the disk temperature can be assumed constant over the disk thickness Δ within experimental accuracy, and, hence, the surface temperature T_s characterises the temperature inside the disk T_{max}. The heat flux to the side surface of the disk is determined as

$$j = -\lambda \nabla T \approx -\lambda \frac{T_{max} - T_s}{\Delta}$$

The following characteristic values were used in the experiment: $j \approx 2000$ W/m^2, $\lambda = 200$ W/m·K, $\Delta = 1$ mm. Then $T_{max} - T_s \approx 0.01$ K. Here, j is the heat flux density over the disk cross section, λ is the heat conductivity of the disk material (in our case, aluminium). Thus, we will consider the heat propagation over the disk within the framework of a two-dimensional heat conductivity problem. For the purpose of determining the angle-averaged characteristics of the flow, we can pass to the one-dimensional case.

Let us try to solve the problem whether the results of our experiment contain information about the heat removal from the disk and, if so, on which scales we can obtain this information. Let us consider a set of functions determined on a set of points r_i. Let us assume the functions $\varphi_1(r_i)$ and $\varphi_2(r_i)$ to be indistinguishable if

$$\sum_{i=1}^{N} (\phi_1(r_i) - \phi_2(r_i))^2 \leq \delta^2 N \tag{1}$$

where δ is the experimental accuracy, N is the number of points on the interval under consideration. Besides, we know the exact solution of the heat conductivity equation for the disk without heat removal:

$$\Delta T = 0$$

$$T(r_1) = T_1; \ T(r_2) = T_2$$

$$T = c_1 \ln r + c_2 \tag{2}$$

$$c_1 = \frac{T_1 - T_2}{\ln(r_1 / r_2)}; \ c_2 = \frac{T_1 \ln r_2 - T_2 \ln r_1}{\ln(r_2 / r_1)}$$

Taking any two radii and appropriate temperature values as the boundary conditions, we solve problem (2), and then compare the resultant analytical solution in terms of condition (1) with an experimental temperature distribution on this interval. If condition (1) is not satisfied, this means that the experiment on the chosen interval r_1 r_2 has information about the heat removal. The next question arises when we obtain an interval where condition (1) is satisfied (i.e., a solution without heat removal appeared in the class of equivalence determined by (1)). This means that the experiment on the scale under consideration (and lower) has no information about the heat transfer. Now we have to find the reason: the real absence of heat transfer or we have a small interval characterising the threshold of spatial resolution of determining the heat removal in our experiment. The following procedure allows us to answer this question. Let us construct all possible solutions of problem (2) in the class of equivalence (1) for this interval. In practice, this is done by varying the boundary conditions at the interval ends within the experimental accuracy. The variation of heat fluxes corresponding to these solutions determines the accuracy with which we can speak about the absence of heat removal.

The following setup parameters were used for experiments described below: D_2=360mm, D_1=120mm, b=8mm, h=120mm, ω=195 s^{-1}. The results of using the above technique are presented in Fig. 2. It shows experimental points, and the solid line presents an analytical solution to problem (2) on the initial interval, determined as described above. It was assumed δ=0.1K. Points from the interval OA satisfy condition (1). By varying the boundary conditions at its ends within $\pm\delta$, we determine the maximum and minimum heat fluxes corresponding to analytical dependences belonging, according to (1), to the class of equivalence on this interval.
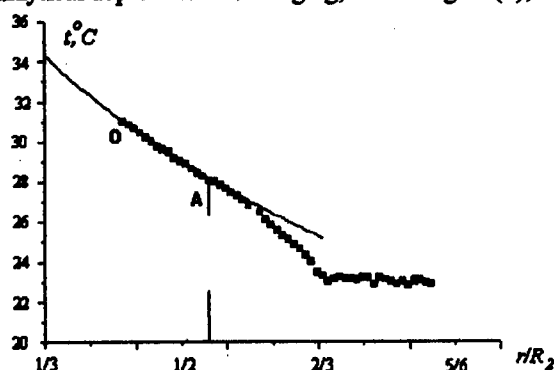

Fig.2

From this we found that the heat fluxes differ by no more than 4%. Thus, we can say that our experiment registers the absence of heat removal from the disk on the interval OA (the heat flux over the radius is constant with an accuracy of 2%). Because of that, we will further assume that there is no heat removal from the disk on this interval, and the temperature is changed only due to heat conduction over the disk and heat withdrawal (no less than 98% of the heat flux entering the disk) occurs outside of it. The absence of heat removal can be explained by the presence of a stagnant region, in which the air flow has no radial velocity component for a noticeable convective heat transfer from the disk (the heat removal due to air heat conductivity in comparison with the disk heat conductivity is neglected). Obviously, the stagnant region is extended to the overall region corresponding to smaller radii than r_A; otherwise, there should be convective heat transfer from the region $r<r_0$ to the region $r>r_A$, which is not possible, as is shown above. This allows us to extend the analytical curve to the overall internal.

The polymer film and a layer of glue partly insulate the LC from the disk and permit the one to measurement not of the disk temperature but its combination with the air temperature to raise the accuracy of determining the stagnant region position. Indeed, the temperatures of the disk and the air are equal there. Thus, the temperature distribution is described by the solution of (2). Let us consider the behaviour of experimental temperature distribution outside the stagnant region. The radial convection transforms the pattern and one no longer follows the solution of the heat conductivity equation for the disk without heat removal. One can see an inflection in the heat transfer region (Fig.2). This means that the second derivative of the temperature changes sign, and a concave curve inside the stagnant region changes to convex outside. It was not seen if the thermosensor measured the disk temperature over all the radius (not only in the stagnant zone). Indeed, the second derivative of the disk temperature over the radius is invariably positive. Taking into account the above, we can consider the external radius of the stagnant region to be equal to 96 mm.

4.2 Measurements of instantaneous temperature distribution

Complementary experiments were carried out to verify the assumption that temperature phase-averaging is allowable. The instantaneous temperature distribution was registered by using a high speed shutter function (exposure time 0.0005 s, frame rate 25 fps) of the CCD camera.

In this case, the model surface made of aluminium was coated by a thermoinsulator layer (thickness of about 0.3 mm). Then the LC film was glued onto it. It was necessary to achieve high quality video images for digital processing and temperature measurements. Therefore,

three narrow-band LC coatings were used (ΔT=2.9; 2.2 and 1.6K) to increase the image brightness. These coatings of ring contour were glued onto the disk surface and covered 1/4 of the disk, as shown in Fig.4. Prior to the experiments, the model was heated for several hours by means of an electric heater mounted inside the shaft up to the blue color of the LC. The video record was started after the stationary pattern was obtained.
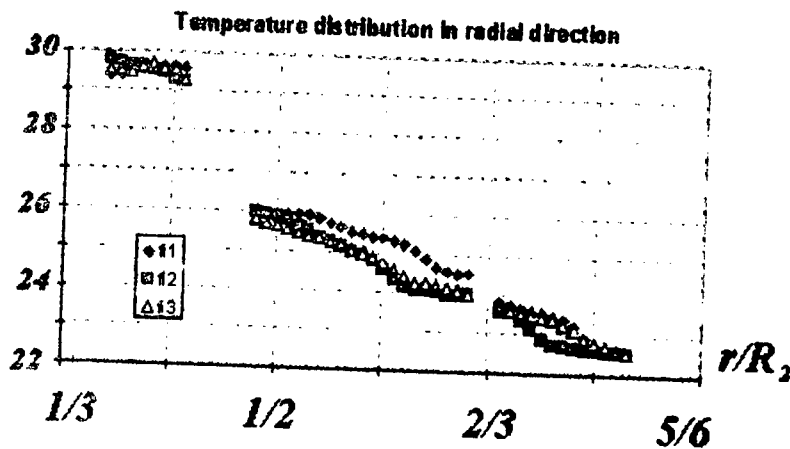

Temperature distribution in radial direction

Fig. 3

Fig.4

Fig.5

Fig. 3 illustrates some results obtained by means of this procedure. The following setup parameters were used : D_2=360mm, D_1=120mm, b=8mm, h=120mm, ω =157 s^{-1}. The flow temperature distribution in the radial direction for 3 angles is shown in this figure. Discontinuities in the experimental data take place just at the point of two LC coatings connection. Besides, in some regions the flow temperature is out of range of selective reflection for a given LC. Therefore, no data were obtained there. The presented distributions were obtained by using three calibrations T(H) which were approximated with two linear function in RG and GB ranges (Fig. 5). The approximation error does not exceed 0.5K (LC1), 0.3K (LC2), and 0.5K (LC3).
It follows from this figure, that the maximum temperature gradient of about 3°C is observed in the range r/R_2 = 0.42-0.47. The temperature gradient is weaker in the region of LC2 and LC3. The scatter in temperature distributions over different angles (fi1-fi3) is small. At the same time, it shows the difference between the input and output flow temperature (limit cases). Thus, the assumption about the validity of averaging of the temperature over an angle is acceptable. On
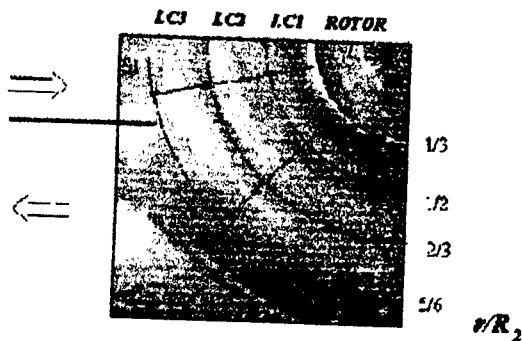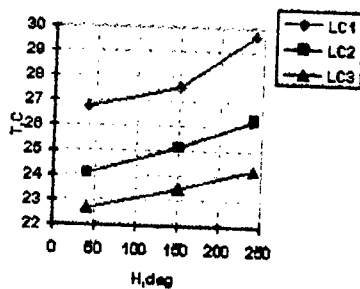
46

the other hand, the response time of the LC coating allows one to observe the temperature variations from frame to frame (20 ms). The data of Figs. 2 and 3 show that it is possible to indicate two regions: stagnation zone and heat exchange zone for both regimes.

Thus, the validity of assumptions forming the basis of the suggested technique and its applicability for determining some important flow parameters are experimentally validated.

4.3 Measurements of temperature distributions with the electric heater on the disk

Experiments to study the heat transfer on the disk with the heater, located inside it were carried out. The electric heater of width 50 mm made of titanum foil was glued on plastic disk base by width of 6 mm from two sides along a radius. Then the rings made of thin plastic by thickness 1mm were glued on both disk surfaces. The tests have shown that isotherms place in parallel to the heater boundaries and on the disk surface above the heater is satisfied condition of regularity of the heat flow when air flow is absent.

Fig. 6

In fig. 6 the isotherms are shown in condition of various heat flows and constant angular velocity. It follows from this figure that the isotherm places approximately in parallel to the leading flow edge of the heater in the region near the disk axis. It means, that the heat tansfer coefficient α varies poorly over the radius in this zone. Outside this region we observe considerable deflection of the isotherm from the leading edge, that testifies the increase of the heat withdrawal in this area. The obtained experimental results, qualitatively confirm the existence at least of two zones: internal with weak and external with intensive heat transfer.

5. CONCLUSIONS

A technique for analysis of experimental temperature distributions is suggested, which permits the finding of specific gas dynamic features of gas flows in diameter disk pumps.

The use of the LCT and above-described technique validated the existence of specific features of the flow, such as the stagnant region where the heat transfer between the disk and the air is not so intensive as outside and allowed one to determine its dimensions.

6. REFERENCES

1. Nikola Tesla. Turbine , US, No 1061206, May 6, 1913.
2. Matsh, W. Rice, 1967, Potential Flow Between Two Parallel Circular Disks With Partial Admission. Journ. of Appl. Mech., vol. 34, N1, pp.129-131.
3. Boyd, W. Rice, 1968, Laminar Inward Flow of an Incompressible Fluid Between Rotating Disks With Full Peripheral Admissor, Journ. of Appl. Mech., vol. 35, N2.
4. W.K. Pratt. Digital Image Processing. N.Y., Toronto, 1978

SPECKLE PHOTOGRAPHY OF TURBULENCE VARIATIONS
AFTER SHOCK WAVE PASSAGE

N. Fomin, **E. Lavinskaja**
Heat and Mass Transfer Institute, Minsk, 220072, Belarus

W. Merzkirch, **D. Vitkin**
University of Essen, Essen, D-45127, Germany

1. Introduction

In turbulent flow both fluid velocity and scalar quantities, like temperature, density, or concentration, may be separated into mean and fluctuating ensemble average components. The "turbulence" of the scalar fields is superimposed on the turbulent velocity field and both velocity and scalar quantity statistics are necessary for a complete turbulent heat and mass transfer description.

Using light sheet illumination, the speckle photography (particle image velocimetry) provides measurements of the "instant" (mean plus fluctuation components) velocity field. Statistical analysis of the obtained data allows to determine turbulence scales directly.

Unlike this, line-of-sight speckle photography measures the deflection angles of the light passed through the flowfield [1-3]. Therefore, direct statistical analysis of the obtained data can give us the scales of this field only. Erbeck and Merzkirch [4] developed mathematical procedure of the reconstruction of 3D density (or refraction index) correlation functions through the obtained 2D deflection angle correlation functions. This procedure is based on the Abel type integral inversion and referred as ill posed mathematical problem. In this article an example of turbulence scales reconstruction is given using this integral inversion for the turbulent flow interacting with a shock wave.

2. Experiments

The optical arrangement for measuring the light deflection angles by means of speckle photography has been described by Wernekinck and Merzkirch [5]. An expanded, parallel beam of laser light is transmitted through the test section. A lens focuses a plane in the test section onto a ground glass plate. A second imaging lens focuses a plane at distance L from the ground glass onto the photographic plate. On this plate a speckle pattern is recorded that is existent in the plane at the small distance L from the ground glass plate.

In the double exposure speckle photography (DESP), two speckle patterns are superimposed by recording two exposures on the same photographic plate. After photographic development, the specklegram is scanned and interrogated with a thin laser beam. By measuring the Young's interferometric fringe spacing and the fringe direction it is possible to determine two components of the speckle displacement at each specklegram interrogation point. These values can be easily converted into the components of the deflection angle of the light passed through the turbulent field.

DESP can be applied for studies both homogeneous isotropic turbulence and turbulent flows with a strong anisotropy. In the latter case, however, the construction of density correlation function using single-projection measurements and integral

transformations [4] could give rise to inaccuracies in such reconstruction. The more correct approach in this case is multi-projection measurements and reconstruction of the local turbulence parameters using computerized tomography. Nevertheless, even in the case of a strong anisotropy, it is possible to obtain useful information about turbulence under study using single-projection data. A good example of turbulence with a strong anisotropy is a turbulent flow after interaction with a planar shock wave. The results of the quantitative flow visualization confirm that the turbulence under study has strong anisotropy and demonstrate a high potential of speckle photography for turbulence structure studies.

The experiments were performed with the unsteady air flow in a shock tube of the Essen University having a quadratic cross-section of 100 by 100 mm^2. The shock propagates into the tube, where it reflects at the closed end. Integrated in the mechanism used for destroying the diaphragm is a turbulence grid, so that the air expanding from the compression tank must pass through the grid. Thereby, a turbulent air flow with density fluctuations is generated in the shock tube, and the front of the turbulent regime coincides with the contact front that moves with the local air velocity and separates the air which was originally in the low pressure side from that in the compression tank. The beam from a pulsed ruby laser is expanded and collimated to form a parallel beam of 10 cm diameter. After having passed horizontally through the optical test section of the shock tube, the laser light illuminates a disk of ground glass, the speckle generating element in the set-up. A plane in the speckle field, normal to the optical axis and at a distance of about 10 mm from the ground glass is imaged onto the photographic plate where the speckle patterns are recorded. We image a field of view of about 10 cm in diameter with an imaging ratio of 1:1 onto the photographic plate. The first exposure is taken without flow and it serves as the reference speckle pattern. The second exposure with flow recorded on the same plate is taken at a desired instant of time, as defined by the instantaneous position of the moving shock wave. Due to variations of the fluid density occurring in the flow, the light rays in the second exposure are deflected with respect to the direction of light propagation in the reference exposure, thus resulting in a (locally inhomogeneous) displacement of the second speckle pattern in comparison to the reference pattern.

The double-exposed speckle photograph is developed and then interrogated with a thin He-Ne laser beam in order to determine the local speckle displacement $\Delta(x,y)$, respectively the local light deflection angle $\varepsilon(x,y)$, via the method of Young's fringes. This evaluation is performed with an automated system that, with the presently used hard- and software, can evaluate 2500 data points per hour. The major part of the evaluation time is needed for moving the interrogating laser beam mechanically, i.e. by stepping motors, from one interrogation point to the next. In most cases we evaluate a specklegram on a grid of 100 by 100 data points, so that approximately 4 hours are needed for the analysis of one specklegram (double-exposure). The interrogation is done in steps of 0.2 mm which corresponds to the diffraction limit of spatial resolution in our system, given by $\sqrt{\lambda L_1}$, with λ being the laser wavelength and L_1 being the depth of the optical test section in the direction of light propagation (z-axis). With the pulse length of the illuminating ruby laser being approximately 50 ns, we freeze in the specklegram the instantaneous distribution of the deflection angles e(x,y) as caused by the turbulent density field. An instantaneous distribution of the deflection angles $\varepsilon(x,y)$ is presented in Fig. 1 in the form of isolines.

The two fields of view shown in Fig. 1 are the distributions before (left) and after (right) passage of the shock. The distance from the instantaneous position of the shock wave is indicated. The visible patterns can be interpreted as turbulent structures, although one must

be aware of the integrating effect of the optical line-of-sight method. Evidently, the structures are more extended in the y-direction than in the x-direction (direction of flow), which can be taken as an indication of the anisotropy of the turbulent field. This anisotropy has also been verified with single-exposure speckle-photographic experiments. A further observation is that the amount of light deflection increases after the passage of the shock (right side in Fig.1), which means that the turbulence intensity increases. These observations can be quantified by determining the spatial correlation function R of the deflection angles in the x-y plane, see the next section.
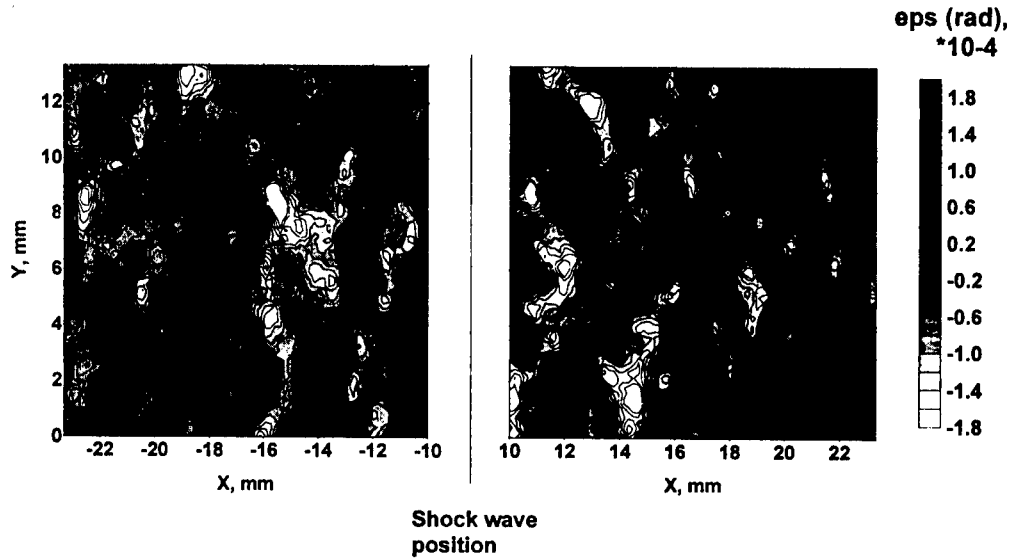

Fig. 1. Instantaneous distribution of the light deflection angles at two positions downstream (left) and upstream (right) of the moving shock. X-values refer to distance from the instantaneous shock position. Deflection angles are measured in radian.

3. Further integral transformations

Denoting by $\bar{\varepsilon}(x,y)$ the light deflection field in recording plane perpendicular to the direction of the parallel light beam propagation, the vector value of deflection angle can be composed of two components, ε_p and ε_q.

$$\bar{\varepsilon} = \bar{i}\cdot\varepsilon_p + \bar{j}\cdot\varepsilon_q \tag{1}$$

The correlation function for deflection angle field according to its definition is

$$R_\varepsilon(\xi,\eta) = \left\langle \bar{\varepsilon}(p,q)\cdot\bar{\varepsilon}(p+\xi,q+\eta)\right\rangle \tag{2}$$

Here the symbol <... > denotes spatial averaging. This correlation function can be composed of two parts:

50

$$R_{\varepsilon_p}(\xi,\eta) = \left\langle \varepsilon_p(p,q) \cdot \varepsilon_p(p+\xi,q+\eta) \right\rangle \tag{3}$$

and

$$R_{\varepsilon_q}(\xi,\eta) = \left\langle \varepsilon_q(p,q) \cdot \varepsilon_q(p+\xi,q+\eta) \right\rangle. \tag{4}$$

In its turn, the correlation functions $R_{\varepsilon_q}(\xi,\eta)$ and $R_{\varepsilon_p}(\xi,\eta)$ can be calculated in directions parallel (denoted by the symbol $\parallel$) or perpendicular (denoted by the symbol $\perp$) to projections of deflection angles

$$R_{\varepsilon_q \perp}(\varepsilon = \tau, \eta = 0) = R_{\varepsilon_q \perp}(\tau) ; \tag{5}$$
$$R_{\varepsilon_q \parallel}(\varepsilon = 0, \eta = \tau) = R_{\varepsilon_q \parallel}(\tau).$$

and

$$R_{\varepsilon_p \perp}(\varepsilon = 0, \eta = \tau) = R_{\varepsilon_p \perp}(\tau); \tag{6}$$
$$R_{\varepsilon_p \parallel}(\varepsilon = \tau, \eta = 0) = R_{\varepsilon_p \parallel}(\tau)$$

For a finite number of measurement points (p_i, q_i) with $0<p_i<m$, $0<q_i<n$ these correlation functions can be approximated by series

$$R_{\varepsilon_q \perp}(\tau) = \frac{1}{1+m-\tau} \sum_{i=0}^{m-\tau} \varepsilon_q(i,q) \cdot \varepsilon_q(i+\tau,q) \tag{7}$$

and

$$R_{\varepsilon_q \parallel}(\tau) = \frac{1}{1+m-\tau} \sum_{j=0}^{n-\tau} \varepsilon_q(p,j) \cdot \varepsilon_q(p,j+\tau). \tag{8}$$

Using relations between density gradients and deflection angles, Erbeck and Merzkirch [4] has received connection between density and deflection angle correlation. Note, that the correlation function of density field depends on three spatial coordinates, namely ξ, η and ζ. For isotropic turbulence the correlation functions depend on one parameter, τ or r respectively

$$\tau = \sqrt{\xi^2 + \eta^2}; \quad r = \sqrt{\tau^2 + \zeta^2} \tag{9}$$

and 3D density correlation function can be expressed through the deflection angle correlation functions in the next form

$$R_\rho(r) = \frac{1}{\pi L_1 K^2} \int_r^\infty \frac{\tau}{\sqrt{\tau^2 - r^2}} \left\{ \int_0^\tau R_{\varepsilon_q \parallel}(\tau^*) d\tau^* \right\} d\tau \tag{10}$$

and

$$R_\rho(r) = \frac{1}{\pi L_1 K^2} \int_r^\infty \frac{\tau}{\sqrt{\tau^2 - r^2}} R_{\varphi\perp}(\tau)d\tau \tag{11}$$

These expressions are very similar to Abel integral transform, when 2D distribution is reconstructed by using 1D line-of-sight data about sought parameter. In our particular case, using integrals (10), (11) 3D density correlation function in a turbulent field can be reconstructed using 2D correlation functions of deflection angles of the light passed through the flowfield. The usual assumption of 2D isotropy in 3D flow is used for this reconstruction.

The results of the reconstruction are shown in Fig.2. It is seen that the spatial structure of the turbulent scalar (density) field in this compressible flow can be visualized quantitatively with the applied optical specklegram technique. The patterns visible in the distributions of the deflection angle isolines are interpreted as large-scale turbulent structures. The turbulence in the flow ahead of the shock is anisotropic, and it remains so for the first short period after the passage of the shock wave, with a slight increase in size of the structures. It is evident that different states of turbulence develop downstream of the shock, depending on the out-of-equilibrium degree as caused by the shock compression. The tendency towards an isotropic state at some distance from the shock is understandable, because the flow velocity behind the reflected shock wave is nominally (under pure
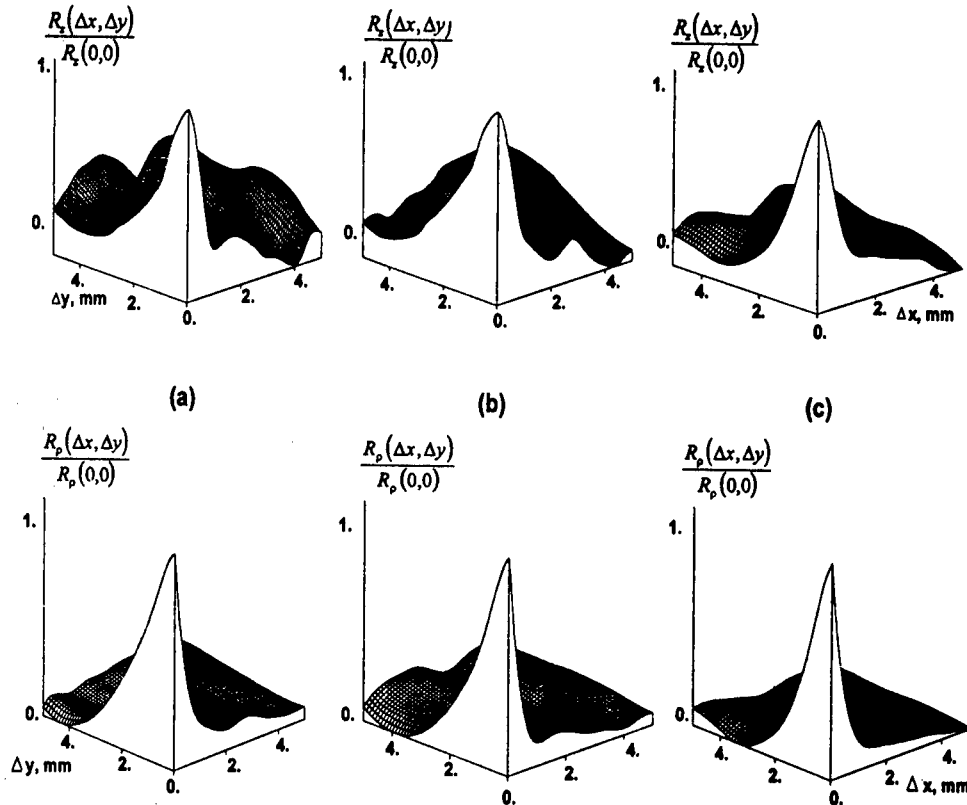

Fig.2. Two-dimensional correlation functions of the light deflection angles φ (on the top) and density (on the bottom).

gasdynamic aspects) zero. In our interpretation of the visible results, however, we have to pay attention to the fact that all optical signals are integrated along the path of the light through the test section. A direct comparison to results of numerical simulations is therefore not possible. Such comparison would require a conversion of the 2D optical data into 3D quantities describing the turbulence characteristics of the density field.

This technique was used for evaluation of interactions of turbulence with combustion front and with shock wave, see [6-8]. Energy spectrum of turbulent density fluctuation was calculated using Fourier analysis of the obtained spatial correlation functions. The speckle photographic results were compared to the cold-wire data and good agreement was obtained.

Acknowledgments

References

1. U.Wernekinck, W.Merzkirch and N.Fomin. Measurement of light deflection in a turbulent density field // Experiments in Fluids, 3:206-208, 1985.
2. N.Fomin Speckle Diagnostics of Turbulent Combustion // Proc. of the ICMAR-94, ITAM-Press, Novosibirsk, 1994.
3. N.Fomin Speckle Photography of Non-Stationary Turbulent Flows // Proc. of the ICMAR-96, Part 1, ITAM-Press, Novosibirsk, 1996, pp.-90-95.
4. R.Erbeck and W.Merzkirch. Speckle photographic measurements of turbulence in an air stream with fluctuating temperature // Experiments in Fluids, 6:89–93, 1988.
5. U.Wernekinck and W.Merzkirch. Measurement of natural convection by speckle photography // In Heat Transfer, C.L.Tien and V.P.Carey and J.K.Ferrell, editors, Hemisphere Publ. Co., Washington, 1986, pp. 531-535.
6. J.Keller and W.Merzkirch. Interaction of a normal shock wave with a compressible turbulent flow // Experiments in Fluids, 8:241-248, 1990.
7. W.Merzkirch and H.Wintrich. Flow visualization by spatial filtering of speckle photographs // In I.Reznichek, editor, Proc. Int. Symp. on Flow Visualization, Hemisphere Publ. Co., N.Y., 1984, pp. 183-187.
8. K.Oberste-Lehn and W.Merzkirch. Speckle optical measurement of a turbulent scalar field with high fluctuation amplitudes // Experiments in Fluids, 14:217-223, 1993.

SPATIAL-ENERGETIC STRUCTURE OF GLOWING DISCHARGE IN A SUPERSONIC GAS FLOW

V.M.Fomin, A.V.Lebedev, and A.I.Ivanchenko

Institute of Theoretical and Applied Mechanics SB RAS
630090, Novosibirsk, Russia

A self-maintained electric discharge in a supersonic gas flow is of interest from he viewpoint of solving a number of gasdynamic problems, in particular, for controlling the flow around aerodynamic bodies by means of local changes of physical properties of the gas flow [1, 2]. The problem of spatial-energetic characteristics of the discharge, however, is poorly studied, and there are no publications with the results of such studies. This paper is the first one presenting the results of the study of spatial-energetic structure of the discharge, as well as the result of the discharge action on the gas flow around the body.

A longitudinal discharge was chosen for the study. The construction of an electric discharge device is shown in Fig. 1. Body 1 is located in a supersonic air flow (the Mach number is M=3.2, the static pressure is P=1230 Pa (9.22 torr), the velocity is V=624 m/s). The body is a cylinder 6 mm in diameter with a spherical forebody, which acts as a cathode. Anode 2 is made of a
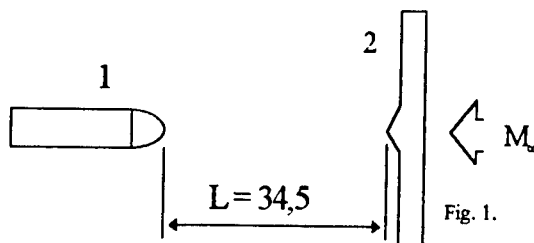

Fig. 1.

plate 0.2 mm thick and located upstream of the body at a distance of 34.5 mm from the cathode in the symmetry plane of the model. Both the plate-anode and body-cathode are at zero incidence. A steady discharge is ignited, its burning time is about 20 s in each experiment.

A visually uniform discharge is formed on the treated anode plate, the boundaries of the anode layer brightness are as sharp as on the cathode. A clearly marked effect of normal current density is observed [3]: as the current increases (decreases), the discharge length along the plate increases (decreases). The discharge occupies a considerable portion of the volume and has a diffuse form. This discharge can be most probably interesting from the viewpoint of its use in lasers. The discharge localization seems to be of interest from the viewpoint of its use in experimental gasdynamics. For this purpose, the back edge of the anode has a linear step parallel to the plate surface (see Fig. 1). In this case the discharge on the anode is attached to the step. Such a discharge was taken as the basis for investigations.

The discharge cross-section area increases from the anode to the cathode. The characteristic current density in the discharge column is $j \approx 5$ A/cm^2, the energy contribution being approximately 1800 J/g. A clear pattern typical of glowing discharge is observed on the cathode. A cathode layer is formed, whose thickness obtained by photography is about 0.3 mm. The characteristic current density on the cathode surface is 0.2 A/cm^2. The Hehl's effect is clearly pronounced qualitatively: the area occupied by the glowing light on the cathode increases with increasing the current. A photograph of the discharge is shown in Fig. 2.
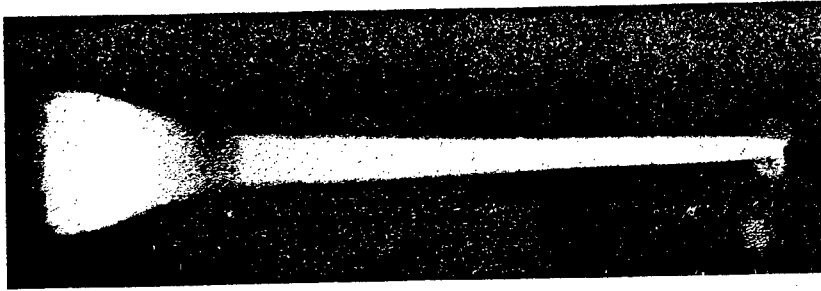
Fig. 2

The Schlieren technique was used for visualization of the discharge effect on the wave pattern of the flow around the body. Figure 3 shows the Schlieren picture of the flow around the body without the discharge. A classical intense detached bow shock wave is seen. Figure 4 shows the Schlieren picture of the flow around the body for the same experimental conditions as in Fig. 3, but in the presence of a discharge with electric power of 200 W. A substantial restructuring of the wave pattern of the flow is observed. The shock wave upstream of the blunted part of the model practically vanishes. The region in which the shock wave are not observed roughly coincides with the region of discharge glowing, having slightly large transverse size than the latter.

The discharge configuration is suitable for studying the potential distribution along the current using electric probes. A standard measurement scheme was employed. Cylindrical probes 0.04 mm in diameter were used. The potential was almost constant in the crossflow direction. The results of potential measurement were independent of the fact which current meets the probe: positive or negative. Both the anode and the cathode were used as a reference electrode. In fact, the potential distribution was measured by the probes within the entire space, except for narrow near-electrode regions (approximately 3 mm in the cathode region and 5 mm in the anode region), which is quite sufficient for constructing the electric field distribution picture in the gap between the electrodes.
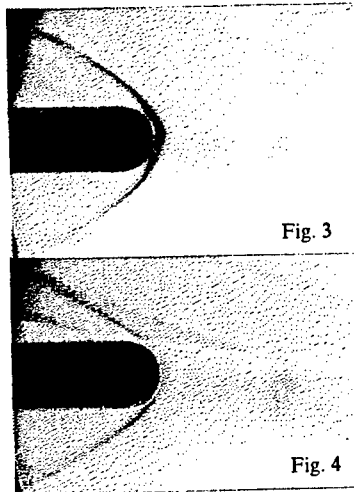

Fig. 3

Fig. 4

The discharge configuration is suitable for studying the potential distribution along the current using electric probes. A standard measurement scheme was employed. Cylindrical probes 0.04 mm in diameter were used. The potential was almost constant in the crossflow direction. The results of potential measurement were independent of the fact which current meets the probe: positive or negative. Both the anode and the cathode were used as a reference electrode. In fact, the potential distribution was measured by the probes within the entire space, except for narrow near-electrode regions (approximately 3 mm in the cathode region and 5 mm in the anode region),

which is quite sufficient for constructing the electric field distribution picture in the gap between the electrodes

It was established as a result of potential measurements in various points of plasma discharge (see the Table) that the discharge is characterized by large values of the near-electrode voltage difference: approximately 700 V in the cathode region and 300 V in the anode region. The difference between the electrodes is 100 V on the length of 26.5 mm.

Potential distribution from the anode to the cathode.

- U, V	0	285	290	300	330	360	380	390	1080
x, mm	0 anode	5	10	15	20	25	30	31,5	34,5 cathode

Let us dwell upon the medium and plasma characteristics. The value of E/N (E is the electric field strength, N is the neutral gas concentration) in the anode region is approximately 120 Td. A low value of E/N, about 20 Td, is obtained in gaps between the electrodes. Using the data on the electron drift velocity and energy versus E/N [4], we obtain the electron concentration n_c=1012-1013 cm-3 and the mean energy of electrons *=1.5 eV. The particle balance equation for electrons can be written as

$$\mathrm{div} j_e = e\nabla(\mu_e E) - e\nabla(n_e V) \approx -e[k_i N n_e - \beta n_e(n_e+n_{-i}) - k_a N n_e + k_d N n_{-i} + \nabla(D_e \nabla n_e)]; \qquad (1)$$

where $j_e \approx j$ is the electron current density, μ_e and e are the electron mobility and charge, n_e and n_i are the densities of electrons and negative ions, k_i, β, k_a, k_d are the coefficients of the Townsend ionization, electron-ion recombination, adhesion, and separation, respectively. It follows from the analysis of [5, 6] that the adhesion of electrons with a threshold of about 5 eV can be neglected. The obtained ionization frequency in the discharge column $v_i \approx 101$ s^{-1} is then clearly insufficient to compensate for the loss of particles in the volume due to electron-ion recombination which occurs with frequency $v_r \approx \beta n_e = 105 \div 106$ s^{-1}.

In this case, the experimental results agree with the model in which it is supposed that the discharge in the volume is not self-maintained, the plasma is formed due to ambipolar drift of charged particles from the near-electrode regions [7]. For low E/N, the electron mobilities in air and in nitrogen are close in value, and they are approximately equal functions of E/N [4]. Then the following relation is obtained from (1), all terms being neglected except for recombination:

$$E/N \approx 3[3\beta j x/(P^3 \mu_+ e(\partial \mu_e/\partial E))]^{1/3}, \qquad (2)$$

where x is the longitudinal coordinate, P is the normalized pressure, μ_+ is the mobility of positive ions. Substituting into (2) numerical values corresponding to our conditions, we obtain E/N=60 Td. Taking into account the adopted simplifications of equation (1), this theoretical estimate is in reasonable agreement with the experiment. However, this does not exclude the presence of the multi-stage ionization effect, and also ionization which results from collisions of excited nitrogen molecules [8].

Thus, the following conclusions can be drawn from the conducted studies.

1. A result unexpected from the classical viewpoint [9] is obtained: for a supersonic flow velocity and fairly large gap between the electrodes, almost all voltage drop takes place in the near-electrode regions rather than in the discharge volume (64% in the cathode region, 27% in the anode region).

2. The potential distribution in the gap between the electrodes is adequately described by the non-self-maintained discharge model.

3. The discharge reconstructs substantially the supersonic gas flow around the body. It induces the dissipation of the bow shock wave responsible for the main share of the body drag.

References

1. V.V.Vitkovsky, L.P.Grachev, N.N.Gritskov, Yu.I.Kuznetsov, V.V.Lebedko, K.V.Khodataev, and V.P.Yankov. The study of unsteady supersonic flow heated by a longitudinal discharge//High Temp. 1990. No. 6, P. 1156-1163.

2. G.I.Mishin, A.I.Klimov, and A.Yu.Gridin. A longitudinal electric discharge in a supersonic gas flow// Pis'ma v ZhTF. 1992. Vol. 18, No. 15. P. 86-92.

3. Yu.S.Akishev, A.P.Napartovich, P.I.Peretyat'ko, and N.I.Trushkin. Near-electrode regions of a glowing discharge and normal current density on the anode//High Temp. 1980. Vol. 18, No.4, P. 873-876.

4. L.G.Huxley and R.W.Crompton. The Diffusion and Drift of Electrons in Gases. Wiley Interscience Publ., New York, 1974.
5. E.W. McDaniel. Collision in Ionized Gases. John Wiley, Inc., New York, 1964.

6. S.H.Massey. Negative Ions. Cambridge University Press, Cambridge, 1976.

7. Yu.S.Akishev, F.N.Vysikailo, A.P.Napartovich, and V.V.Ponomarenko. The study of quasi-steady discharge in nitrogen//High Temp. 1980. Vol. 18, No. 2, P. 266-272.

8. L.S.Polak, P.A.Sergeev, and D.I.Slovetsky. A mechanism of nitrogen ionization in a glowing discharge//High Temp. 1977. Vol. 15, No. 1, P. 15-23.

9. Yu.P.Raizer. Gas Discharge Physics, Nauka, Moscow, 1992.

UNSTEADY EFFECTS FOR A SUPERSONIC FLOW PAST
A PULSING ENERGY SOURCE OF HIGH POWER

P.Yu.Georgievsky, V.A.Levin

Institute of Mechanics MSU, Moscow 119899, Russia

Introduction

The new principle of perfecting of aerodynamic characteristics of flying vehicles is associated with a controlled modification of properties and parameters of a flow upstream by means of the energy supply. In particular, the wave   drag   can be essentially reduced in this way. In terms of linear formulation it is shown [1], that a supply of energy into a segment ahead of a thin body of revolution is not less effective, than an equal supply near the lateral surface [2].

. By means of the energy supply to some local region upstream of a blunt body the flow structure varies radically [3]. Because of large losses of   total pressure in a heated wake downstream of the source, the static pressure on a side surface can exceed the one at the stagnation point, so that a front separated zone is formed. In [4] the phenomenon of restructuring a flow in a shock layer near the sphere is detected, when the slight energy supply into a small volume leads to fundamental modifications of a heading shock wave. Then the appearance of a front separated zone results in a considerable reduction of the wave drag. Simultaneously a saved energy multiply exceeds a supplied one.

In [5] the influence of a local energy supply on a supersonic flow over the axially symmetric cone and in [6] – on a 3-D flow over the ogival form body are investigated. It is shown that for sharp form bodies with attached heading shock wave a separated zone isn't formed, but the wave drag decrease significantly. By means of the correspondent arrangement of the energy supply region, the partial disappearance of the attached shock wave can be obtained. In [7] it is shown, that the energy supply into a shock layer near the blunt-nose cone allows one to get the lift force and the pitching moment. In [8] some results of parametric calculations for a supersonic flow near the spherical bluntness based on full Navier-Stokes equations for a thermal perfect gas are presented. It is shown, that essential decrease of wave and friction drag can be established at the same heat fluxes.

Experimental investigations are a subject of particular interest, because allow one to estimate a possibility of practical realization of the suggested scheme of aerodynamic characteristics perfecting. In [9, 10] the longitudinal electric discharge was used for creating a high temperature region in the wind tunnel. An appreciable modification of flow close to the front surface of a sphere and a blunt cone, which is caused by detachment of the heading shock wave, is noted. In [11] the electric discharge was organized on the body of very

complicated form with the front needle and integrated electrodes. Numerical investigations of a real experimental configuration are executed. Though the needle ahead of the sphere decrease wave drag itself, the additional effect from energy supply is fixed.

In [12] the new quasistationary method of heat supply to the supersonic flow, using the strong optical pulsing discharge formed by CO_2 laser in pulse-periodic mode, is suggested. Later in [13] the flow over various models are investigated. Adduced photographs of the flow structure and results of direct measurement of aerodynamic resistance show the essential dependence of the energy supply effectiveness on the pulse frequency repetition. In [14] conditions of [13] are numerically simulated and integral characteristics of the flow are studied.

In this article the detailed examination of a supersonic flow structure past the pulsing energy source of high power is performed.

1 Formulation of the problem and the method of numerical solution

The supersonic flow past an energy source of a variable power is examined. The system of equations for a two-dimensional unsteady motion of an ideal gas written in cylindrical coordinates r, z looks as follows:

$$\frac{\partial T}{\partial t} + \frac{\partial F}{\partial r} + \frac{\partial G}{\partial z} = H, \tag{1}$$

$$T = \begin{pmatrix} \varrho \\ \varrho u \\ \varrho v \\ e \end{pmatrix}, F = \begin{pmatrix} \varrho u \\ p + \varrho u^2 \\ \varrho u v \\ (e+p)u \end{pmatrix}, G = \begin{pmatrix} \varrho v \\ \varrho u v \\ p + \varrho v^2 \\ (e+p)v \end{pmatrix}, H = \frac{1}{r}\begin{pmatrix} -\varrho u \\ -\varrho u^2 \\ -\varrho u v \\ -(e+p)u \end{pmatrix} + \begin{pmatrix} 0 \\ 0 \\ 0 \\ \varrho \frac{dq^*_{mas}}{dt} \end{pmatrix}.$$

Here p is pressure, ϱ – density, u, v – velocity components along r and z respectively, t – time. Finally, e is the total energy of a unit volume connected with gasdynamic variables by the equation of state:

$$e = \frac{p}{\gamma - 1} + \frac{\varrho}{2}(u^2 + v^2) \tag{2}$$

The energy intensity for the Gaussian (normal) type source of a variable power with an efficient radius R_q is determined by the relationship:

$$\frac{dq^*_{mas}}{dt} = Q_0 \sigma(t) \exp\left(\frac{-(r^2 + z^2)}{R_q^2}\right). \tag{3}$$

Specific parameters of the phenomena are $\gamma, p_\infty, \varrho_\infty, v_\infty, R_q, Q_0$, coordinates r, z and time t. To determine the similarity criteria, let us choose $p_\infty, \varrho_\infty, R_q$ as values with independent dimensions. The characteristic combinations for our problem will be: the specific heat ratio – γ, the Mach number – $M_\infty = v_\infty(\gamma p_\infty/\varrho_\infty)^{-1/2}$, the normalized intensity of energy supply – $\hat{Q}_0 = Q_0 R_q(p_\infty/\varrho_\infty)^{-3/2}$. We would regard, that equations (1), (2) – are dimensionless, where pressure and density are divided by the corresponding parameters upstream, velocity – by $(p_\infty/\varrho_\infty)^{1/2}$, coordinates – by R_q, time – by $R_q(p_\infty/\varrho_\infty)^{-1/2}$. In the relationship (3) – $R_q = 1$, $Q_0 = \hat{Q}_0$.

The calculating domain is bounded by planes $z = z_0, z = z_k$, by the symmetry axis $r = 0$ and surface $r = r_b(z)$. Surfaces are chosen to provide an undisturbed flow at the entrance cross section $z = z_0$ and at the upper border $r = r_b(z)$. On the symmetry axis $r = 0$ the normal velocity u and derivatives with respect to r are assumed to be equal to zero. The MacCormack finite–difference scheme of the second–order accuracy with space and time was applied. Shock waves and tangential discontinuities are not specially allocated and calculated through on detailed mach points.

2 Steady regimes of an energy supply in a supersonic flow

Assume that the energy source is powered on when $t = 0$ at a uniform supersonic flow $\gamma = 1.4$, $M_\infty = 3.0$ (in that way $\sigma(t) \equiv 1$, if $t \geq 0$).

Previously [4], the steady flow past the energy source of a restricted power was considered. The marching method along the z coordinate was applied, so the restriction was that the flow must be a supersonic in a whole calculating domain. We would mention such a case as **subcritical** – $Q_0 < Q_0^*$. Conversely, when the local subsonic zone appear, we would say about a **supercritical** case and a supercritical power $Q_0 > Q_0^*$.

When the energy source is powered on, the blast similarly increasing of pressure proportional to the energy intensity is observed. So the pressure is normally distributed initially. Than the compression wave propagates from the center of the source. In supercritical case ($Q_0 = 100.0$) the compression wave overthrow, the local subsonic zone close to the center of the source and the strong heading shock wave are appeared. In subcritical case ($Q_0 = 20.0$) the source pushes out gas to the peripherals and the hanging shock wave is appeared. Fig.1 illustrates this effect – lines of equal Mach numbers are presented, the subsonic zone designates by bold lines.

Afterward the process stabilized with time, the final approach is presented on fig.2. In subcritical case the primary singularity of the flow is the hanging shock wave. It is necessary to note that no natural geometrical deflections which might exactly define an initial point of the wave exist for the formulated problem, because the energy supply is normally distributed. On the picture of equal Mach numbers it is clear that the hanging shock wave is composed by continuous compression waves. In supercritical case the strong heading shock wave before the subsonic zone bound the disturbed region – the "shock layer".

A wake of heated low–density gas is formed behind the source (fig.3). For supercritical case the wake is more wider and the gas is more heated up by the source ($\varrho_w = 0.1$ for $Q_0 = 100$, $\varrho_w = 0.25$ for $Q_0 = 20$). Thus the more powerful is the energy source, the greater it's displacement effect. The pressure at cross sections downstream of the source is gradually smoothing and at a long distance $p = p_\infty$ regardless of the source power.

When the energy source is powered off the heated zone is carrying away by uniform flow. The subsonic zone is disappearing instantly.

3 The pulsing energy source in a supersonic flow

Consider regimes of energy supply when the power is time-periodic function. For numerical calculations it was assumed that $\gamma = 1.4$, $M_\infty = 3.0$. The type of energy source is determined by the function $\sigma(t)$:
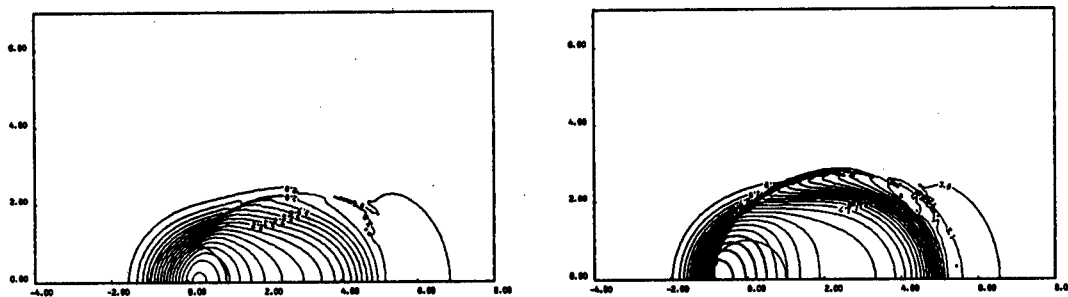
Figure 1: The formation of shock waves (left $Q_0 < Q_0^*$, right $Q_0 > Q_0^*$).
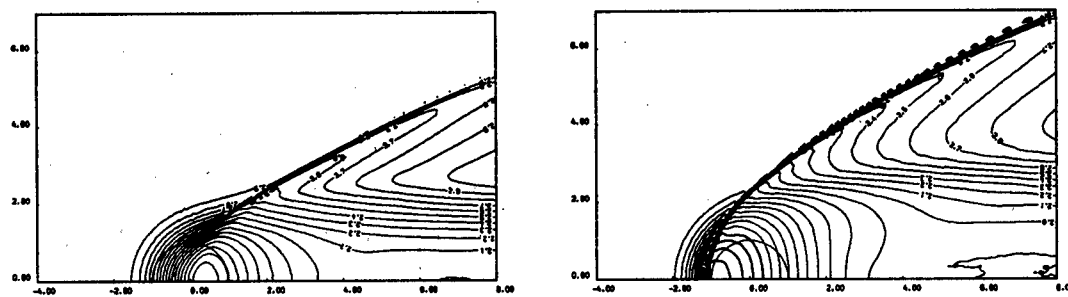

Figure 2: Steady flow past energy source (left $Q_0 < Q_0^*$, right $Q_0 > Q_0^*$).
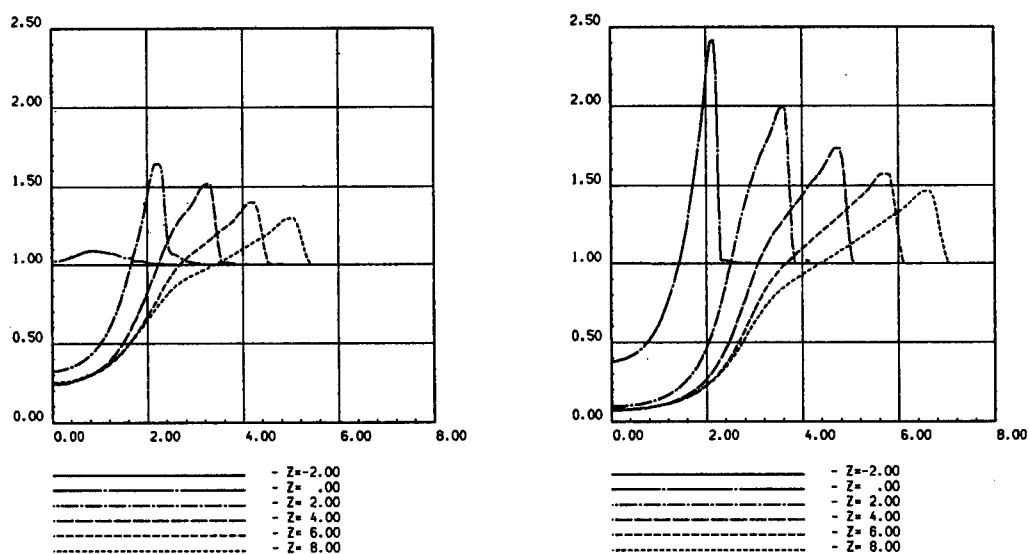

Figure 3: The distribution of the density in cross sections for steady flow (left $Q_0 < Q_0^*$, right $Q_0 > Q_0^*$).
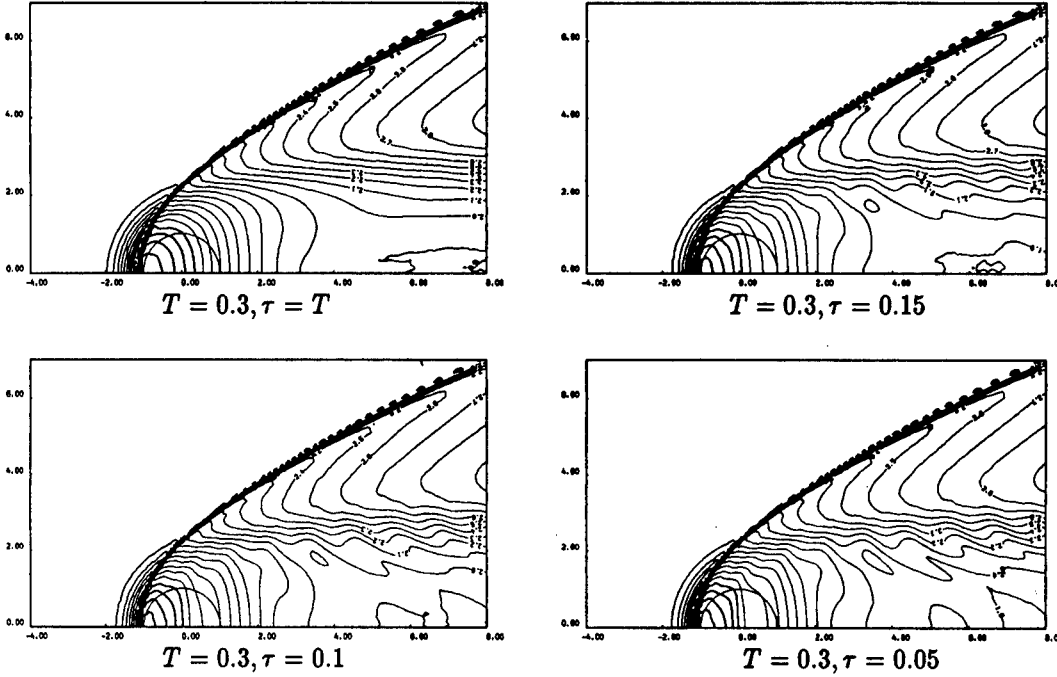
Figure 4: Lines of equal Mach numbers for sources of "rectangle" types for quasistationary mode.

$$\sigma(t) = \begin{cases} \frac{T}{\tau}, & \text{if } 0 \leq \text{mod}(t, T) < \tau, \\ 0, & \text{if } \tau \leq \text{mod}(t, T) < T - \tau. \end{cases} \qquad (4)$$

$$\sigma(t) = \begin{cases} \frac{\pi T}{2\tau} \sin\left(\frac{\pi t}{\tau}\right), & \text{if } 0 \leq \text{mod}(t, T) < \tau, \\ 0, & \text{if } \tau \leq \text{mod}(t, T) < T - \tau. \end{cases} \qquad (5)$$

$$\sigma(t) = 1 + \sin\left(\frac{2\pi t}{T}\right) \qquad (6)$$

Sources (4),(5) are powered at the beginning of every period T for a time τ and operates at pulse-periodic mode. The power of source (6) is changing periodically with time, so that supplied energy is always positive. The common property for sources of any type – the energy supplied to the flow during the fixed period T is the same as in the case of steady regime $\sigma(t) \equiv 1$. For numerical calculations the supercritical regime $Q_0 = 100$ is selected.

In experiments with the pulse-periodic laser [12] for the first time was mentioned that the character of an influence of the energy supply on a supersonic flow is depending on a pulse frequency repetition and vary from essentially unsteady to the quasistationary. This conclusion was drawing on analysis of photographs of the flow structure and direct measurement of some integral characteristics. The numerical investigations confirm the experimental results [12]. The period T is the essential parameter for the pulsing energy source. Altering of T results in quantitative and qualitative changes of the flow structure.

For the quasistationary mode – $T = 0.3$. It was found, that the manner of the energy supply during the period is not essentially. Results are not looks like similarly but the quantitative agreement is observed. Calculations were made for sources (4), (5) and (6)
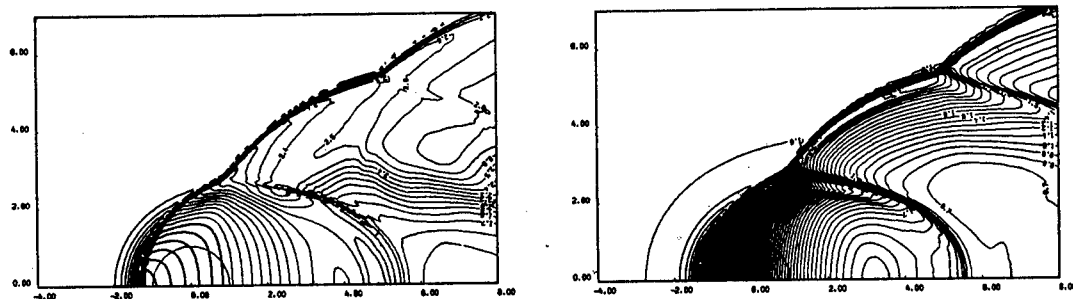
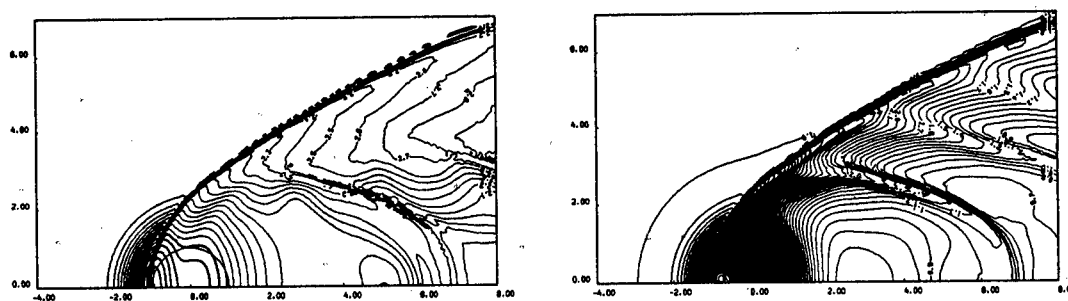Figure 5: The essentially unsteady mode for the "rectangle" source $T = 1.2, \tau = 0.6$.

Figure 6: The transitional mode for the "rectangle" source $T = 0.6, \tau = 0.2$.

with $\tau = 0.15$, $\tau = 0.1$, $\tau = 0.05$. On fig.4 lines of equal Mach numbers are presented for the "rectangle" source (4) in comparison with the corresponding supercritical steady source $Q_0 = 100$. Pictures can be project to each other with hi accuracy. The heading shock wave is stable and the every new pulse pump an additional energy to a flow but not generate compression waves in the "shock layer".

For the essentially unsteady mode – $T = 1.2$. In this case the every new energy pulse is accompanied by a "blast", which generate strong shock wave in the "shock layer". Thus a very complicated shock wave structure appears. The typical picture is presented on fig.5 for $\tau = 0.6$ (lines of equal Mach numbers - left, pressure - right). It is necessary to note, that for this mode the manner of the heat supply, for example τ value, is. significant (compare fig.2 – $\tau = T$ and fig.5 – $\tau = T/2$). Actually, the smaller is τ – the greater must be energy pulse (4) in order to the common energy supplied during the period is not varying. So every "blast" is more powerful and shock waves are stronger.

It is necessary to single out the transitional mode (fig.6). In this case $T = 0.6$ and heading shock wave is stable with time. As distinct from the quasistationary mode the every new pulse generate the compression wave in the "shock layer". The smaller is τ – the more powerful is the wave, which leads to the considerable oscillations of gas dynamics parameters in the heating wake.

References

[1] Georgievsky P.Yu., Levin V.A. Supersonic flow over a body in presence of heat supply before it // Trudy MI AN SSSR. Modern mathematical problems of Mechanics and their applications. 1989. Vol.186. pp.197-201 (in Russian).

[2] Follet M.I. The effect of a small heat supply at the rear surface of a thin, axially symmetric body on its aerodynamic characteristics // Nonequilibrium Gas Flows with Physico-Chemical Transformations, Izdat.Moskov.Gos.Univ., Moscow, 1985, pp.68-77 (in Russian)

[3] Georgievsky P.Yu., Levin V.A. Supersonic flow over bodies in presence of external heat supply sources // Pisma v GTF. 1988. Vol.14, No.8. pp.684-687 (in Russian)

[4] Georgievsky P.Yu., Levin V.A. Modification of regime of the flow over a sphere by means of local energy supply upstream // International Conference on the Methods of Aerophysical Research. Novosibirsk. ITAM. 1996. Vol.3. pp.67-73

[5] Levin V.A., Terentieva L.V. Supersonic flow over cone in presence of heat supply at the neighborhood of its top // Izv.RAN, MGG. 1993. No.2. pp.110-114 (in Russian)

[6] Korotaeva T.A., Fomin V.M., Shashkin A.P. Numerical investigation of the local energy supply effect on the 3-D flow over sharpening bodies // ITAM RAN Preprint. Novosibirsk 1996. No.1, 36 p. (in Russian)

[7] Arafailov S.I. The influence of energy supply at the shock layer on a supersonic flight of bodies // Izv. AN SSSR, MGG. 1987. No.4. pp.178-182 (in Russian)

[8] Levin V.A., Afonina N.E., Georgievsky P.Yu., Gromov V.G., Larin O.B., Terentieva L.V. Investigation of possibility for controlled modification of supersonic flow over flying vehicles by local energy supply // IM MSU Preprint No.24-97, Moscow, 1997, 22p. (in Russian)

[9] Vitcowsky V.V., Grachev L.P., Gritcov N.N. etc. The investigation of unsteady supersonic flow over bodies with air heated by longitudinal electrical discharge // TVT. 1990. Vol.28, No.6. pp.1156-1163 (in Russian)

[10] Mishin G.I., Klimov A.I., Gridin A.Yu. The longitudinal electrical discharge in a supersonic gas flow // Pisma v GTF. 1992. Vol.18, No.15. pp.86-92 (in Russian)

[11] Gridin A.Yu., Efimov B.G., Zabrodin A.V., Klimov A.I. Numerical and experimental research of supersonic flow over blunt-nosed body with the needle in presence of electric discharge on its head // Inst.Appl.Math.RAN im.Keldiesh M.V. Preprint. Moscow 1995. No.19, 31 p. (in Russian)

[12] Tretyakov P.K., Grachev G.N., Ivanchenko A.I., etc. Stabilization of an optical discharge in a supersonic flow of argon // Dokl. Acad. Nauk. 1994. Vol.336, No.4. P.466-467 (in Russian)

[13] Tretyakov P.K., Garanin A.F., Kraynev V.L., Tupikin A.V., Yakovlev V.I. Investigation of local laser release influence on supersonic flow by methods of aerophysical experiments // International Conference on the Methods of Aerophysical Research. Novosibirsk. ITAM. 1996. Vol.1. pp.200-204

[14] Guvernyuk S.V., Samoilov A.V. Control of supersonic flow around bodies by means of pulsed heat source // Pis'ma Zh.Tekh.Fiz.23 (5), May 1997, pp.333-336

THE FLOW STRUCTURE INVESTIGATING IN A CHANNEL AND INTEGRAL INLET CHARACTERISTICS

M.A. Goldfeld, A.V. Starov

Institute of Theorical and Applied Mechanics SB RAS, Novosibirsk, Russia

L. Auneau, X. Montazel

AEROSPATIALE, France

INTRODUCTION

The research of inlet internal flow structure and integral characteristics is of great extend for the development of ramjet and scramjet propulsion. An approach is reported in this paper. Such a technique allows to extend the range of the information obtained during inlets experimental investigations and reduce the duration of tests and therefore their costs.

The approach combines different types of measurements: quantitative and qualitative ones. The inlet concerned in this study was a 2D inlet, whose internal channel was drosseled during the experiments by means of special drossel device of small size. Simultaneously with drosseling, the flow at the inlet throat and diffuser was checked by the pressure distribution, by schlieren visualisation trough the optic glasses on the side walls and finally by the air rate. Such an approach made it possible to obtain the drossel characteristics, pressure fields, flow rates and recording of the changes of the flow picture in the channel at its drosseling during the experiment. In addition, the windows in side walls allowed us to record a soot-oil visualisation of the flow in the throat region during the experiment; that is, without distortion introduced by the flow regime disruption at the wind tunnel stop.

The throat area was being controlled by the height adjustment when the throat inserts or number of vertical pylon were changed. As a consequence, the integral characteristics of the controlled inlet were obtained and the range of the inlet start-up was determined.

A large series of tests were implemented in the hot-shot wind tunnel IT-302M. It has been possible to obtain the inlet characteristics for Mach numbers 5 and 6 at a higher unit Reynolds number than it was applied in the wind tunnel T-313, as well as the range of Mach number, which was extended up to Mach 8. The effect of the cowl leading edge bluntness on the inlet start-up and on the flow characteristics has been studied. The schlieren visualisation pictures of the flow in the channel through the sidewall windows have been obtained thanks to a high-speed videocamera.

The tests results have been compared to 2D and 3D numerical calculations.

MODEL AND EXPERIMENTAL EQUIPMENT

The tests have been carried out with an already existing mock-up, which has been updated to take into account the test specifications.

For example, optic glasses of big size have been placed in the vicinity of the inlet throat and beginning of diffuser, to be able to visualize the internal flowfield. The model is presented figure 1 :
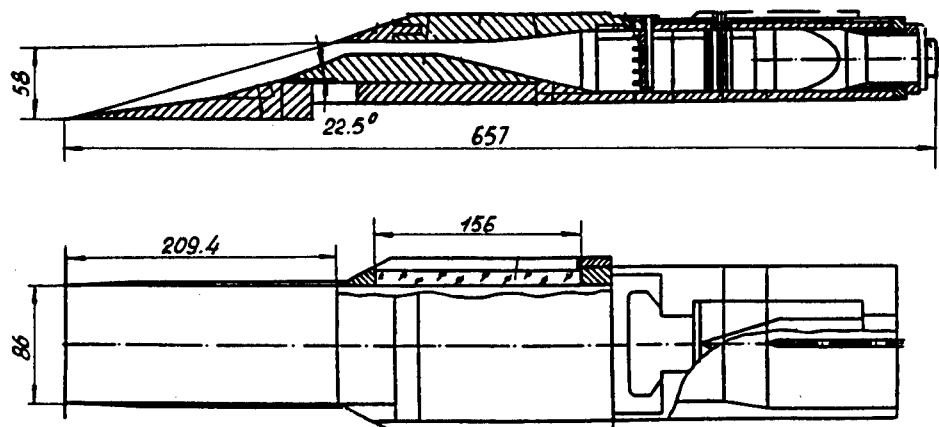

Fig. 1. Modular mock-up.

Notice that the air inlet has been chosen to carry out these tests not in order to reach good performance (it is not optimised that way), but because she was presenting a good potential for modularity and physical inspections.

The following parts could be replaced :
• the cowl (3 available), to study the effect of cowl length and bluntness,
• the throat insertion (5 available),
• the "injection" struts (4 parts available, including from 3 to 6 struts),

Pressure measurements
• 4 static pressure were installed on the throat insertion, along the x-axis, in the symmetry plane,
• a pressure probes rake was placed in the throat region. It had 12 total pressure probes; 4 static pressure were located at the same level.

Hypersonic Tests
The tests have been carried out at ITAM SB RAS at Mach numbers 5, 6 and 8 in the hot-shot wind tunnel IT-302M and in the wind tunnel T-313 (seven runs were performed in this last one to verify the inlet starting and to cross-check the results obtained). The tests conditions are :

	IT-302M			T-313	
Mach number	5	6	8	5	6
Total pressure (bar)	53.6 - 59.9	88.8 - 93.1	276.5 - 407.3	8.12 - 8.17	8.17 - 8.22
Temperature (K)	894 - 959	1032 - 1093	898 - 1309	410 - 430	410 - 440
$Re \times 10^{-6}$ 1/m	27.39 - 29.19	21.53 - 23.98	31.35 - 44.46	13.58 - 15.41	8.75 - 9.41

The tests have been conducted for both ramjet and scramjet cases. For the ramjet case, the throttling device and the flowmeter were placed in the model.

NUMERICAL CALCULATIONS

Several codes of different levels of complexity have been used to compute the 2D air intake. The codes extends from semi-empirical to fully Navier-Stokes solvers; among the codes used, are :

OCEAS

OCEAS has been developed by AEROSPATIALE [1] to assist engineers in the aerodynamic design of supersonic missile inlets. It is a semi-empirical flow solver which uses simple physical models that require little CPU time. The code uses analytical formulas to compute, from upstream to downstream, oblique shocks, expansions waves and their interactions as well as the boundary layer displacement effects. The flow is supposed to be two-dimensional and planar. Global parameters (mass flow ratio, total pressure recovery, Mach number) are obtained trough integration or averaging of the flow in the desired section.

FLU3M

FLU3M is a multidomain solver developed at ONERA [2][3] for the calculation of inviscid or viscous subsonic and supersonic flowfields. It may use either explicit or implicit non centred TVD scheme with MUSCL approach. Boundary conditions are taken into account using either compatibility relations or flux correction.

In the following calculations performed by AEROSPATIALE, upwind numerical approaches are used for the solution of the compressible Reynolds averages Navier-Stokes equations. Three approaches have been undertaken :
- 2D calculations using the Baldwin-Lomax cell-centre model,
- 2D calculations using the k-ε cell-centre model,
- 3D calculations using the k-ε cell-centre model,

COMPARISONS - RESULTS

OCEAS : quantitative comparisons
At Mach 5, several calculations have been implemented for the ramjet case, global performance for two geometry are compared in the table below :

throat/cowl n°	Quantity	Experimental data	OCEAS computation	Difference
1 / 1	η	0.15	0.162	8%
"	ε	0.8	0.841	5%
5/2	η	0.135	0.134	1%
"	ε	0.925	0.982	6%

The results between tests and computations are quite close.
They are in good agreement, although the code used is "simple".

FLU3M : quantitative and qualitative comparisons

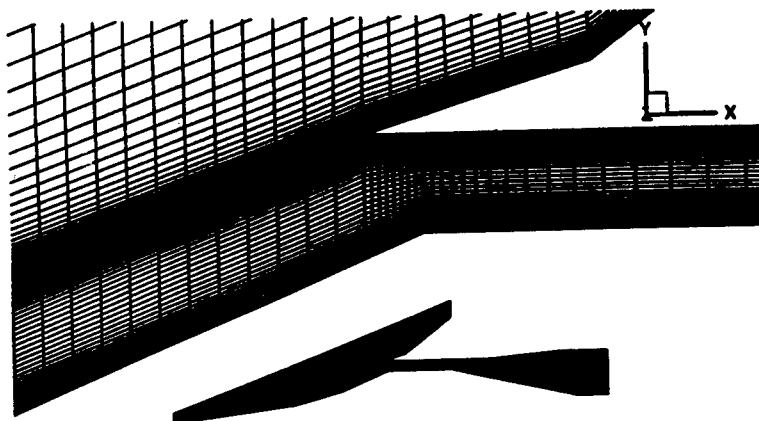The mesh generation of the calculated geometry is presented figure 2 :

Fig. 2. Mesh generation.

The chart below presents a comparison of static pressure evolution along the x-axis between the test and the numerical result :
- 2D calculations, k-ε cell-centre model (figure 2),
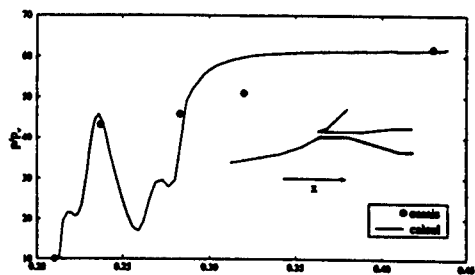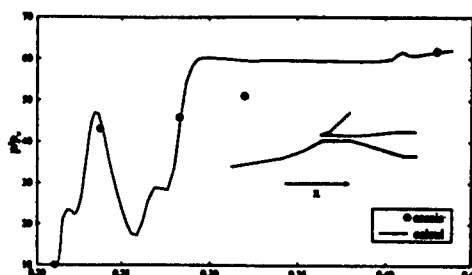- 3D calculations, k-ε cell-centre model (figure 3) :

Fig.3. 2D calculations.

Fig. 4. 3D calculations.

The calculations curves, for both 2D and 3D calculations, are in good agreement with the tests results; in particular, the static pressure upstream of the separation and in the separated zone are correctly cross-checked.

For both cases, the biggest difference between experience and tests appears just before the end of the constant area cross-section.

The figures presented hereafter show the Mach number and the static pressure ratio distributions calculated.
The code used is the 3D k-ε cell-centre model.
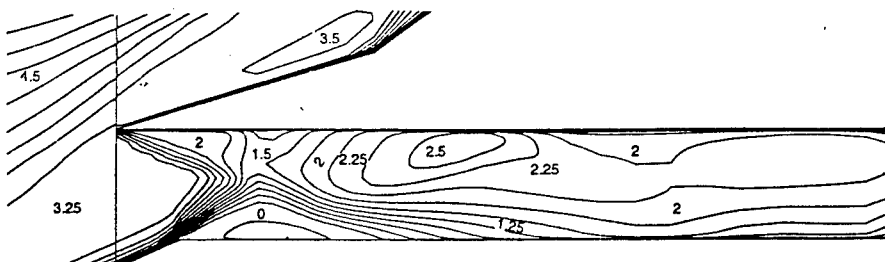
68
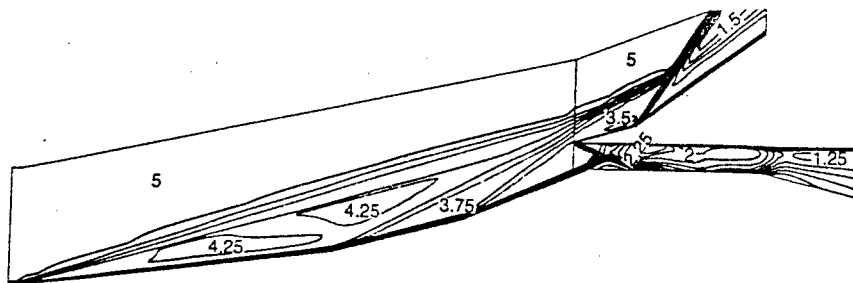
Fig. 5. ISO - Mach lines.

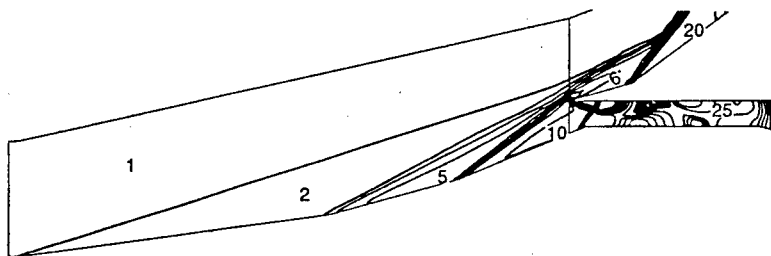Fig. 5b. ISO - Mach lines : zoom in throat region.

Fig. 6. ISO - static pressure.

Fig. 7. Oil visualization: streamlines along the sidewalk in the throat - diffuser region.

69

The observation of, on the one hand, the ISO Mach and static pressure lines, and on the other hand, the oil visualisation are in good agreement : the separation is correctly modelled through the calculations; the shock coming from the cowl is also comparable.
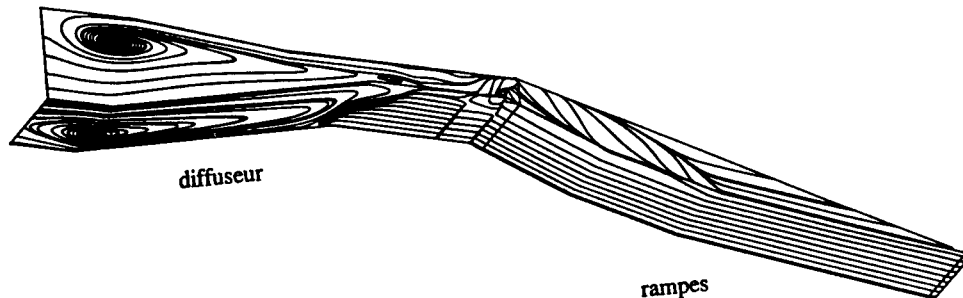

Fig. 8. Calculated streamlines, using 3D k-ε model.

This figure is particularly interesting, as it shows the separated regions and the swirls (in the diffuser). The agreement with the oil visualisation is good.

CONCLUSION

The tests using "classical" measurements, such as pressure measurements are, in a lot of cases concerning air inlets tests, not sufficient as they are allowing only to get its "global" characteristics, unless installing a lot of pressure probes.
For "complicated" geometry, dominated by the viscous interactions, the optimisation of the air intake means the knowledge of the internal flowfield behaviour. This knowledge can be obtained in two different ways : firstly, through numerical calculations, using 3D Navier-Stokes solvers, and secondly, through tests using complementary measurement devices : the schlieren pictures as well as the oil visualization movies are of highest interest to describe the internal flow throughout the working range of the inlet accurately.
The combination of "classical" and "qualitative" measurements linked with numerical calculations can lead to time and cost reductions for air inlets development.

ACKNOWLEDGEMENTS

REFERENCES

1. R.G. Lacau, P. Garnero, F. Gaible. Computation of supersonic intakes — AGARD Special Course on Missiles Aerodynamics: AGARD report 804, 1994.
2. Ph. Guillien. M. Dormieux. Design of a 3D multidomain code // Int.Seminar on Supercomputing. Boston (USA). 3-5 oct., 1989.
3. C. Jouet, P. d'Espiney. 3D laminar and 2D turbulent computations with the Navier-Stokes solver FLU3M // 8th Int. conf. on Numerical Methods in Laminar and Turbulent flow. University of Swansea (UK), July 18-23, 1993

THE STUDY OF RELAMINARIZATION OF A SUPERSONIC TURBULENT BOUNDARY LAYER

M.A. Goldfeld, R.V. Nestoulia, S.B. Nikiforov, A.N. Shiplyuk
Institute of Theoretical and Applied Mechanics SB RAS, Novosibirsk, Russia
B. Aupoix, A. Seraudie
ONERA-CERT, Aerothermodynamics Department, Toulouse, France

INTRODUCTION

The understanding of the process of relaminarization of a turbulent boundary layer and the possibility of predicting it are important problems for aerospace engineering. Relaminarization involves a decrease in heat transfer intensity, which can lead to an increase in efficiency of nozzles, turbine blades, etc. The first studies devoted to relaminarization of a turbulent boundary layer were performed in 50-60s [1, 2]. The flows in nozzles and behind expansion fans were studied in these papers. The results on decreasing heat transfer intensity in the boundary layer were obtained for the first time. Relaminarization researches were then performed both for subsonic [3-8] and supersonic [9-11] flows. These studies yielded the data on the boundary layer structure and averaged parameters, pulsation characteristics under the conditions of favorable pressure gradient. It should be noted that the above studied were conducted for free-stream Mach numbers $M_\infty \leq 3$. Thus, the range of hypersonic Mach numbers, for which the designing of various aircraft elements taking into account the relaminarization is especially important, remains poorly studied. Theoretical works on relaminarization are based on solving the Reynolds-averaged Navier-Stokes equations with the use of various turbulence models [12-13]. The purpose of numerical and experimental studies is to create simple and reliable criteria of relaminarization and to develop numerical methods for calculating these flows. Several relaminarization criteria are currently used [9, 13, 14]. They are based on various combinations of longitudinal pressure gradient, skin friction coefficient, and gradient Reynolds number. The use of different relaminarization criteria, however, leads to contradictory results. This can be explained both by inadequacy of relaminarization criteria themselves and by contradictory experimental data.

The objective of the present work is to obtain experimental data on relaminarization of initially turbulent boundary layer under the action of favorable pressure gradient at $M_\infty=4$ and $Re_1=10\text{-}26*10^6$ 1/m, as well as to evaluate the applicability of various relaminarization criteria at hypersonic speeds.

EXPERIMENTAL TECHNIQUE

The present experiments were performed in the low-turbulent wind tunnel T-325 of ITAM SB RAS. The model was a cone-cylinder body with a 60-mm cone diameter. The models with cone half-angles $\theta=10^0$, $\theta=15^0$ were tested (Fig. 1). The following quantities were measured:
  - transition length on the cone;
  - static pressure on the model surface;
  - temperature on the model surface;
  - total pressure in the boundary layer;
  - mass flow fluctuations in the boundary layer;
  - skin friction [15].

Preliminary theoretical and subsequent experimental estimates showed that under the conditions of low-turbulent wind tunnel the cone generatrix length is insufficient for the formation of natural turbulent boundary layer. Therefore, a boundary layer trip was placed on the cone. The conclusion about relaminarization attainment was drawn on the basis of analysis of velocity and pulsation profiles, relaminarization criteria being also applied.

EXPERIMENTAL RESULTS

The pressure measurements showed that the pressure gradient value behind the inflection point for the model with $\theta=15^0$ (Fig. 1) is higher than the corresponding values for the model with $\theta=10^0$ by a factor of 1.5-2. A low-pressure gradient on the model with $\theta=10^0$ did not allow the relaminarization process. It is also seen that a moderate increase of the Reynolds number leads to a substantial decrease of the longitudinal pressure gradient. The decrease of pressure gradient is explained by a smaller boundary layer thickness
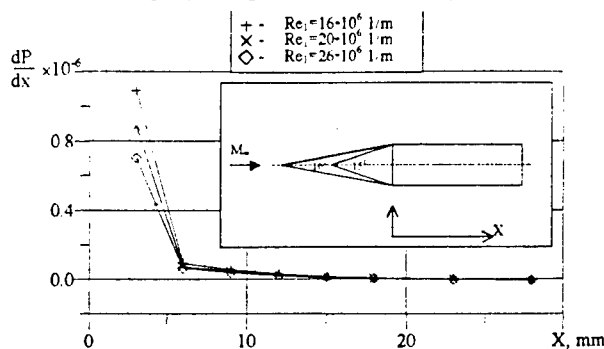

Fig.1 Pressure gradient for model with $\theta=15^0$

on the cone, which leads to an increase of the static pressure level, whereas the static pressure on the cylinder depends weakly on the Reynolds number.

The use of Schlieren pictures allowed one to determine the point of transition of the laminar boundary layer on the cone to a turbulent state. For both models (with $\theta=10^0$ and $\theta=15^0$) the distance between the transition point and the model contour inflection was at least 60 mm, which roughly amounts to 100 boundary layer thicknesses. Figure 2 shows the velocity profiles upstream of the contour inflection in the form of the "wall-wake" law for the cone with $\theta=15^0$. It is seen that a turbulent boundary layer is formed ahead of the contour inflection.
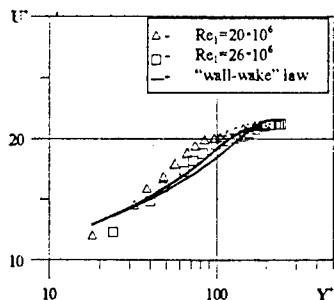

Fig.2 Velocity profile on the cone

The experiments conducted in the Reynolds number range $Re_1=16-26 \cdot 10^6$ 1/m for the model with $\theta=15^0$ showed that partial relaminarization is realized downstream of the inflection point. The near-wall part of the boundary layer (up to 0.4δ) becomes laminar, while the outer part of the boundary layer remains turbulent. A pronounced effect of the free-stream Reynolds number on the shape of velocity profile was observed beginning from the coordinate $X=12-15$ mm (10δ). Velocity profiles for $X=48$ mm for the Reynolds number range $Re_1=16-26 \cdot 10^6$ 1/m are presented in Fig. 3 in a logarithmic scale. The solid line here corresponds to the "wall-wake" law, and the dashed line shows a theoretical profile of the laminar Blasius boundary layer. On the whole, the velocity profile shape for the Reynolds number $Re_1=16 \cdot 10^6$ 1/m is typical of the region $0<X<33$ mm for all Reynolds numbers. It is

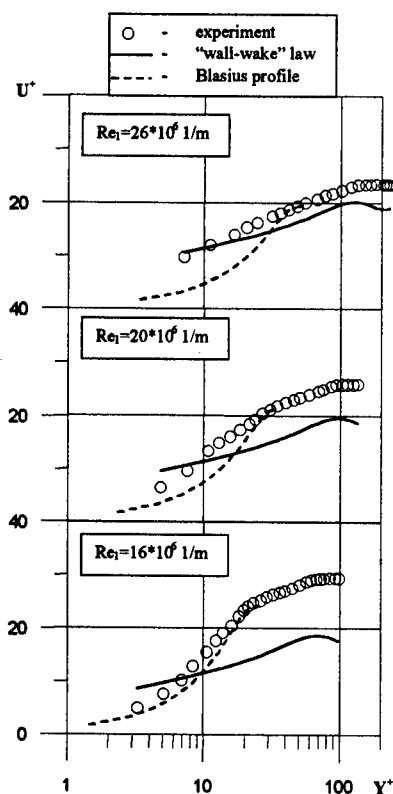seen that the near-wall part of velocity profile is in good agreement with the theoretical Blasius profile, whereas a logarithmic section and wake component are retained in the outer part of the boundary layer. The main specific feature of the flow at X=48 mm is that the velocity profiles depend strongly on the free-stream Reynolds number. For the Reynolds number $Re_1=16{*}10^6$ 1/m the velocity profile consists of two parts: thick near-wall laminar part and outer turbulent part. As the Reynolds number increases, the near-wall laminar part deviates at first from the theoretical laminar profile ($Re_1=20{*}10^6$ 1/m), and then the boundary layer profile becomes fully turbulent ($Re_1=26{*}10^6$ 1/m). Thus, a conclusion can be drawn that the free-stream Reynolds number affects mainly the relaminarization region length, an increase of the Reynolds number leading to a decrease of the relaminarized flow region or to its complete vanishing.

Fig.3 Velocity profiles for X=48mm

An example of the profiles of mass flow pulsations $<m>_\Sigma$ versus the longitudinal coordinate is shown in Fig. 4 for the free-stream Reynolds number $Re_1=26{*}10^6$ 1/m. It is seen that the level of mass flow pulsations decreases appreciable (by a factor of 2-3) immediately downstream of the interaction region. A specific feature of the boundary layer pulsation profile behind the inflection corner is that it has two peaks of pulsations. One of them is located in the outer part of the boundary layer, the other is in the near-wall layer. The level of pulsations at the boundary layer edge depends weakly on the longitudinal coordinate, while the level of the near-wall peak of pulsations rapidly increases as the longitudinal coordinate increases, and at X=33 mm it becomes higher than the level of pulsations in the free-stream boundary layer on the cone (X=-13 mm). The existence of the near-wall peak of pulsations is apparently due to the formation of a "new" layer directly behind the inflection point, which can be considered as a singular point similar to the leading edge of the plate, which is supported by the total pressure measurements. The increase of near-wall pulsations can be attributed to the transition process in this "new" layer. The character of variation of the near-wall maximum of pulsations along the model is shown in
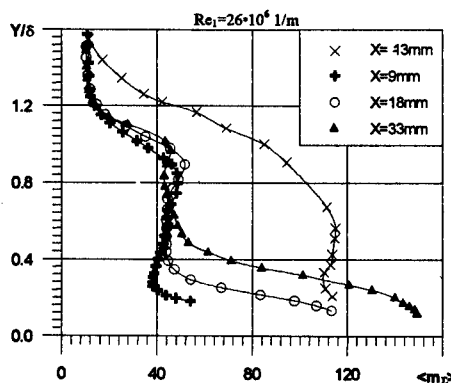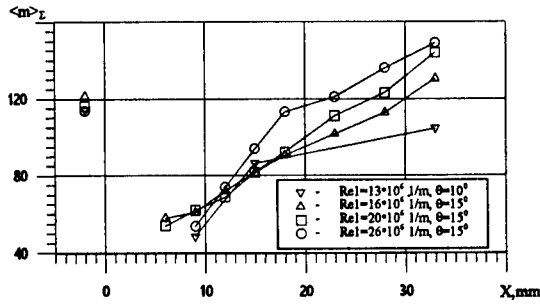

Fig.4 Mass flow pulsation

Fig.5 Near-wall maximum of fluctuations versus X

Fig.5. The decrease of pulsations immediately downstream of the inflection point is approximately equal for all Reynolds numbers. It is also seen that for all Reynolds numbers for the model with $\theta=15^0$ the magnitude of the near-wall maximum of pulsations, beginning from a certain value of X, is higher than the level of free-stream fluctuations.

The general analysis of the flow, obtained experimental data and the data of other authors testify that the beginning and the process of relaminarization are determined by nondimensional complexes based on combinations of the parameters U_e, ρ_e, ρ_w, dU_e/dx, τ_w, $\tau(y)$, μ_e, μ_w, T_e, T_w, q, and δ^{**}. Several relaminarization criteria are currently used [9, 13]. Figure 6 shows a comparison of experimental data of the present work with one of these criteria based on the relation C_p/C_{fcone} [14], where $C_p=0.5\cdot(P_{cyl}-P_{cone})/\rho V^2$ and $C_{fcone}=0.5\cdot\tau_{wcone}/\rho V^2$. In accordance to this criterion, the relaminarization occurs if the ratio C_p/C_{fcone} is larger than 75; if the ratio C_p/C_{fcone} is lower than 60, the flow remains turbulent.
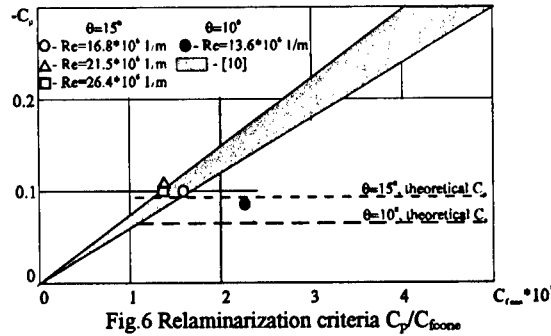

Fig.6 Relaminarization criteria C_p/C_{fcone}

A transitional flow is formed within C_p/C_{fcone} =60-75. It is seen from Fig. 6 that the boundary layer on the model with $\theta=15^0$ corresponds to the transitional region in the entire range of Reynolds numbers, which is validated by pressure measurements and hot-wire anemometry, while the boundary layer on the model with $\theta=10^0$ is turbulent. This relaminarization criterion takes into account only the pressure difference and ignores the longitudinal pressure gradient. Therefore, it is of interest to compare the data of the present work with a criterion taking into account the longitudinal pressure gradient. The calculated results for the relaminarization criterion $\Lambda = -\dfrac{\delta}{\tau_{wcone}}\dfrac{dP}{dx} \geq 50-70$ [13] based on experimental data of the present work are presented in Table 1.

Table.1

θ	15^0			10^0
$Re\cdot10^{-6}$ 1/m	16	21	26	13.6
Λ	55.4	52.5	60.9	18.6

Like previously, these results show that the boundary layer on the model with $\theta=15^0$ corresponds to the transitional regime, and the boundary layer on the model with $\theta=10^0$ corresponds to the turbulent flow.

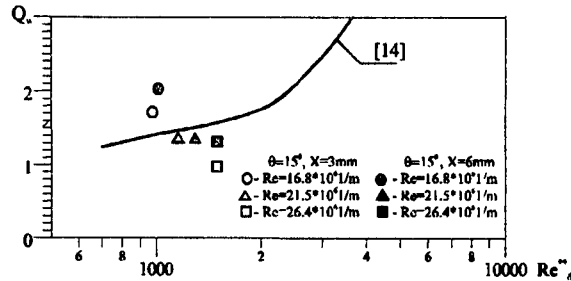Fig.7 Relaminarization criteria Q_w

A comparison with the relaminarization criterion $Q_w(\text{Re}_\delta^{**}) = \mu_w \dfrac{dU}{dx}\dfrac{1}{\rho_e U_e^2}$ [14] showed that

in this case the boundary layer on the model with $\theta=15^0$ corresponds again to the transitional region (Fig. 7). The maximum values of relaminarization criterion correspond to the Reynolds number $\text{Re}_1=16*10^6$ 1/m. It can be also noted that the value of Q_w depends on the coordinate in which it was calculated.

Skin friction measurements allow one to determine the flow regime in the boundary layer, since the friction value is substantially different in the laminar and turbulent layers. The skin friction was found in the present work from the results of optical measurement [15] and processing of velocity profiles. As was shown above, the boundary layer on the model cylinder in the region of relaminarization is neither turbulent nor laminar. Therefore, two skin friction coefficients were calculated on the basis of velocity profiles. The first coefficient was found on an assumption that the velocity profile corresponds to a turbulent flow. The second coefficient was calculated assuming that the main contribution to skin friction is formed by the near-wall part of the boundary layer, which is laminar, and the friction coefficient was found on the basis of velocity derivative. An example of skin friction distribution can be seen in Fig. 8. It is seen from the figure that a dramatic decrease of skin friction takes place immediately behind the inflection point. The skin friction on the cone depends on the free-stream Reynolds number, whereas on the cylinder surface, where partial relaminarization takes place, the skin friction depends only weakly on the free-stream Reynolds

Fig.8 Friction force

number. Obviously, the near-wall laminarized part of the boundary layer makes the major contribution to the skin friction value in the relaminarization region.
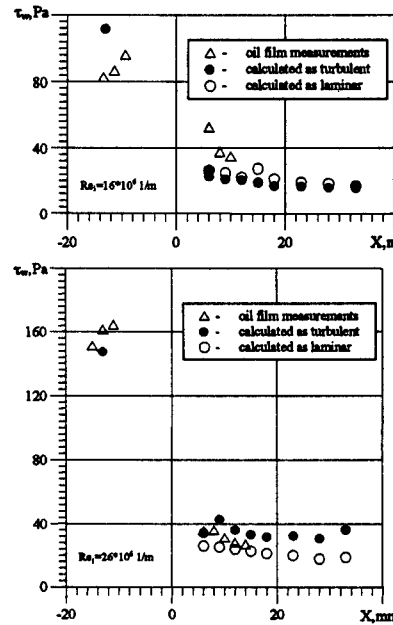
CONCLUSION

Thus, the following conclusions can drawn from the obtained results:
- experiments on two models with $\theta=10^0$ and $\theta=15^0$ showed that the boundary layer relaminarization takes place on the model with $\theta=15^0$;
- longitudinal pressure gradient affects strongly the origin of the relaminarization process;
- a composite boundary layer with laminar near-wall and turbulent outer parts is formed in the region of partial relaminarization;
- free-stream Reynolds number affects mainly the relaminarization region length, an increase of the free-stream Reynolds number leading to a decrease of relaminarization region length.

REFERENCES

1. Wilson D.G., Pope J.I. Convective heat transfer to gas turbine blades // Proceedings of the Institute of Mechanical Engineers. -1954.
2. Stenberg J. The transition from a turbulent to a laminar boundary layer: Report 906/ Ballistic Research Laboratory. -Aberdeen. -1954.
3. Launder B.E. Laminarization of the turbulent boundary layer in a severe acceleration // Trans of ASME. –1964. –V.34. –Part 2. –P. 707-709.
4. Badri-Narayan M.A., Ramjee V. Criteria for reverse transition in a two dimensional boundary layer flow//J. of Fluid Mechanics. –1969. –V.35. –P. 225-241.
5. Narasimha R., Sreenivasan K.R. Relaminarization in highly accelerated turbulent boundary layers. -J. of Fluid Mechanics. –1973. –V.61. –P.417-473.
6. Sibulkin M. Transition from turbulent to laminar pipe flow//The Physics of Fluids. –1962. –V.5. -№3. –P. 280-284.
7. Kline S.J., Reynolds W.S., Schraub F.A., Runstandler P.W. The structure of turbulent boundary layer. -J. of fluid Mechanics. –1967. –V.30. –P. 741-773.
8. Romanenko N.P., Leontiev A.I., Solivin A.N. The investigation of skin friction and heat flux transfer in turbulent flow in the asymmetric channels with longitudinal pressure gradient. –Applied Mechanics and Technical Physics. –1961. -№5. –P. 16-25.
9. Goldfeld M.A. On reverse transition of compressible turbulent boundary layer in a transverse flow around a convex corner configuration // In Proceedings of Laminar-Turbulent Transition Symposium. –19-13 July 1984.
10. Narasimha R., Vishwanath P.R. Reverse transition at an expansion corner in supersonic flow. —IAA Journal 13(5). –May1975. –P. 693-695.
11. Page R. H., Sernas P. Apparent reverse transition in an expansion fan. –AIAA Journal. –V.8. -№1. –1970. –P. 189-190.
12. Jones W.P., Launder B.E. The prediction of laminarization with two equation model of turbulence. –International Journal of Heat and Mass Transfer. -№15. –1972. –P. 372.
13. Aupoix B., Viala S. Prediction of boundary layer Relaminarization uzing low Reynolds number turbulence models // 33rd Aerospace Meeting and Exhibit. –Reno. –January 9-12. –1995.
14. Nash-Webber J.L., Oates G.C. An engineering approach to the design of laminarizing flows. –Journal of Basic Transactions of the ASME, -№4, -1972, -P.897-904.
15. Kornilov V.I., Pavlov A.A., Shpak S.I. On the techniques of skin friction measurements using optical method // Proceed of International Conference on the Methods of Aerophysical Research. –Novosibirsk. –Part 2. –1994. –P112-117.

EXPERIMENTAL AND NUMERICAL SIMULATION OF NONEQUILIBRIUM IONIZATION BEHIND STRONG SHOCK WAVE IN MARTIAN ATMOSPHERE

V.A.Gorelov, M.K.Gladyshev, A.Yu.Kireev, V.G.Tchebureev, S.V. Shilenkov

Central Aerohydrodynamic Institute (TsAGI), 140160, Zhukovsky-3, Moscow Region, Russia

The results of investigation of nonequilibrium processes, when a strong shock wave propagates in gas mixture simulating Martian atmosphere, are presented. The investigation includes the experiments in Arc-Driven Shock Tube and numerical simulations. The measurements of ionization parameters (electron and ion concentrations n_e, n_i , electron temperature T_e) have been performed over the range of shock wave the velocity V_s=4.5 to 9.5 km/s. The data obtained during the tests are used to verify a numerical model of nonequilibrium ionization behind a shock wave. A multitemperature kinetic scheme, that takes into account different models of kinetics, has been used in the calculations.

The physical model of nonequilibrium processes in hypersonic shock layer under the Martian atmosphere entry conditions is verified with using experimental results obtained in the Arc-Driven Shock Tube (ADST). In this approach the ionization characteristics of gas mixture behind the shock wave, measured in the ADST, are compared with corresponding computational characteristics obtained by the numerical model of a strong shock wave (SSW-model). Experimental investigations have been carried out in ADST where studies on physical-chemical processes behind strong shock waves with propagation velocities of 4-15 km/s, have been performing for the last years [I,2].

A discharge driver chamber of ADST had ceramic walls and molibden electrodes. Driver gas was helium heated by a powerful electric discharge. A low pressure driven channel represented a glass sections structure with the length about 5m and diameter of 57mm assembled by means of metallic flanges. The structure's sections had a sealed lead-in for probe devices and windows for the optical recording. The channel was preliminary evacuated up to the pressure 10^{-3} torr. A gas mixture, simulating Martian atmosphere, was the medium under study in the main part of the experiments. The simulation of the atmosphere composition was carried out by using the mixture of CO_2 and air. A certified carbon dioxide (99.9% CO_2) was used . It was delivered into the ADST channel evacuated up to the pressure at which the channel was filled with the mixture containing CO_2 (96%), N_2 (3%), O_2 (1%). The difference between the mixture used and the gas medium of Martian atmosphere is in the increased concentration of O_2. However, the calculations of the gas species behind the shock wave front specially carried out have shown that the change in the content of O_2 before the shock wave within 0-3% does not actually influence the gas species and relaxation processes behind the shock wave. The main portion of the experiments was carried out at the pressure in the channel P_1 = 0.2 (±1%) torr. The velocity of shock wave propagation was measured by a system of photomultipliers with the accuracy of 2%. The investigations have been carried out within the range of the shock wave velocities 4.5-9.5 km/s. In the studies on the measurements of ionization parameters probe techniques of diagnostics with required characteristics of the resolution and range of measuring the ionization parameters are used. To define ion and electron concentration the electric probes of different type are used. Single probes

with cylindrical electrodes were installed parallel and normal to the gas flow under study. Probes operated in the regimes of gathering the ion and electron current. The diameters of electrodes changed from 0.1 to 0.01mm (their length varies within 2-5mm depending upon the type of the experiment). All probes are expendable. To interpret the results of probe measurements the data of detailed studies on the peculiarities of the operation of cylindrical probes under conditions of the supersonic flow behind the shock wave in the transitional Knudsen regime are used [3]: $0.1 \leq Kn \leq 10$ ($Kn = \lambda_{i,e}/r_p$, $\lambda_{i,e}$ is the length of free path of ions and electrons, r_p is probe radius). For the longitudinal cylindrical probes in the transitional regime the probe currents $J_{e,i}$ are related with n_e and n_i in the regime of gathering electrons and ions as follows:

$$J_{e,i} = \bar{j}_{e,i} \, S_p \, n_{e,i} \, e \, (k \, T_e / 2\pi \, m_{e,i})^{0.5} \qquad (1)$$

where S_p is the area of the probe electrode, e is electron charge, $\bar{j}_{e,i}$ is the nondimensional current density depending on the conditions of the probe operation in the plasma under study, which is defined for the conditions of the experiment in ADST on the basis of the results presented in [1,3], where $\bar{j}_{e,i}$ as functions of Kn are given.

The use of a thin cylindrical probe located normally to the flow makes it possible to increase the spatial resolution of the probe technique. In the regime of a thin probe layer and $Kn \geq 1$ for the coupling between J_i and n_i with the error not exceeding about 20% the following relation can be used [3]: $\qquad J_i = 2 \, r_p \, l_p \, n_i \, e \, u_i \qquad (2)$
where l_p is the length of the probe electrode, u_i - mass velocity of the ion flow equal to the mass velocity of gas u. The relation (2) permits to define n_i without introducing T_e and m_i , but requires the data on the velocity u. When a longitudinal cylindrical probe is used in the regime of gathering the electrons a strong function of $\bar{j}_e$ from Kn is observed with the number of the latter less than 10. The influence of Kn can be taken into account if the electron free path lengths λ_e are known. However, $\bar{j}_e$ may be determined under experimental conditions by using simultaneously a pair of single probes with different diameters d_1 and d_2 [4]. In this case, for the characteristic conditions of the experiments in the ADST, an approximate relation for $\bar{j}_e$ of the second probe can be obtained:

$$\bar{j}_{e2} \cong (1-J_{e1}/J_{e2}) / ((d_1/d_2-1) \cdot (J_{e1}/ J_{e2})) \qquad (3)$$

In (3) J_{e1} and J_{e2} are measured in the experiment currents to the probe with diameters d_1 and d_2 , respectively. Using (3) through the relation (1) it is possible to derive n_e , if T_e is known.

The measurement of electron temperature T_e is required not only for defining $n_{e,i}$ from probe measurements, but is of a special interest because T_e is an important parameter in determining radiation properties of gas. Besides, T_e can be used to verify numerical models of nonequilibrium processes related to the propagation of strong shock waves in gas medium under consideration. The method of a triple probe [5] and the experience gained in applying this method during experiments in the ADST [1,6] are used to measure T_e. In [7] analogous method was used in Arc-Driven Devices. A spatial resolution of the measuring system along the flow velocity vector is about 0.5mm. A resolution time of the measuring system $\tau \sim 0.1mks$ is much higher than the time required for determining the structure of a spatial charge of the near-probe electrodes (10^{-8} s).
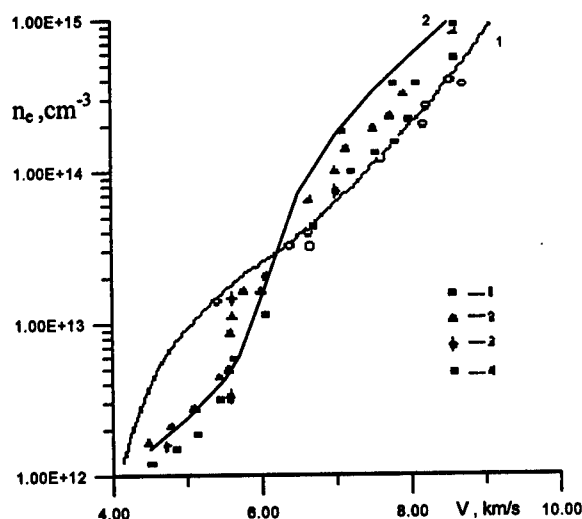
Fig.1 Measured and calculated electron concentration in quasistationary region behind shock wave. $P_1 = 0.2$ torr

Fig.1 presents the results of determining $n_{e,i}$ by different probe techniques. Here, toning points correspond to the measurements carried out in Martian mixture CO_2; contour points represent measurements in air; the curve 1 shows computational equilibrium values $n_{e,i}$ for air. The measurements in air were aimed at refining and approbation of the probe method. A satisfactory agreement of calculated and experimental data obtained for air allows one to hope that they can be used when conducting experiments in the mixture of CO_2+air. Points 1,2 represent the results obtained with probes arranged parallel to the flow velocity in the regime of gathering ions by using the relation (1). In this case it was assumed that C^+ was a dominating ion - points 1; for CO^+ assumed as a dominating ion - points 2 .

Points 3-the results which were obtained using probes of different diameters, operating in the regime of electron current (relation (3)) The results marked as points 4 were obtained by using a transverse probe at high velocities ($V_s > 7$ km/s). The values u, T_e used in estimating $n_{e,i}$, were taken from the calculations of these value for the mixture 97%CO_2+ 3%N_2 at corresponding shock wave velocities. Numerical results on electron densities in quasistationery zone, where measurements in ADST were done, are presented in Fig. 1 by curve 2. These calculations are executed using our approach for kinetics validity, when numerical kinetical model is corrected by comparison with measured data on ionization parameters behind shock wave.

At elaboration of numerical model Martian gas mixture in shock layer is simulated by species: CO_2, CO, N_2, CN, C_2, O_2, O, N, NO, NCO, C, C^+, O^+, N^+, N_2^+, CO^+, O_2^+ and e. Under conditions of a vehicle entry into Martian atmosphere physical-chemical processes in the shock layer are of nonequilibrium nature, that is, the relaxation of the inner degrees of freedom of the mixture species occurs in times comparable with gasodynamic processes. Of a nonequilibrium character are: vibrational relaxation of CO_2, CO, N_2, CN, C_2, O_2, NO molecules; dissociation and exchange reactions; ionization and the processes of charge exchange. The electron temperature T_e differs, in general case, from the translational T and vibrational temperatures of the molecules and is defined from the equation of the electron-gas energy balance. It's assumed that molecule rotational degrees of freedom are assumed in an equilibrium state with the translational ones.

Models of physical-chemical processes
Vibrational Molecule Relaxation
a).Vibrational excitation of CO_2.
Carbon dioxide constitutes the main mass fraction (97%) in the undisturbed Martian atmosphere.

As the vibrational degrees of freedom of a CO_2 molecule are highly energy-intensive, its impact on the gasthermodynamics of nonequilibrium flow is great. The CO_2 molecule has the following vibrational modes: symmetric with characteristic vibrational temperature θ = 1903K; doubly degenerated deformation θ = 945K; asymmetric θ =3339K. Due to Fermi resonance a fast energy exchange takes place between the symmetric and deformation CO_2 modes. This effect enabled in [8] to conclude that it is possible to describe the carbon dioxide VT-relaxation with using the Landau-Teller equation and the relaxation time in terms of:

$$\ln(P\tau_V) = 36.5T^{-1/3} - 17.71$$

b).Vibrational relaxation of C_2, CO, CN molecules.

For carbon-containing molecules the times of VT-relaxation have been computed according to the known semi-empirical formula of Millikan and White [9].

To describe the time of VT-relaxation for air-containing molecules, two approaches are used:

1).Computation of the relaxation time from the formula Millican-White with the following parameters: (θ =2359 cm^{-1} (N_2), θ =1580cm^{-1}(O_2) and θ =1904cm^{-1} (NO).

2).Computation of the relaxation time by the formulae allocated by the data base of the AVOGADRO system [10] in terms of $P\tau_V$ =$AT^n\exp(BT^{-1/3})$. Non-physical description of the vibrational relaxation at high temperatures with using the above expression was adjusted by introducing the Park correction [11]:

$$\tau_p = (n_t\sqrt{\frac{8kT}{\pi m}}\,\sigma_V)^{-1}$$

here n_t is the density of the colliding particles, m is an average mixture mass, σ_V is the collision section $\sigma_V = \sigma_V' (50000/T)^2$, $\sigma_V' = 3.10^{-17}$ cm^2 (N_2, O_2, NO); 3.10^{-18} cm^2 (CO); and 1.10^{-16} cm^2 (CO_2).

The relaxation time with due regard for τ_p is of the form:

$$\tau = \tau_V + \tau_p$$

The computational model makes use of data on dissociation and exchange reactions, recommended by AVOGADRO and [12].

Vibrational-Dissociative Coupling (VDC).

The vibrational-dissociative coupling and its impact on the characteristics of flow in the shock layer are taken into consideration using following models:

1). Park's model. The model based on replacing the value of the translational temperature in the expression for the reaction rate constant with an effective temperature $T_{ef} = T^s T_V^{s-1}$. The varying parameter s is selected by means of fitting the computed data to the experimental results. The value s =0.5 is used in test calculation.

2). Model CVDV. It is one of the widely used models. The effect of the vibrational nonequilibrium on the dissociation is taken into account through introducing the parameter $Z(T,T_V)$:

$$k(T,T_V) = Z(T,T_V)\, k_0(T) \;\; ; \;\; Z(T,T_V) = \frac{Q(T)Q(T_f)}{Q(T_V)Q(-U)},$$ where $T_f = (1/T_V - 1/T - 1/U)^{-1}$, U is an

empirical parameter of the model, D is the molecule dissociation energy of molecule. It is assumed in our computational program that U=D/3 and U=D/8 .

3).Modified N.M.Kuznetsov's model.

The value of the rate constant is determined in a similar manner as with the CVDV model. However, the parameter $Z(T,T_V)$ has a somewhat different form:

for polyatomic molecules :

$$Z(T,T_V) = \frac{\prod\limits_{j=1}^{m} Q_j(T)}{\prod\limits_{j=1}^{m} Q_j(T_{Vj})} \exp(-E_V^*(\frac{m}{\sum\limits_{j=1}^{m} T_{Vj}} -1/T)); \quad Q_j(T_f) = (1-\exp(-\theta/T_f))^{-dj} \quad ; T_f = T \text{ or } T_{Vj}$$

for a diatomic molecules.

$$Z(T,T_V) = \frac{Q(T)}{Q(T_V)} \exp(-E_V^*(1/T_V-1/T))$$

For CO_2 molecule: $m=3$, $\theta_1 =1903K$, $d_1 =1$, $\theta_2 =945K$, $d_2 =2$, $\theta_3 =3339K$, $d_3 =1$, $E_V^* =34600K$; for diatomic molecules $E_V^* =D/2$.

Ionization and Charge Exchange Reactions.

The computational model includes a number of ionization reactions and processes of charge exchange between neutral and positively charged components of the mixture. Electrons and ions appear behind the wave front in the associative ionization reaction. The processes involving the electrons are defined by the reaction rate constant, which depends on the temperature of electrons T_e. The temperature of free electrons T_e is derived from the master equation for electron-gas energy balance. The electrons gain (lost) their energy during the reactions of the associative ionization, elastic collisions with heavy mixture species and nonelastic collisions with exciting rotational, vibrational (N_2 and CO molecules) and metastable electron levels of several molecules, dissociation and ionization of molecules and ionization atoms by electron impact, excitation of lower electron states of atoms N, C, O.
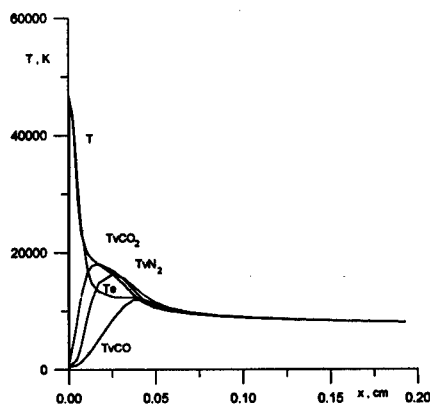

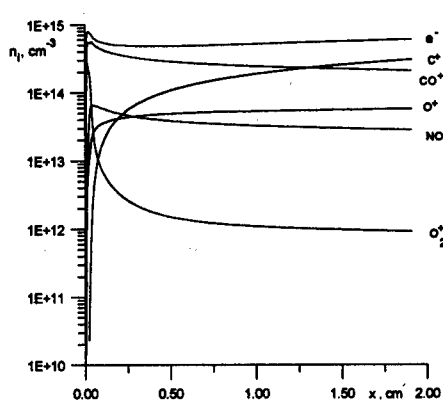Fig.2 Calculated temperatures profiles behind shock wave, V=8 km/s, $P_1 =0.2$ torr

Fig.3 Calculated charge species concentration profiles behind shock wave, V=8 km/s, $P_1 =0.2$ torr

81

The results of test computations, can be divided into two groups. The first group includes the data obtained when selecting the data base of kinetics, which defines the vibrational relaxation, the constants of equilibrium and rate reaction. The second group includes the results proper for computing the flow behind the wave in Martian mixture. This group also includes the influence of selecting some or other kinetical model on the parameters of the flow in the region of relaxation. Fig.2 presents the profiles of the distribution of temperatures T, T_{VCO2} , T_{VN2} , T_{VCO} and T_e behind the shock wave front at V_S =8 km/s, P_1= 0.2 torr. The conditions selected for computations agree with those existing in TsAGI's shock tube ADST. It is not difficult to notice in Fig.2 a significant level of temperature nonequilibrium behind the shock wave front. Test results of computing charged gas species in the zone of relaxation for the conditions of Fig.2 are presented in Fig.3.

REFERENCES

1.Gorelov V.A., Kildushova L.A. and Kireev A.Y. Ionization particularities behind intensive shock waves in air at velocities of 8-15 km/s.- AIAA Paper 94-2015, 1994.

2.Gorelov V.A., Gladyshev M.K., Kireev A.Y., Fedotov I.V., Plastinin Y.A. and Karabadzhak G.F., Nonequilibrium shock layer radiation in the systems of molecular bands NO and N_2^+(1-): experimental study and numerical simulation.- AIAA Paper 96-1900, 1996.

3.Gorelov V.A. and Kildushova L.A. Particularities of performaces of cylindrical electrical probes under transitional regime in hypersonic plasma flow.- Teplofiz. Vys. Temp (High Temperatures). – 1985,Vol.23,- N2,- (in Russian).

4.Gorelov V.A. and Kildushova L.A .Cylindrical electrical probes in hypersonic plasma flow.- Journal of Technical Physics, vol.54, N3, pp 653-655, 1984, (in Russian).

5.Chen S.L. and Sekiguchi.Instantaneous direct-display system of plasma parameters by means of triple probe.- Journal of Applied Physics, vol.36, N8, pp 2363-2375, 1965.

6.Gorelov V.A. and Kildushova L.A. Particularities of ionization processes and radiation behind the strong shock waves in air,- Journal of Applied Mathematics and Technical Physics, vol.6, 1987, (in Russian).

7.Habiger H.A., Anweter-Kurtz M. and Kurtz H. Electrostatic probes for the investigation of arc-driven electric propulsion devices.- IEPC Paper 3-124, September 1993.

8. Camac M. CO_2 relaxation processes in shock waves.- Fundamental Phenomena in Hypersonic Flow ed. by Hall J.G., Cornell Univ. Press, Ithaca, NY,1966.

9.Milliken R.C., White D.R. Systematics of vibrational relaxation .- Journal of Chem Phys., N12, 1963.

10.Losev S.A. et al. Thermochemical nonequilibrium kinetics models in strong shock waves in air.- AIAA Paper 94-1990,1994.

11.Park C., Howe I.T., Jaffle R.L. and Candler G.V. Review of chemical-kinetic problems of future NASA missions, II- Mars entries.- Journal of Thermophysics and Heat Transfer vol.8, N1, Jan.-March 1994.

12.R.N.Gupta, K.P.Lee. An aerothermal study of MESUR Pathfinder aeroshell.-AIAA Paper 94-2025,1994

ORIGINATION AND DOWN-FLOW DEVELOPMENT OF THE LONGITUDINAL LOCALIZED DISTURBANCES ("PUFF"-STRUCTURES) IN SOME BOUNDARY LAYERS

G.R. Grek, V.V. Kozlov, D.S. Sboev

Institute of Theoretical and Applied Mechanics SB RAS,
630090 Novosibirsk, Russia

1.   Introduction. This paper deals with some aspects of the receptivity problem in boundary layers (BL) subjected to high level of free stream turbulence (FST). Transition in a such BL occurs at low Reynolds numbers for which all eigenvalues are stable. Consequently, there must be some other amplifying mechanism of importance, than Tollmien-Schlichting instability. A powerful candidate to explain observed phenomena is so-called transient or algebraic growth (see [1] for critical review). An important ingredient in transient growth is three dimensionality of the disturbances. In an experimental field, it was Grek *et al.* [2], who were first to found disturbances similar transients-disturbances in the theory. They showed that three different types of disturbances could be obtained from a point source positioned inside flat plate BL. Beside the TS-wave packet and turbulent spot, the third type of disturbance was found. The spanwise spreading of this structure was remarkable small throughout its evolution (in contrast to TS-wave packets). It was named the "boundary layer puff". In [3], following the early ideas by [2], an artificial localized free stream disturbance was used to study the BL receptivity. Appearance of the "puff'-structures was found as a result of the interaction of a free stream disturbance with the leading edge and flat plate BL. It was in close similarity to the "streaky structures" in the "natural" transition at high level of FST (for instance [4]). The "puff" consisted of a long and narrow streaks of positive and negative disturbance velocity in u -component with streaks symmetrically located to the centerline.

A free stream disturbances in [3] has been orientated along flow. In practice, especially for anisotropic FST, one can expect the vortices be randomly orientated to the flow direction. Another important element of the receptivity process is mean flow conditions close to the leading edge of a model. The aims of the present study were in investigation the receptivity of different BLs to free stream localized disturbances orientated at various angles to the flow. All the experiments were conducted in the same conditions, i. e. the free stream speed and disturbances source were invariable. The changing mean flow has been achieved by changing of models.

2.   Experimental set-up. The experiments were performed under controlled conditions in the MT-324 wind tunnel at the ITAM. A general sketch of the set-up is shown in Fig. 1. The experiments were carried out on a flat plate, a straight and swept wing models. The wings has one of the same cross-section. The angle of attack was -3° for straight wing and -8° for swept ones. All measurements were undertaken at the free stream speed (U_∞) 6,6 m s^{-1} as in [3]. The FST-level was 0,1%.

A vortical perturbations was generated in the free stream by introducing a short duration jet through a pipe mounted in the vicinity of the leading edge, as shown in Fig. 1. The pipe was slightly inclined in the normal direction at the angle 18° to the X axis. It can be installed at the various angles θ to the X axis in (X,Z)-plane. A disturbance was produced by a loudspeaker located below test section and connected to the pipe with a flexible tube. The loudspeaker was driven from the amplified output of a function generator. The pulse amplitude was kept constant in all measurements. The pipe was positioned below stagnation streamline and no effect of the wake could be detected in the undisturbed BL. The disturbances were registered using a constant-temperature anemometer with the single-wire probe.

3.   Results. Fig. 2 shows the outer disturbances streamwise velocity, measured in the spanwise direction at X-position of 2 mm from the pipe end without any model in the test section. In the case of θ = 0°, the disturbance is orientated along flow and dominated by a positive

perturbation in u. For the case $\theta = 40°$, the disturbance consists of two regions of positive and negative perturbations. However, the plot in (Z,t)-plane do not adequately represents the structure of disturbance with $\theta = 40°$ in (X,Z)-plane cause by its non-zero propagation speed in spanwise direction. From analysis a different data (not shown) it was concluded that the disturbance is orientated as whole at some angle to the flow. At this position the perturbations amplitude is rather high. However, the amplitude of the outer disturbances decays quickly, and close to leading edge its peak-to-peak value is about 20% of U_∞ for $\theta = 0°$ case and 10% for $\theta = 40°$.
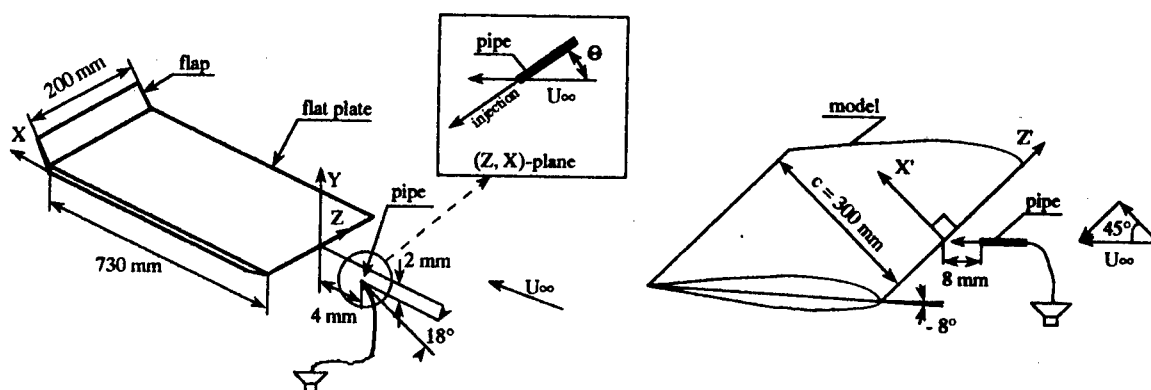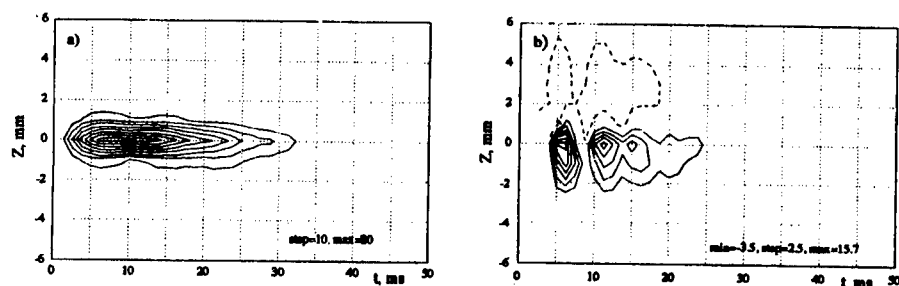

Fig. 1. Outline of experimental set-up.

Fig. 2. Isocontours of streamwise perturbation velocity of the outer disturbances
obtained for $\theta = 0°$ (a) and $\theta = 40°$ (b). Solid and dashed lines represent
positive and negative contours respectively. The "step" is contour spacing.

Fig. 3 shows the distributions of u in BLs. As can be observed, symmetrical disturbances in the BL were generated in both the flat plate and straight wing BLs (see Fig. 3a and c) when the propagating along flow outer disturbance were used. For the flat plate BL case the good agreement between present results and those in [3] were obtained. Such symmetrical disturbances in the following referred to as "symmetrical puff" (SP). New type of the disturbances in 2D - BLs was formed as the outer disturbances were introduced to a stream at the angle to the flow (see Figure 3b and d). It consists of only two streaks of the positive and negative perturbations located side-by-

84

side in (Z,t)-plane. This disturbance has the same integral characteristics as the SP, i.e. the downstream propagation speed of its leading edge, the localization and small spreading in the spanwise direction etc. Such disturbances in the following referred to as "asymmetrical puff" (ASP). Our results on ASP characteristics are in close similarity with the channel flow DNS [5]. It should be noted that although the perturbation amplitude is high close to the leading edge, the downstream development of the puff shows a slowly decaying amplitude, without any changes in the disturbances structures. It is because the nondimensional units were used, that length to width ratio of the disturbances is not correctly described in Fig. 3, but should be stretched in X-direction.

As one can see from Fig. 3 in the straight wing model BL both the SP and ASP disturbances shows greater spanwise scale both in the normalized and physical units than the ones in the flat plate BL at the same experimental conditions. Hence, it is obviously due to the different mean flow conditions close to the leading edges of the models. In particular, the BL thickness close to the leading edge of the wing is larger, it might be resulted in larger spanwise scale of the initial region of perturbation inside the BL. The measurements indicate that the main characteristics of the disturbances development is not affected by streamwise pressure gradients.
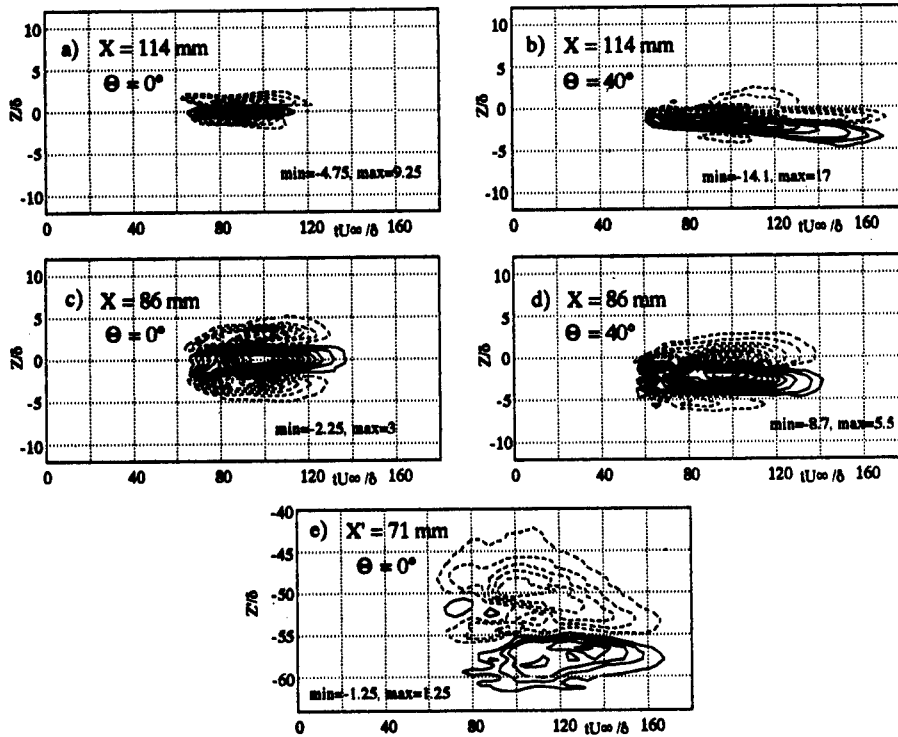

Fig. 3. Isocontours of streamwise perturbation velocity of the BL disturbances.
(a,b) Flat plate BL. (c,d) Straight wing BL. (e) Swept wing BL. Contour
spacing: $0,0025U_{\infty}$. (δ is the local BL thickness)

In the Fig. 3e the disturbance in swept wing BL is shown for $\theta = 0°$ case. In comparison with the straight wing its main feature is asymmetrical structure in horizontal plane. It is probably due to the presence of cross - flow in the such 3D - BL. From measurements [3] of v and w components of velocity it is following that spanwise component directed outwards from centerline of SP disturbance. The sketch of perturbations streamlines in (Y,Z) - plane is shown in Fig. 4. The cross-flow leads to suppress of spanwise motions directed against it and this resulted in asymmetrical disturbance generation. When initial disturbance is propagating at some angle to the flow in the 2D - BL, the mean flow also could be decomposed in two components as shown in Fig. 4. In this case the "cross"-component also leads to asymmetrical disturbance generation.
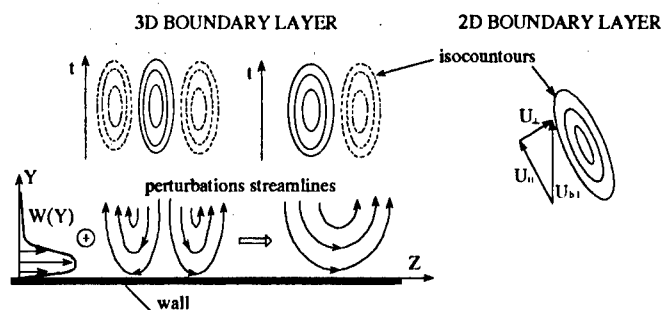

Fig. 4. On the asymmetrical disturbances generation.

Spectral decomposition of the spanwise u -distributions given in Fig. 2 and 3 are shown in Fig. 5. The transformed distributions are displayed as amplitude spectra in the frequency (f) - spanwise wave number (β) domain. In order to provide the possibility for direct comparisons between different measurements, the size of the transformed time and space domain is always kept constant. The perturbation energy for the free stream disturbances is spread over wide range of frequencies and spanwise wave numbers. The spectrum of the free stream disturbance obtained at θ = 40° is dominated by oblique waves, whereas the spectrum obtained at $\theta = 0°$ is dominated by plane waves. All of the spectra inside the BL show a concentration of energy to low frequencies, dominated by two peaks which have the different wave numbers for the different spectra. The main difference between spectra of the SP and ASP disturbances is the smaller spanwise wave number (β_{max}) that is observed for the major peaks in the spectrum of ASP (Fig. 5c and d). The wave number β_{max} corresponds to a dominant spanwise wave length λ_z. The development of the ratio λ_z/δ (δ is *local* BL thickness) are plotted as function X in Figure 6a. Also, one can see the smaller spanwise scale of the disturbances in flat plate BL than those in the wings BLs. It is in agreement with the larger distance between streaks in (Z,t)-plane. The spanwise scale of swept wing disturbances is about three times larger than those in straight wing. The reason of it are yet unknown for further investigation.Fig. 6b shows the downstream development of the straight wing model SP dominant wavelength together with those obtained by [3]. The each curve was normalized by its value at X = 160 mm. Despite the presence of a pressure gradients in wing model BL it is shows the good agreement between the curves. It seems, that downstream development of the dominant wavelength is independent from presence of a the pressure gradients.
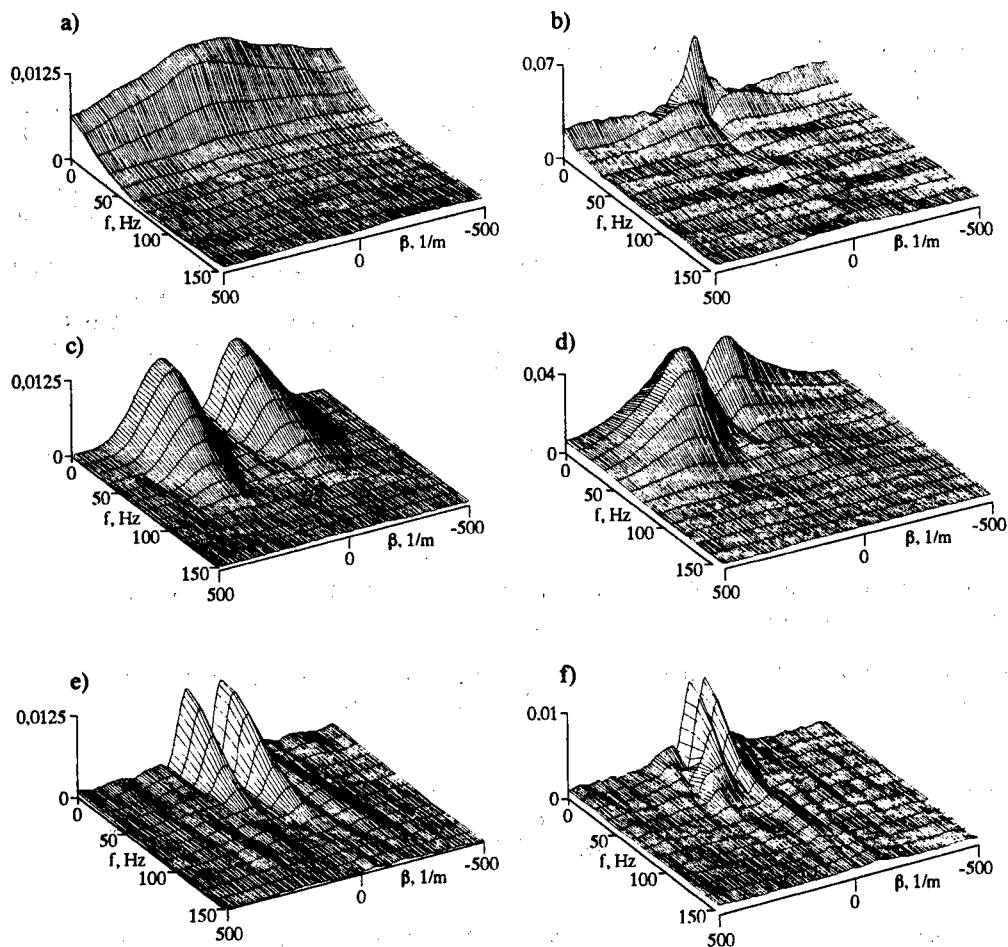
Fig. 5. Spectral decomposition (f,β) for different spanwise distributions. The free stream disturbances: $\theta = 0°$ - a), $\theta = 40°$ - b). The flat plate BL: $\theta = 0°$ - c), $\theta = 40°$ - d). The straight wing BL, $\theta = 0°$ - e). The swept wing BL, $\theta = 40°$ - f).
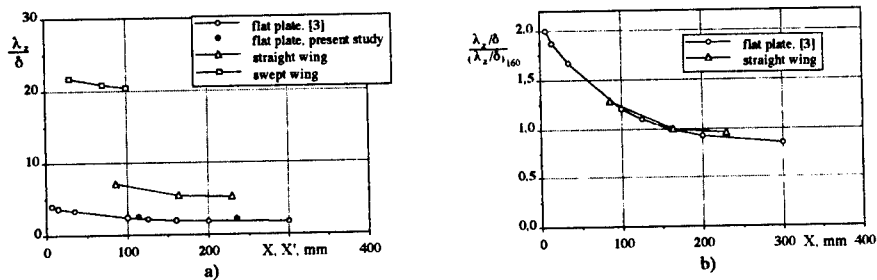

Fig. 6. Downstream development of the dominant wavelength, $\theta = 0°$.

4. Conclusions. The results shown in above can be summarized as follows:

(i) A controlled free stream perturbations with the various orientation and propagation direction relatively to the flow has been used to generate a localized boundary layer disturbances ("puff"-structures). The latter shows a simple structure, consisting of streaks of positive and negative perturbations in the u - component.

(ii) The various orientation and propagation direction of the free stream disturbances can leads to origination in the boundary layer of the "puff"-disturbances with asymmetrical structure in (Z,t)-plane.

(iii) The mean flow characteristics in vicinity of the models leading edge is crucial for the boundary layer receptivity to the localized free stream disturbances. In the present set-up the spanwise scale of the disturbances in the straight wing model boundary layer is two times larger than in the flat plate case. The cross-flow leads to asymmetrical disturbances generation in swept wing boundary layer, whereas the generation of symmetrical disturbances take place on straight wing at the same experimental conditions.

References

1. **Waleffe F.** Hydrodynamic stability and turbulence: beyond transients to a self-sustaining process // Stud. Appl. Math.- 1995.- vol. 95, - p. 319 - 343.

2. **Grek G.R., Kozlov V.V., Ramazanov M. P.** Laminar - turbulent transition at high free stream turbulence level. review // Izv. SO AN SSSR. Ser. tech. nauk. -1991. - No. 6. - p. 106-137. (in Russian)

3. **Alfredsson P.H., Bakchinov A.A., Kozlov V.V., Westin K.J.A.** On by-pass transition in the Blasius boundary layer. Part 1: Receptivity and evolution of a localized free stream disturbance: TRITA-MEK. Technical Report 97:8, Dept. of Mechanics, Royal Institute of Technology. Stockholm, 1997.

4. **Alfredsson P.H., Bakchinov A.A., Kozlov V.V. & Matsubara M.** Laminar-turbulent transition structures at a high level of a free stream turbulence // IUTAM Symposium on Nonlinear Instability and Transition in Three-Dimensional Boundary Layers: Proc. Manchester, UK/Ed. P.W. Duck . July, 1995. - P. 423-436.

5. **Henningson D.S., Lundbladh A., Johansson A.V.** A mechanism for bypass transition from localized disturbances in wall-bounded shear flows // J. Fluid Mech. - 1993. - vol. 250. - p. 169 - 207.

METHOD OF PHASED ROUGHNESS FOR DETERMINING THE ACOUSTIC RECEPTIVITY COEFFICIENTS

A.V. Ivanov, Y. S. Kachanov, D.B. Koptsev
Institute of Theoretical and Applied Mechanics, 630090, Novosibirsk, Russia

1. INTRODUCTION

The paper is devoted to an experimental investigation of the problem of laminar-turbulent transition in 3D boundary layers on swept-wings. In various practical situations the aircraft surface vibrations, steady surface nonuniformities (roughness, waviness and so on), and acoustic perturbations represent the most important sources of the instability waves which can lead to a premature transition to the turbulence. In recent experimental studies in this field the receptivity of a swept-wing boundary layer with respect to the surface vibrations and steady surface non-uniformities was studied in detail [1,2]. The present experiments are devoted to a quantitative investigation of a generation of the cross-flow instability modes by acoustic waves in the presence of stationary surface non-uniformities.

It is known that the acoustic perturbations can be most effectively transformed into the instability waves on different localized non-uniformities, in particular on the wing surface non-uniformities. In previous experiments [3,4] it was failed to find an excitation of some cross-flow instability modes (significant for transition) by acoustic waves. At the same time, theoretical investigations (see [5,6]) show that the mechanisms of generation of the cross-flow instability wave by acoustics do exist and they can play a significant role in the transition process under certain flow and disturbance conditions. In the experimental study [7] a generation of the cross-flow instability modes by an acoustic wave scattering on a localized surface vibration was found and investigated quantitatively for the first time.

On of the main difficulties of the experiments on the acoustic-roughness receptivity consists in a problem of an extraction of a relatively weak instability mode in the presence of powerful signals attributed to the acoustic wave itself and to the vibrations of the hot-wire probe and the experimental model (due to an influence of the acoustics) which have the same frequency as the instability wave. This problem is especially difficult when investigating the 3D instability waves in the 3D boundary layers, as in the present case. An idea of the present work consists in a simplification of this problem by means of designing of a special roughness that would generate (in the presence of the acoustics) a single normal cross-flow instability mode inclined at a certain angle to the flow direction, i.e. with a certain value of the spanwise wavenumber β_1. Such a roughness can be easily arranged in a completely uniform flow in a form of a strip pasted onto the surface at a necessary angle. However: (i) the swept-wing boundary layer is not uniform, (ii) the typical inclination angle of such a strip has to be very large for the most unstable cross-flow mode (around 85°) that suggests a very big length of the strip if we want to obtain a real normal mode that would be uniform along the span rather than localized along the span, and (iii) a streamwise length of the strip has to be short enough if we want to investigate the localized (along the chord) receptivity. These three circumstances make the problem quite difficult. A "phased roughness" designed and used in the present experiments gives possibility to solve all these problems and to obtain quantitative experimental data on the localized acoustic receptivity.

2. EXPERIMENTAL PROCEDURE

The experiments were conducted in a low-turbulence subsonic wind-tunnel T-324 of the Institute of Theoretical and Applied Mechanics at the experimental conditions that were approximately the same as in the previous investigations devoted to the cross-flow receptivity [1,2,7] and the cross-flow stability [8,9]. The model represents a flat plate with the leading and trailing edges having a sweep angle $\chi = 25.0°$. The 3D pressure gradient, directed normally to the plate leading edge, was induced by a 3D contoured wall bump (which had the same sweep angle) mounted just above the plate surface on the test-section ceiling.

Design of "phased roughness" and its rated parameters. As was mentioned above, the cross-flow instability waves were generated by the acoustic wave on a specially designed "phased roughness" put onto the model surface. An idea of the "phased roughness" is rather simple — to design a special shape of the roughness that would be localized in the chordwise direction but periodic in span and which would generate (in the presence of a harmonic acoustic wave) a single normal cross-flow instability mode with a certain spanwise wavenumber $\beta' = \beta'_1$, i.e. the mode inclined at a particular desirable angle to the flow direction. Unfortunately, in case when the roughness has only positive height in every spatial point (this is a technological restriction) it is impossible to avoid a possible generation (in addition) of a quasi-2D instability mode with the spanwise wavenumber $\beta' = 0$. The matter is that in the spectrum of the roughness shape the spanwise-wavenumber harmonic with $\beta' = 0$ has the same order of magnitude as the main (rated) mode with $\beta' = \beta'_1$. But, fortunately, the amplitude and phase of this mode are independent of the z'-coordinate similar to the acoustic and vibrational signals (produced by the acoustics). This means that it is not difficult to subtract this quasi-2D mode from the total signal in the same way as the acoustic and vibrational signals.

A sketch of the phased roughness is shown in Fig. 1 in the (x', z')-plane [In the present paper x' and z' are the chordwise and spanwise coordinates respectively, the coordinate system (x,z) is connected with the free stream velocity upstream from the model, and the system (x^*, z^*) is local one coupled with the potential-flow velocity vector and directed along the x^*-coordinate.] The spanwise period of the roughness elements (i.e. of the strips) λ_z' corresponds to the spanwise wavenumber $\beta'_1 = 2\pi/\lambda_z'$ of the cross-flow instability wave which generation we want to investigate. In the present experiments λ_z' was chosen to be equal to 13.12 mm that corresponds to $\beta'_1 = 0.48$ rad/mm ($\beta'_1\delta_{1r} = 0.506$) which is close to the most unstable cross-flow instability mode in the frequency range studied (see [9]). The axis of each roughness (strip) is inclined to the x-axis at angle $\xi = 90 - \theta_1^* - \gamma = 9°$ that corresponds to the propagation angle $\theta_1^* = 83.0°$ of the normal cross-flow instability mode with $\beta' = \beta'_1$. (Note, that the yaw angle of the flow γ is equal to $-2°$ in the center of the roughness.) The length of the roughness elements is conditioned by a distance λ_1^*, on which the wave generated on a given strip is to be displaced along the x^*-axis for its front coincidence with the axis of the next strip. This distance is equal to 107.2 mm, that gives the streamwise wavenumber $\alpha_{r1}^* = 0.059$ rad/mm ($\alpha_{r1}^*\delta_{1r} = 0.0617$). This wavenumber was chosen from the dispersion curve $\alpha_r^* = \alpha_r^*(\beta^*)$ determined for the cross-flow instability waves in the previous experiments [9] for the mode with the frequency $f = 42.0$ Hz and the spanwise wavenumber $\beta_1^* = 0.494$ rad/mm that corresponds to $\beta' = \beta'_1 = 0.48$ rad/mm.
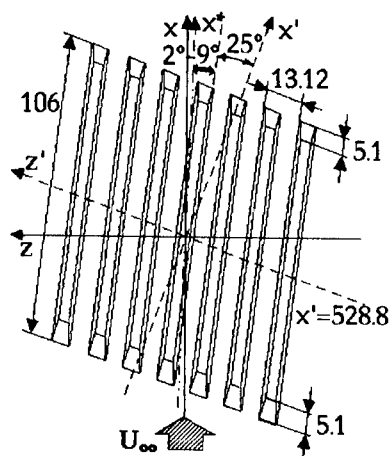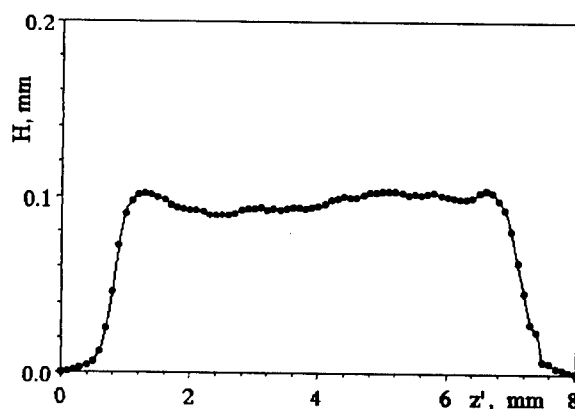

Fig. 1. Sketch of the phased roughness.

Fig. 2. Cross-section of the phased roughness strip.

It was shown in previous experiments that the dispersion function depends significantly on the disturbance frequency. Therefore the rated parameters of the phased roughness (described

above) correspond to a fixed frequency f of the acoustic wave that was chosen to be equal to 41.96 Hz in the present case.

All roughness strips were practically identical to each other. Each strip was made of a paraffin that was poured on the surface of the model from a special device. After that, the strips were shaped by means of a special cutter mounted on the supporting mechanism. The shape of the strip is shown in Fig. 2 in the plane normal to its axis. It was obtained with the help of measuring the cutter profile by means of the optical micrometer (with an accuracy ± 5 μm).

Properties of the acoustic waves. The acoustic disturbances were produced by a loudspeaker positioned downstream of the experimental model and the wave was radiated upstream. In the chosen regime of measurements the wavelength of the acoustic wave was very long (about 8 m) and no any significant non-uniformities of the acoustic field was observed in the flow, in particular in the vicinity of the phased roughness. The amplitude of the signal that supplied the loudspeaker was constant.

3. BASIC FLOW CHARACTERISTICS

The characteristics of the 3D mean flow field over the model used were measured carefully in both the potential flow and the boundary layer using, in particular, X- and V-shaped hot-wire probes [8,10]. It was shown that this flow is identical in practice (for except the wall curvature effects) to the flow over a real swept-wing with the sweep angle 25 degrees (see [10] for more detail). Some additional information about the mean flow characteristics observed under the conditions of the present set of measurements is presented below.
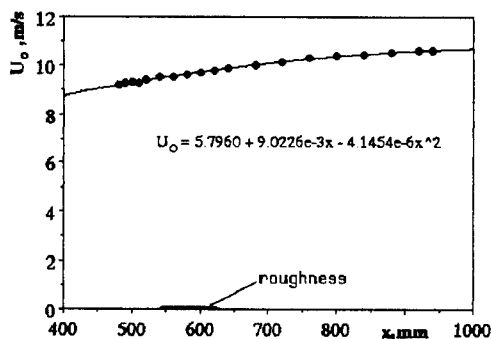

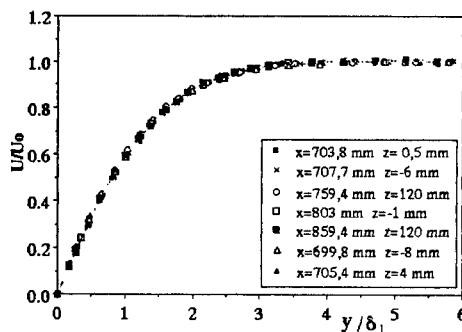Fig. 3. Streamwise distribution of the edge velocity.   Fig. 4. Normal-to-wall profiles of mean velocity.

The present experiments were conducted at the free-stream velocity $U_\infty = 8.7$ m/s. A downstream distribution of the streamwise component of the potential flow-velocity $U_0(x)$, measured in the present experiments outside the boundary layer (at $y \approx 10$ mm), is shown in Fig. 3. In the center of the roughness at $x = x_c = 583.5$ mm ($x'_c = 528.8$ mm) the value of U_0 was equal to 9.64 m/s and the value of the boundary-layer displacement thickness in the initial chordwise position at $x' = 637.6$ mm was $\delta_1 = 1.053$ mm.

A set of normal-to-wall profiles of the x-component of the mean-flow velocity, taken at several chordwise and spanwise positions, is presented in Fig. 4. Comparison of these profiles demonstrates a local self-similarity of the boundary-layer flow and an independence of the profile shapes on both the streamwise and the chordwise position.

4. DISTURBANCE EVOLUTION DOWNSTREAM OF THE PHASED ROUGHNESS

Spanwise distributions. Shown in Fig. 5 with curves 1 are the spanwise distributions of the disturbance amplitude (Fig. 5a) and phase (Fig. 5b) in the total signal at the frequency of excitation measured in the boundary layer downstream the phased roughness at $x' = 601.3$ mm and $U/U_0 = 0.68$. It is seen that the total signal has a quite complicated spanwise distributions which represent, as expected, a superposition of three main types of signals: (a) a signal produced by the acoustic wave itself (that corresponds to the Stokes layer in the near-wall

91

region), (b) a signal attributed to a hot-wire probe vibrations forced by the acoustic wave in presence of a strong normal-to-wall mean-velocity gradient, (c) a signal conditioned by a (possible) presence of a quasi-2D instability mode with the spanwise wavenumber $\beta' = 0$, and (d) a signal corresponded to an essentially three-dimensional cross-flow instability modes consisted mainly of a single mode with the spanwise wavenumber $\beta' = \beta'_1$. Note, that under the conditions of the present experiments all instability modes (signals "c" and "d") are generated due to a scattering of the acoustic wave on the phased roughness only.
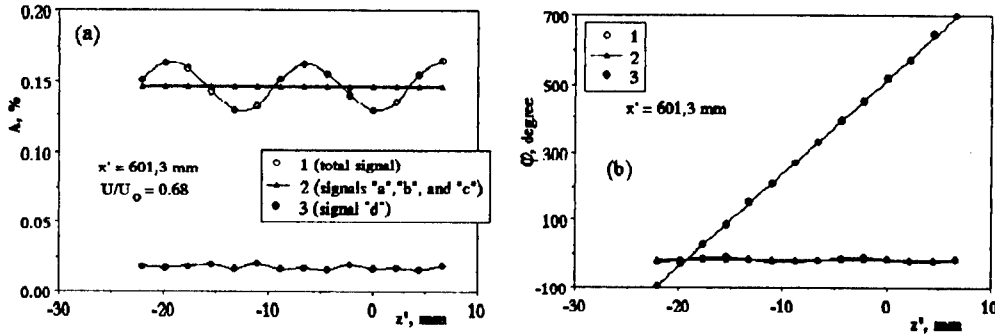

Fig. 5. Streamwise distributions of amplitudes (a) and phases (b) of total and extracted hot-wire signals.

A spanwise wavenumber spectrum of the disturbances generated by the acoustic wave is shown in Fig. 6. This spectrum is obtained by means of Fourier decomposition of the spanwise distribution described above and normalized by the amplitude of the mode with $\beta' = 0$, i.e. by the amplitude of a mixture of the signals "a", "b", and "c", were the signals "a" and "b" (the acoustics and vibrations) dominate. It is seen that the rated mode with $\beta' \delta_1 = \beta'_1 \delta_1 - 0.506$ ($\beta'_1 = 0.48$ rad/mm) is the greatest one after the "acoustic" mode with $\beta' = 0$. Thus, the main mode ($\beta' = \beta'_1$) is a dominant wave in signal "d".

In order to investigate in more detail the properties of mode "d" a procedure of a rough extraction of the main cross-flow instability modes (with the spanwise wavenumber $\beta' = \beta'_1$) from the total signal was used. The idea of this procedure is based on three circumstances. First, the all signals obtained in the boundary layer at the frequency of excitation are independent of the z'-coordinate except for signal "d". Second, signals "a" and "b" are very weakly dependent on the x'-coordinate while signals "c" and "d" are strongly dependent on it. Third, in the rated regime signal "d" consists mainly of a single cross-flow instability mode with the spanwise wavenumber $\beta' = \beta'_1$.

Some results of application of the rough extraction procedure are presented in Fig. 5 with curves 2 and 3. Generated instability mode "d" is really very close to a normal wave with a definite value of the spanwise wavenumber that can be determined as a tangent of inclination angle of the curve 3 in the distribut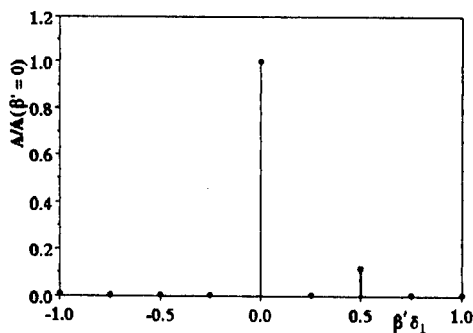ion $\phi_d(z')$. In average, the spanwise wavenumber of the generated instability mode turned out to be $\beta' = 27.5$ degr/mm $= 0.479$ rad/mm ($\beta' \delta_1 = 0.505$) that coincides, in practice, with the rated value $\beta'_1 = 0.48$ rad/mm despite the method used in the present section for decomposition of the signals is rather rough.

Normal-to-wall profiles. Shown in Fig. 7 are the amplitude (Fig. 7a) and phase (Fig. 7b) y-profiles obtained for the total signal at the frequency of excitation at the chordwise position $x' = 637.6$ mm. Two of three profiles presented are obtained at the spanwise positions that correspond to the disturbance amplitude maximum ($z'_c = 0.55$ mm), and minimum ($z'_c = -6.6$ mm) in the spanwise distributions
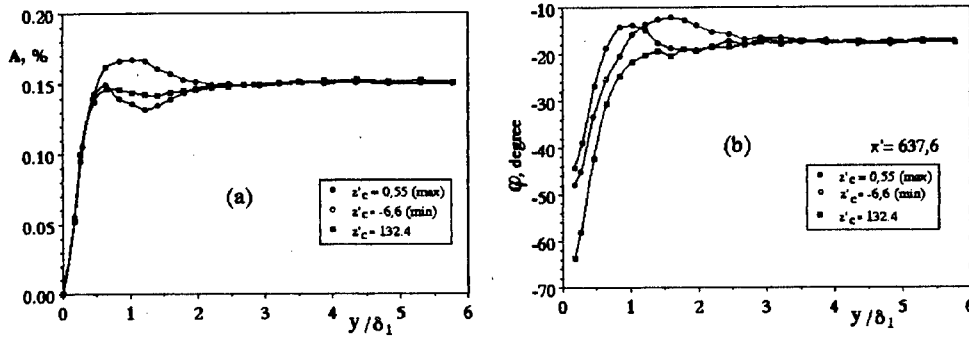

Fig. 6. Spanwise wavenumber spectrum of disturbances.

Fig. 7. Amplitude (a) and phase (b) profiles for total signal.

measured at $y/\delta_1 = 1.25$ ($U/U_0 = 0.68$) similar to that presented in Fig. 5 (where z'_c is the z'-axis with an origin on the axis of the model). The third profile is measured at a side from the roughness ($z'_c = 132.4$ mm) where the surface of the model was smooth and no generation of the instability wave by the acoustics was observed.

Applying the procedure of rough extraction of signals to a pair of distributions discussed above it is not difficult to obtain the normal-to-wall profiles of the amplitude and phase of the instability wave (i.e. the mode "d"). The result is presented in Fig. 8. It is seen that the amplitude and phase profiles of the disturbance "d" have shapes that are typical for the cross-flow instability modes (see [9]). The amplitude profile has a single maximum at $y/\delta_1 \approx 1.25$. The phase decreases in a linear way with the normal-to-wall coordinate.
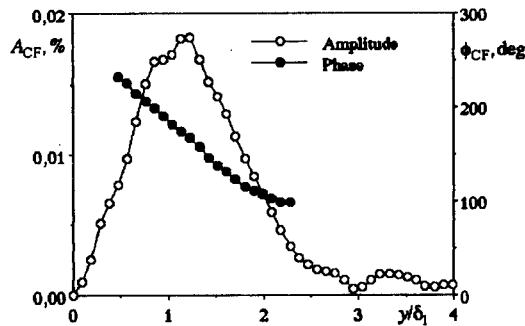

Fig. 8. Normal-to-wall profile for mode "d".

Dispersion and receptivity characteristics. Using the values of the spanwise wavenumber obtained for the instability mode "d" (with the help of curves like curve 3 shown in Fig. 5b) and the corresponding values of the streamwise wavenumber found from x-distributions of the phases of spanwise-wavenumber spectral modes (not shown) it is not difficult to estimate the other dispersion characteristics of the instability waves generated by the acoustic wave on the roughness presented in Table. It is seen that all dispersion characteristics are very close to those used for design of the phased roughness (see section 2.) and corresponds to a cross-flow instability mode close to the most unstable one (see [9]).

β', rad/mm	α'_r, rad/mm	θ', deg	θ^*, deg
0.48	-0.114	107	82

Let us designate the initial (i.e. at in the roughness center) amplitude of the excited instability wave as A_{CF}, the amplitude of the corresponding "resonant" mode in the spectrum of the roughness shape as C_r, and the acoustic wave amplitude as A_a. Then the amplitude of the acoustic-roughness receptivity coefficient can be determined as [7]

$$G_r = \frac{A_{CF}}{C_r A_a}.$$

The "resonant" mode in the spectrum of the roughness with amplitude C_r have the same value of the streamwise wavenumber as the cross-flow instability mode generated in the flow. The

initial amplitude of the cross-flow mode A_{CF} was obtained by means of an upstream extrapolation of x '-distribution of the spectral amplitude with $\beta' = \beta'_1$ to the position of the phased roughness center. This amplitude is equal to 0.024%. The flow velocity oscillations produced by the acoustic wave had amplitude of 0.15%. Finally, the value of the acoustic-roughness receptivity coefficient G_r was found to be equal to 0.0297. This coefficient is non-dimensional. All dimensional values were normalized with the potential flow velocity (in the center of the roughness) and/or with the boundary layer displacement thickness (that was nearly independent of the streamwise coordinate).

6. CONCLUSIONS

1. The experiments on the acoustic-roughness receptivity of a swept-wing boundary layer have been conducted successfully at controlled disturbance conditions with the help of a special 'phased roughness' designed and manufactured for the purposes of the present experiments.

2. It is shown that a signal, measured at the frequency of excitation by a hot-wire, consists mainly of a mixture of three different signals attributed to: (i) the acoustic wave itself, (ii) the probe and surface vibrations, and (iii) the instability waves generated by the acoustics on the roughness. For separation of these signals and extraction of the cross-flow instability waves several special procedures of the signal processing were developed and used.

3. It is found that the disturbance generated by acoustics in the flow represents, as expected, a normal cross-flow instability mode inclined at a high angle to the flow direction. This wave is very close to the most unstable cross-flow instability mode for a given frequency.

4. Finally, the experimental method created in the present study gives possibility to obtain, for the first time, quantitative characteristics of the acoustic-roughness receptivity of the swept-wing boundary layer which can be used for validation of receptivity theories.

REFERENCES

1. Gaponenko V.R., Ivanov A.V., Kachanov Y.S. Experimental study of 3D boundary-layer receptivity to surface vibrations // Nonlinear Instability and Transition in Three-Dimensional Boundary Layers / Eds. P.W. Duck, P. Hall - Dordrecht: Kluwer, 1996, P. 389-398.
2. Kachanov Y.S., Gaponenko V.R., Ivanov A.V. Experimental study of swept-wing boundary-layer receptivity to stationary and non-stationary surface non-uniformities // Stability and Transition of Boundary-Layer Flows. EUROMECH Colloquium 359, Collection of Abstracts. - Stuttgart: Universität Stuttgart, March 10-13, 1997, Abstr. No 5.
2. Ivanov A.V., Kachanov Y.S., Koptsev D.B. An experimental investigation of instability wave excitation in three-dimensional boundary layer at acoustic wave scattering on a vibrator // Thermophysics and Aeromechanics. - 1997. - V. 4, No. 4. - P. 359-373.
3. Muller B., Bippes H. Experimental study of instability modes in a three-dimensional boundary layer //Proc. AGARD Symp. on Fluid Dynamics of Three-Dimensional Turbulent Shear Flows and Transition. AGARD-CP-438, 1988.
4. Takagi S., Saric W.S., Radeztsky R.H., Spencer S.A., Orr D.J. Effect of sound and micro-sized roughness on crossflow dominated transition // Bull. Am. Phys. Soc. - 1991. - V. 36. - P. 2630.
5. Crouch J.D. Receptivity of Three-Dimensional Boundary Layers. – AIAA Paper 93-0074, 1993.
6. Crouch J.D. Theoretical studies on the receptivity of boundary layers. – AIAA Paper 94-2224, 1994.
7. Gaponenko V. R., Ivanov A. V., Kachanov Y. S. Experimental study of cross-flow instability of a swept-wing boundary layer with respect to traveling waves // Laminar-Turbulent Transition / Ed. R. Kobayashi - Berlin: Springer-Verlag, 1995, P. 373-380.
8. Kachanov Y.S., Tararykin O.I. The experimental investigation of stability and receptivity of a swept-wing flow // Laminar-Turbulence Transition / Eds. D.Arnal, R.Michel - Berlin: Springer, 1990, P. 499-509.
9. Gaponenko V. R., Ivanov A. V., Kachanov Y. S. Experimental study of a swept-wing boundary-layer stability with respect to unsteady disturbances // Thermophysics and Aeromechanics. - 1995. V. 2, No. 4. - P. 287-312.
10. Kachanov Y.S., Tararykin O.I., Fyodorov A.V. Experimental simulation of swept-wing boundary layer in the region of secondary flow formation // Izv. Sib. Otd. Akad. Nauk SSSR, Ser. Tekh. Nauk. - 1989. - Vol. 3. - P. 44-53 (in Russian).

EXPERIMENTAL SIMULATION OF A BOUNDARY LAYER WITH A CONSTANT NEGATIVE HARTREE PARAMETER AND ITS 3D STABILITY.

Y.S. Kachanov, D.B. Koptsev
Institute of Theoretical and Applied Mechanics, 630090, Novosibirsk, Russia

1. Introduction

The problem of influence of an adverse streamwise pressure gradient on characteristics of the laminar-boundary-layer stability to three-dimensional waves is not enough investigated at present. Some quantitative experimental studies were performed either for two-dimensional perturbations or for the three-dimensional waves but in the non-gradient (Blasius) boundary layer [1-6] (see also for review [7]). The only similar quantitative measurement in a two-dimensional boundary layer was performed in [8] for the case of an airfoil with a variable streamwise pressure gradient (favorable, zero, and adverse one). In particular this experiment provides first quantitative experimental information about the growth rates of the normal instability modes (inclined at various angles to the flow direction) in the region of a variable adverse pressure gradient (APG) that increased in the streamwise direction and leaded to a laminar flow separation. It was found in [8] (see also [7]) that in a vicinity of the separation point the three-dimensional modes inclined at about 40° to the flow direction were the most amplified ones despite the flow had very low (subsonic) speed. This result was in a contradiction with the parallel linear stability theory (calculations by Michalke [9]) but it was in consistence with a non-parallel asymptotic theory [10] (see also [7]). A predominant growth of the 3D instability modes was also predicted by calculations [11] used the PSE approach for a self-similar Falkner-Skan boundary layer with an APG. This phenomenon was observed at low frequency parameters close to the lower branch of the neutral stability curve. Note that similar faster growth of the 3D modes was observed in a vicinity of the lower branch in experiments [5,6] performed in the Blasius flow. The parallel stability theory is not able, however, to explain this behaviour. This strongly suggests a significant influence of the basic flow non-parallelism on the 3D instability, especially in presence of an APG.

The goal of the present experiments was to clarify the problem discussed above by means of conducting a detail quantitative experimental study in a self-similar APG boundary layer with a constant Hartree parameter. To perform such an experiment it was necessary to create the basic flow and to investigate a behavior of the 3D controlled perturbations excited in it.
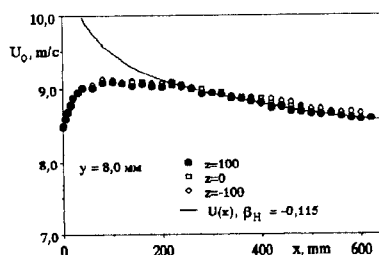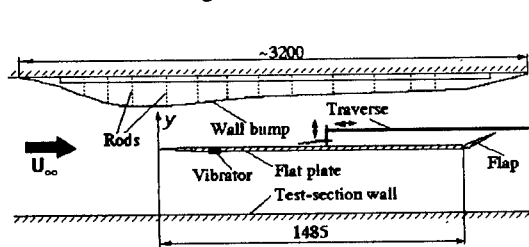

Fig. 1. Sketch of experimental model and wall bump.　　*Fig. 2.* Streamwise distributions of potential velocity.

2. Experimental Procedure

The experiments were conducted in the low-turbulence subsonic wind tunnel T-324 of the ITAM at the free-stream velocity $U_0 \approx 9$ m/s and turbulence level less than 0.02 %. The wind-tunnel has a 4 m long test section with a 1 m $\times$ 1 m cross-section. A sketch of the experimental setup is shown in Fig. 1. The APG was induced over a flat plate with the help of an adjustable wall-bump. The bump was made of a Plexiglas sheet equipped with cross beams and special fasteners for spatial positioning of the sheet. The fasteners could moved along rods, which were hingedly connected with two longitudinal power beams mounted at the wind-tunnel test-

section ceiling. The power beams, the fasteners, and the rods, were placed symmetrically with respect to the vertical plane of symmetry of the model. The flat plate was mounted horizontally directly under a wall-bump and was equipped with a flap. With the help of an adjustment of positions of the fasteners the form of a wall-bump could be significantly changed that resulted in a change of the longitudinal pressure distribution in a flow. The flap attack angle could also be varied and influence the pressure distribution in a vicinity of the model leading edge.

The instability waves were excited in the boundary layer by means of a circular surface vibrator (the source) described in detail in [12]. The source introduced into the boundary layer so-called wave trains of instability modes, i.e. the disturbances localized in space but harmonic in time. The vibrator had a plastic membrane (20 mm in diameter), mounted flush with the plate surface. The pressure fluctuations generated under the membrane by a loudspeaker (positioned outside the test-section and connected with the source by means of a plastic pipe) forced the membrane to oscillate. The amplitudes of excitation were chosen small enough to provide a linearity of mechanisms of the disturbance development.

The measurements were carried out by means of a hot-wire anemometer with a single-wire probe at three frequencies of the disturbances: $f = 55.1$, 81.4, and 109.1 Hz. At the streamwise coordinate $x = 520$ mm these frequencies correspond to the frequency parameters $F = 2\pi v f/U_0^2 = 74.0 \cdot 10^{-6}$, $106.8 \cdot 10^{-6}$, and $143.1 \cdot 10^{-6}$ respectively (in this point $U_0 = 8.67$ m/s).
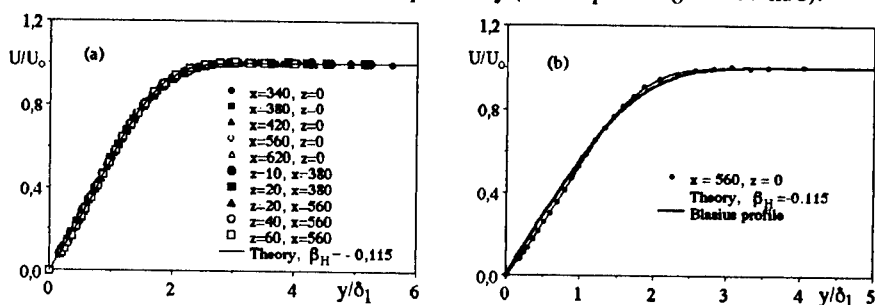

Fig. 3. Mean velocity profiles (a) and comparison with Blasius profile (b).
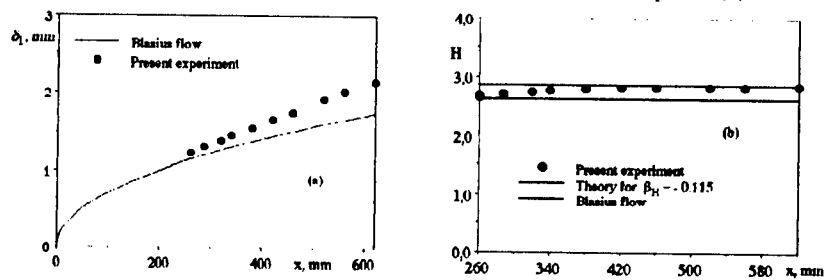

Fig. 4. Streamwise dependences of boundary-layer displacement thickness (a) and shape factor (b).

3. Basic Flow Characteristics

At an initial stage of the experiments a required streamwise distribution of the potential mean-flow velocity U_0, corresponded to a constant value of the Hartree parameter $\beta_H = -0.115$, was obtained by means of iterations with variation of the wall-bump geometry and position of the flap. The results of the measurements, performed at a fixed distance $y = 8.0$ mm from the plate surface, are shown in Fig. 2 for three fixed values of the spanwise coordinate z. The dependencies show that the created potential flow is practically two-dimensional and in the range of the streamwise coordinate x from 220 to 620 mm (i.e. up to the end of the region of measurements) corresponds to a flow with a constant Hartree parameter specified above.

The mean velocity profiles measured inside the boundary layer for various streamwise and spanwise positions are presented in Fig. 3a (δ_1 is the boundary layer displacement thickness). A rather good coincidence of the profiles with each other testifies that the designed flow is

rather close to a self-similar one (see below for more detail). It is also seen that the experimental points are in agreement with the theoretical profile calculated by B. Smorodsky for a Falkner-Skan flow with $\beta_H = -0.115$. A comparison of one of the obtained distributions with the Blasius profile, shown in Fig. 3b, demonstrates an essential difference between the boundary layer under investigation and the flow developing at the zero streamwise pressure gradient.

A streamwise distribution of the boundary-layer displacement thickness δ_1 is shown in a Fig. 4a together with the corresponding distribution for the Blasius flow. It is seen that due to an influence of the APG the boundary layer thickness increases much faster than in the non-gradient case. A streamwise dependence of the boundary-layer shape factor $H = \delta_1/\delta_2$ (where δ_2 is the momentum thickness) is presented in Fig. 4b in comparison with the corresponding values for the Blasius flow and self-similar boundary layer with $\beta_H = -0.115$. Despite the potential flow corresponds locally to a constant Hartree parameters (see Fig. 2) and the mean-velocity profiles look as self-similar ones (in the range $x = 340 \div 520$ mm, Fig. 3a) the flow prehistory influences the values of the boundary-layer shape factor H (Fig. 4b). In the initial region between $x = 260$ and 420 mm the shape factor increases gradually from values close to 2.60 (the Blasius flow) to those which are very close to 2.87 — the value computed for $\beta_H = -0.115$. In the range $x = 420$ to 620 mm ($Re = U_0\delta_1/v = 924$ to 1165) the shape factor saturates and its measured and calculated values become very close. Thus we can conclude that in this region the flow is self-similar and corresponds to the theoretical flow with $\beta_H = -0.115$.
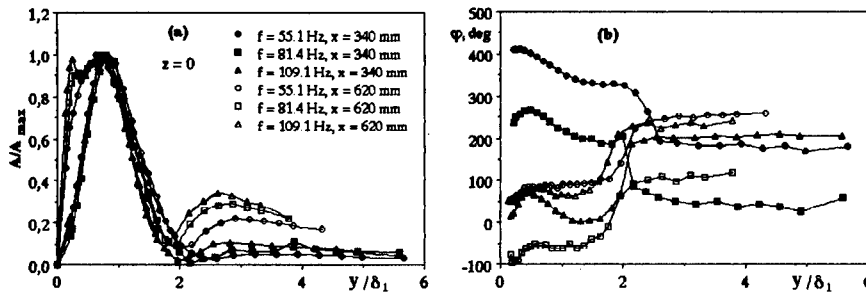

Fig. 5. Normal-to-wall profiles of disturbance amplitudes (a) and phases (b).

4. Evolution of Wave Trains

Shown in Fig. 5 is a set of the normal-to-wall disturbance profiles measured at the wave-train axis ($z = 0$) for two values of the x-coordinate. The profiles have shapes that are typical for the instability waves but, in contrast to the case of the non-gradient flow [4], an appearance and growth of a second near-wall amplitude maximum is observed. An averaged position of the main maximum corresponds approximately to the non-dimensional velocity $U/U_0 = 0.45$ for all frequencies studied. This value is close to a position of an inflexion point in the mean velocity profiles. [Calculations predict it at $U/U_0 = 0.42$.] The value $U/U_0 = 0.45$ corresponds to a non-dimensional distance $y/\delta_1 = 0.86$ that was chosen for the main stability measurements.
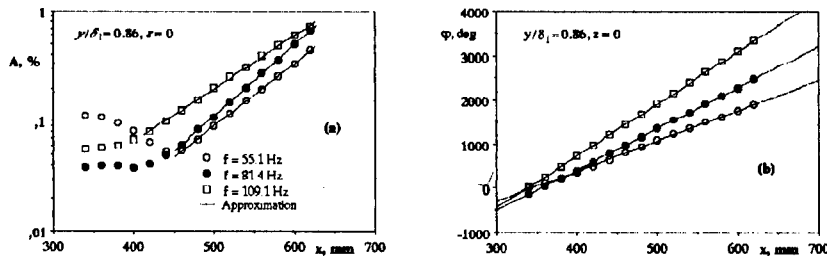

Fig. 6. Downstream evolution of disturbance amplitudes (a) and phases (b).

A set of streamwise distributions of the disturbance amplitudes and phases obtained at the wave-train axis ($z = 0$) is shown in a Fig. 6. It is seen that starting with a certain distance from

the vibrator the disturbance amplitudes increase exponentially for all studied frequencies. This behaviour is very different from that observed in the Blasius boundary layer for the wave-trains excited by the same source [4]. In particular, in the present case there is no any significant attenuation of the perturbation amplitudes in the region close to the source (Fig. 6a). The phases increases in a linear way and can be very well approximated by straight lines (Fig. 6b).
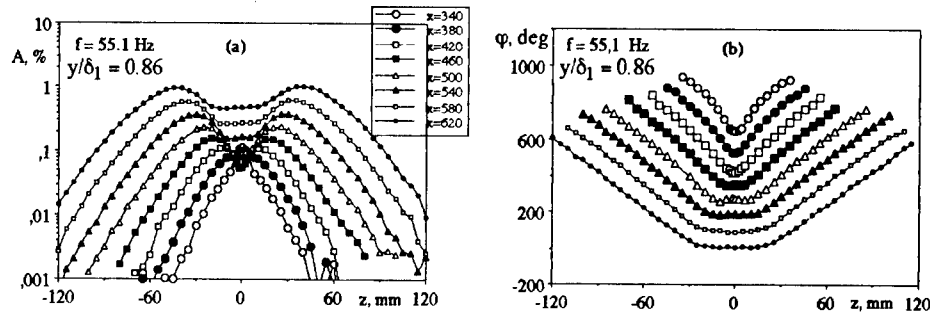

Fig. 7. Evolution of spanwise distributions of disturbance amplitudes (a) and phases (b) at $f = 55.1$ Hz.

Downstream evolution of the spanwise disturbance distributions obtained at a constant non-dimensional distance to the wall $y/\delta_1 = 0.86$ is illustrated by Fig. 7 for frequency 55.1 Hz. The distributions are almost symmetric with respect to the axis z = 0. Qualitatively their shapes are similar to those obtained in [2,4] in the Blasius flow for the same source and close frequency parameters. However, there is a very significant difference between the downstream amplitude evolution observed in the present case and in the Blasius flow, namely the typical growth rates obtained in the APG case are dramatically greater than those found in the Blasius flow.
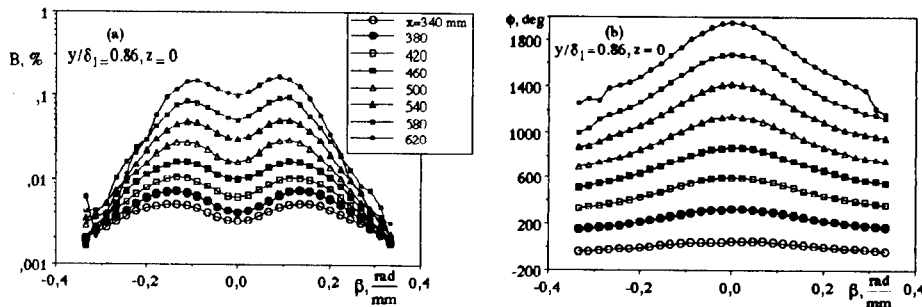

Fig. 8. Evolution of amplitude (a) and phase (b) parts of spanwise-wavenumber spectrum at $f = 55.1$ Hz.

5. Flow Stability to 3D Normal Oblique Modes

After Fourier decomposition of the distributions like those shown in Fig. 7 the spanwise wavenumber spectra of perturbations were determined. A typical set of the spectra obtained for frequency $f = 55.1$ Hz is presented in Fig. 8 for several streamwise positions. With the help of these spectra all stability characteristics of the boundary layer were obtained.

Shown in Fig. 9 is a set of streamwise distributions of the amplitudes (B) and phases (ϕ) of some normal oblique instability modes obtained at frequency $f = 55.1$ Hz for various values of the spanwise wavenumber β. Similar results were obtained for two other frequencies. The amplification curves (Fig. 9a) show an increase of the normal-mode growth rates at initial stage until $x \approx 460$ mm (Re = 969), while further downstream (al least until $x = 580$ mm, Re = 1124) the growth rates become constant and the normal-mode amplitudes grow exponentially. This property is qualitatively the same for the two other frequencies and for all important values of the spanwise wavenumber. The increase of the growth rates in the initial region is, probably, conditioned by the downstream evolution of the mean-velocity profile shape (see section 3 and Fig. 4b). The exponential growth of the normal-mode amplitudes differs significantly from that

98

observed in the non-gradient flow (see [2,6]) where the growth of the Reynolds number leads to a strong variation of the amplification rates with the streamwise coordinate.
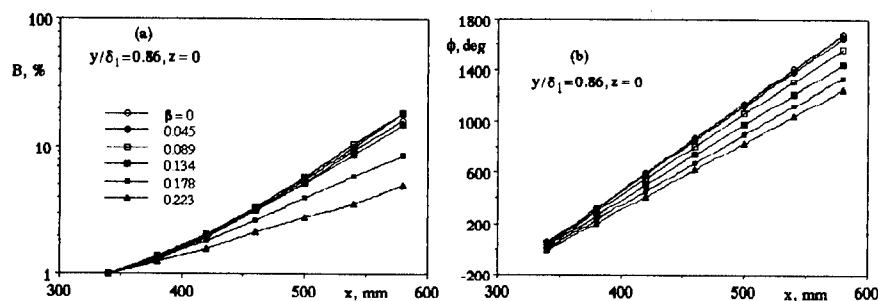

Fig. 9. Evolution of normal-mode amplitudes (*a*) and phases (*b*) at *f* = 55.1 Hz.

The normal-mode phases (shown in Fig. 9*b*) increase linearly in the whole region of the measurements similar to the Blasius flow [2,6] and a boundary layer on an airfoil in the region of a variable APG [8]. This gives possibility to determine the streamwise wavenumbers α_r and the wave propagation angles θ for every fixed spanwise wavenumber and frequency.
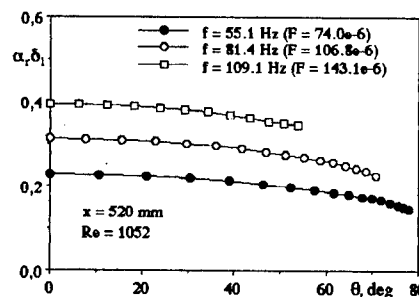

Fig. 10. Normal-mode streamwise wavenumbers versus wave propagation angle for three frequencies.
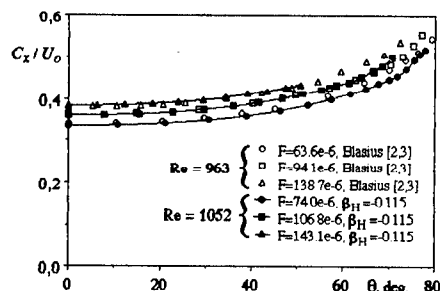
Fig. 11. Normal-mode phase velocities versus wave propagation angle for three frequencies.

The values of the dimensional streamwise wavenumber α_r obtained for various values of the spanwise wavenumber are independent of the *x*-coordinate in the range *x* = 340 ÷ 620 mm (Re = 814 ÷ 1165). The non-dimensional streamwise wavenumbers $\alpha_r\delta_1$ depend, in contrast, on the *x*-coordinate due to a growth of the boundary layer displacement thickness δ_1. Therefore the distributions of $\alpha_r\delta_1$ versus the wave propagation angle θ presented in Fig. 10 were determined for a fixed streamwise coordinate *x* = 520 mm (Re = 1052) that is in the region of a self-similar flow with the constant Hartree parameter and shape factor (see section 3). These dependences look very similar to those obtained for the Blasius flow in [3,6] for somewhat lower values of the Reynolds number. The normal-mode phase velocities C_x/U_o are very weakly dependent on Re (see [3,6]) and can be compared directly with the Blasius case for close frequency parameters. An almost complete coincidence of the phase velocities of all 3D normal modes with those obtained in the non-gradient case (Fig. 11) is a surprise which is difficult to explain.

In contrast to the phase speeds the normal-mode amplification rates (Figs. 12 to 13) are very different from those measured in the Blasius flow. At frequencies 55.1 Hz and 81.4 Hz the growth rates of the most unstable normal modes are greater in the APG case than those in the Blasius flow by 5 to 7 times. At the highest frequency studied the maximum amplification rates are close to 0.03 while in the Blasius flow all modes attenuate. At the same time a general behaviour of the growth rates with the wave propagation angle is similar in the two flows. In particular, for the lowest frequency the most amplified instability modes are three-dimensional ones in the two cases. This fact is not trivial and testifies to an importance of the 3D linear modes evolving in the subsonic APG boundary layers. Note, that at frequency 55.1 Hz the most unstable modes propagate at angles close to 30°. Similar result was obtained in theory [11] were it was also found that the predominant growth of the 3D waves is observed both in the

Blasius flow and in the APG boundary layer. In the latter case this phenomenon is stronger both in theory and experiment.
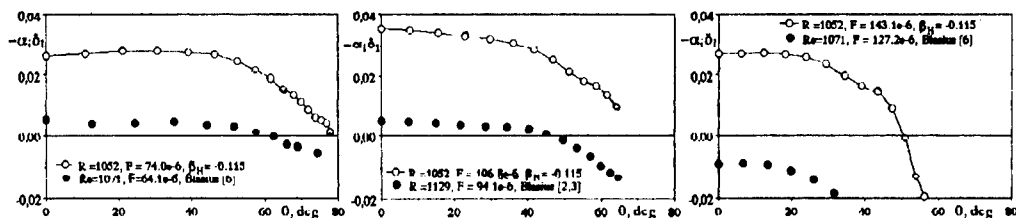

Fig. 12. Growth rates of normal modes versus propagation angle for three disturbance frequencies.

6. Conclusions

A self-similar boundary-layer flow with an adverse pressure gradient and constant Hartree parameter is realized experimentally. The experiments carried out under controlled disturbance conditions give possibility to obtain, for the first time, all main stability characteristics of the APG self-similar flow with respect to the 3D normal instability modes for various values of the wave propagation angle and frequency. It is found, in particular, that the dispersion characteristics of the 3D instability modes are very weakly dependent on the pressure gradient, while the growth rates depend on it significantly. At low frequency parameters a predominant growth of the 3D waves is found. The results obtained represent an extensive experimental base for a subsequent analysis and utilizing for verification of the theoretical approaches.

References

1. Gaster M., Grant T. An experimental investigation of the formation and development of a wave packet in a laminar boundary layer // Proc. Roy. Soc. London. - 1975. - A 347. - P. 253-269.
2. Gilyov V.M., Kachanov Y.S., Kozlov V.V. Development of a spatial wave packet in a boundary layer // Izv. Sib. Otd. Akad. Nauk SSSR, Ser. Tekh. Nauk. - 1983. – V. 13. – P. 27-37 (in Russian). (See also Kachanov Y.S. // Laminar-Turbulent Transition / Ed. V.V. Kozlov – Berlin: Springer, 1985, P. 115-123.)
3. Kachanov Y.S., Michalke A. Three-dimensional instability of flat-plate boundary layers: Theory and experiment // Eur. J. Mech. B/Fluids. – 1994. – V. 13, No 4. – P. 401-422.
4. Kachanov Y. S., Obolentseva T.G. Development of three-dimensional disturbances in the Blasius boundary layer. 1. Wave-trains // Thermophysics and Aeromechanics. - 1996. - V. 3, No. 3. - P. 225-243.
5. Kachanov Y.S., Obolentseva T.G. A method of study of influence of the flow nonparallelism on the 3D stability of Blasius boundary layer // Proc. Int. Conference on Methods of Aerophysical Research. Pt. 2. - Novosibirsk: Inst. Theor. & Appl. Mech., 1996, P. 100-105.
6. Kachanov Y.S., Obolentseva T.G. Development of three-dimensional disturbances in the Blasius boundary layer. 2. Stability characteristics // Thermophysics and Aeromechanics. - 1997. - V. 4, No 3.
7. Kachanov Y.S. Experimental studies of three-dimensional instability of boundary layers. – AIAA Paper. 96-1978, 1996.
8. Gilyov V.M., Dovgal A.V., Kachanov Y.S., Kozlov V.V. Development of spatial disturbances in a boundary layer with pressure gradient // Izv. Akad. Nauk SSSR, Mekh. Zhidk. i Gaza. - 1988. - No 3. - P. 85-91 (in Russian).
9. Dovgal A.V., Kozlov V.V, Michalke A. Laminar boundary layer separation: instability and associated phenomena // Progr. Aerospace Sci. – 1994. – V. 30. - P. 61-94.
10. Stewart P.A., Smith F.T. Three-dimensional instabilities in steady and unsteady non-parallel boundary layers, including effects of Tollmien-Schlichting disturbances and cross flow // Proc. Roy. Soc. London. - 1987. - A 409. - P. 229-248.
11. Bertolotti F.P. Linear and nonlinear stability of boundary layers with streamwise varying properties. - PhD thesis. The Ohio State Univ., USA, 1991.
12. Ivanov A.V., Kachanov Y.S., Koptsev D.B. Experimental study of generation of instability waves in 3D boundary layer at scattering of an acoustic wave on a vibrator // Thermophysics and Aeromechanics. - 1997. - V. 4, No 4.

THE USE OF THE THIN LAYER MODEL FOR NUMERICAL SIMULATION OF THE FLOW AROUND THREE-DIMENSIONAL BODIES

T.A.Korotaeva
Institute of Theoretical and Applied Mechanics SB RAS,
630090, Novosibirsk,Russia

1. Let us consider a compressible flow around a body at a high supersonic speed. The region of disturbed parameters is located between the body surface and the bow shock wave. The existing methods of hypersonic approximation (e.g., thin layer [1]) imply a number of assumptions, especially concerning the shock wave position, and need proper refinement. We consider the flow around pointed bodies, i.e., the flow is supersonic everywhere in the disturbed region. This makes it possible to use the marching methods of computation.

2. Since we consider the case $M_\infty \gg 1$, the shock layer is assumed thin

$$\frac{h}{\ell} < 1, \quad \frac{h}{R} \ll 1, \tag{1}$$

where h is the shock layer thickness, ℓ is the characteristic length of a cell, and R is the radius of surface curvature. Thus, the shock wave shape cannot be much different from the body surface shape, and the pressure on the body will be mainly determined by the shock shape [1].

The disturbed region between the shock wave and the body is split into two layers: the layer adjacent to the shock wave (external) and the layer adjacent to the body (internal). Different algorithms are used for solving the problem in these subdomains. This approach is well justified [2]. Indeed, small changes in the shock wave position lead to large changes of parameters in the disturbed region, therefore, it is necessary to determine this position as accurately as possible. At the same time, a moderate thickness of the disturbed region allows one to make some simplifying assumptions and replace the differential equations in the vicinity of the wall by algebraic equations. The calculation in the external layer is performed by the method of finite volumes for inviscid gas flow.

After determining the flow parameters from the Euler equations [4], the shock wave position is corrected:
- the shock wave velocity is determined on the basis of pressure difference (behind the shock and in the free stream);
- a new shock wave position is determined on the basis of the shock wave velocity.
Having determined the shock wave position and taking into account the preliminary data in the internal layer, we determine numerically the parameters at the boundary between the layers. Using the obtained results, we refine the internal layer parameters. Then the process is repeated. The iteration is performed by the pseudo-transient method.

3. The thin layer approximation is used in the internal region and on the body surface. The body surface is a streamline, thus, the following algorithm is used to compute the parameters at points which belong to the body:

a) an approximate position of the streamline lying on the body surface and passing through a test point is determined;

b) the pressure at the test point is obtained from the solution for the external layer;
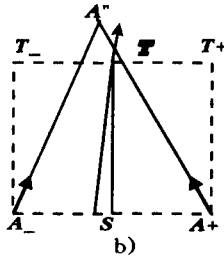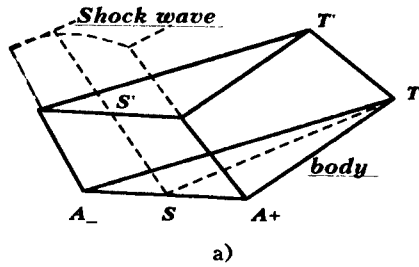
a)

b)

Fig.1 a) a part of the finite volume in the vicinity of the test point;
b) determination of a streamline passing through the test point.

c) the remaining gas dynamic parameters are determined on the basis of the pressure value and relations along the streamline.

Let us consider stages a), b), and c) in more detail

Stage a):

Figure 1a shows a part of the finite volume in the vicinity of the test point. Here $A_- A_+$ is the previous cross-section with all parameters known, $T_- T_+$ is the test cross-section.

Condition (1) allows us to use the ideas of the local theory: the influence of distant points is small. If a point T belongs to the triangle $A_- A''A_+$ (Fig.1b), we determine a point S such that the velocity vectors at points S and T had the same direction. Otherwise, we extend the "influence region", taking instead of A_- and A_+ the neighboring points.

Stage b):

Let an element of the body surface, with respect to velocity at the surface $A'_- T'A'_+$, satisfies the condition $\overline{w}_{t's'}, \overline{n}_t \leq 0$, where $\overline{w}_{t's'}$ is the velocity vector at the upper face of the cell. The pressure at the point T is determined as

$$p_t = p_{t's'}(1 + \frac{\gamma}{2} C_{p_t} M_{t's'}^2),$$

where the subscript "$t's'$" refers to the medium point of the line "$t's'$", the subscript "t" denotes the test point, C_{p_t} is the excess pressure coefficient on the wall with respect to the pressure in the external layer.

Let us estimate the value of C_{p_t}. For this purpose, let us write the momentum conservation equation in the direction normal to the body. In an integral form, this equation is

$$\oint (\rho w_n (\overline{w}, \overline{n}_t) + p(\overline{n}, \overline{n}_t)) ds = 0, \tag{2}$$

where $\overline{w}$, $\overline{n}$ are the mean values of velocity and the normal on the face, $\overline{n}_t$ is the normal at the test point. The normal vector $\overline{n}$ to the face can be decomposed in orthogonal directions: normal $\overline{n}_t$ and tangent $\overline{\tau}_t$ to the face on the wall. Equation (2) can be written in the finite-difference form, taking into account that $\overline{n} = (\overline{n}, \overline{n}_t) \overline{n}_t + (\overline{n}, \overline{\tau}_t) \overline{\tau}_t$:

$$\sum_{i=1}^{5} \rho_i (\overline{w}_i, \overline{\tau}_t)(\overline{w}_i, \overline{n}_t) \frac{\Delta S_i}{\Delta S_t} (\overline{n}_i, \overline{n}_t) + \{\rho_{t's'} (\overline{w}_{t's'}, \overline{n}_t)^2 + p_{t's'} - p_t\} = 0 \tag{3}$$

From equations (3) near the wall we can obtain the estimates [3,4]

$$\rho(\xi, \eta, \zeta) = \rho_0(\xi, \eta) + O(\zeta^2)$$

$$w_n(\xi, \eta, \zeta) = w_1(\xi, \eta)\zeta + O(\zeta^3) \tag{4}$$

$$w_\tau(\xi, \eta, \zeta) = w_0(\xi, \eta) + O(\zeta^2).$$

where $\bar{w} = (u, v, w)$ is the velocity vector, ξ, η, ζ are the unit vectors of the natural coordinate system. The ζ axis is directed normal to the surface, ξ and η are on the body surface. Let $\ell = \max(\xi, \eta)$. Then, using the Taylor expansion, we can write

$$\rho(\xi, \eta, \zeta) = \rho^* + \rho_\xi^* \xi + \rho_\eta^* \eta + O(\ell^2)$$

$$w_n(\xi, \eta, \zeta) = w_n^* + w_{n\xi}^* \xi + w_{n\eta}^* \eta + w_{n\zeta}^* \zeta + O(\ell^2) \qquad (5)$$

$$w_\tau(\xi, \eta, \zeta) = w_\tau^* + w_{\tau\xi}^* \xi + w_\tau^* \eta + O(\ell^2).$$

where * denotes the parameters at the medium point of a cell. From here and (4), with accuracy to ζ^2, we obtain

$$(\rho w_\tau w_n)_i \frac{\Delta S_i(\bar{n}_i, \bar{\tau}_i)}{\Delta S_t} = \rho^* w_\tau^* w_n^* \frac{\Delta S_i(\bar{n}_i, \bar{\tau}_i)}{\Delta S_t} + O(\zeta^2).$$

Taking into account the above estimates, (3) takes the form

$$\rho^* w_\tau^* w_n^* \sum_{i=1}^{5} \frac{\Delta S_i(\bar{n}_i, \bar{\tau}_i)}{\Delta S_t} + \{\rho_{t's'}(\bar{w}_{t's'}, \bar{n}_t)^2 + p_{t's'} - p_t\} + O(\zeta^2) = 0$$

For a closed volume

$$\sum_{i=1}^{5} \frac{\Delta S_i(\bar{n}_i, \bar{\tau}_i)}{\Delta S_t} = 0.$$

Thus, with accuracy to ζ^2, the initial equation can be written as

$$\rho_{t's'}(\bar{w}_{t's'}, \bar{n}_t)^2 + p_{t's'} - p_t = 0, \text{ or}$$

$$C_{p_t} = 2\frac{p_t - p_{t's'}}{\rho_{t's'} w_{t's'}^2} = 2\frac{(\bar{w}_{t's'}, \bar{n}_t)^2}{w_{t's'}^2},$$

which is analogous to the Newton's formula for a finite volume.

If $(\bar{w}_{B's'}, \bar{n}_t) > 0$, then we suppose (since velocities are high) that there is a diffuse separation with the pressure on the concave part of the surface, corresponding to base expansion [5]. The local pressure here is $Cp_t = Cpd(M_{t's'})$,

$$Cpd(M_{t's'}) = -0.01 - 0.64\frac{1}{\frac{\gamma}{2}M_{t's'}^2} + 0.306\frac{1}{\frac{\gamma}{2}M_{t's'}^2}$$

The method of expansion waves can be also used in these regions.

Stage c):

Having determined p_t and the position of a streamline arriving at a given point along the body surface, we can calculate the remaining gas dynamic parameters:

$$\tau(M_t) = \tau(M_s)\left(\frac{p_s}{p_t}\right)^{\frac{\gamma-1}{\gamma}}, \quad \rho_t = \rho_s\left(\frac{\tau(M_s)}{\tau(M_t)}\right)^{\gamma-1}, \quad v_t = v_s\frac{M_t}{M_s}\left(\frac{\tau(M_s)}{\tau(M_t)}\right)^2,$$

where $\tau(M_t) = 1 + \frac{\gamma-1}{2}M_t^2$. Here we do not know only the velocity components $\bar{w}_t$ on the body. It follows from (4) that the dependence of the normal component of velocity on ζ near the solid surface is close to linear. The tangential component of velocity and density can be considered changing little along the normal to the body. Hence,

$$w_\tau = w_\tau' \frac{|\bar{w}_t|}{|\bar{w}'|},$$

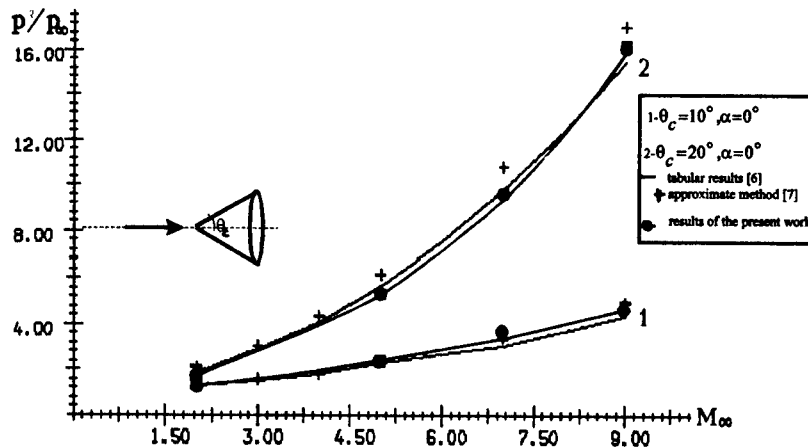where τ is the tangent direction to the body surface, $\bar{w}'$ is the velocity vector at a distance ζ

Fig.2 The pressure on the cone surface for two cone half-angles $\theta_c=10°,\theta_c=20°$ at zero incidence.

from the boundary.

Thus, the proposed approach combines the identification of the shock wave front by means of numerical solution of three-dimensional Euler equations using the method of finite volumes and an approximate determination of the parameters on the body.

The described approach is a rational approximation applied to three-dimensional bodies, which is more general than the irrational methods of local cones and wedges used in practice.

4. Let us consider now the results of computations based on the above algorithm.

Figure 2 shows the pressure on the cone surface normalized to the free-stream pressure as a function of the Mach number within the range $M_\infty=2\div9$, for two cone half-angles $\theta_c = 10°, \theta_c = 20°$ at zero incidence (the solid lines show the tabular values from [6]).

The same figure shows the results (marked by crosses) calculated using the approximate method of the paper [7], where the accuracy of the law of plane sections is analyzed. It is seen that for the cone half-angle $\theta_c = 10°$ the results of the present work, the results obtained using the method of unsteady analogy, and tabular values are is reasonable agreement within the entire range of Mach numbers. Meanwhile, for the cone half-angle $\theta_c = 20°$ the present approach
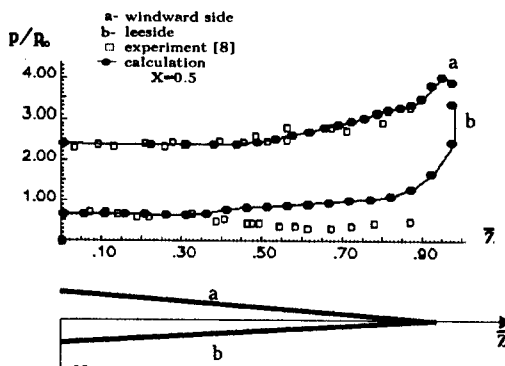

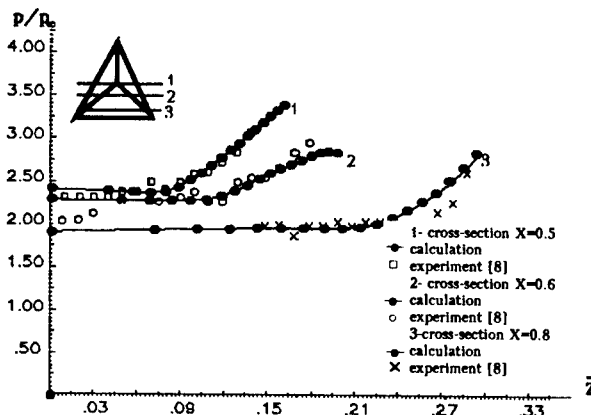**Fig.3** p/p_∞ over the wing span for one cross-sections up to a fracture forming.

Fig.4 p/p_∞ over the wing span for various cross-sections.

yields the pressure values which are closer to tabular ones.

Figures 3 and 4 show a comparison of numerical data and experimental results [8] for a triangular wing with a rhombus profile at incidence ($\alpha = 10°, M = 4.05$, $\chi = 75°$, $\overline{C}_{max} = 3{,}3\%$). A spanwise distribution of pressure in one of the cross-sections up to the generatrix inflection on the leeward and windward sides of the wing is shown in Fig. 3.
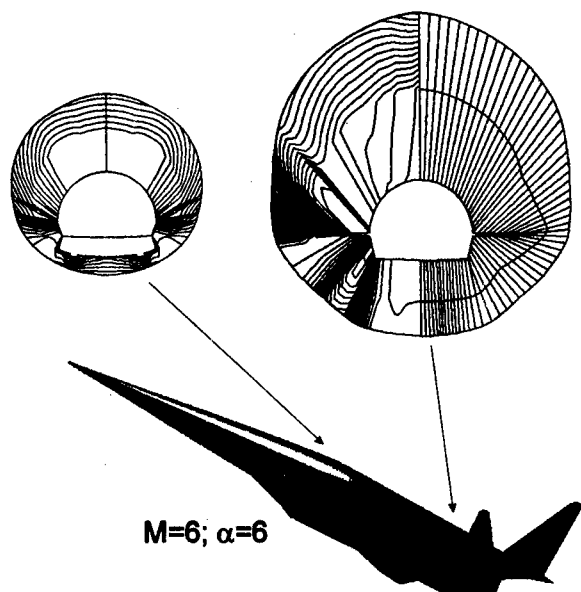
A good agreement is observed on the windward side. A noticeable discrepancy is observed only in the local expansion region behind the generatrix inflection near the symmetry plane. On the leeward side, a noticeable disagreement is again observed in the local expansion region near the wing edge, wherein condition (1) is violated. It should be noted, however, that the discrepancies in the above example refer to narrow regions, and there are grounds to believe that they cannot affect appreciably the aerodynamic characteristics of bodies in a supersonic flow (fig.5).

M=6; α=6

Fig.5

REFERENCES

1. Hayes W.D., Probstein R.F. Hypersonic Flow Theory. -New York: Academic Press, 1959.
2. D'yachenko V.F. On nonasymptotic principles of approximation// Numerical Modeling in Mechanics. -Moscow: Nauka, 1986. –p.97-103.
3. Ladyzhensky M.D. Three-Dimensional Hypersonic Gas Flows. –Moscow: Mashinostroenie, 1968.
4. Shashkin A.P. The study of some gas dynamic flows by the shock-capturing method: Ph.D.Thesis. -Novosibirsk, 1975.
5. Kiselev V.Ya., Kornilov V.I., Korotaeva T.A., Maslov A.A., Shashkin A.P. Determination of the aerodynamic characteristics of hypersonic flight of bodies in dense atmosphere// Teplofizika I Aeromekhanika. – 1995. -No. 1. –p.9-14.
6. Kopal Z. Tables of supersonic flow around cones: Technical Report № 1. -Massachusetts,, 1947.
7. Voevodenko N.V., Shironosov V.A. The study of accuracy of the law of plane sections// Uch. Zap. TsAGI. – 1985. No. 16. –p.35-43.
8. Vasenev L.G.and Kharitonov A.M. Supersonic interference of a triangular wing and cylindrical body with an ogival forebody. -Novosibirsk, 1984 -(Preprint /SB RAS ITAM; No. 28-84).

EXPERIMENTAL STUDY OF ANOMALOUS WAVE PROCESSES IN SUPERSONIC BOUNDARY LAYER

A. D. Kosinov, Yu. G. Ermolaev, N. V. Semionov

Institute of Theoretical and Applied Mechanics SB RAS
630090, Novosibirsk, Russia

INTRODUCTION

Stability experiments with controlled disturbances in supersonic boundary layers have been carried out [1, 2]. In these works linear stability theory was investigated for wave disturbances with fixed propagation angles. Similar experiments on linear development of wave trains in supersonic boundary layer have been conducted in [3]. Works [2, 3] enabled us to consider that three-dimensional waves are more unstable in supersonic boundary layer.

Experiments [4], being conducted for comparatively low-level amplitudes of initial disturbances, have shown that parametric resonance is the mechanism of nonlinear interaction of unstable waves in supersonic boundary layer. At this the main energy portion of subharmonic disturbances belongs to perturbations with wave propagation angles approximately equal to 80°. However experiments [5, 6] showed that an increase of initial disturbance amplitude led to nonlinear amplification of quasi two-dimensional subharmonic pulsations. This is generally accepted concept that laminar-turbulent transition in supersonic boundary layer are connected with the amplification of three-dimensional disturbances [7]. So it is possible to call the excitation of quasi two-dimensional waves in supersonic boundary layer as "anomalous", as far as this fact stands apart from our general concepts. The essence of our approach, applied in [5, 6] for studying the nonlinear stability of supersonic boundary layer, is that we used the initial disturbance amplitude as a parameter in experiments. Presented below experiments have been performed for the highest amplitude level of initial disturbances, which was possible with our source of controlled pulsations. These experiments are an extension of investigations described in [6].

EXPERIMENTAL CONDITIONS

Experiments were carried out in T-325 supersonic wind tunnel in ITAM SB RAS at Mach number M=2, unit Reynolds number $Re_1=6.5\times10^6$ м$^{-1}$, and flow velocity in the test section U=504 m/s. A flat steel plate 450 mm length, 200 mm wide and 10 mm thick with a sharp leading edge [8] was used as a model. The plate was installed in the central plane of test section under zero angle of attack. The localized generator of disturbances was used for the introduction of periodic controlled pulsations into boundary layer. The generator's design was based on the glow discharge in camera and was described in [8]. Artificial perturbations were triggered in the boundary layer through the hole in the working surface of model, 0.42 mm in diameter. Coordinates of the source were x=(38±0.25) mm, z=0 (x is the distance from the leading edge and z=0 corresponds to the central line of plate).

Constant temperature hot-wire anemometer with bridge 1:10 and frequency range up to 500 kHz was used for the pulsation measurements. Tungsten wire probes 5 micron in diameter and 0.95 mm long were in use. Measurements were conducted at

cross boundary layer position where natural pulsation profiles had maximum (at y/δ, where δ is a boundary layer thickness). Hot-wire moved down into certain position with coordinates (x, y, z) using a traversing gear. An accuracy of determination of sensor position was 0.1 mm in (x, z) coordinates and 0.01 mm in y. Measurements were executed under conditions ρU=const (ρU is a mass flux) and y/δ =const when moving a sensor in x direction. Measurements were conducted under conditions x=const and y=const when moving a sensor in z direction.

Value of overheat ratio of hot-wire was installed 0.8 and measured perturbations corresponded to mass flux pulsations.

Pulsation and mean characteristics of flow were measured by means of automated measurement system, which was similar to presented in [8]. Pulsation from the hot-wire anemometer was written by 12-bit ADC with the frequency 750 kHz. Start ADC was produced with synchronous generator which determined the frequency of introduced disturbances. An accuracy of start ADC was less than 0.2%. Synchronous signal summation through 128 realization was applied for improving the ratio signal/noise. Averaged voltage from the hot-wire anemometer was written by PC through input registers, connected to the voltmeter. Frequency harmonicas were defined by means of discrete Fourier-transformations (DFT) of averaged oscillograms. The length of each realization was 900 signal points.

For data processing DFT was used in the form:

$$e'_{\beta\omega}(x,y) = \frac{1}{T}\sum_{j,k} e'(x,z_j,y,t_k) \cdot \exp(-i[\beta z_j - \omega t_k]) = A_{\beta\omega} e^{i\Phi_{\beta\omega}},$$

where $e'(x, z_j, y, t_k)$ are pulsations averaged through realization; T is the length of realization in time.

RESULTS

Under the given experimental conditions with controlled disturbance excitation, laminar-turbulent transition on model occurred on 20% closer to the leading edge (streamwise coordinate x_{tr}=205 mm, Reynolds number $Re_{tr}=\sqrt{Re_1\, x_{tr}}$ =1150), than for natural pulsations (x_{tr}=250 mm and Re_{tr}=1280).

The measurements of controlled disturbances in boundary layer were carried out at different spanwise coordinates z for x=60, 70, 90 and 110 mm (Reynolds number $Re=\sqrt{Re_1\, x}$ =624, 674, 765, 846 - accordingly). Fig.1 presents oscillograms for controlled pulsations at different z positions for x=60 and 110 mm. Here the scale of hot-wire signal amplitude corresponds to 12-bit of ADC. For x=60 mm in the wave packet center the «thorn»-type oscillograms were observed while for x=110 mm measured oscillograms were almost sinusoidal. Thereby, experiments have shown that downstream flow evolution of periodic wave train brought about harmonic disturbances. Two-dimensional character of flat plate boundary layer flow means that it is uniform in z. This fact was checked repeatedly in experiments (see, for example, [3, 8]). However as far as amplitude of initial disturbances was high, a local change (stagnation and displacement) of the mean flow in the center of wave packet occurred. Averaged voltage defect in the wave packet center was about 0.05 V at x=60 mm and about 0.15V at x=110 mm (fig.2). Consider the value of averaged voltage defect of stationary perturbation amplitude, introduced by the point source, a possibility of
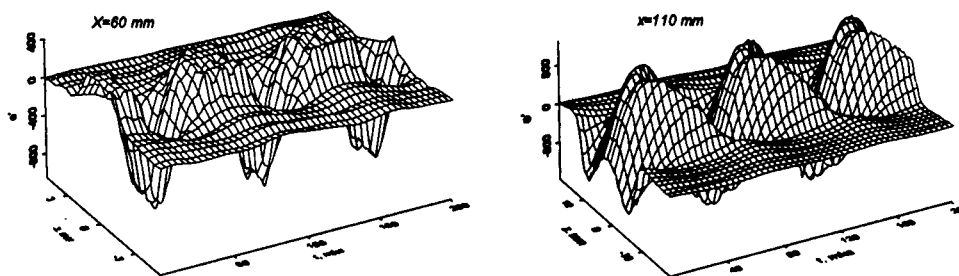
Figure 1.

downstream growth of stationary perturbation amplitude was confirmed. For measured distributions, z width of nonstationary wave packet agreed with z width of averaged voltage defect of stationary perturbations. Fig.2 demonstrates an example of averaged voltage distribution in z and pulsations for the frequencies 10 and 20 kHz (frequency parameters $F = \dfrac{2\pi f}{Re_1\, U_\infty} = 0.192\times10^{-4}$ and 0.384×10^{-4}) at x=110 mm. Here amplitude represents a percentage the non-dimensional value e'/E for pulsations.
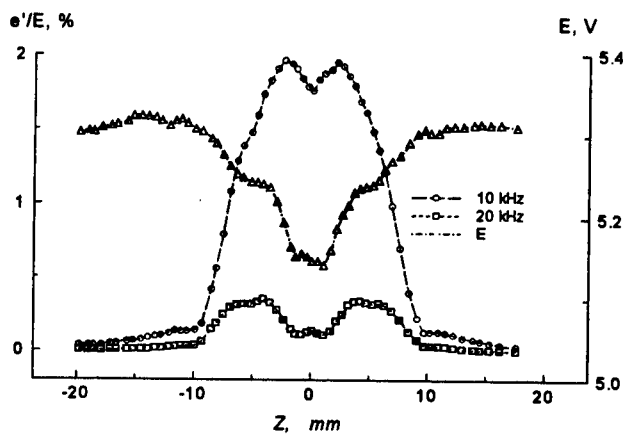

Figure 2.

Perturbations distorted the mean velocity profile across the boundary layer so that boundary layer thickness increased. For example, at x=110 mm the boundary layer thickness in the center of wave packet was twice as much as compared with the thickness δ, observed at natural conditions. The observed profiles of controlled disturbances had maxima in y. At x=110 mm, z=0, f=10 kHz this maxima in pulsation profiles were at 0.6 mm from the model, but at 20 kHz these maxima were located two times higher from the wall. At this measurements for frequency 10 kHz were conducted close to the maximum in y-distribution contrary to measurements for frequency 20 kHz, which were executed below these maxima in y. That was connected with the following circumstance: for coordinate value y=const the same value was chosen at which spanwise measurements at the maximum of natural pulsations across the boundary layer were executed.

108

However it is impossible to confirm that maximum in y of controlled pulsations stayed at the same distance from the model surface when a spanwise coordinate z changed .

In fig.3 β spectra of disturbance amplitudes are shown. Results are presented in the frequency range from 5 up to 50 kHz ($F=0.96\times10^{-5}\div0,96\times10^{-4}$), so long as high-frequency pulsations were observed. We note that the wave train width Δz increased from 4 mm at $x=60$ mm up to 20 mm at $x=110$ mm, at this corresponding propagation angle for the wave train was $\pm9°$, that is 1.5 times more than for linear case [3] and six times more than for nonlinear evolution of wave train at M=3 [6]. Referring to fig.3a, at $x=60$ mm β-spectra have the maximum at $\beta=0$ for all frequencies. We received similar result earlier at Mach=4, when initial wave spectra had also maxima at $\beta=0$ at frequency 20 kHz. These results have been described in [9].
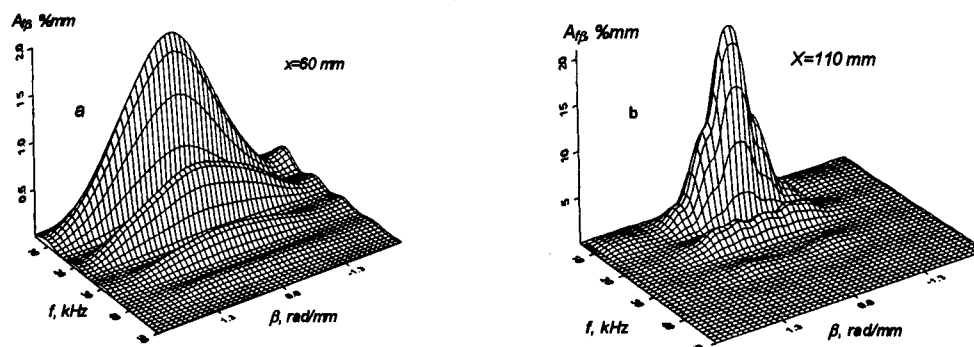

Figure 3.

However the further linear evolution of disturbances in boundary layer at M=4 showed the transformation of initial spectra from profiles with the maximum at $\beta=0$ to profiles with the maximum at $\beta=0.4\div0.7$ rad/mm, i.e. just as is was expect by linear stability theory for growing three-dimensional disturbances. Now such behavior was not observed. But we observed the strong growth (nearly 10 times from $x=60$ mm to $x=110$ mm) of 10 kHz disturbances , while two-dimensional nature of wave spectra did not change through entire coordinate range (fig.3a).

Growing disturbances with frequency 20 kHz were observed. This growth averaged 4 times when x changed from 60 to 90 mm. Only at $x=110$ mm, disturbances with frequency 20 kHz began to dominate three-dimensional waves ($|\beta|\approx0.6$ rad/mm) in wave spectra. According to the linear stability theory, disturbances with frequency 20 kHz should grow more intensively than disturbances with $f=10$ kHz at given boundary layer conditions.

The phase velocities of disturbances $C(\chi)=\dfrac{\Delta x}{\Delta\Phi_{f\beta}}\times F\times\mathrm{Re}_1$ have been

determined based on received phase spectrums evolution. These results are shown in fig.4. Fig.4 represents disturbance phase velocities for frequencies 10 kHz and 20 kHz. Obtained dependencies $C(\chi)$ are unique and for the first time have been observed in stability experiments in supersonic boundary layer. For comparison, linear stability calculations for $C(\chi)$ [3]) are displayed in fig.4, which show a distinctive maximum at

109

χ=0 and minimum at $\chi \approx \pm 55°$. The dependencies received in the experiments show that phase velocities grow with the growth of wave propagation angle, but values of phase velocities averages 30-40% higher than for the case of eigenmodes for supersonic boundary layer.
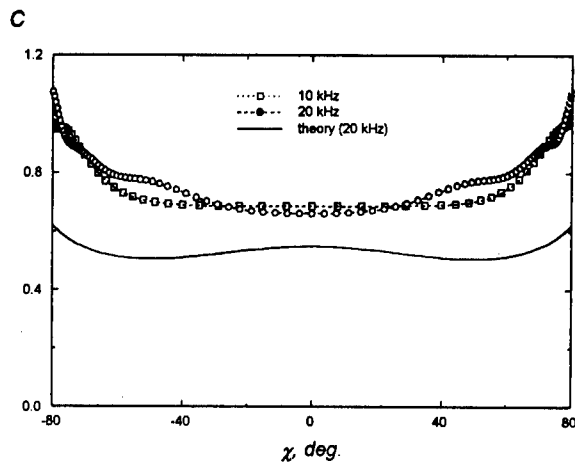
C

Figure 4.

The harmonic nature of wave train evolution was observed in these experiments up to x=150 mm (Re=987). Measurements in this experiments were executed only till this downstream position. Pulsation distribution across boundary layer at x=140 mm (Re=954) showed that wave train amplitude decreased quickly with the distance from model surface increased, that was inherent for vortex disturbances. The distortion of harmonic disturbances to smoothed saw-tooth shape and later back to the sinusoidal shape was observed near the external edge of boundary layer. Such changes in oscillograms corresponded to the appearance of high-frequency pulsations at external edge of boundary layer.

CONCLUSIONS

Our study of nonlinear wave packet evolution has shown an amplification of two-dimensional disturbances in supersonic boundary layer at M=2. Degeneration of high-frequency harmonics occur as a result of disturbance evolution. Perturbations are shown to be vortexes. Their phase velocities are 30-40% higher as compared with eigenmodes of supersonic boundary layer. The strong growth of quasi two-dimensional disturbances is probably connected with the growth of stationary vortex generated by the source of controlled pulsations in the experiments.

ACKNOWLEDGMENTS

REFERENCES

1. Laufer J., Vrebalovich T. Stability and transition of a laminar boundary layer on an insulated flat plate // J. Fluid Mech. -1960. - Vol.9. - P.257-299.

2. Kendall J.M. Supersonic boundary layer stability experiments // Boundary Layer Transition Study Group Meeting: Proc. Vol.II. - Aerospace Corp., San Bernardino, CA, 1967, P.10-1, 10-8.
3. Kosinov A.D., Maslov A.A., Shevelkov S.G. Experiments on stability of supersonic boundary layers // J. Fluid Mech. - 1990. - Vol.219. - P.621-633.
4. Kosinov A.D., Semionov N.V., Shevelkov S.G., Zinin O.I. Experiments on the nonlinear instability of supersonic boundary layers // Nonlinear Instability of Nonparallel Flows. Proc.: Springer-Verlag, 1994. - P.196-205.
5. Ermolaev Yu.G., Kosinov A.D., Semionov N.V. Experimental investigation of laminar-turbulent transition process in supersonic boundary layer using controlled disturbances // Nonlinear Instability and Transition in 3D Boundary Layer. UK, Manchester: Kluwer, 1996. - P.17-26.
6. Ermolaev Yu.G., Kosinov A.D., Semionov N.V. Experimental study of nonlinear development of unstable waves on flat plate at Mach number M=3 // J. Appl. Mech. Tech. Phys. - 1997. - No 2. - P.107-114.
7. Morkovin M.V. Critical evaluation of transition from laminar to turbulent shear layers with emphasis on hypersonically traveling bodies // AFFDL TR-68-149, 1969. - 140 p.
8. Kosinov A.D., Semionov N.V., Shevelkov S.G. Investigation of supersonic boundary layer stability and transition using controlled disturbances // Int. Conf. ob the Methods of Aerophys. Research: Proc. Pt.2. - Novosibirsk, 1994, P.159-166.
9. Kosinov A.D., Maslov A.A., Shevelkov S.G. Experimental investigation of harmonic disturbances development in flat plate boundary layer at Mach number M=4 // Izv. AN SSSR. Mech. Zhid. i Gasa. - 1990. - No 6. - P.54-58.

EXPERIMENTAL AND NUMERICAL MODELLING OF SWIRLING TURBULENT WAKE

V. A. Kostomakha, G. G. Chernykh, A. G. Demenkov

Institute of Computational Technologies SB RAS
Lavrentyev Institute of Hydrodynamics SB RAS
630090, Novosibirsk, Russia

Abstract

The numerical model of axisymmetric swirling turbulent wakes is presented. This model is based on averaged equations for the motion, incompressibility, normal Reynolds stresses transfer and algebraic relations for determination of shear stresses. The results of computations are in a good agreement with experimental data.

The present study is dedicated to formulation of a mathematical model describing the decay of free swirling turbulent flows. The model is implemented to the problem of numerical simulation of decay of axisymmetric wake having zero total excess momentum and non-zero angular momentum conditioned by swirling motion in the wake. The wake of this type is observed for example in the wake past a body having a screw propeller and moving at constant forward speed. The momentumless wake with non-zero swirling past a slender axisymmetric body has been analysed numerically using a simplified e–model of turbulence [1, 2]. The critical review of above-mentioned and some successive works may be found in [3]. The self-similar solutions for swirling wake behind a self-propelled body have been analytically and numerically obtained in [4] based on classic $e - \varepsilon$–model.

Below presented are the results of computations using the semi-empirical turbulence model including averaged equations for motion combined with differential transport equations for normal Reynolds stresses. One component of shear stress is obtained as a solution of differential equation while the other components are calculated using the non-equilibrium algebraic approximations. The comparison of experimental and numerical data is presented.

1. To describe the flow the following system of averaged equations for the motion and continuity in the thin shear layer approximation is used

$$U\frac{\partial U}{\partial x} + V\frac{\partial U}{\partial r} = -\frac{1}{r}\frac{\partial}{\partial r}r < u'v' > +\frac{\partial}{\partial x}\int_{r}^{\infty}\frac{[W^2 + (< w'^2 > - < v'^2 >)]}{r}dr-$$

$$-\frac{\partial(< u'^2 > - < v'^2 >)}{\partial x}, \tag{1}$$

$$U\frac{\partial W}{\partial x} + V\frac{\partial W}{\partial r} + \frac{VW}{r} = -\frac{1}{r}\frac{\partial}{\partial r}r < v'w' > - \frac{< v'w' >}{r}, \tag{2}$$

$$\frac{\partial U}{\partial x} + \frac{\partial V}{\partial r} + \frac{V}{r} = 0. \tag{3}$$

Here x, r, φ—is cylindrrical coordinate system with the origin at the trailing edge of the body; x –axis is directed opposite to the direction of the body motion; U, V, W, u', v', w' — are relevant velocity components of averaged and fluctuating motion; $< u'^2 >$, $< v'^2 >$, $< w'^2 >$, $< u'v' >$, $< u'w' >$, $< v'w' >$ — Reynolds stresses; the symbol $<>$ denotes the averaging. In the right-hand sides of Eqs. (1), (2) the terms containing co-factor in the form of the coefficient of the laminar viscosity have been omitted under assumption of their smallness.

Closed mathematical model includes the following equations [5, 6] for determination of Reynolds stresses in addition to Eqs. (1)–(3)

$$U\frac{\partial < u'^2 >}{\partial x} + V\frac{\partial < u'^2 >}{\partial r} = -2(1-\alpha) < u'v' > \frac{\partial U}{\partial r} - \frac{2}{3}\varepsilon - C_1\frac{\varepsilon}{e}\left(< u'^2 > -\frac{2}{3}e\right) +$$
$$+\frac{2}{3}\alpha P + \frac{C_s}{r}\frac{\partial}{\partial r}\left(\frac{re < v'^2 >}{\varepsilon}\frac{\partial < u'^2 >}{\partial r}\right), \tag{4}$$

$$U\frac{\partial < v'^2 >}{\partial x} + V\frac{\partial < v'^2 >}{\partial r} - 2\frac{W}{r} < v'w' > = 2(1-\alpha) < v'w' > \frac{W}{r} - \frac{2}{3}\varepsilon - C_1\frac{\varepsilon}{e}\left(< v'^2 > -\frac{2}{3}e\right) +$$
$$+\frac{C_s}{r}\frac{\partial}{\partial r}\left[\frac{re}{\varepsilon}\left(< v'^2 > \frac{\partial < v'^2 >}{\partial r} - \frac{2< v'w' >^2}{r}\right)\right] -$$
$$-\frac{2C_s e}{r\varepsilon}\left[< v'w' > \frac{\partial < v'w' >}{\partial r} + < w'^2 > \frac{(< v'^2 > - < w'^2 >)}{r}\right] + \frac{2}{3}\alpha P, \tag{5}$$

$$U\frac{\partial < w'^2 >}{\partial x} + V\frac{\partial < w'^2 >}{\partial r} + 2\frac{W}{r} < v'w' > = -2(1-\alpha) < v'w' > \frac{\partial W}{\partial r} - \frac{2}{3}\varepsilon -$$
$$-C_1\frac{\varepsilon}{e}\left(< w'^2 > -\frac{2}{3}e\right) + \frac{C_s}{r}\frac{\partial}{\partial r}\left[\frac{re}{\varepsilon}\left(< v'^2 > \frac{\partial < w'^2 >}{\partial r} + \frac{2< v'w' >^2}{r}\right)\right] +$$
$$+\frac{2C_s e}{r\varepsilon}\left[< v'w' > \frac{\partial < v'w' >}{\partial r} + < w'^2 > \frac{(< v'^2 > - < w'^2 >)}{r}\right] + \frac{2}{3}\alpha P, \tag{6}$$

$$U\frac{\partial < u'v' >}{\partial x} + V\frac{\partial < u'v' >}{\partial r} - \frac{W}{r} < u'w' > = -(1-\alpha) < v'^2 > \frac{\partial U}{\partial r} - C_1\frac{\varepsilon}{e} < u'v' > +$$
$$+\frac{C_s}{r}\frac{\partial}{\partial r}\left[\frac{re}{\varepsilon}\left(< v'^2 > \frac{\partial < u'v' >}{\partial r} - \frac{< v'w' >< u'w' >}{r}\right)\right] -$$

$$-\frac{C_s e}{r\varepsilon}\left[<v'w'>\frac{\partial<u'w'>}{\partial r}+<w'^2>\frac{<u'v'>}{r}\right], \tag{7}$$

$$<u'w'>=\alpha_1\left(<u'v'>\frac{\partial W}{\partial r}+<v'w'>\frac{\partial V}{\partial r}\right), \tag{8}$$

$$<v'w'>=\alpha_1\left(<v'^2>r\frac{\partial}{\partial r}(W/r)+\frac{W}{r}(<v'^2>-<w'^2>)\right). \tag{9}$$

Here $\alpha_1=-\lambda\frac{e}{\varepsilon}, \lambda=\frac{1-C_2}{C_1+P/\varepsilon-1}$.

The energy balance equation is the consequence of normall stress transfer equations (4)-(6)

$$U\frac{\partial e}{\partial x}+V\frac{\partial e}{\partial r}=\frac{C_s}{r}\frac{\partial}{\partial r}\left(\frac{re<v'^2>}{\varepsilon}\frac{\partial e}{\partial r}\right)+P-\varepsilon, \tag{10}$$

To determine the values of the rate of dissipation ε we make use of the relevant differential equation

$$U\frac{\partial\varepsilon}{\partial x}+V\frac{\partial\varepsilon}{\partial r}=\frac{C_\varepsilon}{r}\frac{\partial}{\partial r}\left(\frac{re<v'^2>}{\varepsilon}\frac{\partial\varepsilon}{\partial r}\right)+\frac{\varepsilon}{e}(C_{\varepsilon1}P-C_{\varepsilon2}\varepsilon). \tag{11}$$

The value P is the energy production caused by averaged motion

$$P=-\left(<u'v'>\frac{\partial U}{\partial r}+<v'w'>r\frac{\partial(W/r)}{\partial r}\right).$$

The quantities C_s, C_ε, α, C_1, C_2, σ_ε, $C_{\varepsilon1}$, $C_{\varepsilon2}$ are empirical constants. Their values are taken to be equal 0.22, 0.17, 0.93, 0.6, 2.2, 1.3, 1.45, 1.92.

The problem variables can be made dimensionless by using the characteristic length D (the body diameter) and the velocity scale U_0. At a distance $x=x_0$ from the body the initial conditions for $U, W, <u'_i u'_j>, \varepsilon$, are specified as functions consistent with the experimental data. At $r\to\infty$ the free stream conditions are specified, the boundary values at $r=0$ are determined from conditions of symmetry for functions U, $<u'^2>$, $<v'^2>$, $<w'^2>$, $<v'w'>$, ε and antisymmetry for W, V, $<u'v'>$, $<u'w'>$.

2. The algorithm of the problem solution is similar to presented in [7]. Beforehand the equations of model were reduced to conservative form in which the laws of momentum and angular momentum are a consequence of the integration of equations (1), (2) over the total cross section of the wake. Finite difference approximations of equations and boundary conditions conservative with respect to these laws have been constructed. Numerical algorithm testing was performed using Loitsiansky asymptotic solution of the problem of laminar submerged swirling jet degeneration.

3. The experimental data used for comparison with numerical results have been obtained in the wake past the sphere of diameter $D=25$ mm. The hydrodynamic resistance of the sphere was balanced by momentum of the swirling jet issued at its rear end. The experiments were carried out in a wind tunnel. The sphere was placed in uniform air flow having the velocity $U_0=15.2$ m/sec. Three components of velocity and all components

of the Reynolds stress tensor were measured by hot-wire anemometer using the technique of probe orientation along the vector of mean velocity. The experimental conditions, technique and obtained results are presented in more detail in [8].

4. The results of calculations are presented below. At a distance $x = 10D$ the initial values were specified using experimental data. For the sake of simplicity the computations were performed on uniform stationary grids. The selection of grid parameters was performed in numerical experiments so that simultaneous twofold decrease of the values of grid steps in variables r, x led to deviations which did not exceed 2 % in uniform norm.

Normalized mean velocity defect profiles $U_1 = U - U_0$ and tangential velocity component W are presented in Fig. 1 a,b. Profiles of Reynolds shear stresses $< u'v' >$, $< v'w' >$ are plotted in Fig. 2 a,b. The results of numerical analysis are denoted by solid curves, points correspond to experimental data which are presented for distances $x/D = 20, 50, 100$.
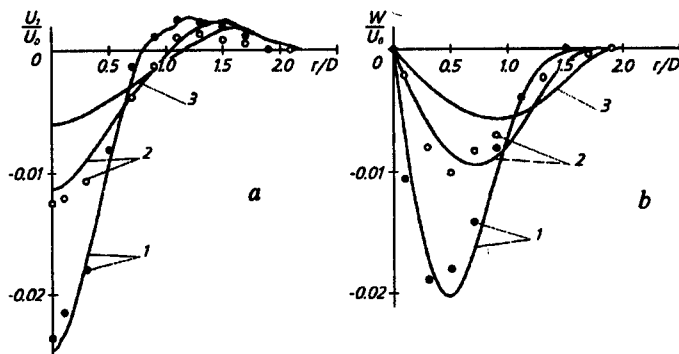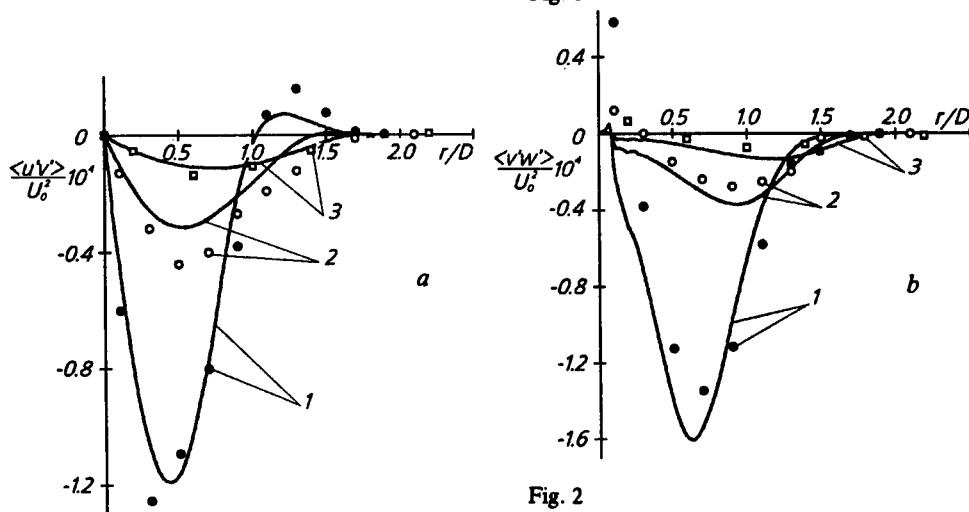

Fig. 1

Fig. 2

Figure 3 shows decay of centerline values of velocity deficit U_{10}, maximum axial turbulence intensity σ_u^0 (values σ_u^0, σ_v^0, σ_w^0 are practically identical), half-width $r_{1/2}/D$ (which is defined from relation $\sigma_u(x, r_{1/2}) = \sigma_u(x, 0)/2$), maximum value of tangential

velocity component $|W|_{max}/U_0$ as functions of the axial distance x/D. As shown in these Figs. results of numerical modelling (solid curves) are in satisfactory agreement with experimental data (markers).

The present research has been supported by Russian Foundation of Basic Research (grants No 95-01-00910, 95-01-01339).
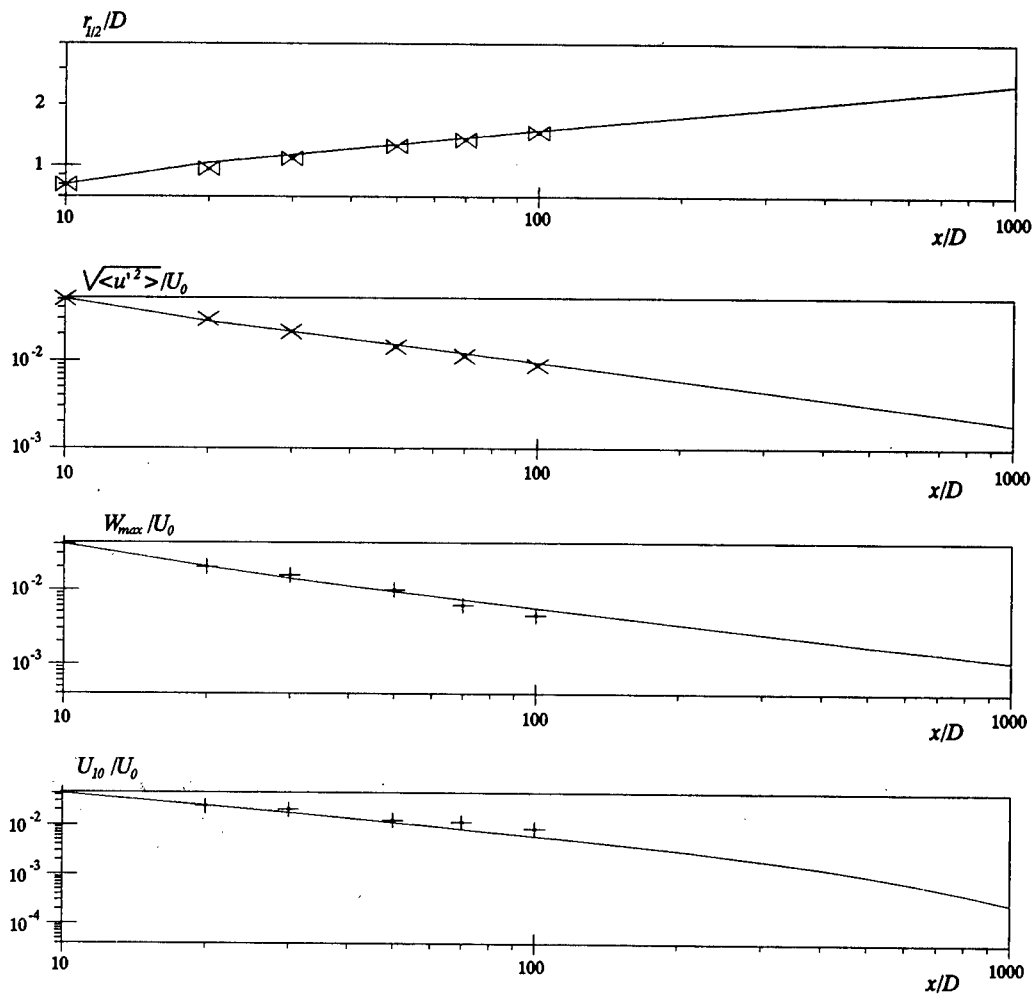

Fig. 3

REFERENCES

1. Schetz J.A., Favin S. Numerical solution for the near wake of a body with propeller // J. Hydronautics — 1977.— Vol.11, No.10.— P.136–141.

2. Schetz J.A., Favin S. Numerical solution of a body-propeller combination including swirl and comparison with data // J. Hydronautics — 1979.— Vol.13, No.4.— P.46-51.

3. Schetz J.A. Injection and mixing in turbulent flow //   Progress in astronautics and aeronautics.— Vol.68 (Ed. by M. Summerfield). New York University, 1980.

4. Gumilevskii A.G. Self-similarity and decay laws in wakes with momentum and angular momentum compensation // Izv. Rus. Acad. Nauk, Ser. Mechan. Zidkosti i Gaza.- 1993. —No.5. — P.35-41 (in Russian).

5. Launder B. E., Morse A. Numerical prediction of axisymmetric free shear flows with a second-order Reynolds stress closure //   Turbulent Shear Flows 1 (Ed. by F. Durst, B.E. Launder, F.W. Schmidt, J.H. Whitelaw). Berlin: Springer, 1979.

6. Sharif M.A., Wong J.K.E. Evaluation of the performance of three turbulence closure models in the prediction of confined swirling flows // Computers and Fluids. —1995. — Vol.24, No.1. — P.81-100.

7. Chernykh G.G., Demenkov A.G. On numerical simulation of jet flows of viscous incompressible fluids // Russian Journal of Numerical Analysis and Mathematical Modelling.— 1997. — Vol. 12, No.2. — P.111-125.

8. Kostomakha V.A., Lesnova N.V. Turbulent swirling wake behind a sphere with complete or partial drag compensation // J. of Appl. Mech. and Tech. Phys. — 1995. — Vol.36, No.2. — P.226-233.

SIMULATION OF FLIGHT CONDITIONS FOR SPACE PROBES IN MARTIAN ATMOSPHERE IN U-21 TRANSONIC WIND TUNNEL

V.A. Kozlovskii, V.I. Lapygin, Yu.M. Lipnitski, A.S. Merkishin, K.A. Stekenius

(TSNIIMASH, 4 Pionerskaya St., Korolev 141070, Moscow region, RUSSIA)

The peculiarity of simulating conditions for a space vehicle flight in rarefied Martian atmosphere is the necessity to obtain rather low Reynolds number. As an example Fig.1 presents Mach number plotted against Reynolds number Re_D for possible descent trajectories of the probe-penetrator landing on the planet surface, the penetrator is intended to investigate the planet ground. The main similarity criterion respectively to static aerodynamic characteristics at subsonic portion of the probe descent trajectory (before landing) is Reynolds number $Re_D=\rho VD/\mu$, where ρ, V, μ are undisturbed flow density, velocity and dynamic viscosity coefficient, correspondingly, and D- the vehicle diameter.

Linear dimension D has usually upper - defined by conditions of acceptable flow blockage by the model, and lower - defined by in-model arrangement of required measuring means and geometric similarity with the real vehicle , bounds . Therefore due to limitations imposed on the model minimum size it is necessary to tests models in a flow with low density ρ in order to obtain low Reynolds number Re_D. Herewith it is required to take into consideration that when unsteady aerodynamic characteristics are examined using dynamically similar models, the density value ρ is also imposed on by restrictions in order to provide required value of Strouhal value Sh and Newton value Ne_2 which are similarity criteria for the vehicle oscillation motion with respect to its centre of mass. It is seen from the relations Sh = $[(\pi/8m_z{}^\alpha Ne_2]^{1/2}= [(\pi/8m_z{}^\alpha(\rho D5/I_z]^{1/2}$, here $m_z{}^\alpha$ and I_z are pitch moment coefficient with respect to the angle of attack, a characteristic of the vehicle static longitudinal stability , and moment of inertia with respect to the vehicle/model transverse axis Z, correspondingly.

Thus working flow density ρ and total pressure P_o are selected in such a way that required values of similarity criteria Re_D and Sh are provided at the same time taking into account probable linear dimension D of the model.

Specifications of U-21 large-scale transonic wind tunnel (Aerogasdynamic Centre, TSNIIMash) are in substantial compliance with the above conditions in case of simulating a vehicle flight in the Mars atmosphere at transonic and subsonic velocity. The cross section of the wind tunnel working section is 1.4×1.4 m, where flows are provided at Mach number M = 0.2...1.4 and 1.8. U-21 wind tunnel may operate using pressure ejector with exhaust into atmosphere (open scheme), and also with the help of turbo-exhauster system (semi-closed or closed circle).

The diagram "M-Re_1" for U-21 wind tunnel is shown in Fig.2, here Reynolds number is based on reference linear dimension L=1m. Regions of working parameters have the following bounds:

A - the upper bound for Re_1 based on the conditions of sufficient safety margin for the structure of the wind tunnel units and efficiency of pressure ejector operation (Re_1=4·10^7...1.1·10^8);

B - the lower bound for Re_1 when the tunnel operates with exhaust into atmosphere (Re_1=5·10^6...3·10^7);

D - the upper bound for Re_1 basing on turbo-exhauster system operation regime (Re_1=8·10^6...2·10^7);
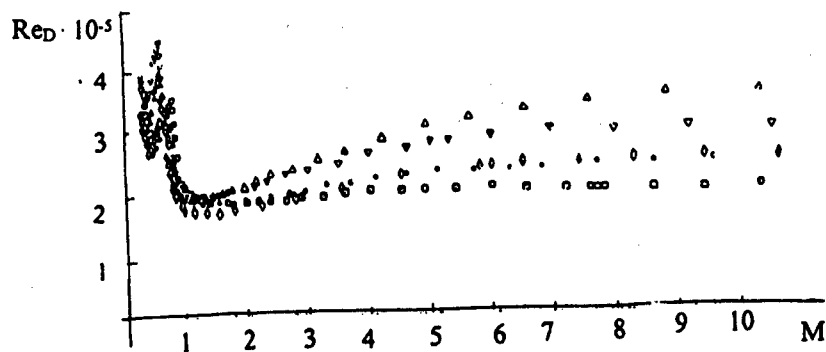
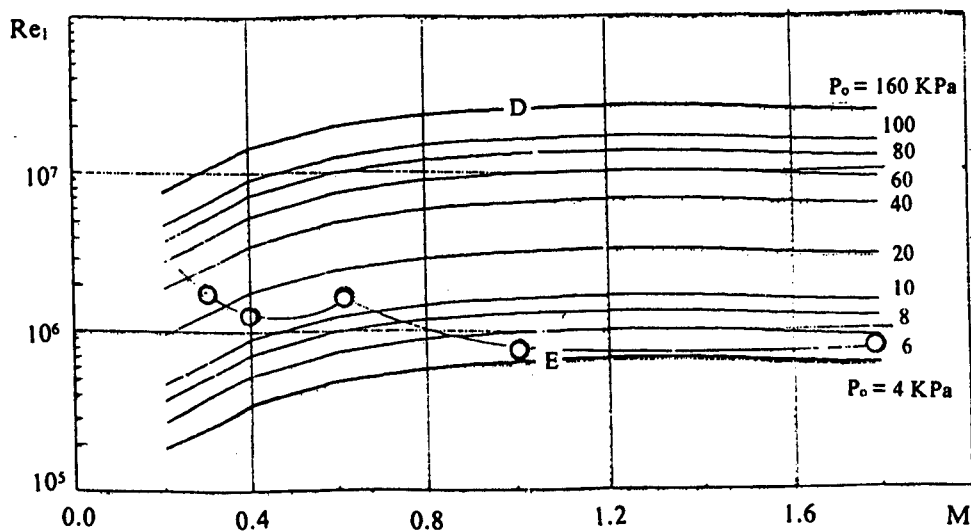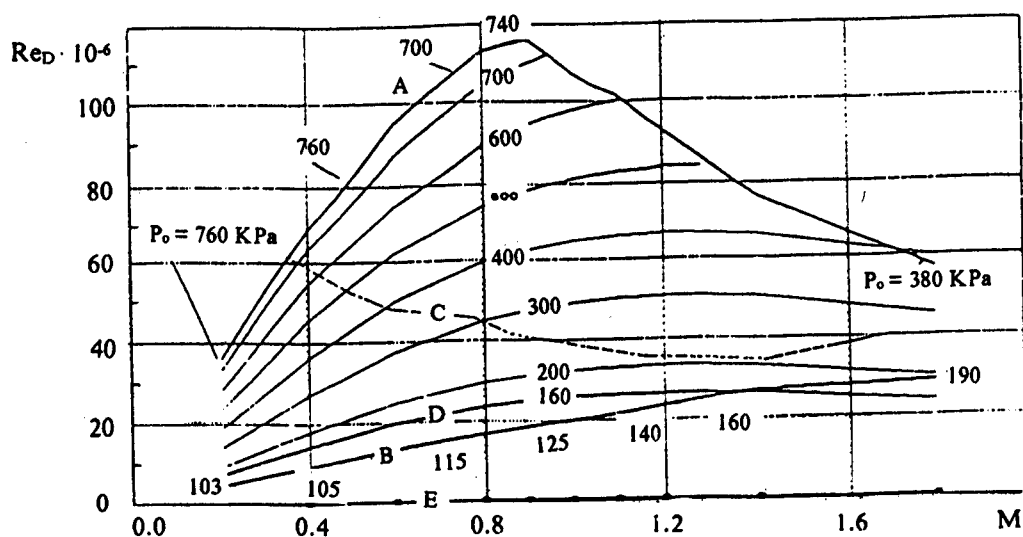Fig.1. Mach number and Reynolds number for the penetrator flight trajectory

Fig.2. Simulation parameters of U-21 wind tunnel

119

E - the lower bound for Re_1 provided by turbo-exhauster system ($Re_1 = 2 \cdot 10^5 ... 6 \cdot 10^5$).

Fig.2 illustrates also Mach number and Reynolds number for Martian probe-penetrator flight trajectory (see Fig.1) reduced to the reference length 1m. The values of indicated simulation criteria for Martian probe lay in the region of U-21 working parameters provided by operation with the turbo-exhauster system. That is why U-21 wind tunnel was chosen for final aerodynamic development of Martian-probe-penetrator configuration.

Initial configuration for such testing was determined in Lavochkin Association (Khimky, Russia) during the probe design. As a result of the probe aerodynamic testing it was required to find the modification of initial shape which corresponds to the conditions for reliable penetration of the probe nose needle-like part into the planet ground. For this purpose at subsonic portion of flight trajectory near the planet surface the penetrator has to possess drag coefficient $C_x \geq 0.82$ and oscillation amplitude A not more than 5°.

Fig.3 illustrates the probe initial shape (Variant 1) and some of its examined modifications (variants 2, 3-5, 6-9). The initial configuration includes needle-like nose part, conical central and toroidal base parts, and base toroid is set on 8 cylindrical inclined pillars placed in meridian planes. Windows (ducts) are between the pillars of the initial configuration.

Investigation of the model for testing the probe static and unsteady aerodynamic characteristics which satisfies all above conditions of aerodynamic simulation had shown that for such off-beat initial configuration the diameter of the model torus is D = 250 mm. The model is 1:15 scaled.

The nose and partially central conical parts of the model are manufactured from aluminium alloy. The most part of the central part, toroidal base part and pillars are manufactured from a hard foam, and the base and pillars are reinforced by aluminium plates according to a special force scheme. The model structure includes mounting of balancing loads from different materials, wolfram alloy among them.

General results of experimental investigation of static characteristics for various modifications of the probe-penetrator using the balance technique are presented in Fig.4 as plots with drag coefficient C_x and stability factor m_z^α for examined configurations. Comparative tests with initial and chosen modifications were carried out at low flight and moderate values of Reynolds number. Some intermediate tests were carried out with moderate Re_D only, because it requires economic operation regime of U-21 wind tunnel.

Drag coefficient for initial configuration (Variant1) is equal to 0.63 at moderate $Re_D = 1.4 \cdot 10^6$, and at low flight value $Re_D = 2.6 \cdot 10^5$ it is equal to 0.77, that is significantly lower than required value 0.82 (Fig.4.)

At the same time tests with dynamically similar model using free oscillation technique have shown that the probe initial configuration is dynamically unstable in the vicinity of zero angle of attack. Anti-damping coefficient and amplitude of self-excited oscillations realised in flight depend essentially on Reynolds number. Self-excited oscillations amplitude increases when Reynolds number decreases and reaches the value $A_o = 10°$ at flight value $Re_D = 2.6 \cdot 10^5$, it is significantly higher than admissible level (Fig.5).

Flexible strips connected to the torus by their front ends (Variant 2) allow to rise C_x and m_z^α, but efficiency of the strips with acceptable length is not sufficient (Fig.4). Besides, free oscillating strips (due to their chaotic motion with an extent span) may influence negatively on oscillation amplitude of the vehicle body,

The more effective mean for rising C_x coefficient is something like strip parachute when downstream ends of the strips are connected to one ring (Fig.3, Variants 3-5). The strips have a shape of parachute canopy in the flow. Tests have shown that free strips (Variant 2) and

$l_3 = l_3/D$
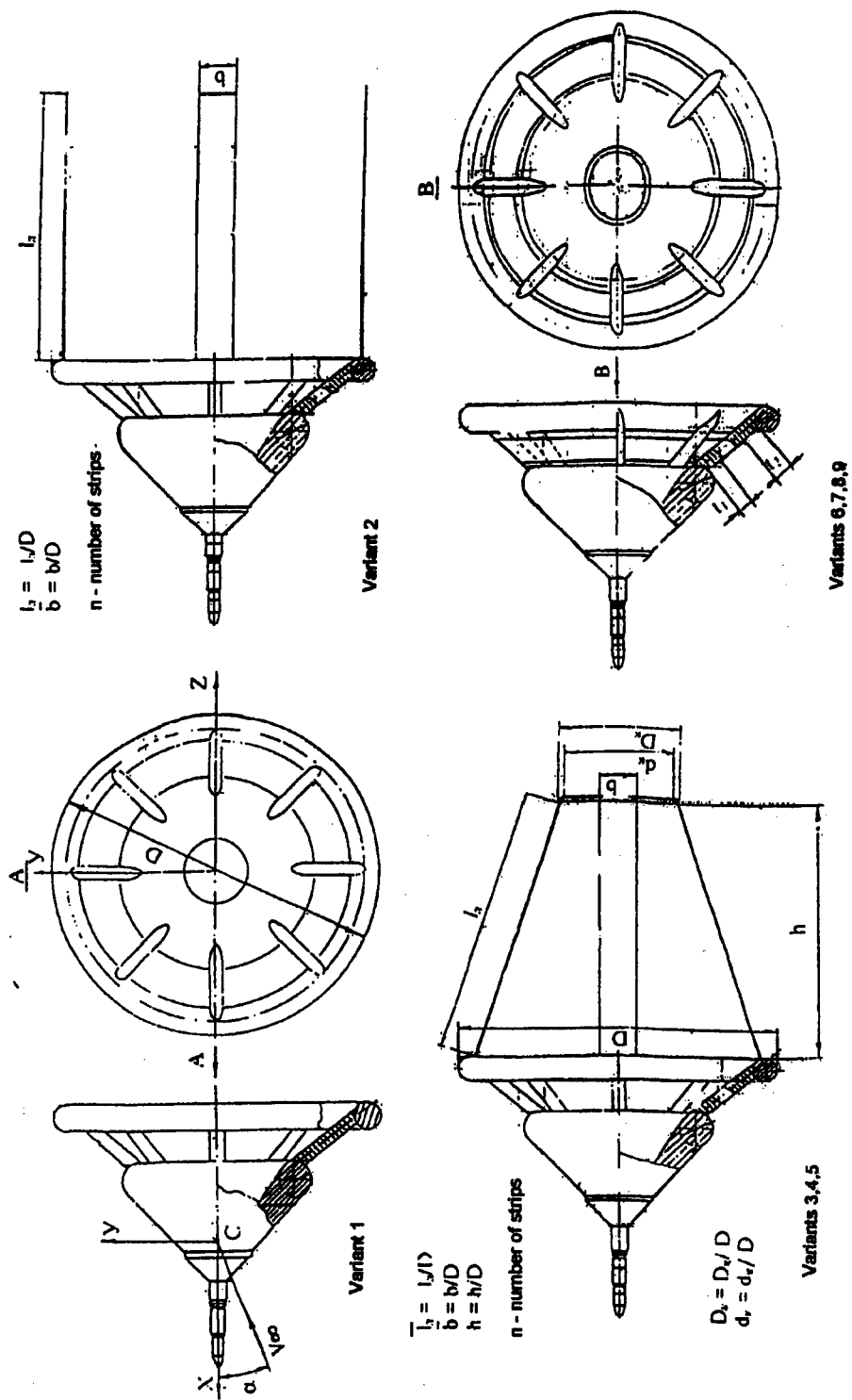$b = b/D$

n - number of strips

Variant 2

$\overline{l_3} = l_3/l$
$b = b/D$
$h = h/D$

n - number of strips

Variant 1

$D_x = D_x/D$
$d_r = d_r/D$

Variants 3,4,5

Variants 6,7,8,9

Fig.3. Modification of the penetrator - Martian probe shape.

121

$M\infty = 0.52$

C_i 1.0

0.9

0.8

0.7

0.6

0.5

Re D · 10⁻⁵

13.69   13.69
    13.68   2.69
        13.69
    2.33   13.69
2.58   13.61   13.61
    13.61
13.68

$-m_z^\alpha$

0.008

0.006

0.004

0.002

0.000

13.68   13.69
    13.69   Re D · 10⁻⁵
2.33   13.64
13.68   13.64   2.69
    13.69
2.59

| 1 | 2 free strips | 3 strip-like | 4 | 5 parachute | 6 | 7 circular partition | 8 | 9 | number of variants |

initial shape

| $I_n = 1$ n = 1 | | $I_n = 0.9$ n = 1 | $I_n = 0.52$ n = 1 | $I_n = 0.35$ n = 8 | $\bar{S}_n = 0.13$ | $\bar{S}_n = 0.06$ | $\bar{S}_n = 0$ | $\bar{S}_n = 0$ |
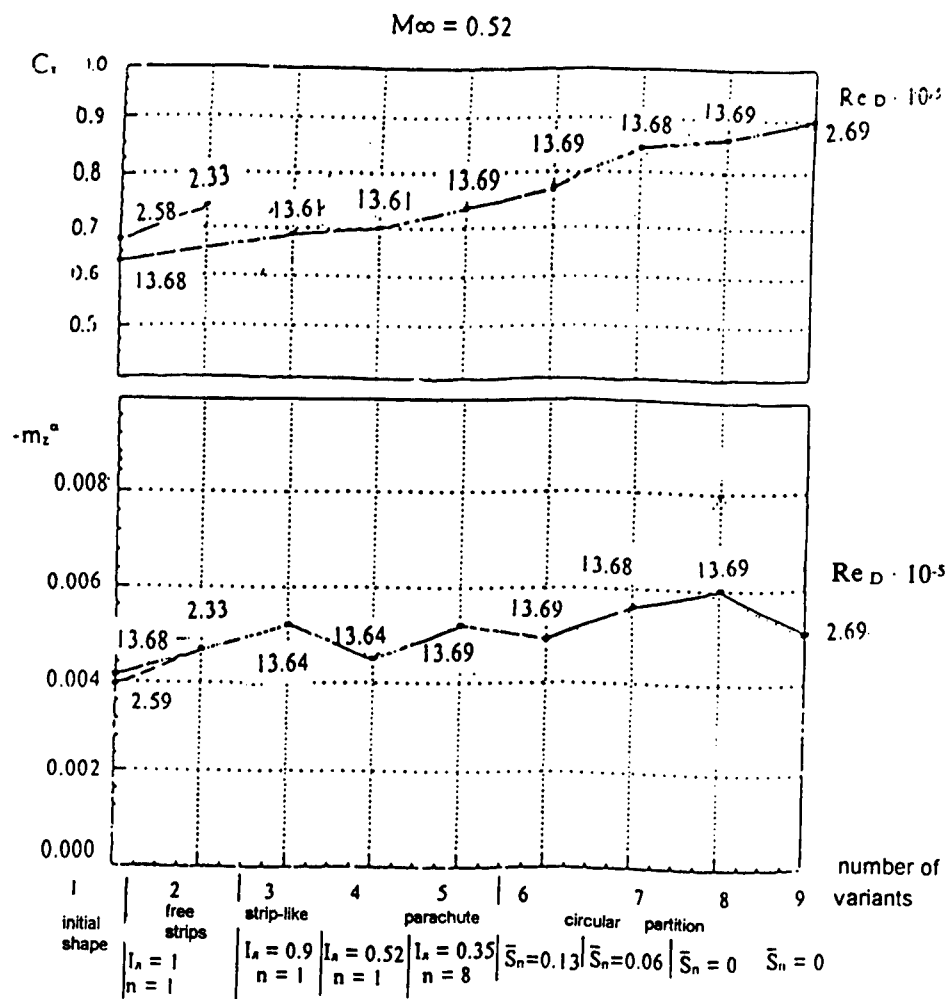
Fig. 4. Static aerodynamic characteristics of the probe - penetrator

A_o

O – $M\infty = 0.3$

● – $M\infty = 0.5$

10

5

1.5   2.0   2.5   3.0   3.5   4.0   4.5   5.0
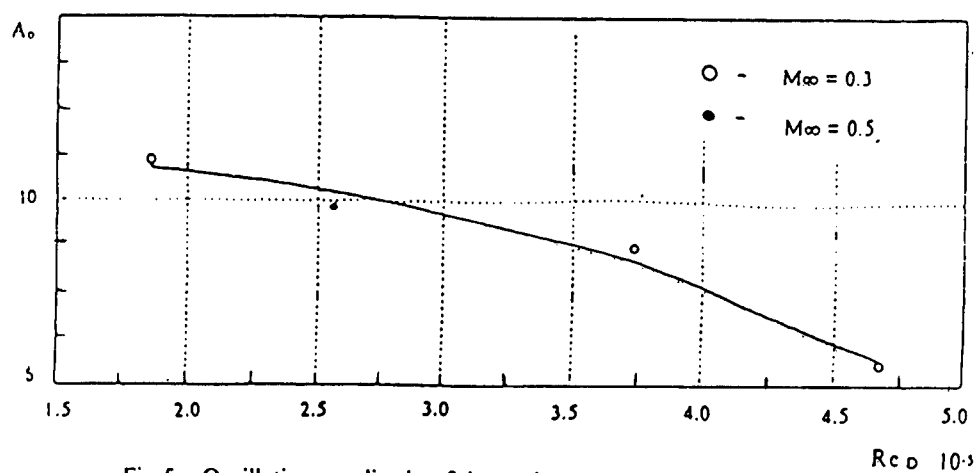
Re D 10⁻⁵

Fig.5. Oscillation amplitude of the probe - penetrator

122

strips parachute with the same strip length (Variant 3) provide practically the same growth of the probe drag (Fig.4). When the strip length is reduced and also if their number is increased (Variants 4,5) C_x coefficient increases noticeably (the effects of free strips reduced length and reduced number of strips in the parachute are the contrary). But strip parachute with acceptable geometrical parameters does not provide yet the required value $C_x \geq 0.82$, and its compact folding inside the probe (while the probe flights from the planet to planet) is difficult.

The testing of the strip parachute (Variant 5) has shown that blockage of the windows between the pillars may cause rise of the drag with no negative consequences with respect to the vehicle stability (Fig.4). Taking this fact into account, the probe modification with circular partitions on pillars which blockage at some or another degree the windows between the pillars was examined (Fig.3., Variants 6-9). The tests have shown that C_x coefficient increases with increasing covered area of the windows between the pillars, and decrease of integral area of the duct to 6% of the probe midsection area (Variant 7) and less (variant 8) provides the rise of drag coefficient C_x up to required value $C_x > 0.82$ (Fig.4, Variants 6-8). A degree of the probe static stability m_z^α increases in this case too (Fig.4).

Next tests were intended to determine static and unsteady characteristics for the penetrator with the windows between the pillars covered completely at low flight Reynolds number. In order to provide required Strouhal value the circular partition was made from a light parachute silk. Tests have shown that if Reynolds number Re_D is reduced to $\sim 2.7 \cdot 10^5$, the probe drag increases more, and stability factor m_z^α falls, but is still acceptable (Fig.4, Variant 9). After placing circular partition self-excited oscillation amplitude at Reynolds number closed to its flight value was reduced to admissible level and for examined range of the flow parameters (M=0.38...0.69) didn't exceed A_o=5...5.6°.

Thus U-21 large-scale variable density sub- and transonic wind tunnel provides simulation of the conditions for the vehicle flight trajectory in rarefied Martian atmosphere. Therefore modifications of Martian probe-penetrator were investigated in U-21 wind tunnel and one with required aerodynamic characteristics was found. It was the configuration with closed windows between the pillars which was realised as a structure of the real Martian probe-penetrator.

NUMERICAL ANALYSIS OF THE PROCESSES OF SHOCK IGNITION AND WAVE-EVOLUTION OF HETEROGENEOUS COMBUSTION IN A NONUNIFORM UNITYFUEL IN DISPERSION LAYER

A.G. Kutushev, S.P. Rodionov
Tyumen division of Institute of Theoretical and Applied Mechanics SB RAS
625000, Tyumen, Russia

One-dimensional detonation waves evolution in mono- and polydispersed gas suspension of unitary (oxide containing) fuel were considered in [1, 2]. Critical conditions of detonation wave initiation by impulse impact on reactive dispersed media are established in [3]. Present work is devoted to the numerical analysis of two-dimensional problem of shock ignition of detonation in square void part of which is filled by propellant suspension layer.

Two-dimensional nonstationary flow of reactive mixture is described by the following equation set [4]

$$\frac{\partial \rho_{1k}}{\partial t} + \frac{\partial \rho_{1k} v_{1x}}{\partial x} + \frac{\partial \rho_{1k} v_{1y}}{\partial y} = (k-1)J, \quad \rho_1 = \sum_{k=1}^{2} \rho_{1k},$$

$$\frac{\partial \rho_2}{\partial t} + \frac{\partial \rho_2 v_{2x}}{\partial x} + \frac{\partial \rho_2 v_{2y}}{\partial y} = -J, \quad \frac{\partial n}{\partial t} + \frac{\partial n v_{2x}}{\partial x} + \frac{\partial n v_{2y}}{\partial y} = 0,$$

$$\frac{\partial \rho_i v_{ix}}{\partial t} + \frac{\partial \rho_i v_{ix} v_{ix}}{\partial x} + \frac{\partial \rho_i v_{ix} v_{iy}}{\partial y} + (2-i)\frac{\partial p}{\partial x} = (-1)^i (F_x - Jv_{2_x}),$$

$$\frac{\partial \rho_i v_{iy}}{\partial t} + \frac{\partial \rho_i v_{iy} v_{ix}}{\partial x} + \frac{\partial \rho_i v_{iy} v_{iy}}{\partial y} + (2-i)\frac{\partial p}{\partial y} = (-1)^i (F_y - Jv_{2_y}),$$

$$\frac{\partial \rho_2 e_2}{\partial t} + \frac{\partial \rho_2 e_2 v_{2x}}{\partial x} + \frac{\partial \rho_2 e_2 v_{2y}}{\partial y} = Q\eta(-J) - Je_2,$$

$$\sum_{i=1}^{2} \left[\frac{\partial \rho_i E_i}{\partial t} + \frac{\partial (\rho_i E_i + \alpha_i p) v_{ix}}{\partial x} + \frac{\partial (\rho_i E_i + \alpha_i p) v_{iy}}{\partial y} \right] = 0,$$

$$\rho_{1k} = \rho_{1k}^0 \alpha_1, \quad \rho_i = \rho_i^0 \alpha_i, \quad \rho_1^0 = \sum_{k=1}^{2} \rho_{1k}^0, \quad E_i = e_i + 0.5 v_i^2,$$

$$v_i^2 = v_{ix}^2 + v_{iy}^2 \quad (i, k = 1, 2), \quad \alpha_2 = \frac{1}{6}\pi d^3 n, \quad \alpha_1 + \alpha_2 = 1.$$

Here subscripts "i" indicates parameters of phases: "$i=1$" gaseous phase, "$i=2$" dispersed phase (particles), index k denotes parameters of gaseous phase component: $k=1$ - inert gas, $k=2$ - gaseous product of burning.

Here ρ_{1k} and ρ_{1k}^0 are reduced and true densities of the k-th component of gaseous phase; ρ_i, ρ_i^0, v_i, α_i, e_i, E_i - are reduced and true densities, velocity, volume concentration, internal and total energy i-th phase ($i=1; 2$) respectively; v_{ix} and v_{iy} - are components of velocity vector v_i; n is number concentration of dispersed particles; d is

diameter of particles; p is pressure in gaseous phase; F_x and F_y are components of interphase interaction force; Q is heat flux between gaseous and dispersed phases; J mass transformation rate.

Equations of phase state, heat and mass transformation are considered and given in [1-4].

The following problem was considered. Long square channel $(0 \leq x < \infty, 0 \leq y \leq Y)$, is filled partially $(x_f < x < \infty, 0 \leq y \leq y_0)$ by gas suspension of monodispersed unitary fuel propellant, the rest of channel is occupied by gas. In the initial moment $t = 0$ the gas in a part of the channel $(0 \leq x \leq x_f, 0 \leq y \leq Y)$ is disturbed by shock wave with linear shape of mass velocity behind the shock. The process of shock wave interaction with the suspension is considered main features of detonation ignition are analysed.

Boundary conditions involve zero normal velocity components the walls.

"Coarse particles" method of numerical calculation is used, one run on IBM PC AT 486 takes ~(1-5) hours of CPU-time. All calculations were performed for the size of initial shock wave $x_f = 0.5$m and channel cross section $Y = 0.2$m. Space distribution of particle concentration was as follows

$$\alpha_2 = \alpha_{20}\left[1 - \eta\left(\frac{x_f - x}{x_f}\right)\right]\eta\left(\frac{y_0 - y}{Y}\right) \quad (0 \leq x < \infty, 0 \leq y \leq Y; y_0 \leq Y),$$

here y_0 - top size of propellant layer.

Increase or damp of particle combustion in gas suspension is determined by relative dispersed phase content $m = \rho_{20}/\rho_{10}$, particle size d_0 and initial shock wave amplitude determined by Mach number - M_0 [4]. Let analyse this effect in the presented problem.

Scheme of problem and formation of damp combustion wave in unitary fuel suspension $(m = 10, d_0 = 30$мкм, $y_0 = Y/2, M_0 = 3.5)$ at $y = 0$ (solid lines), $y/Y = 0.5$ (dashed lines) and $y/Y = 1$ (dash-dot lines) in moments of time $t_i = 3.3 \cdot (2 \, i \, -1)$ ms $(i = 1 \div 3)$ is shown on fig.1. It was established that the shock wave front practically did not move in vertical cross section of the channel. Horisontal movement of shock front slightly decrease from bottom to top of the channel. The reason of this front velocity decrease is explained by different acoustic velocity in gas and suspension.

Evolution of detonation wave in reactive suspension $(m = 10, d_0 = 30$мкм, $y_0 = Y/2)$, initiated by shock wave $(M_0 = 9)$ is presented on fig.2. The highest pressure behind detonation front occurs near the bottom $(y = 0)$. Maximum pressure amplitude drops from bottom to top and approximately constant in the gas region of the channel. Pressure shock wave velocity in gas region larger than detonation wave velocity in the suspension region. Detonation wave propagation is followed by pressure wave configuration caused by reflection front boundaries, inclined front shape and expansion of reaction.

Calculations results on dependence of critical (minimum) Mach number of initial shock wave from initial particle size for relative particle content $m = 5$ and various dispersed phase configuration at $y_0/Y = 1$; 0.75; 0.5 (curves $1 \div 3$) are given on fig.3. Case $y_0/Y = 1$ denotes uniform particle distribution in the whole channel.

Decrease of suspension region size for $m = const$ causes rize of critical Mach number (M_0^*) over value of Mach number for uniform suspension distribution in the whole channel. This tendency increase with particle size rize. This effect may be explained by partial energy impact of initial shock wave on suspension layer nevertheless that surface contact of energy impact is larger than front contact in uniform suspension distribution case.
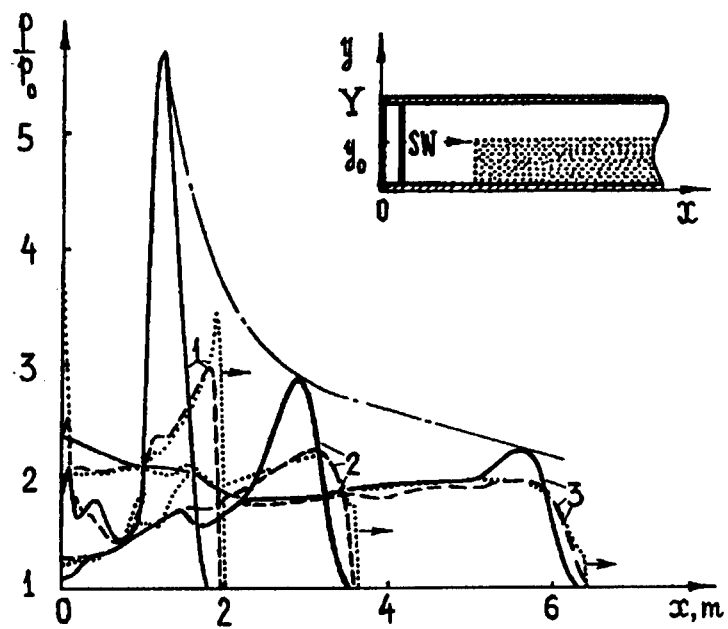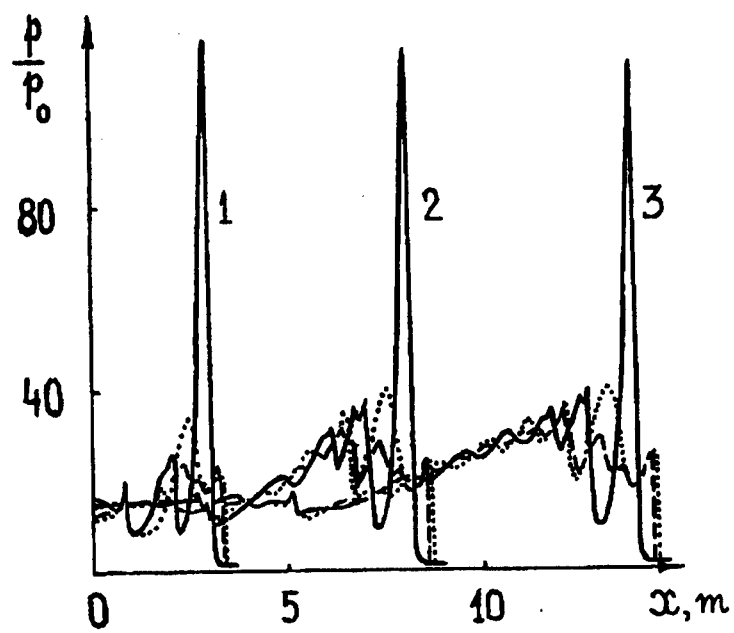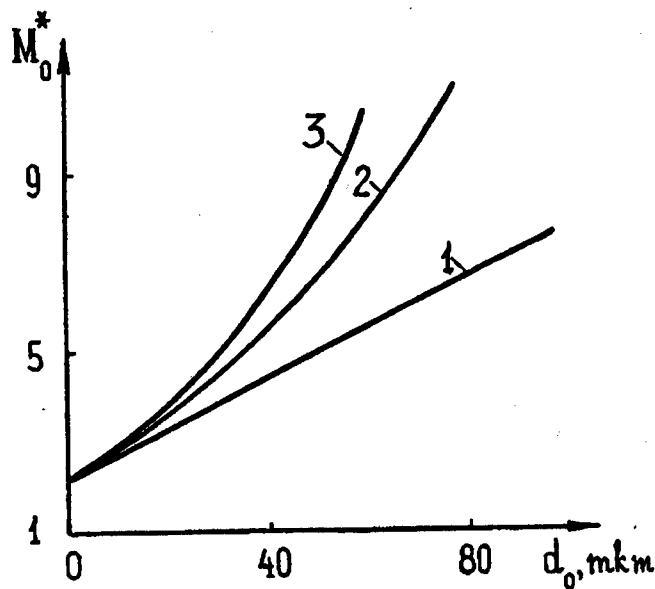
125

Fig.1

Fig.2

Fig.3

The main conclusion of the presented numerical analysis establishes that increase of suspension layer size in square channel causes rize of critical (minimum) Mach number of initial shock wave.

REFERENCES

1. Ivandaev A.I., Kutushev A.G., Rodionov S.P. Formation of heterogeneous detonation due to explosion // FGV. 1995. V.31, No.3. P. 83-91.
2. Ivandaev A.I., Kutushev A.G., Rodionov S.P. Detonation waves in polydispersed gas suspension // PMTF. 1995. V.36, No.6. P. 14-23.
3. Kutushev A.G., Rodionov S.P. Numerical investigation of critical condition of detonation wave formation of unitary fuel gas suspension due to shock initiation // FGV. 1996. V.32, No.4. P. 110-112.
4. Kutushev A.G., Rodionov S.P. Detonation waves in gas suspension with non-uniform distribution of particles concentration // Sterlitamak, 22-25 Sept. 1997, V.3. P.24-25.
5. Belotserkovskii O.M., Davydov Yu.M. Coarse particle method in gas dynamics. Nauka. 1982.

NUMERICAL INVESTIGATION OF INFLUENCE OF LAYER POWDERY MEDIA AND INCIDENT SHOCK WAVE PARAMETERS ON PROCESS OF VARIATION OF PRESSURE ON WALL

A.G. Kutushev, S.P. Rodionov
Tyumen division of Institute of Theoretical and Applied Mechanics SB RAS
625000, Tyumen, Russia

Numerical modelling of the process of sanded layer shielding of shock wave influence at the face of the tube in the frameworks of two-phase sandedmedia with non-linear-elastic equation of state for powder skeleton was fulfilled in the paper [1]. Comparing numerical solutions with experimental data [2] an adequate description of wave process by used mathematical model of powdery medium was shown. In the present paper which logically continues [1] numerical analysis of poured layer parameters influence on the full powder pressure variation at a shielded rigid wall is been fulfilled.

The set of equations of plane one-dimensional nonstationary motion of gas and particles has the following form [1-3]:

$$\frac{\partial \rho_g}{\partial t} + \frac{\partial \rho_g v_g}{\partial x} = 0, \quad \frac{\partial \rho_s}{\partial t} + \frac{\partial \rho_s v_s}{\partial x} = 0,$$

$$\frac{\partial \rho_g v_g}{\partial t} + \frac{\partial \rho_g v_g^2}{\partial x} + \alpha_g \frac{\partial p_g}{\partial x} = -\alpha_g F_{gs}, \quad \frac{\partial \rho_s v_s}{\partial t} + \frac{\partial \rho_s v_s^2}{\partial x} + \alpha_s \frac{\partial p_g}{\partial x} - \frac{\partial \sigma_{s*}^{xx}}{\partial x} = \alpha_g F_{gs},$$

$$\frac{\partial \rho_s e_{sT}}{\partial t} + \frac{\partial \rho_s e_{sT} v_s}{\partial x} - \xi_{sT} \sigma_{s*}^{xx} \frac{\partial v_s}{\partial x} = Q_{gs}, \quad \frac{\partial \rho_s e_{se}}{\partial t} + \frac{\partial \rho_s e_{se} v_s}{\partial x} - (1 - \xi_{sT}) \sigma_{s*}^{xx} \frac{\partial v_s}{\partial x} = 0, \quad (1)$$

$$\frac{\partial (\rho_g E_g + \rho_s E_s)}{\partial t} + \frac{\partial (\rho_g E_g v_g + \rho_s E_s v_s)}{\partial x} + \frac{\partial ((p\alpha_g v_g + p\alpha_s v_s) - \sigma_{s*}^{xx} v_s)}{\partial x} = 0,$$

$$\rho_i = \rho_i^0 \alpha_i, \quad E_i = e_i + 0.5 v_i^2, \quad (i = s, g), \quad \alpha_g + \alpha_s = 1, \quad e_s = e_{sT} + e_{se}.$$

This set of equations represents conservation laws of mass, momentum, energy of dispersed phase and total energy of mixture. Indexes "g" and "s" indicate parameters of gaseous and dispersed phases respectively;. ρ, ρ^0, α, v, e, E - reduced and true densities, volume concentration, velocity, internal and total energy respectively of one or another component of a mixture; p_g - gas pressure; σ_{s*}^{xx} - longitudinal component of "efficient" stress tensor in porous powdery medium, this tensor is determined by a strain of solid particles due to intergranular contacts of particles; F_{gs} and Q_{gs} -drag force and rate of heat transfer to particles; e_{sT} and e_{se} -thermal and elastic components of internal energy of powdery medium; ξ_{sT} .- coefficient defining a share of work of intergranular interaction forces, ($-\sigma_{s*}^{xx} \partial v_s / \partial x$), which responds for heating of powder skeleton ($0 \leq \xi_{sT} \leq 1$).

The set of differential equations is being closed by equations of phases state and lows of interphase interaction [1].
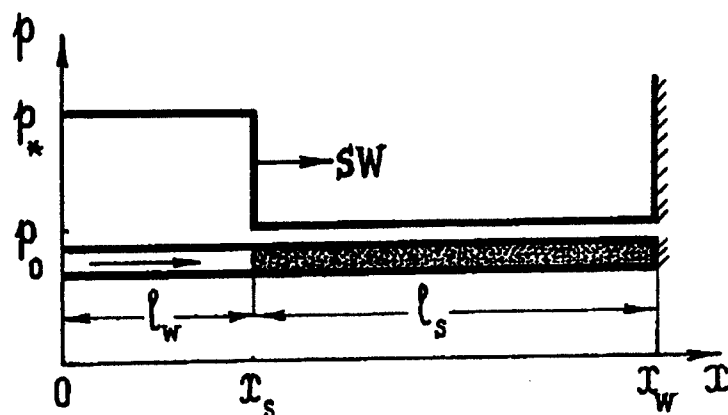
Fig.1

In the frameworks of presented set of equations we consider following problem schematically shown on fig.1. A rectangular form shock wave penetrates from gaseous region into uniform dispersed layer of poured powdery medium with length l_s which shields a rigid nonmoveable wall. The aim of research is investigation of influence of parameters of powdery medium and poured layer on the process of shock wave loading of a rigid wall.

On the left boundary ($x = 0$) we have condition of free flow for gaseous phase and on the right boundary ($x = x_w$) - velocities of gas and particles equal to zero.

"Coarse particle" method was used to receive numerical solution of set of equations of powdery medium motion. It took approx. 10 hours to calculate one variant using IBM PC AT 486. Specifications of air and polistirol particles [1,2] were used in calculations.

Value of pressure of shock wave falling at shielding layer considered to be equal $p_* = 2p_0$. Extension of powdery layer l_s varies in intervals 10 - 40 mm. Volume content and particle diameters of poured medium varies in intervals $0,48 < \alpha_{s0} < 0,7$ and $200 < d < 1000$ mkm. Sound velocity (a_{s0}) in poured powdery medium considered to be 420 m/s. Phase parameters in nondisterbed state correspond to normal atmosphere conditions ($p_0 = 0,1$МПа; $T_0 = 293$ K).

Let's see solutions of numerical simulation. On fig.2. calculated "oscillograms" of full pressure at the obstacle corresponding to the length of poured layer $l_s = 10$ (solid lines), 15 (dashed lines) and 20 (dash-dot lines) mm are shown. Dot lines denote pressure of porous gas. One can see a pulse character of full stress of powdery layer at the wall and monotonous behaviour of gas pressure. Continuous increase of gas pressure at the barrier is determined by process of gas filtration in porous medium. Pulsation width of dispersed phase full pressure (p_Σ) increases with l_s increase. An amplitude of the first maximum of mixture's full pressure also increases while length l_s increase. A growing character of pressure p_Σ variation at the barrier from l_s is determined by the fact that formation of compression wave pressure in powder skeleton occurs in finite time period, and an amplitude of reflection wave in powder is proportional to amplitude of falling wave.

Calculated dependencies of mixture's full pressure at a face of a tube at values of powder particle diameters $d = 200$ (solid lines), 500 (dashed lines) and 1000 (dash-dot lines) mkm are shown on fig.3. Particle sizes and therefore the force of interphase interaction do not influence the amplitude of the first maximum of full pressure at the wall which is determined by
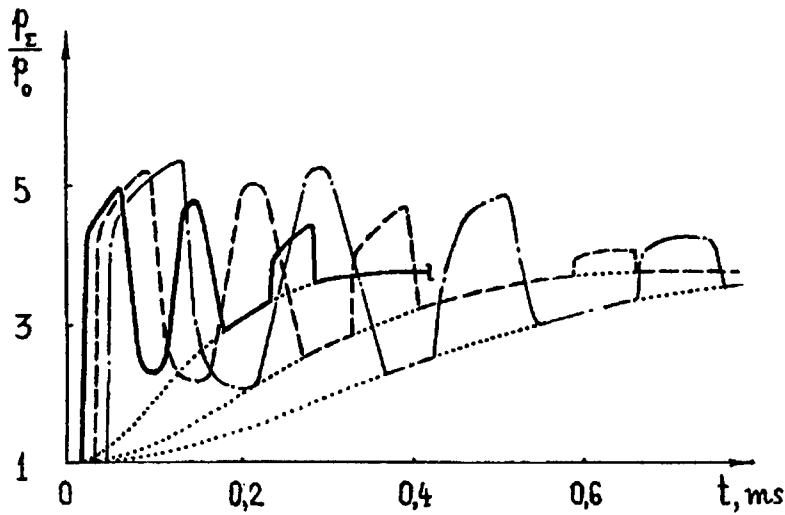
Fig.2

quick (deformation) wave of compression. At the same time a size of dispersed particles influences greatly a slow (filtration) gas pressure wave. Increase of particle size results in more rapid damping of deformation wave induced by orientated infiltrate gas motion in powdery medium.
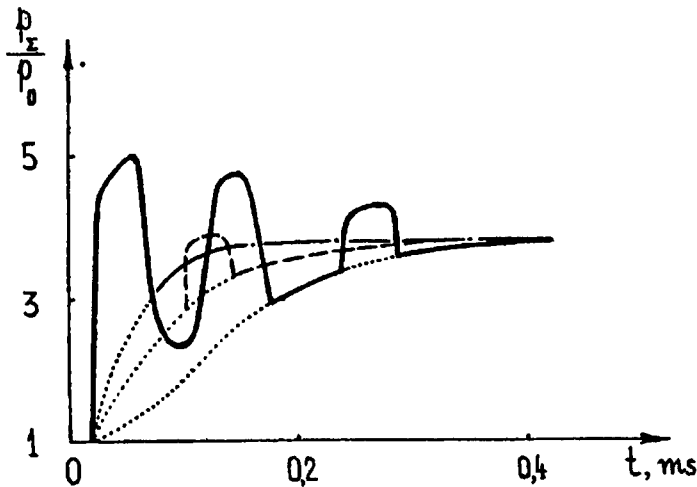

Fig.3

Calculated "oscillograms" of mixture's full pressure at the face of a tube shielded by porous powdery layer with α_{s0}=0,48 (solid lines); 0,6 (dashed lines); 0,7 (dash-dot lines) are shown on fig.4. One can see that α_{s0} increase leads to the increase of the first and posterior amplitudes of maximums p_Σ and to increase of filtration wave duration. This mentioned fact can be explained by the following: an increase of forces acting on the particles of powdery medium occurs with α_{s0} increase, thus increases a share of impulse transferred from gas to

130

disperse phase. The later means that with the growth of α_{s0} an increase of amplitude of deformation wave falling at the wall takes place and therefore increase of reflecting wave amplitude. We can also mentioned the fact of number of p_Σ maximums increase at the wall of a tube.
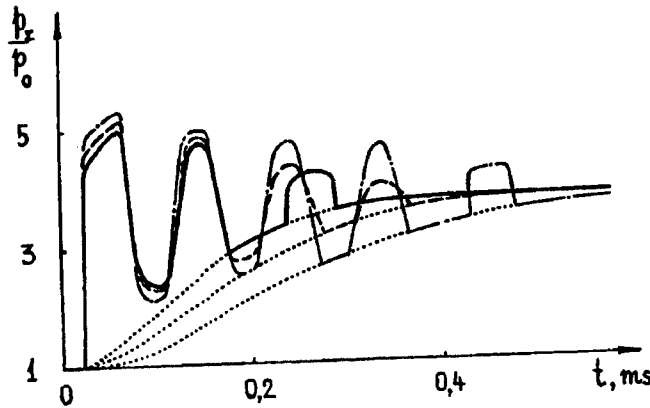

Fig.4

It is convenient to make analysis of above mentioned influence of parameters of poured medium and shielded layer (α_{s0}, d, l_s) on value p_Σ at rigid wall using characteristic times of deformation wave circulation in poured medium (τ_c) and gas filtration in porous layer (τ_f)

$$\tau_c = \frac{2l_s}{a_{s0}}, \quad \tau_f = \frac{l_s^2}{\kappa} = \tau_f^0\left(1 + \frac{1{,}75\alpha_g}{150\alpha_s}\mathrm{Re}_{gs}\right), \tag{2}$$

$$\kappa = \frac{k}{\mu_g}\rho_g^0 a_g^2, \quad k = k_0\left(1 + \frac{1{,}75\alpha_g}{150\alpha_s}\mathrm{Re}_{gs}\right)^{-1}, \quad k_0 = \frac{\alpha_g^2 d^2}{150\alpha_s^2}.$$

Here: κ coefficient of powder permeability; k_0 and τ_f^0 - coefficients of powder permeability and characteristic time of gas filtration with Reynolds number of relative phase motion $\mathrm{Re}_{gs} < 1$; μ_g - gas dynamic viscosity.

It is obvious that ratio of characteristic times (2)

$$n = \frac{\tau_f}{\tau_c} = \frac{l_s a_{s0}}{2\kappa} \quad \left(\kappa \cong \frac{\alpha_g^2 d^2}{\alpha_s^2}\left(1 + \frac{1{,}75\alpha_g}{150\alpha_s}\mathrm{Re}_{gs}\right)^{-1}\right) \tag{3}$$

is quite informative characteristic of filtration influence on the process of impulse transfer from gas to powdery medium particles and full mixtures pressure on walls of a tube. In marginal cases $n \gg 1$ and $n \leq 1$ maximum and minimal impulse transfer of gas in disperse phase takes place. The number of mixture's full pressure maximums on the wall is ~ n and ~ 1. The date of numerical simulation shown on fig.2÷4 satisfies good dependence (3).

The results of numerical simulation allow to make the following conclusions: amplitude of the first maximum of mixture's full pressure on a rigid wall increases with the growth of

131

poured layer length and volume concentration of dispersed phase; size of particles does not influence greatly an amplitude of the first maximum of full pressure at the barrier, but at the same time influence much on the character of posterior maximums damping.

REFERENCES

1. Kutushev A.G., Rudakov D.A. Numerical investigation action of shock wave on wall by powdery medium layer // PMTF. 1993, No.5. P. 25-31.
2. Gelgand B.E., Medvedev S.P., Polenov A.N. et. al. Transmission of shock-wave loading by powdery media // PMTF. 1988, No.2. P.115-121.
3. Akhatov I.Sh., Veinstein P.B. Transmission of combustion of porous propellants in detonation // FGV. 1984. V.20, No.5. P. 8-14.
4. Belotserkovskii O.M., Davydov Yu.M. Coarse particles method in gas dynamics. Nauka. 1982.
5. Kutushev A.G., Rudakov D.A. Mathematical simulation of dynamics loading of porous powdery layer by compressed gas // MM. 1991. V.3, No. P.65-75.

NUMERICAL INVESTIGATION OF PROCESS OF FLOW OF BURNING GAS-PARTICLE SUSPENSION FROM SHOCK TUBE TO FLOOD SPACE

A.G. Kutushev, S.P. Rodionov, V.V. Kutenkov

Tyumen division of Institute of Theoretical and Applied Mechanics SB RAS
625000, Tyumen, Russia

Equations set of differential two-dimensional axisymmetrical nonstationary motion of mixture of gas and particles of the propellant suspension have following form [1]:

$$\frac{\partial \rho_{1k}}{\partial t} + \frac{\partial r \rho_{1k} v_{1r}}{r \partial r} + \frac{\partial \rho_{1k} v_{1z}}{\partial z} = (k-1)J, \quad \rho_1 = \sum_{k=1}^{2} \rho_{1k},$$

$$\frac{\partial \rho_2}{\partial t} + \frac{\partial r \rho_2 v_{2r}}{r \partial r} + \frac{\partial \rho_2 v_{2z}}{\partial z} = -J, \quad \frac{\partial n}{\partial t} + \frac{\partial r n v_{2r}}{r \partial r} + \frac{\partial n v_{2z}}{\partial z} = 0,$$

$$\frac{\partial \rho_i v_{ir}}{\partial t} + \frac{\partial r \rho_i v_{ir} v_{ir}}{r \partial r} + \frac{\partial \rho_i v_{ir} v_{iz}}{\partial z} + (2-i)\frac{\partial p}{\partial r} = (-1)^i (F_r - J v_{2_r}),$$

$$\frac{\partial \rho_i v_{iz}}{\partial t} + \frac{\partial r \rho_i v_{ir} v_{ir}}{r \partial r} + \frac{\partial \rho_i v_{iz} v_{iz}}{\partial z} + (2-i)\frac{\partial p}{\partial z} = (-1)^i (F_z - J v_{2z}), \qquad (1)$$

$$\frac{\partial \rho_2 e_2}{\partial t} + \frac{\partial r \rho_2 e_2 v_{2r}}{r \partial r} + \frac{\partial \rho_2 e_2 v_{2z}}{\partial z} = Q \eta(-J) - J e_2,$$

$$\sum_{i=1}^{2} \left[\frac{\partial \rho_i E_i}{\partial t} + \frac{\partial r (\rho_i E_i + \alpha_i p) v_{ir}}{r \partial r} + \frac{\partial (\rho_i E_i + \alpha_i p) v_{iz}}{\partial z} \right] = 0,$$

$$\rho_{1k} = \rho_{1k}^0 \alpha_1, \quad \rho_i = \rho_i^0 \alpha_i, \quad \rho_1^0 = \sum_{k=1}^{2} \rho_{1k}^0, \quad E_i = e_i + 0.5 v_i^2,$$

$$v_i^2 = v_{ir}^2 + v_{iz}^2 \ (i, k = 1, 2), \quad \alpha_2 = \frac{1}{6}\pi d^3 n, \quad \alpha_1 + \alpha_2 = 1.$$

Here subscripts "i" indicates parameters of phases: "$i=1$" gaseous phase, "$i=2$" dispersed phase (particles), index k denotes parameters of gaseous phase component: $k=1$ - inert gas, $k=2$ - gaseous product of burning.

Here ρ_{1k} and ρ_{1k}^0 are reduced and true densities of the k-th component of gaseous phase; ρ_i, ρ_i^0, v_i, α_i, e_i, E_i - are reduced and true densities, velocity, volume concentration, internal and total energy i-th phase ($i=1$; 2) respectively; v_{ix} and v_{iy} - are components of velocity vector v_i; n is number concentration of dispersed particles; d is diameter of particles; p is pressure in gaseous phase; F_r and F_y are components of interphase interaction force; Q is heat flux between gaseous and dispersed phases; J mass transformation rate; η - Heavyside's function.

Equations of phase state, heat and mass transformation are considered and given in [1-4].

Presentation of the Problem.

There is a horisontal shock tube with diameter D and length L. The left end of the tube ($Z=0$) is clouded, and the right one ($Z=L$) is open. Inside the tube, at a distance $Z=Z^*$ from the clouded and of the tube $Z=0$ there is a partition, dividing chambers of high ($0<Z<Z^*$) and low ($Z^*<Z<L$)

pressures. The chamber of high pressure is filled by uniform gas-particle suspension of the particles of the propellant suspension, and the chamber of low pressure is filled by inert gas. At the time moment $t=0$, particles of the propellant suspension ignate instantly in all the area of the chamber of high pressure. At the time moment $t = t^*$ pressure there reaches its critical point $P=P^*$ at which the partition is burst. The object of the research is to study the process of flow of burning gas-particle suspension from shock tube to flood space. Schematical presentation of the problem is on fig.1.
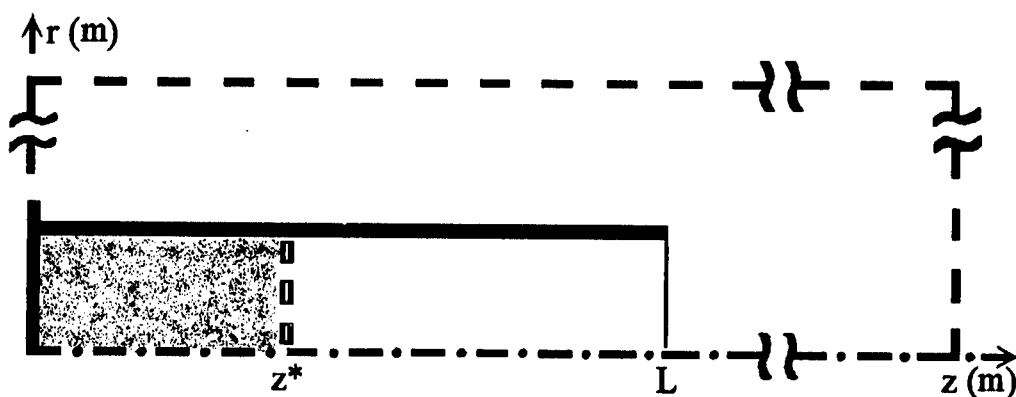

Fig.1

Initial conditions of the problem have the following form: in the chamber of high pressure: $P = P_0$, $T_1 = T^*$, $T_2 = T_s$, $v_1 = v_2 = 0$, $\alpha_1 = \alpha_{10}$, $d = d_0$; in the chamber of low pressure and in flood space: $P = P_0$, $T = T_0$, $v_1 = 0$, $\alpha_1 = 1$.

Boundary conditions are taken as: on the axis of symmetry ($r=0$): $-\dfrac{\partial v_{zi}}{\partial r} = v_{ri} = 0$, ($i=1,2$); on the lateral wall of the tube ($r = 0.5d$, $0 \leq Z \leq L$): $v_{ri}=0$; on the clouded part of the tube ($0 < r < 0.5d$, $Z=0$): $v_{zi}=0$.

The equations of motion of gas-particle suspension were solved by "coarse-particle" method on the grid consisted of 52×102 cells. Time for calculation of one variant on IBM PC AT 486 is about 1-2 hours. The calculations were made for the mixture of air and particles of propellant [1;2].

The results of the calculations.

How of burning gas-particle suspension from the shock tube to flood space is a difficult nonstationary ware process, which can be divided into two phases.

To describe the first phase, it is convenient to apply to "z - t" - wave diagram, corresponded to the scheme of gas particle suspension as "effective gas" shown on fig .1. At initial moment ($t=0$) particle of propellant suspension ignate. As a result of isolation, of energy, and gaseous products, the temperature, density and gas pressure increase equally. At the time moment $t^*=0,4$ms the pressure in the chamber of high pressure reaches its critical point $P^*=10P_0$, at which the partition is burst (fig.2, aren "0"). At the pace of the partition, on the boarderline letween" compressed burning gas-particle suspension-inert gas". An unstable gas-dynamics break appeared, which later disintegrate, as a result a shock wake S is spread inside the chamber of low pressure and a centre wake of rarefaction R is spread in the chamber of high pressure. The surface C (dash-dot line, fig.2) divides the gas-particle suspension and gas. In the area close to the wall "I" (fig.2.) both phases are at rest, and the temperature, gas density and pressure continue increasing equally, exceeded the points they were at the burst of the partition.
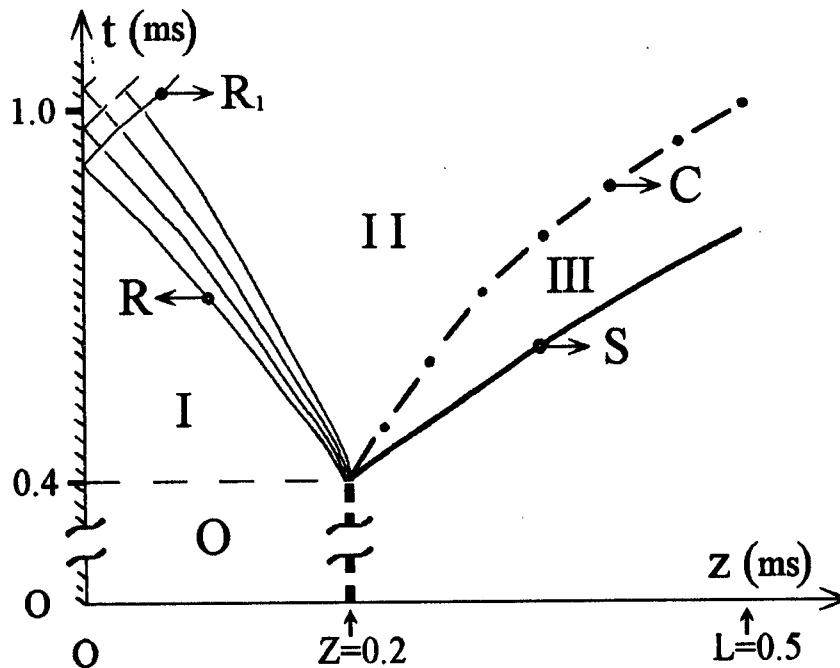
Fig.2

Yradually, the centre wave R of rarefaction reaches the particle cloud of the shock tube where it's reflected as a wake of rarefaction R_1. Behind these wakes the pressure, density and temperature decrease gradually. In the wake R the gas accelerates ,involving the dispersed phase. Behind R_1 gas-particle suspension applies the brake. In the wake S all gas parameters as well as its velocity increase. In the "II" (fig.2), inaccessible for the wakes R and R_1 the pressure increases by the processes of burning, and wakes of compression are formed that go to the shock wake S, increasing it and giving an additional dispersal to gas. In the area "II" from the surface C wakes of rarefaction gas, promoting gradual change of pressure between "II" and "III", and accelerating the gas-particle suspension.

The second phase of flow begins when the wave S reaches flood space, schematic presentation of flow of the wake is shown in the upper part of fig.3 with the help of contour lines correspond to a time moment $t=2,1$ms. In the bottom of fig.3 with the help of a long line, a part of the shock wave S (DEF) is shown: DE - disturbed, EF - undisturbed. The bound of condensation AO is reflected on the axis of symmetry with forming Mach's configuration. It should be mentioned that this forming happens in places where particles of powder are found. Behind Mach's disc ($J \sim P^{\varphi}$, $\varphi > 0$), this means the appearance of additional waves of compression, which move reflected bound OB. As a result along the current (II) gas accelerates in the centre wave of rarefaction ($v_1 > a$), goes through the bound AO, where his velocity decreased(v_{r1}). The current (II) turns to be parallel to the axis Z. Then the gas, passing OB loses its velocity v_{z1} and the current bends from the axis Z. The velocity of the gas at this point became less than sound velocity ($v_1 < a$).Along the current (I) supersonic stream ($v_{z1} > a$).(enlarges in Prandtl-Maier's wake and accelerates to the axis Z, after that it loses its velocity in Mach's disk ($v_{z1} < a$). The motion of the particles happens in the condition of gradual change of their velocity.
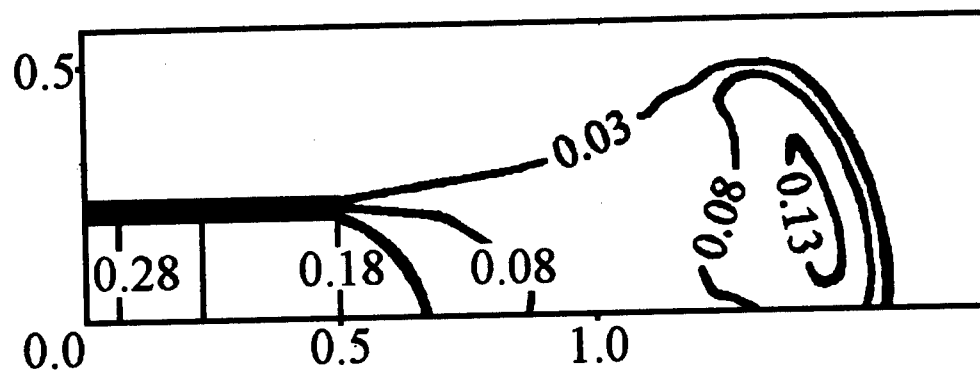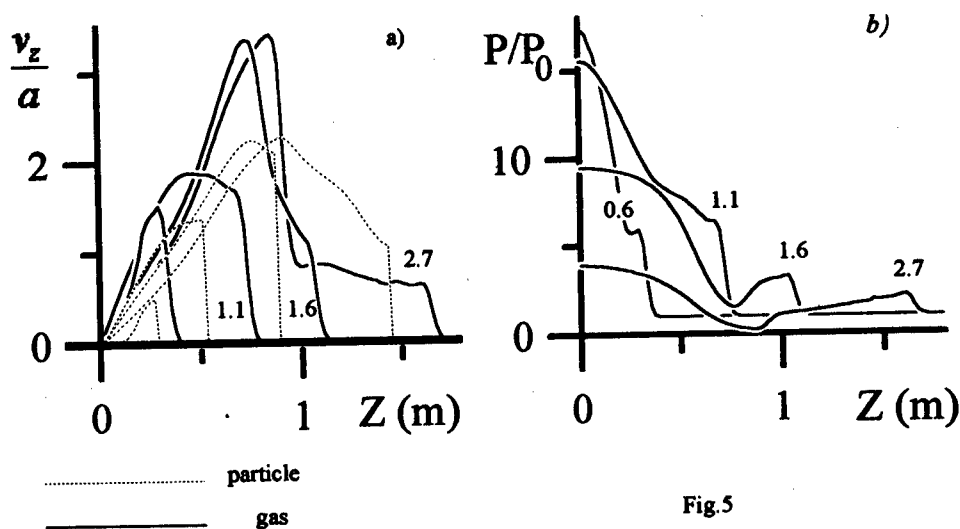
Fig.3

The dispersed particles acquire velocity which is less than in the gaseous phase. Thus, two-phase stream inside the gas stream is formed.

Behind Mach's disc the velocity of the phase decreased and the velocity of their inertness. Changes gradually because of their inertness. As a result , behind Mach's disc the particles pass ahead of gas. Before the dispensed ring gas accelerates back strata of the gas-particle suspension, behind it decelerates the suspension, which leads to the raising of the dispersed ring behind Mach's disc and the concentration of the particles is in the fore - part of the ring (fig.4) where dispersed particles contour lines correspond to the time moment t=3.1 ms.

It should be mentioned that the particle foil to overtake the shock ware S. At the time moment t=1,6 ms (fig.5a) the velocity of the particles are more than sound velocity. At the time moment t=2.7 ms velocity of particle's front down letter of sound's velocity. As a result the waves of compression come up with the wave S whose velocity is more than the sound velocity. Later the ring is divided into two parts: one continue to flow from the shock tube ,the other moves away along the axis Z (5).

Summary

Owing to the results of numerical investigation the following conclusion can drawn. The dispersal of the particles is a difficult wave process. Processes of burning promote the reinforcement of the shock wave. The flow of this wake to flood space is accompanied by the appearance of Mach's configuration in such a way that it doesn't let barrel Mach appear. The motion of the dispersed particles happen inside the supersonic gas stream before Mach's disk and only after it they move away from the axis of symmetry that leads to appearance of the dispersed ring which burns down later.

Fig.4

Fig.5

REFERENCES

1. Kutushev A.G., Rodionov S.P. Numerical investigation of critical condition of detonation wave formation of unitary fuel gas suspension due to shock initiation // FGV. 1996. V.32, No.4. P. 110-112.
2. Ivandaev A.I., Kutushev A.G., Rodionov S.P. Formation of heterogeneous detonation due to explosion // FGV. 1995. V.31, No.3. P. 83-91.
3. Belotserkovskii O.M., Davydov Yu.M. Coarse particle method in gas dynamics. Nauka. 1982.
4. Ivandaev A.I., Kutushev A.G., Rodionov S.P. Detonation waves in polydispersed gas suspension // PMTF. 1995. V.36, No.6. P. 14-23.
5. Kutushev A.G., Rodionov S.P. Detonation waves in gas suspension with non-uniform distribution of particles concentration // Sterlitamak, 22-25 Sept. 1997, V.3. P.24-25.

A STUDY OF MIXING PROCESSES
OF A SUPERSONIC FLOW IN A RECTANGULAR CHANNEL

A.V. Lokotko, A.M. Kharitonov, and A.V. Tchernyshyev

Institute of Theoretical and Applied Mechanics SB RAS,
630090 Novosibirsk, Russia

INTRODUCTION

One of the important problems arising in the development of scramjets for aerospace plane with horizontal take-off and landing is the study of the mixing processes of supersonic flows for the purpose of obtaining the maximum increase in mixing intensity in order to organize combustion within a limited length with the minimum momentum loss. The mixing of supersonic turbulent jets in the channel under the conditions of strong nonuniformity of the fields of gas dynamic parameters behind the inlet is a very complicated problem for numerical simulation. The difficulties are also aggravated by the desire to obtain the maximum splitting of injected substance. The development of these numerical techniques is also limited by the absence of reliable experimental data that satisfy the requirements of verification of numerical models.

The results of an experimental study of the mixing process of supersonic jets and a cocurrent flow are presented in this paper. The jets with various degree of dispersion are injected into a rectangular channel modeling one of the versions of real propulsion.

EXPERIMENTAL CONDITIONS. MODEL.

The experiments were carried out in the supersonic wind tunnel T-313 with a closed 0.6×0.6 m test section based at ITAM SB RAS. Experimental conditions were as follows: Mach number $M = 4.03$, Reynolds number $Re = 55 \cdot 10^{6}$ m^{-1}, stagnation temperature 286 K.

A sketch of the model with geometric characteristics of its basic elements is shown in Fig. 1. The model inlet has a flat lower compression surface *1* with a 6° wedge, the upper cowl *2*, side walls *3*, and pylon *4* with a 40° sweep angle of the leading edge and 10° plan apex angle, which is mounted at the longitudinal axis of symmetry. The wedge surfaces of the pylon are also compression surfaces; thus, the construction as a whole is a three-dimensional inlet. In the base part of the pylon, there is a rake of conical supersonic nozzles, the high-pressure gas being injected from them. Two types of pylons were used in experiments. The characteristics of the two pylons and the relative inlet throat area determined by pylon geometry are listed below.

Table 1

Parameter	Pylon 1	Pylon 2
Number of nozzles	12	6
Throat diameter, mm	6	8
Nozzle exit diameter, mm	12	16
Exhaust Mach number	2.94	2.94
Total throat area, mm^2	339.3	301.6
Relative inlet throat area	0.488	0.537

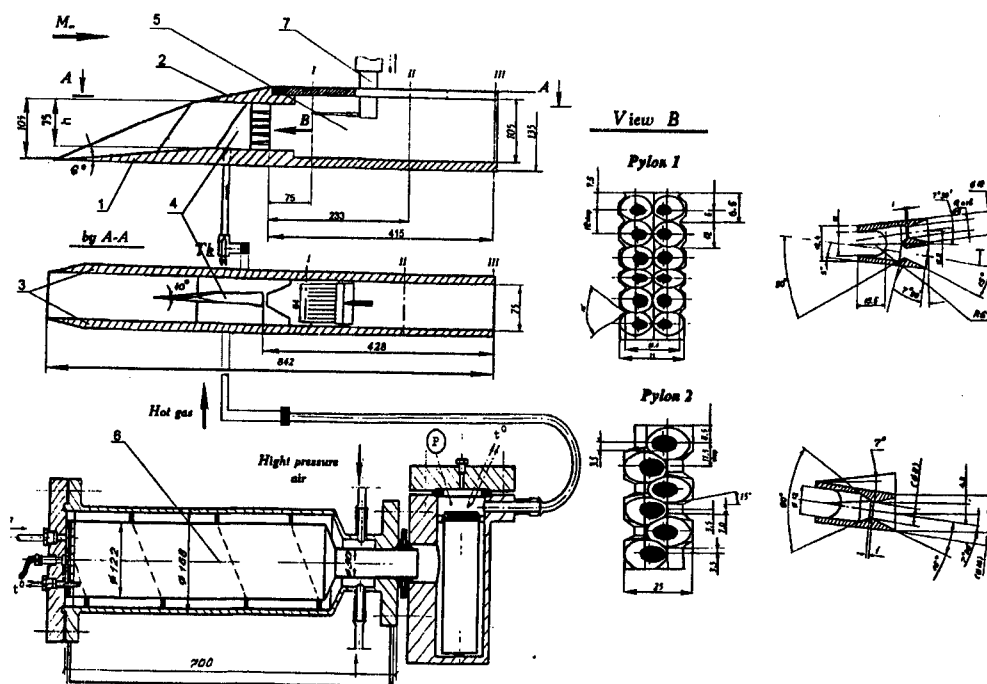Pylon 1 has a symmetric nozzle disposition and shallow turbulizing grooves between the

Fig. 1 Sketch of the model

nozzles at the side surface. Pylon 2 differs from it by an asymmetric nozzle arrangement and deep notches between the nozzles which introduce appreciable disturbances to the flow at the mixing chamber (MC) entrance.

The mixing chamber is a channel with a 75×105 mm cross-section and 420 mm length. At the top and bottom of the MC entrance there is a system of 3D oblique steps with a sweep angle of 70° connected with each other by straight steps.

For jet identification, a hot gas (473 – 483 K), the products of hydrogen combustion in the air) is supplied to the pylon nozzles. The source of gas is the gas generator 6 (Fig. 1) which is a high-pressure combustion chamber. To ensure a sufficient stability of the measurement means for flow probing in the model, the above mentioned comparatively low temperature was sustained at the gas generator exit. The gas generator operation regime, therefore, corresponded to a poor region, i.e., the air-to-fuel ratio was much higher than unity (about 10). The hydrogen flow rate was kept at a level of 1.4 g/s, the air flow rate was 0.47 kg/s, the pressure in the gas generator was about 1.8 MPa, which provided the following values of the flow parameters: ejection factor $n = G_{in}/G_{gg} = 3.71$ (G_{in} and G_{gg} are the flow rates in the inlet (low-pressure flow) and gas generator nozzles (high-pressure flow)). The nozzle pressure ratio was varied from 1 to 4.5 (for upper and lower nozzles, respectively), which, in turn, was determined by the pressure variation over the channel height in the inlet throat cross-section coinciding with the nozzle exit cross-sections.

In the course of experiments, we measured the fields of total pressures p_0' (behind the normal shock), static pressures p, and stagnation temperatures T_0 in three measurement cross-sections (I–III) along the channel. The cross-section coordinates are shown in Fig. 1. The pressure p_0' and temperature rakes consisted of ten probes with a step of 7 mm, the pressure p rake

had six probes located with a step of 12.6 mm. The temperature probes were screened thermocouple junctions with lateral orifices. The inner diameter of the screen-pipe was 3 mm, the diameter of two lateral orifices of the channel was 1 mm. Thermocouples of the chromel-alumel group were used. The temperature of hot gases in the pipeline, called conventionally the "temperature at the control point" T_k (see Fig. 1), was taken as the initial temperature, the current temperature distribution in the flow being compared with it.

All three rakes were fixed in one traverse gear 7 that ensured the motion accuracy of 0.1 mm along the $0Y$ axis at a distance of 105 mm. Each type of measurements corresponding to the type of its rake was performed in a separate test.

The pressure was measured using the MID-100 system with scannivalves designed for the p_0' range of 0–0.6 MPa and p range of 0–0.2 MPa. The instrument accuracy of the system was 0.3 %. A digital voltmeter was used as the primary analog-to-digital converter in temperature measurements.

Table 2

Cross-section	G, kg/s (δ%)	I, N	T_0, K
I	2.201 (0.14)	1569.0	334.8
II	2.186 (0.82)	1531.7	338.4
III	2.224 (0.91)	1524.9	337.3

The flow parameters in each cross-section were calculated using the results measured at 160 points. The static pressure at points corresponding to positions of total pressure probes, which do not coincide with the coordinates of static pressure probes, was calculated using the measured results and Lagrange interpolation formula.

The integral parameters in three cross-sections were calculated from the conditions of mass flow and momentum conservation in the mean and initial non-uniform flows.

A comparison of integral parameters in three cross-sections made it possible to evaluate the changes in the mixing degree for two pylon configurations. Regularities of propagation of high-pressure jets were revealed. The specific momentum loss and the changes in turbulent Prandtl numbers along the channel were estimated.

VALIDATION OF MEASUREMENT RESULTS

The validity of measurement results is determined by the equality of the measured mass flow rates in three cross-sections along the channel, balance of momentum measured in the mixing chamber cross-sections and calculated on the basis of parameters of the high-pressure and low-pressure flows entering the mixing chamber, and constancy excess heat content. The flow rate G, momentum I, and temperature T_0 obtained on the basis of measurements for pylon 2 are listed in Table 2.

It is seen that the maximum flow rate deviation δ (%) from the mean value (2.204 kg/s) is 0.91 %. The flow rates are absolute quantities measured in different tests, and they indirectly characterize the reproducibility of parameters both in the settling chamber of the wind tunnel and in the gas generator.

The total momentum is $I = I_{in} + I_{gg} = 1603.2$ N. Taking into account that the total momentum loss in the inlet and in turbulizing grooves, by the base pressure of stabilizing steps and friction losses in the channel, this value is fairly close to that measured in cross-section I.

Under the conditions of weak heating, the excess heat content is equivalent to a constant mean temperature which was determined by averaging with respect to flow rate. The flow temperature value of 332.8 K in the mixing channel was calculated on the basis of temperatures at the inlet entrance and behind the gas generator nozzles, taking into account the corresponding fractions of gas flow rate and percentage of water vapor from hydrogen combustion.
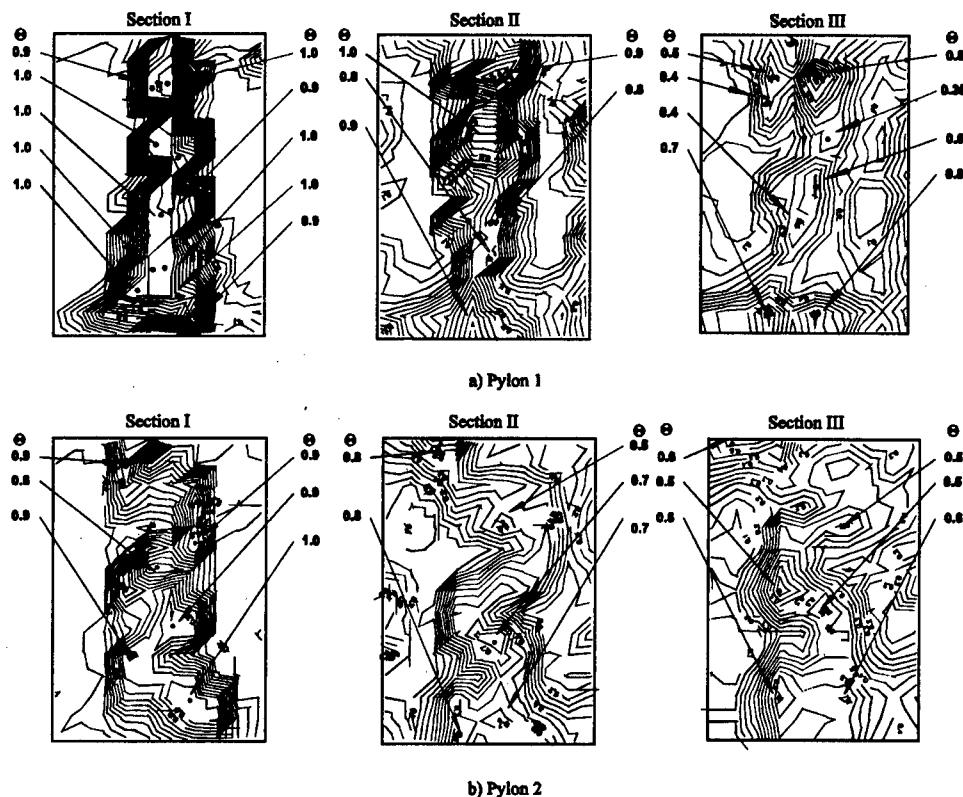
a) Pylon 1

b) Pylon 2

Fig. 2

Thus, the data obtained demonstrate an acceptable credibility of these measurements.

EXPERIMENTAL RESULTS

Figure 2a, b shows the fields of relative excess temperatures θ = $= (T_i - T_c)/(T_{0s} - T_c)$ where T_i and T_{0s} are the temperatures at the ith measurement point and in the settling chamber, respectively. The black dots indicate the zones of the maximum relative excess temperatures and their numerical values. Obviously, the temperature maxima in the cross-sections are associated with jet axes.

The narrowest heating zone is observed in cross-section I (x/h=1), it has clear vertical boundaries that roughly cover a half of the channel width (h is the throat height). The highest values of θ are also observed here, $\theta \approx 0.8 - 1$. In cross-section II (x/h=3.4) the heating extends to the entire channel width with decreasing θ. A specific feature inherent here is almost complete merging of all jets for pylon 1 and jets2 and 3 for pylon 2 (the nozzle notation is presented below in Fig. 3). In cross-section III (x/h=5.7) the positions of the axes of most jets becomes clear again.

The data on θ distribution make it possible to construct three-dimensional jet trajectories in the channel. They are shown in Fig. 3, a, b in projections onto the vertical and horizontal planes. The nozzle positions are also marked here. The main structural feature for pylon 1 is almost complete merging of jets in the vertical plane of symmetry in cross-section
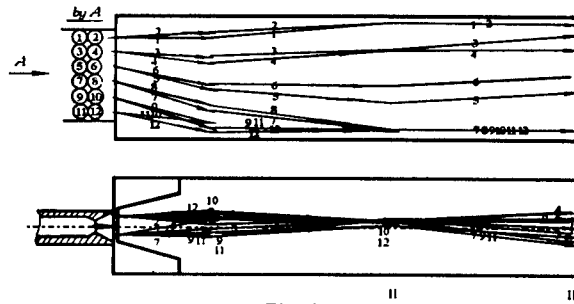
Fig. 3a

II with comparatively high values of θ. Noticeable dispersion of jet axes is observed in the exit cross-section, which is, however, considerably lower than for pylon 2. Hence, the jet merging shifts the effective beginning of mixing for pylon 1 almost to a half of the channel length. The process of jet merging was registered previously in [1], where the laser sheet revealed a certain merged jet conglomerate which resembled a tree. The jet trajectories from pylon 2 are located more uniformly along the channel.
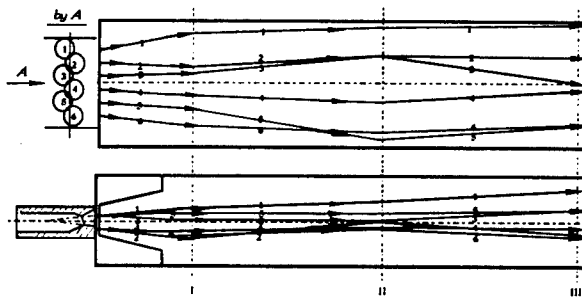
Using the known analogies of similarity theory [2, 3] and representing the jets as separate structures (moles) propagating in a cocurrent, rather nonuniform flow, we estimate the comparative degree of momentum (based on velocity) and heat

Fig. 3b

equalization, i.e., calculate a certain analog of the turbulent Prandtl number Pr_t. The Prandtl model for the mixing path length based on velocity (l_u) and temperature (l_t) is used, and the analog of pressure gradient in the shear layer is assumed to be the root-mean-square deviation of the corresponding parameter: σ_λ for velocity coefficient and σ_{T_0} for temperature. The maximum difference of these parameters was taken from the distribution of isotherms (Fig. 2, a, b) smoothed by cubic splines.

Then

$$l_u = |\Delta\lambda_{max}/\sigma_\lambda|, \qquad l_t = |\Delta T_{0max}/\sigma_{T_0}|; \grave{e} \qquad Pr_t = l_u / l_t$$

The values of quantities that characterize the transfer processes are listed in Table 3.

The obtained values of Pr_t fluctuate approximately around 0.5, which corresponds to the known data for free turbulence [2, 4]. Meanwhile, the Prandtl number Pr_t for pylon 1 decreases along the channel appreciably faster than for pylon 2. This is mainly due to relatively larger values of the temperature-based mixing length, namely, due to higher ΔT_{0max}, which testifies to a larger nonuniformity of the temperature field, i.e., a worse quality of mixing for pylon 1.

Table 3

Parameter	Pylon 1			Pylon 2		
	Cross-sections			Cross-sections		
	I	II	III	I	II	II
σ_λ	0,379	0,339	0,327	0,393	0,328	0,242
$\Delta\lambda_{max}$	1,183	0,709	0,586	0,795	0,706	0,465
l_u	3,121	2,093	1,790	2,023	2,153	1,924
σ_{T_0}	43,98	30,77	23,78	63,30	41,84	28,49
ΔT_{0max}	188,8	194,1	153,7	186,9	151,2	113,4
l_{T0}	4,29	6,31	6,46	2,95	3,61	3,98
Pr_t	0,73	0,33	0,28	0,69	0,60	0,48

142

The changes in specific momentum I [m/s]=I/G between cross-sections I and III for the both pylons are presented in Table 4.

Table 4

Cross-section	Pylon 1	Pylon 2
I	710,66	712,85
III	666,08	685,65
Momentum loss δ%	6,27	3,82

It is seen that the loss in I along the mixing tract for pylon 1 is larger than for pylon 2 by a factor of 1.64. This agrees with the previous data for the same model, which were observed in experiments with injection of cold jets with a different ejection factor [1].

The results obtained show that an increase of the number of cocurrent jets injected into a supersonic flow does not always ensure a more effective mixing. The level of dispersion of supersonic jets during their mixing in particular conditions should be the subject of subsequent special research.

The authors are thankful to A.S.Rudakov and L.V.Gogish for initiation of the present work.

REFERENCES

1. Lokotko, A.M. Kharitonov, and A.V. Tchernyshyev, A study of mixing processes of a supersonic flow in a rectangular channel. 1. Cold jet injection// Thermophysics and Aeromechanics. 1997, Vol. 4, No. 4, P. 385–395.
2. Abramovich, S.Yu. Krasheninnikov, A.N. Sekundov, and I.P. Smirnova, Turbulent Mixing of Gas Streams, Nauka, Moscow, 1984, 715 p.
3. Gukhman, The Use of the Similarity Theory for the Study of Heat-and-Mass-Transfer Processes, Vysshaya Shkola, Moscow, 1967, 303 p.
4. H. Schlichting, Boundary-Layer Theory, McGraw-Hill, New York, 1968.

ON THE POSSIBILITY OF APPLICATION OF THE FOCAL SPOT OPTICAL METHOD FOR THE INVESTIGATION OF TURBULENT CHARACTERISTICS OF SUPERSONIC FLOWS

V.M.Mal'kov and V.A.Lebiga

Institute of Theoretical and Applied Mechanics, 630090 Novosibirsk, Russia

Traditionally, hot-wire anemometry is the most widespread tool for turbulence studies. The basic principles of the pulsational hot-wire measurements have been developed in [1-3]. From these measurements, for the main part, information as to the intensity and spectral characteristics of pulsations can be obtained. To determine the characteristic scales of turbulence, one has to measure the correlation function, i.e., in this case two hot-wire probes are to be used in order to perform simultaneous measurements at two different points, and for data to be obtained at large numbers of points, the experiment becomes too labour-consuming.

The most comprehensive analysis of the pulsational processes occurring in a flow can be performed on fully automated and computerized setups. However, some additional assumptions should be made in this case as well, since the hot-wire probe registers simultaneously pulsating velocity, temperature, and density, and in case of gas mixture the resulting signal depends also on the concentrations of the constituing components. Besides, the wide frequency range of the pulsations of interest (up to several hundreds of kHz) requires complex software facilities to be implemented to process the signal in real time, and high-power computers to be employed.

However, in many cases full information as to the structure and frequency spectrum of pulsations is not required. To solve many physical problems, one has to possess information only about some definite or mean flow parameters. For example, information on pressure pulsations can be obtained using different types of microphones, while the Schlieren method coupled with light sources operating in pulsed modes is capable of providing qualitative (and sometimes even quantitative) data on the turbulence scales provided that the pulsations dealt with are sufficiently uniform.

Applying various optical methods seems to be most profitable and justified when one investigates average characteristics, since in this case averaging along the light beam occurs automatically. In addition to the simple Schlieren technique, more evolved methods are being used, first of all, interferometry. However, in this case, to study characteristics of a turbulent stream, one has to register instantaneous interferograms, but in order to obtain a representative amount of data, a large number (tens) of interferograms [4] should be recorded, i.e., here again a great body of information is to be processed.

In aero-optical studies [5], to obtain information as to the wave fronts of a light beam having passed through a turbulent medium, some new approaches have been developed. The Small Aperture-Beam Technique was put forward [6], where instantaneous deflections of a narrow laser beam were registered, which resolved the turbulent structure of the layer under examination. Using the Fourier transform, one can reconstruct the position of the wave front in time, which is determined naturally by turbulent characteristics of the flow. To more exactly and adequately describe the shape of the wave front, it is required to simultaneously employ a great number of beams [7].

To measure average characteristics, the Focal-Spot Method (FSM) is widely used in aero-optics, the corresponding procedure being sometimes called either the Far-Field Power-in-Bucket Measurements [8], or - in fact, the same procedure - the Line-Spread

Instrumentation [9]. In the latter case, variations in the intensity of a laser-emitted light beam having passed through a turbulent layer of interest are being registered at the central spot of the far zone. These variations are determined by averaged (both along beam and in time) turbulence characteristics of the flow.

In optics, where the case of the Fraunhofer diffraction is being commonly considered, distributions of the radiation intensity in the far zone $I(x,y)$ are represented through the Fourier transform of the transfer function τ being in the general case the product of τ_p and τ_T ·, which are determined by aberrations on regular and random flow inhomogeneities, respectively. In a number of aero-optical problems, it is required to obtain a plane wave front. The general slope of the front is determined by τ_p, and it can be improved in principle by using adaptive optics methods. The effect due to turbulence resulting in a distortion of wave front, however, is hard to improve, since the pulsational frequencies turn out to be too high. Therefore, it is the study of τ_T which presents the problem of primary interest.

In [11], an analytical expression for τ_T has been obtained for the diffraction light scattering on a uniformly isotropic turbulent laser-active layer of a thickness L. Under some assumptions having been made, it has been found [12] that the r.m.s. phase error accumulated on the optical path and characterizing the curving of the plane front of the wave having passed through the layer L is determined by the following expression:

$$< \Delta\varphi^2 > = \frac{8\pi^2}{\lambda^2} \cdot \beta^2 \cdot \Lambda \cdot L \cdot \frac{<\rho'^2>}{<\rho>^2} \cdot \frac{<\rho>^2}{\rho_{ref}^2}, \qquad (1)$$

here Λ is the turbulent scale, ρ' is the density pulsations, ρ_{ref} is a constant entering the Gladston-Dale formula, and $<>$ denotes averaging over time).

According to the Strehl relationship [13], the value $<\Delta\varphi^2>$ determines the decrease in the radiation intensity at the central spot of the far zone $\Delta I=(I_0-I)$ relative to the I_0 value obtainable in case of diffraction divergence of beam: $\Delta I/I_0 \sim <\Delta\varphi^2>$. In the case when the regular flow structure is resolved by the FSM, the relationship (1) can be used in principle for interpreting the data obtained.

To resolve the flow structure, in the paper the use of the small-aperture version of the FSM was proposed. In contrast to the commonly employed wide-aperture variant, where the whole region under study is probed and τ contains both regular and random components, here the regular (shock-wave) structure of the flow is assumed to be resolvable, the turbulent structure of flow being averaged over the the diameter of the probing beam (i.e., the diameter of the probing beam is to be chosen with taking into account particular features of the flow under study). In its "ideology", the advanced method seems to be an intermediate one between the SABT and the wide aperture FSM (the method is discussed in detail [14]). The method was approbated on a sufficiently complex object. Supersonic flows behind multy-nozzle banks (MNBs) used in gas dynamic lasers, were considered, (Fig. 1).
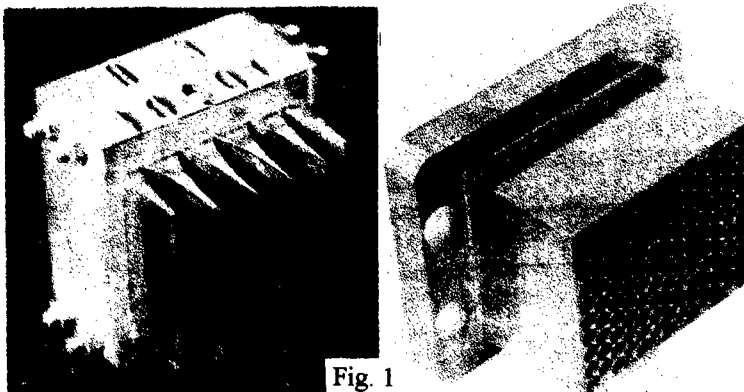

Fig. 1

145

Both plane constructions and the so-called screen nozzle banks (SNBs), consisting of a large number of axisymmetric conical or contoured micronozzles were used. Since the MNBs had base areas, the flow contained a regular structure, which included compression shock waves, rarefaction waves and turbulent wakes.

Photographs of the flow pattern behind the both types of MNBs are presented in Fig. 2 (in Fig. 2a, the blade ends of the plane bank are seen; the outlet Mach number of each of the micronozzles equalled 5 for both types of MNBs).
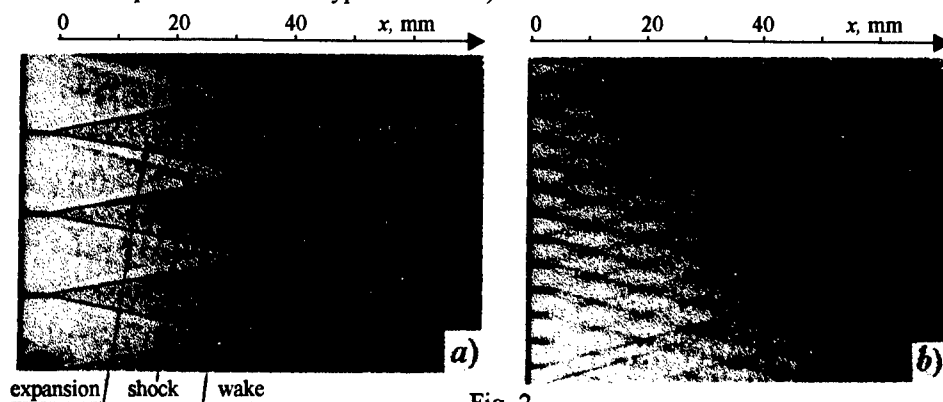
Fig. 2

The flow geometry behind the plane banks allowed detailed data on averaged stream parameters (with the help of static- and Pitot pressure probes) to be extracted together with information on the evolution of the intensity of the regular shock-wave structure downstream of nozzles, on the ρ distribution and on the distribution of velocity in the wakes, as well as to determine wake thicknesses. It has been shown that the fall in ρ in the expantion wave restores practically up to the initial level of ρ in the stream core (between neighbouring blades) inside the final compression shock. Therefore, when calculating optical paths, one has to take account of the presence of the both disturbing factors (in [15], density variations were associated merely with the presence of compression shocks).

The intensity of disturbances, being determined by the shock-wave structure, decays downstream rather rapidly, over a distance of 7-8 H, where H is the separation between neighbouring blades. Figure 3 presents the corresponding results for blades of different trailing edge thicknesses t and for different trailing edge angles α. The increase in the mean density observed downstream is mainly due to growing thickness of the boundary layer at channel walls.

In spite of the influence the shock and expantion waves on the wake (these two factors having opposite signes and close intensities may be said to compensate each other), the wakes behind blades in the region where they have not yet interacted with each other exhibit the classical behaviour. The distribution of parameters across the wake remains self-similar. The velocity distributions measured in different cross-sections along the

Fig. 3

146
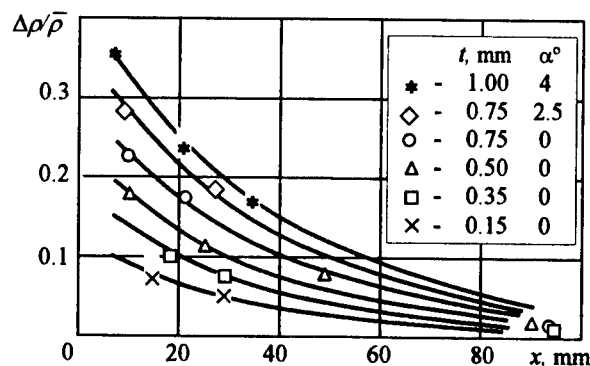
wake length and expressed in terms of the far-wake variables are presented in Fig 4 which shows that the self-similarity retains and the wake thickness is proportional to $\sqrt{x}$.
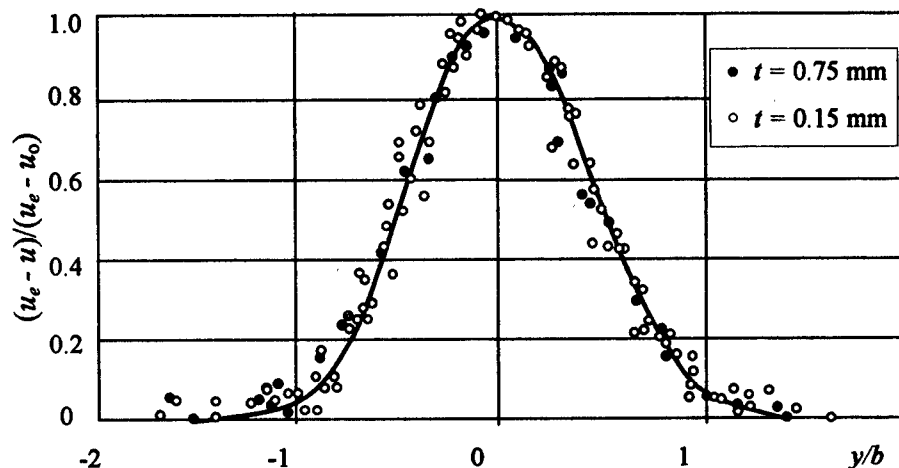
Fig. 4

Pulsational characteristics of plane wakes were studied in [15], where it was shown that $<\rho'>/\rho\sim$const and $\Lambda\sim b(x)$ in the turbulent region of wake. Substitution of the above characteristics of free wakes into Eq. (1) shows that the asymptotic behaviour of $\Delta I(x)$ is determined by the expression $\Delta I(x) \sim x\rho^2$. It was just this dependence which was obtained experimentally (Fig. 5): a linear dependence on x over the starting section of flow and a quadratic one on ρ father on. However, the wakes, expanding and filling the whole flow field farther downstream, start interacting with one another at a distance 12-13 H. As a result of this interaction, the large-scale turbulence developing in the free wakes (see Fig. 2) gets disintegrated here and turns into a small-scale one (Fig. 6), the stream under study becoming
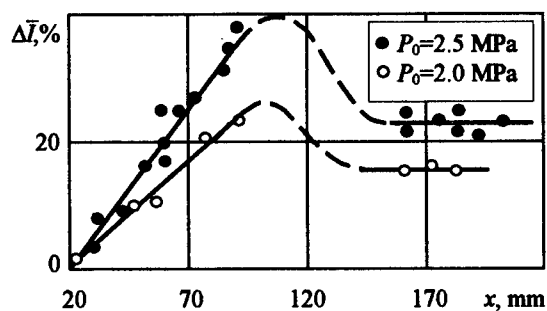
Fig. 5

a) horizontal knife   b) vertical knife

Fig. 6

147
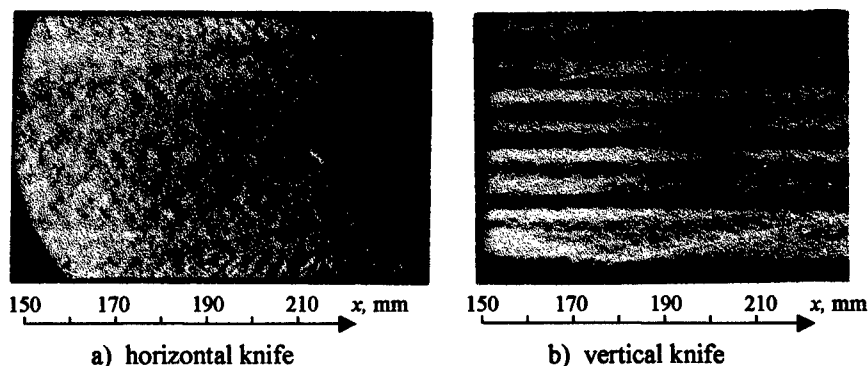
homogeneous from the optical point of view. Therefore, at $x > 12\,H$ the scattered portion of radiation ΔI diminishes in accordance with decreasing A. The fact that ΔI at $x > 160$ mm remains a constant quantity provides an indication that both A and $\Delta\rho/\rho$ stop changing here.

However, the supersonic wakes are known to retain in the flow for a long time. Measurements employing probes and flow visualization technique (Schlieren photographs taken with horizontal knife are shown in Fig.6) are indicative of the latter. But due to the interaction, the behaviour of the developing wakes changes: the wakes transform into parallel layers, the averaged structure of the flow as a whole becoming layered. Upon probing across the parallel inhomogeneities, no phase shift $\Delta\varphi$ (across this regular structure) over the beam aperture takes place, of course, i.e. $\tau_p=1$. The shocks generated by blade ends does not contribute to $\Delta\varphi$ over the starting section as well, since they also cross the whole beam aperture. A large phase shift is caused by the regular structure formed by the shocks propagating from the throat of each individual nozzle (these shocks are not seen in Fig.2: they are registered when viewed from the perpendicular direction; for more detail about these shocks see [17]), since the plane of such shocks stretches along the probing beam. However, it is this structure which has been resolved by the FSM in its small-aperture version, i.e., in our case $\tau_p=1$, the latter making sense of using the small-aperture variant.

The mechanism of the formation of the layered structure of flow considered in detail for the plane case has allowed us to explain the flow pattern for screen nozzle banks as well (Fig. 7). The shock-wave structure is seen to rapidly decay in this case as well at distances $\bar{x}= x/d \sim 10$ calibers from the bank exit (d is the outlet diameter of an individual micronozzle).
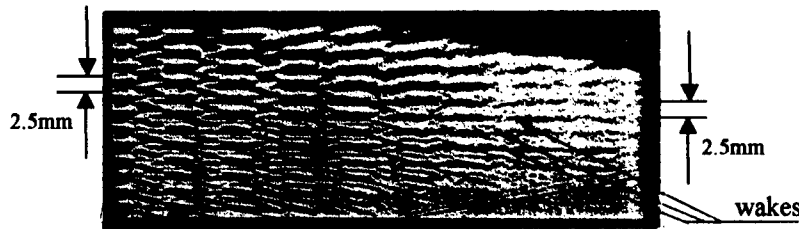
Fig. 7

The downstream flow considered from the viewpoint of regular density inhomogeneities is determined by the parallel wakes forming behind the base regions of banks, rather than by shock waves as was believed in [15,18], which is clearly seen in the photographs Fig.7 obtained with horizontal knife.

Therefore, the $\Delta\bar{I}$ value falls abruptly over the starting section of the flow (Fig.8), as the intensity of the shock-wave structure diminishes, since in this case the latter cannot be resolved because its characteristic size is smaller than the diameter of the probing beam. But further downstream at distances $x > 10$ the behaviour of $\Delta\bar{I}(x)$ turns out to be determined to a larger extent by the turbulent properties of the whole stream (the wakes of neighbouring
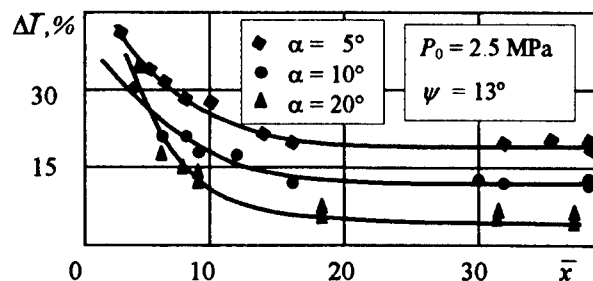

Fig. 8

148

base regions here have got merged already). Figure 9 illustrates the behaviour of intensity of the mass flow rate fluctuations m' for conical SNBs (α is the semi-angle of divergence of an individual micronozzle). As neig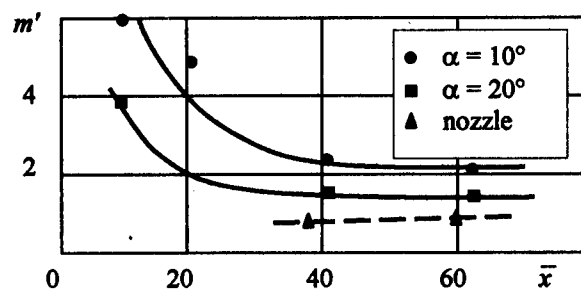hbouring jets get mixed, the m' value drops, attaining its lowest at distances $x > 30$. The $\overline{\Delta I}$ value varies with x in the same manner, the best optical quality (OQ) of stream (lower ΔI) being obtainable for conical SNBs with large α angles. The latter is in line with the data shown in Fig. 9. The constancy of ΔI in the region $x > 30$ is indicative of the fact that here not only the intensity of pulsations, but also the integral scale stop changing.

Fig. 9

Since, as noted above, the wakes retain in the stream over a large distance - in our case up to 100 calibers [18] - in the experiments the ΔI vs ψ dependence is registered, ψ being the angle between the probing direction and the micronozzle array of the bank. (The above is due to that the given wake structure is has not been resolved in the measurements. If the latter had been resolved (in case of a sufficiently narrow beam), no averaging of the turbulent structure would take place over such an aperture). With it, there existed a ψ_{optim} angle, for which the presence of wake structure results in no phase shift over the beam aperture, i.e. the stream viewed from this direction becomes optically homogeneous. The angle ψ_{optim} can be easily estimated from nozzle bank geometry, which determines the structure of flow as a whole [19]. The results of testing in this direction (in the region $x > 0$) can be treated by using Eq.(1).

Thus, it is shown that the results of measurements of the scattered portion of radiation made with the small-aperture version of the FSM are determined primarily by the behaviour of the developing turbulent characteristics of flow either in case when the regular flow structure - if the latter does exist - is resolved, or in the case of measurements being conducted at such an angle, for which the structure exerts no effect on $\Delta\varphi$ obtained with using such beam aperture. Therefore, in case when data on the intensity of pulsations are available (obtained, for instance, with the help of hot-wire anemometry), the values of mean integral scales of flow can be easily obtained from the measured ΔI values. The use of this variant (combining the two techniques) seems to be quite reasonable in case of studying turbulence in supersonic flows with high Mach numbers, when measuring correlation functions at large number of points appears to be too cumbersome a procedure. Besides, there exists a high probability of damaging the hot wire in a stream of a high supersonic speed caused by inevitable presence of dust in it. Optical techniques, apart from their easy implementation, allow to cut the duration of the experiments, i.e. to save the time required for testing in a tunnel, the equipment needed for the realization of the FSM being simple enough [8,10].

References

1. J.O.Hinze. Turbulence. An Introduction to Its Mechanism and Theory. McGraw-Hill Book Corp.,Inc. N.Y.,1959.

2. L.S.Kovasznay. Turbulence in Supersonic Flow. J.A.S. v.20, No 10, 1953.

3. V.A.Lebiga. On Measurements Turbulence of Compressible Flow // Metody i Tekhnika Aerofizicheskih Issledovanii.Novosibirsk, ITAM. p.44-56, 1978. (In Russian).

4. G.Havener, C.Stepanek. Aero-Optics Testing Capabilities at AEDC. AIAA- Paper N92-0760.N.Y.:AIAA, 1992.

5. Aero–Optical Phenomena. Progress in Astronautics and Aeronautics . V.80/ Eds. by Gibert K.G., Otten L.J. –N.Y.: AIAA, 1982.

6. M.Malley, G.Sutton. Beam-Jitter Measurements of Turbulent Aero-Optical Path Differences // Applied Optics. v.31 No 22, 1992 p.4440-4443.

7. E.J.Jumper, R.J.Hugo. Optical Phase Distortion Due to Turbulent–Fluid Density Fields: Quantification Using the Small–Aperture Beam Technique. AIAA–Paper №92–3020. – N.Y.: AIAA, 1992.

8. D.W.Bogdanoff. Optical Quality of Supersonic Jets of Various Gases // Applied Optics. – 1982. –V.21, №5. –P.893–903.

9. W.H.Baily. Line Spread Instrumentation for Propagation Measurements // Aero–Optical Phenomena. Progress in Astronautics and Aeronautics. V.80/Eds.Gilbert K.G., Otten L.J. –N.Y.: AIAA, 1982. –P.189–199.

10. V.M.Malkov, M.G.Ktalkherman. Some Aspects of Aero–Optics of GDL Nozzle Banks. AIAA–Paper №94–2447. –N.Y.:AIAA, 1994.

11. G.E.Sutton. 'Effect of Turbulent Fluctuations in an Optically Active Fluid Medium // AIAA J. –1969. –V.7. –№9. –P.1743–.

12. H.H.Legner, J.H.Otis, G.A.Theophanis, R.M.Feinberg. Laser Beam Degradation through Turbulent Interfaces. AIAA–paper №78–71. –N.Y.: AIAA, 1978.

13. M.Born, E.Wolf. Principles of Optics . IV Edition, Pergamon Press, 1968.

14. V.M.Malkov, M.G.Ktalkherman. Aero-Optics of GDL Nozzle Banks // Applied Math. and Technical Physics. 1993. No 6. p.20-28. (in Russian).

15. T.S.Vaidyanathan, D.A.Russel. Wave–Generated Disturbance Downstream of Nozzle Array // AIAA J. –1985. –V.23. –№5. –P.749–751.

16. A.Demetriades. Turbulent Mean Flow Measurements in Two–Dimensional Supersonic Wake // Physics of Fluids. –1969. –V.12. –№1. –P.24–32.

17. M.G.Ktalkherman, V.M.Malkov, G.V.Klimchik. Investigation of Flow Under the Nozzle Side Wall // Thermophysics of High Temperature. 1996. v.32, № 1. p.583-589 (in Russian).

18. D.A.Russel, S.E.Neice, P.H.Rose. Screen Nozzles for Gasdynamic Lasers // AIAA J. – 1975. –V.13, No 5. –P.593–599.

19. V.M.Malkov. Aero-Optics of Flow after the Nozzle Banks of Fast Flow Lasers // Applied Math. and Technical Physics. 1996. No 6. p.26-34 (in Russian).

SPATIAL EVOLUTION OF RESONANT WAVE TRAINS
IN SUPERSONIC BOUNDARY LAYERS

I. I. Maslennikova, S. A. Gaponov

Institute of Theoretical and Applied Mechanics, SB RAS,
630090, Novosibirsk, Russia

Introduction

Due to a large number of theoretical and experimental studies, the theory of laminar-turbulent transition in incompressible flows is investigated rather in details. Laminar- turbulent transition investigations at supersonic velocities are not so numerous. Before early 90s, available experiments in supersonic boundary layers provided adequate bases only for linear theory of stability. However the method of introduction of controllable disturbances developed over the last 5 years [1, 2], made it possible to investigate experimentally the nonlinear stage of disturbance evolution and stimulated the development of theoretical models for nonlinear mechanisms.

The cited above experimental technique allowed to introduce wave packet with fixed frequency into supersonic boundary layer. Flat plate experiments at Max number M=2 have shown that when artificially modulated disturbances of frequency F_1=20 kHz were introduced, downstream oscillograms displayed the signals with subharmonic frequency F_2=F_3=10 kHz along with fundamental frequency F_1. From some downstream distance and on, subharmonics dominated the process. The wave spectra of these disturbances are typical for three-dimensional Tollmien-Schlichting waves. The measured increments for subharmonics could not be explained as a linear growth of TS waves. The analysis of Fourier - spectra has shown that spanwise wave numbers β_j (j=1, 2, 3) associated with maxima in spectra, answered to resonant condition $\beta_2 + \beta_3 = \beta_1$. It was assumed that the behavior of dominant disturbances could be explained as subharmonic resonance.

The early theoretical studies were based mainly on the model of secondary instability. Later a number of results were obtained by direct numerical simulation. In work [3] an averaging method, which has been developed for incompressible case [4], was applied to supersonic boundary layer. Some numerical results were obtained which confirmed the possibility of subharmonic resonance.

Model of resonant triads

In works [5, 6], three-wave model has been suggested for an explanation of behavior of dominant disturbances in experiments. That model includes low-amplitude three-dimensional subharmonic TS waves pumped up through parametrical

resonance in the field of unstable three-dimensional TS wave of greater amplitude A_1 $(A_{2,3}/A_1 \ll 1)$. On the basis of weakly nonlinear theory a method was suggested for the numerical analysis of the evolution of resonant disturbances in the form $A_j \zeta(y) exp\,i(-\omega_j t + \beta_j z + \int \alpha_j dx)$ (here α is a complex and β - a real value) in supersonic boundary layer. The method is based on decomposition of the solution in the terms of small parameter ε (this parameter is of the order $A_{2,3}/A_1$) and two-scale decomposition of streamwise coordinate: $x_1 = x$ and $x_2 \equiv X = \varepsilon x$. The opportunity of two-scale decomposition is proved by a large difference between growth rates for disturbance phases and amplitudes.

The equations describing amplitude evolution for resonant triad $a_j = A_j exp\,(-i\alpha_j)$ were written as follows:

$$\frac{da_1}{dX} = -Im(\alpha_1)a_1 + \varepsilon S_1 a_2 a_3 exp(i\Delta_1)$$

$$(1)$$

$$\frac{da_2}{dX} = -Im(\alpha_{2(3)})a_{2(3)} + \varepsilon S_{2(3)} exp(i\Delta_{2(3)})$$

as well as a procedure for calculation of complex coefficients of nonlinear interaction S_j ($j=1,2,3$). Terms with Δ_j take a detuning $\Delta_1 = Real(\int(\alpha_2 + \alpha_3 - \alpha_1)dx) = -\alpha_{2,3}$ into account.

In works [5, 6] numerical results were obtained which proved that the selection of dominant disturbances as itself occurs as a result of parametrical resonance of background disturbances which formed a nonsymmetric subharmonic triad. The calculated eigenvalues were very close to those received in experiments for central wave vectors of wave trains.

Numerical results for isolated triad model

In this work (see also [7]) the behavior of a resonant triad with spectral parameters corresponding to experiments at $M=2$ is numerically investigated at various initial amplitudes of disturbances. For each wave mode dimensionless frequency parameter F, connected with frequency as $\omega = Re \times F$ and dimensionless parameter $b = 10^3 x \beta / Re$ were kept constant.

As shown in Fig.1, in supersonic flow an interaction has not got an "explosive" character when initial amplitudes grow which is peculiar for incompressible flows. In this case, at nonlinear stage phase relationships between coefficients of nonlinear interaction S_j ($j=1,2,3$) take such values that quasiperiodical regime with energy exchange between modes is established. By this is meant that subharmonic resonance hardly is the direct mechanism of laminar - turbulent transition in supersonic flow. But it likely plays an important role in complicated nonlinear process of disturbance
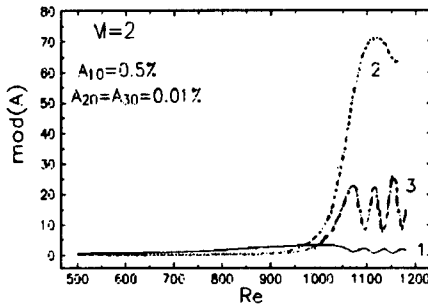
Fig.1 Evolution of resonant triad amplitudes: 1- fundamental wave, 2,3 - subharmonic.
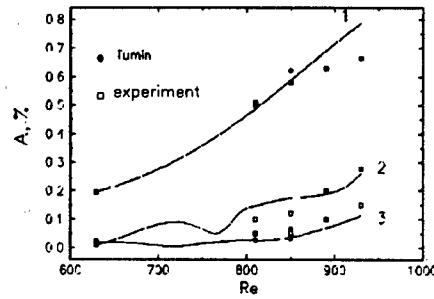
Fig. 2 Evolution of resonant triad amplitudes in comparison with experiments [1, 2].

spectrum formation in transitive zone. In support of this conjecture it can be noted, for example, a detection in experiments of disturbance with frequency $F_1/4$ having rather large amplitude. That can testify the resonant cascade energy transfer through spectrum to the region of strongly dissipated low frequencies.

On the basis of three-wave model a spatial evolution of triad amplitudes for experimental conditions was numerically designed. Fig. 2 shows the results (in arbitrary units) in comparison with experiment data. Admittedly, an agreement is quite good for the case of simple three-wave model.

Interaction of wave trains

It is obvious, that the three-wave model is a limiting simplification of real nonlinear process. The wave spectra, received by Fourier - decomposition of experimental amplitudes, testify, that the disturbances represent rather wide spatial wave packets. In this case, bearing in mind that $a_j = a_j$ (X, ω_j, β_j), an amplitude of a disturbance with certain frequency ω_j can be defined as follows:

$$a_j(\omega_j) = \int a(\omega_j, \beta_j) d\beta. \tag{2}$$

Substituting integration in (2) by summation, we should present each disturbance of frequencies ω_1 and ω_2 as a wave packet consisting of a sum of N narrow wave packets:

$$a_j = \sum_{n=1}^{N} a(\omega_j, \beta_n) \tag{3}$$

In this case amplitude equations (1) can be generalized easily:

$$\frac{da_{1n}}{dX} = -Im(\alpha_{1n})a_{1n} + \varepsilon \sum_{k,l=1}^{N} S_1 a_{2k} a_{2l} \, exp(i\Delta_{1nkl})$$

$$\frac{da_{2m}}{dX} = -Im(\alpha_{2m})a_{2m} + \varepsilon \sum S_{2mkl} a_{1k} a_{2l}^* \, exp(i\Delta_{2mkl})$$

(4)

Right-hand sums include those pairs which answer resonant condition for β.

In this work numerical calculations of the evolution of resonantly interacting wave packets with frequencies $F_1=38\times10^{-6}$ and $F_2=19\times10^{-6}$ are presented (M=2 and other parameters answer experimental conditions) according to the formulas (2). Spanwise wave number interval (-2; + 2) rad/mm was divided into 20 narrow wave packets, i.e. N=20. Initial conditions for amplitudes were set by two ways: (1) at x=44 mm partial amplitudes are set equal for every wave mode; (2) initial amplitudes were set according to experimental distributions at x=60 mm.
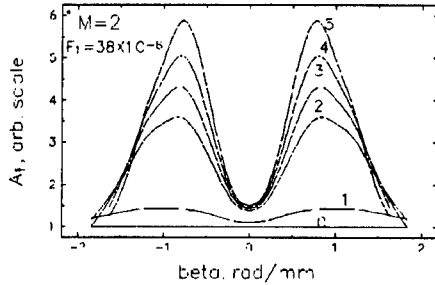
Fig.3a. Spanwise amplitude
distribution: 0-X=44 mm;
1-X=60 mm;2-X=100 mm;
3-X=110 mm; 4-X=120 mm;
5- X=130 mm.
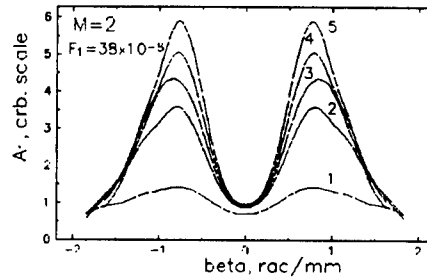
Fig. 3b. Spanwise amplitude
distribution: 1-X=60 mm;
2-X=100 mm; 3-X=110 mm;
4-X=120 mm; 5-X=130 mm.

Numerical results for fundamental mode are displayed on Fig. 3a and Fig. 3b. As it can be seen, the initial spectrum undergoes significant transformation downstream which does not depend on the way of initial condition definition. Fig. 3a shows that for the case (1), when equal initial amplitudes were determined at
x=44 mm, one wave length downstream from the sauce of disturbances, placed at
x=38 mm, two wide maxima appeared in $a(\beta)$-distribution at x=60 mm, that is only

two wave lengths downstream. This maxima were located in the vicinity of $\beta = 1$ rad/mm, in full accordance with linear stability theory. At the next section, the maxima shifted to $\beta = 0.8$ rad/mm, where remained in all subsequent sections and became significantly narrow. Comparison of these distributions demonstrates a good qualitative agreement with experimental distributions [1, 2].

REFERENCES

1. Kosinov A. D., Maslov A.A., Shevelkov S. G. Experiments on the stability of supersonic laminar boundary layers //J.Fluid Mech. - 1990.-V.219.-P. 621-633. (See also: Applied Mechanics Reviews, 1991, N5, p.1080).
2. Ermolaev Yu. G., Kosinov A.D., Semionov N.V. Experimental investigation of laminar-turbulent transition process in supersonic boundary layer using controlled disturbances //Nonlinear Instability and Transition in Three-Dimensional Boundary Layers (IUTAM Symp.) .-1995.-P.17-26.
3. Kosinov A. D., Tumin A.M. Resonant interaction of wave trains in supersonic boundary layer //Nonlinear Instability and Transition in Three-Dimensional Boundary Layers (IUTAM Symp) - 1995.-P.379-388.
4. Zelman M. B., Maslennikova I. I. Tollmien-Schlichting-wave resonant mechanism for subharmonic-type transition //J. Fluid Mech.-1993. -V.252.-P.449-478.
5. Gaponov S. A., Maslennikova I. I. Subharmonic instability of supersonic boundary layer //Methods of Aerophys. Research (Intern. conf.) -1996. V.1.-P.102-107.
6. Gaponov S. A., Maslennikova I. I. Subharmonic instability of supersonic boundary layer //Termophysics and Airomechanics.-1997.-V.4.- N1.-P.1-9.
7. Gaponov S. A., Maslennikova I. I., Tyushin V. Y. Stability investigation of supersonic boundary layer flow on the basis of weakly nonlinear theory // Models of the mechanics of continuous matter. (Intern. conf.) 1997. -V.1.-P. 82- 86 (in Russian).

EXPERIMENTAL INVESTIGATION OF THE HYPERSONIC BOUNDARY LAYER STABILITY ON A CONE WITH A FLARE

A.A. Maslov, A.N. Shiplyuk, A.A. Sidorenko

Institute of Theoretical and Applied Mechanics SB RAS,
630090, Novosibirsk, Russia

Ph. Tran

Aerospatiale Espace and Defense, Aerodynamic and Electromagnetism
Department 66, Route de Verneuil - BP 2 78133 Les Mureaux Cedex, France

INTRODUCTION

When solving applied problems the necessity to define the flow characteristics in the interaction area of the hypersonic boundary layer with the flow inhomogeneities such as an expansion fan, shock wave etc. often arises. The major effect of the inhomogeneities listed is connected with appearance the pressure gradient that not only changes mean flow characteristics but also influences on the boundary layer stability.

Few theoretical and experimental studies on the effect of pressure gradients on the primary instability of compressible boundary layers have been performed. The review of these investigations can be found in [1,2]. It was shown that the effectiveness of favorable pressure gradients for natural laminar flow control decreases at hypersonic Mach numbers and three-dimensional first-mode waves are much more unstable with adverse pressure gradients than two-dimensional ones.

The only experimental investigations of the supersonic boundary layer stability to artificial disturbances at the interaction with the compression ramp on the axis-symmetric model were carried out at Mach 2 [3]. Amplitude spectra on wave numbers in transversal direction for different values of the longitudinal coordinate were obtained. It was noted of a considerable increase of the disturbance amplitude practically for all wavefront inclination angles. The most intensive increase of disturbances begins at the wavefront inclination angle $\chi = 60°$. For comparison notice that disturbances in the boundary layer of a cone were mostly increasing at $\chi = 50°$.

These results assure us that with the increase of the Mach number some specific features in the supersonic boundary layer stability appear. Besides that, it is known from the theory that high instability modes appear starting from $M \geq 4$. Investigation of artificial disturbances development on a model of cone with a flare will allow one to make a study of the laminar-turbulent transition process in the inhomogeneous boundary layer.

TEST FACILITIES, MODELS AND DATA ACQUISITION

Hypersonic wind tunnel T-326 ITAM SB RAS was used for measurements at the free stream Mach number $M_\infty = 5.92$ and unit Reynolds number $Re_1 = 11.8 \cdot 10^6 \, m^{-1}$. The test section of this wind tunnel represents Effel chamber, the diameter of axisymmetrical nozzle is 200 mm. Stagnation pressure P_0 and temperature T_0 in the experiments were kept constant
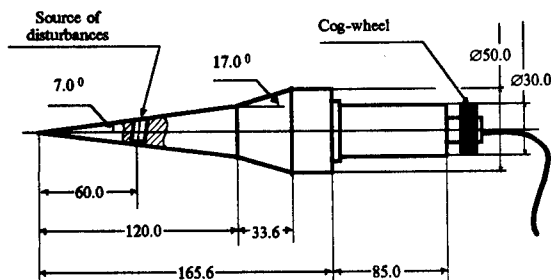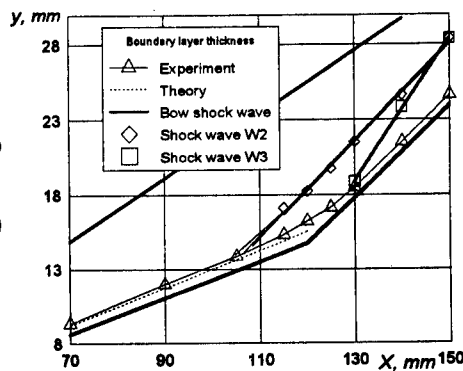
Fig.1 Scheme of the model

Fig 2 Flow pattern near compression ramp

(P_0= 10 kg/cm^2, T_0= 390 K). In order to define flow parameters in each of experiments, P_0 and T_0 were measured with accuracy of 0.5% and data were stored on hard disk of IBM computer. Moreover this computer was used for control of moving of the Pitot probe and hot wire.

For research of static pressure distribution, Pitot pressure measurements and investigation of disturbances development in the boundary layer two geometrically similar models were made. They were installed in the test section with the same model support. The first model was manufactured from steel and designed for the studies of artificial and natural disturbance development in the boundary layer over the compression ramp. The source of artificial disturbances had construction similar to one described in [4] and was installed in the model at 60 mm from the cone nose. Also one thermocouple was installed on the model. The model could be rotated about longitudinal model axis by means of the rotating gear with an accuracy of 0.1°. The scheme of the model is presented in Fig. 1. The second model was designed for static and Pitot pressure measurements. It had the same geometry and fitted 30 pickup holes. Models had the same stings and were installed in the test section with zero incidence angle.

A constant-current hot-wire anemometer TPT - 4 with the frequency band up to 200 kHz was used in the measurements. The method of measurements by means of constant-current hot-wire anemometer is commonly used in hypersonic flows and described, for example in [6]. The alternate and constant electric signals from the anemometer output were transferred to a personal computer of IBM type using a 2-channel 10-bit ADC. A hot wire with length of approximately 1.5 mm made of 5 µm tungsten wire was used to measure the flow pulsations. The hot wire was moved along the x coordinate by the three-component traversing gear with an accuracy of 0.1 mm. The motion along normal coordinate y was performed by the microtraversing gear with an accuracy of 0.01 mm. The hot wire position was correlated with the model surface by an electric contact of the hot wire with the model. Then to the y coordinate was added the half diameter of the wire support (0.05 mm).

For determining the pulsation spectra, the alternate signal from the hot-wire anemometer was digitized with the clock frequency of 333 kHz by means of ADC and transferred into the personal computer. This clock frequency of data acquisition allowed for the analysis of signals with frequency up to 166 kHz. To exclude a possible spurious effect of signals with a higher frequency, a low-frequency filter was used that cut off the signals with frequency higher than 165 kHz. A realization of about 2·10^5 readings was recorded for each point of the boundary

layer profile. The spectra of signals with frequencies higher than 100 kHz were not sufficiently smooth despite a large realization size due to a low value of the signal on these frequencies.

RESULTS

Mean flow characteristics The study of the static pressure distribution on the model surface and Pitot pressure P_0' profiles inside boundary layer has been performed [5]. Model was in adiabatic conditions. The obtained results have shown that a laminar separation of the boundary layer with a laminar reattachment is formed on the examined model. The presence of a slight increase of pressure inside the region testifies to a concave shape of the separation region boundary. The flow pattern near compression ramp is shown in Fig. 2. The positions of shock waves and both of theoretical and experimental boundary layer thickness values are presented in figure. It is seen that separation zone is located between $x = 105$ and $x = 130$ mm (x - the longitudinal coordinate counted from the nose along model axis).

Natural disturbances The integral level of mass flow pulsations $<m>$ with respect to the local mass flow versus y/δ (where δ is boundary layer thickness) ahead of the separation region, in the separation region and after the boundary layer reattachment is shown in Fig.3 (a, b, c), respectively. The level of pulsations in the boundary layer is higher than one in the
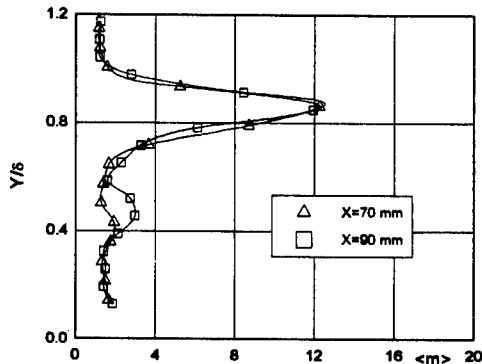
Fig.3 (a)
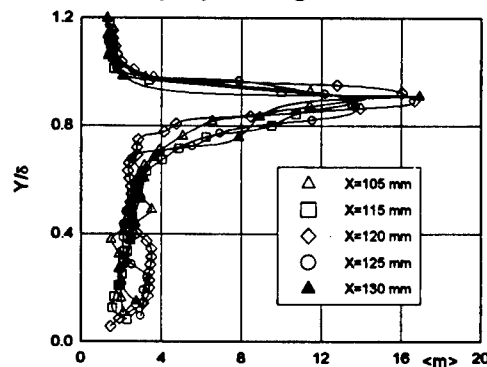
Fig.3 (b)
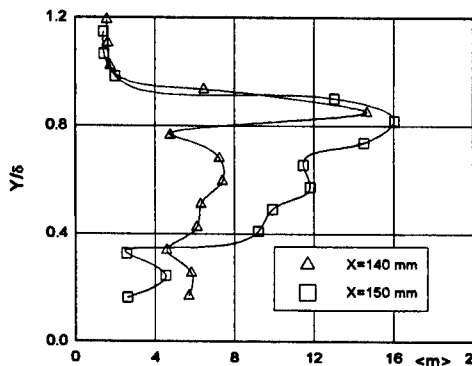
Fig.3 (c)
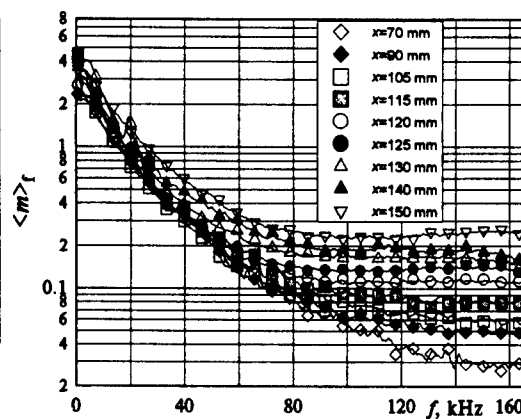
Fig.3 Distribution of integral pulsation $<m>$ across boundary layer before (a), inside (b) and after (c) separation zone.

Fig.4 The spectra of $<m>$ for all nine cross-sections measured in the maximum of fluctuations.

158

inviscid flow. There are large peaks of disturbances at $y/\delta \cong 0.8 \div 0.9$, their amplitude being higher than in the inviscid flow by a factor of $8 \div 10$. Approaching the wall, the disturbances are rapidly damped. An increase of fluctuations of all frequencies in the near-wall region is observed in the separation region. This is especially well seen in Fig.3(b). Disturbances increase after the reattachment in the entire boundary layer. This is apparently caused by the beginning of the boundary layer turbulization (see Fig. 3 (c)).

Figure 4 shows the spectra of $<m>$ for all nine cross-sections measured in the maximum of fluctuations. Since the amplitude of pulsations decreases rapidly with increasing the frequency, the $<m>$ axis is built in the logarithmic scale. According to their behavior, pulsations can be divided into three regions: low-frequency (<20 kHz), medium-frequency ($20 \div 80$ kHz) and high-frequency (>80 kHz). Low-frequency disturbances in the separation region increase slowly (by approximately 1.5 times). Disturbances of the medium-frequency region are neutral. High-frequency pulsations in the separation region increase strongly (about by a factor of 5). The boundary between the medium-frequency and high-frequency pulsations is not fixed but moves gradually to the region of lower frequencies. After the reattachment ($x = 140$, 150 mm) disturbances of all frequencies increase, which indicates the beginning of the boundary layer turbulization. Since the fraction of high-frequency disturbances is small, as it is seen from the spectra, the eigenfunctions presented above reflect mainly the amplification of low-frequency disturbances.

Artificial disturbances development Disturbances with the frequency 40 kHz were introduced into the boundary layer with aid of an electric discharge source. This frequency corresponds to the frequencies-medium region from the measurements of natural disturbances. The electric signal from the generator whose frequency was checked by a frequency meter was amplified and used to trigger an electric discharge in the chamber of the source of disturbances. The technique of artificial disturbances introduction into the boundary layer was similar to supersonic one which is circumstantially described in [4]. The exit orifice of the source had a diameter of 0.4 mm. To eliminate the influence of random noise and contribution of natural disturbances, multiple accumulation and averaging of the alternate component of the hot-wire signal were carried out. For this purpose, the signal was recorded simultaneously with the discharge initiation, and a narrow-band filter was used.

The measurements were taken in the layer of the maximum value of pulsations. For this purpose, the hot wire in each cross-section was set in the position corresponding to the maximum variable component of the hot-wire signal, and then the signal amplitude and phase distributions over angle of model rotation θ were recorded with an interval of $3°$. Thus, the amplitude and phase distributions of disturbances were obtained in nine cross-sections.

From the data obtained, the transverse wave spectra for all cross-sections were calculated. The amplitude and phase distributions versus the transverse wavenumber β are presented in Fig.5 One can see from the figure that the source generates a wave packet with a large content of waves with small inclination angles. Then the plane wave ($\chi = 0$) is rapidly attenuated, and inclined waves play the major role. An inclined wave propagating at an angle of $\sim60°$ ($\beta \cong 0.7$) is revealed already in the second cross-section, which is found afterwards in the wave spectra of all subsequent cross-sections. It should be noted that a plane wave appears in the wave spectrum again in the cross-section located immediately behind the beginning of the separation region. This testifies that the circular separation line is a generator of two-dimensional disturbances. In the course of the wave packet development in the separation region, the plane wave is rapidly attenuated, and an inclined ($\sim60°$) wave is revealed. A peak corresponding to
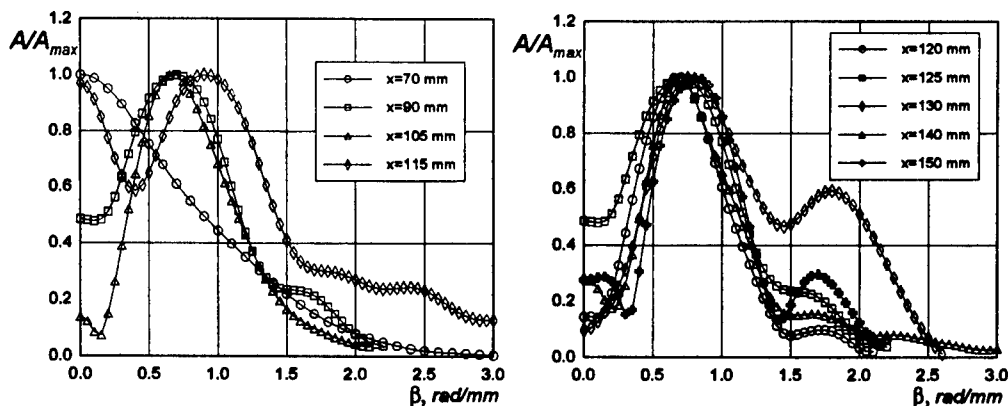
Fig.5 The transversal spectra of artificial disturbances for all cross sections

the wave propagating at an angle of ~80° is identified in transverse wave spectra for cross-sections located downstream of the separation region. Appearance of this peak may testify to the beginning of nonlinear processes in the boundary layer.

Since the flow under study is rather complicated and the number of cross-sections is limited, it does not seem possible to perform a full spectral analysis in the streamwise direction. A simplified technique was used to obtain the values of phase velocity of the waves with different inclination angles. The streamwise wavenumber α_r was estimated from the formula

$$\alpha_r(\beta) = \frac{\Delta\varphi(\beta)}{\Delta x}$$ and the phase velocity of disturbances was determined as $C_x(\chi) = \frac{\lambda \cdot f}{U_e}$ where

$\chi = arctg\frac{\beta}{\alpha_r}$ is the of wavefront inclination angle to the main stream, U_e - velocity at the edge

of boundary layer and $\lambda = \frac{2\pi}{\alpha_r}$ is the disturbance wavelength. It should be noted that such

evaluation has integral nature, therefor only approximate conclusions about structure of wave packet can be made. Such an estimate was carried out for all three flow regions separately: upstream separation zone, inside it and downstream it. Figures 6 (a, b, c) show the phase velocity of disturbances versus the wavefront inclination angle for three flow regions. The solid line in the figures indicates the maximum propagation velocity of acoustic disturbances as a

function of the wavefront inclination angle $\tilde{C}_x(\chi) = 1 - \frac{1}{M_e \cdot \cos\chi}$. One can see that a plane

a)   b)   c)
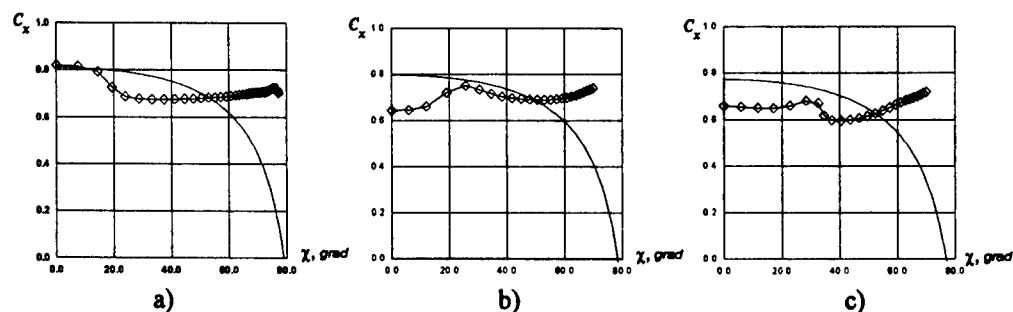
Fig.6 Phase velocity of artificial disturbances: upstream (a); inside (b) and downstream of separation zone (c).

160

wave is developed near the source, while inclined acoustic waves show up downstream. In the separation region and downstream , the phase velocities of disturbances with χ less than $55°$ are less then $\tilde{C}_x$. Thus, in these regions acoustic waves are prevalent. At the same time increase of integral C_x for $\chi = 20 \div 35$ degree points out existence of vortex like waves with same χ.

It should be noted that these results are only estimated, since the minimum number of cross-sections was examined in each region, therefore, the value of phase velocity could be obtained with a considerable error.

CONCLUSIONS

The structure, mean and fluctuating characteristics of a hypersonic boundary layer in the separation region have been experimentally studied on the model of the 7^0 cone with a flare at the free-stream Mach number $M_\infty = 5.92$ and unit Reynolds number $Re_1 = 11.8 \cdot 10^6 \, m^{-1}$.

The development of natural disturbances in the boundary layer over the compression ramp has been studied, the eigenfunctions and pulsation spectra have been obtained. It is shown that the main fluctuations are concentrated in a narrow region near the upper edge of the boundary layer. From the changes in disturbance spectra downstream, three typical regions (low-frequency, medium-frequency and high-frequency ones) are identified. After the reattachment disturbances of all frequencies increase, which indicates the beginning of the boundary layer turbulization.

The evolution of artificial disturbances in the boundary layer in the separation region has been studied. Wave spectra have been obtained, and the wave inclination angles have been estimated. The onset of two-dimensional disturbances in the separation region is shown, which is apparently related to a high receptivity of the boundary layer in the inhomogeneous region. Phase velocities of disturbances have been estimated, which show that acoustic disturbance prevail at small wave inclination angles $<55^0$, and vortex disturbances prevail at high angles.

ACKNOWLEDGEMENT.

REFERENCES

1. Malik, M.R. 1987 Prediction and control of transition in hypersonic boundary layers. AIAA–87–1414 Paper.
2. Weil, H. 1951 Effect of pressure gradient on stability and skin friction in laminar boundary layers in compressible fluids. J. Aeronaut. Sci., 18, pp. 311–318.
3. Kosinov, A.D. & Shevel'kov, S.G. 1991 Experimental investigation of separation and stability of supersonic laminar boundary layer. Proc. IUTAM Symp. Berlin: Springer-Verlag, pp. 741–745.
4. Kosinov, A.D., Maslov, A.A. & Shevel'kov, S.G. 1990a Experimental study of the harmonic disturbances development in the boundary layer of flat plate at Mach number M = 4. Izv. AN SSSR, Mekh. Zhidk. i Gasa, No. 6, pp. 54–58 (in Russian). (Fluid Dynamic 1991, v. 25, pp. 654–658).
5. A.A. Maslov, A.N. Shiplyuk, A.A. Sidorenko and Ph. Tran, Study related to hypersonic boundary layer stability on a cone with a flare. - Novosibirsk, 1997. - 40 p. - (Preprint / SB RAS, Institute of theoretical and applied mechanics; № 2 - 97)
6. Stetson K.F., Thompson E.R., Donaldson J.S., Siler L.G. Laminar boundary layer stability experiments on a cone at Mach 8. Part 1: sharp cone. AIAA–83–1761 Paper.

LEADING EDGE RECEPTIVITY OF THE HYPERSONIC BOUNDARY LAYER TO 3-D ACOUSTIC WAVES

A.A. Maslov, A.N. Shiplyuk, A.A. Sidorenko,
Institute of Theoretical and Applied Mechanics, SB RAS
630090, Novosibirsk, Russia

D.Arnal
Centre D'Études et de Recherches de Toulouse, ONERA
Toulouse, France

The subject of laminar-turbulent transition is of considerable practical interest and has a wide range of engineering applications, due to the fact that transition controls the evolution on important aerodynamic quantities such as drag or heat transfer. The mechanisms that drive the dynamics of transition to turbulence depend on the environmental disturbance level. If the free stream disturbances are weak enough and if the wall is smooth, the first stage of the transition process is so-called boundary layer *receptivity*. Receptivity refers to the mechanism that cause the environmental disturbances to enter the boundary layer and to generate unstable waves. At the present time, the receptivity mechanisms are poorly understood, especially at high Mach numbers. However, the understanding of these phenomena is of great importance because the receptivity makes the link between the amplitude of the free stream disturbances and the initial amplitude of the unstable waves.

The first experimental study of the boundary layer receptivity to external disturbance at supersonic flow velocities was presented in [1]. It was measured the correlation coefficients between the free stream and boundary layer pulsations.

A method using controlled disturbances has been developed at ITAM SB RAS to study the wave processes in supersonic flows [2]. Using the acoustic waves incident onto the leading edge of the model from below, receptivity studies were performed at Mach numbers M=2 [3] and M=3.5 [4]. It was established in [3] that external disturbances propagating upstream do not excite the boundary layer pulsations, only external acoustic waves propagating downstream were responsible for the excitating of boundary layer pulsations. Receptivity coefficients were obtained for the latter case. The maximum receptivity coefficients were observed for the waves with inclination angles in XZ plane $\chi=20°\div40°$. The field of controlled disturbances in the free stream at M=3.5 was studied in [4]. The field of disturbances had a more complicated structure than at M=2. The absolute amplitudes and the mode structure of controlled pulsations were obtained. It was shown that disturbances introduced into the free stream had an acoustic nature. The excitation of pulsations in the boundary layer by external disturbances at M=3.5 was much more intensive than at M=2. Inclined waves had larger receptivity coefficients than the waves with $\chi=0°$. Experimental investigation of boundary layer receptivity to 2D acoustic waves at M=6 was presented in [5]. It was shown that hypersonic boundary layer has bigger receptivity than supersonic one.

The experimental study of the leading edge receptivity to external acoustic waves at hypersonic speeds using a point source of controlled disturbances was performed in the present work.

Experimental equipment. The experiments were performed in hypersonic blowdown wind tunnel T-326 ITAM SB RAS at the free stream Mach number $M_\infty=5.92$

and unit Reynolds number $Re_1=13\cdot10^6$ m^{-1}. The test section of the wind tunnel is an Eiffel chamber, the diameter of axisymetrical contoured nozzle is 200 mm. The time of continuous operation of the wind tunnel is up to 20 minutes. The Mach number flow field non-uniformity in the flow core at M$\cong$6 is 0.7%. During the experiment P_0 and T_0 were kept constant with the maximum possible accuracy; thus, the free stream mass flow rate was varied in the course of experiment by no more than 1%. The models surfaces were under adiabatic conditions. Receptivity to acoustic disturbances introduced into the external flow by a point source was studied for two disturbance frequencies f=31.6 and 50 kHz (F=0.19$\cdot$10^{-4} and 0.30$\cdot$10^{-4}, respectively).

An automated system for measurements of the mean and fluctuating flow parameters is based on two personal computers with Pentium-133 processors. One computer is connected to a CAMAC crate, it is used for acquisition and processing of the information about the mean flow parameters and for traverse gear control. Using a two-channel built-in ADC, the second computer is responsible for measurements of the mean and alternate signals of the hot-wire anemometer. The data transfer between the computers is carried out via the TCP/IP protocol of the Ethernet network with a rate of 10 MBit/s.

A constant-temperature hot-wire anemometer made at ITAM was used for measurements of the mass flow fluctuations. The hot-wire probes were made of tungsten wire 5 μm in diameter and 1 mm long, which was welded to pointed stings. Probes were moved with an accuracy of 0.01 mm in Y direction and 0.1 mm in the X and Z directions. The alternate signal from the hot-wire was fed to a selective amplifier with a 1% transmission band width, thus improving the signal-to-noise ratio. The constant and alternate components of the hot-wire signal were measured by a two-channel 10-bit ADC with a sampling frequency of 1 MHz. To exclude random fluctuations and reveal artificial disturbances, a synchronous summation of the signal was used. For this purpose, the recorded realizations of 128 samples were summed 1000 times.

To generate a high-frequency discharge, an electric pulse generator was developed. It generated high-voltage (up to 1000 V) electric pulses with duration 2 μs and repetition frequency 30$\div$180 kHz. This device was triggered by a master frequency generator with a frequency stability better than 0.01% and was fed from a DC source.

Models. Two models (**P** and **T**) were made for experiments on the leading edge receptivity to acoustic disturbances. The models were flat steel plates with sharp leading and side edges. The edge angle is 15°. The radii of the models leading edges were less than 0.05 mm. The working surfaces of the models were carefully polished.

Model **P** had a point electric discharge source of disturbances. The construction of this source is based on a spark electric discharge in the chamber and is similar to the construction described in [2]. Artificial disturbances were introduced into a hypersonic boundary layer through an orifice 0.4 mm in diameter, made in the working surface of the plate. The source coordinates were X=45 mm, Z=0 mm, where X is the streamwise coordinate counted from the leading edge of the model, Z is the spanwise coordinate counted from the symmetry plane of the plate.

Model **T** located in the region of influence of disturbances from the sources of model **P**. A possibility of moving the model **T** in the vertical direction between the runs was ensured. The models were installed at zero incidence with an accuracy of 0.3°. The X distance between the leading edges of models **P** and **T** was 99 mm. The Y distance between the models was chosen after the field of disturbances in the flow was investigated.
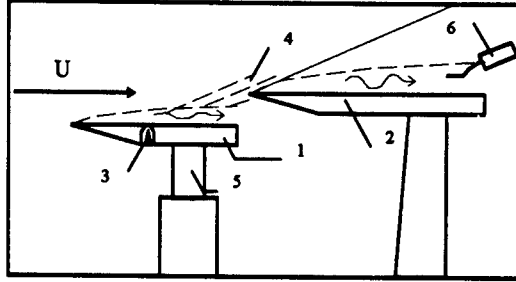
A scheme of model positions is shown in Fig. 1.

163

Fig.1 The model disposition in the hypersonic wind tunnel T-326 ITAM SB RAS. (1–model P, 2–model T, 3–source of disturbances, 4–acoustic radiation, 5–model pylon, 6–hot wire).

Data processing It was assumed in data processing that at a high overheating the hot-wire is sensitive only to mass flow fluctuations, since the mass flow fluctuations are much larger than the temperature fluctuations. In this case, the output voltage pulsations of the constant temperature hot-wire anemometer are proportional to mass flow fluctuations [6]:

$$< E > = \frac{n}{2}\left(1 - \frac{L}{E^2}\right) < m >$$

The factor L is found from the dimensional calibration dependence: $E^2 = L + N \cdot m^n$.

A further simplification of the data processing procedure was made using the results presented in [7]. It was experimentally found in this work for the free stream Mach number M=2 that the factor $Q = \frac{n}{2}\left(1 - \frac{L}{E^2}\right)$ is practically independent of the Reynolds number and hot-wire probe overheating. It was shown that Q=0.24±0.01.

The discrete Fourier transform was used to determine the amplitude and phase of controlled disturbances. To obtain the spatial wave spectra, discrete Fourier transforms with respect to X, Y, Z coordinates using a spectral window were used.

When determining the wave inclination in the XY plane, one can take into account that disturbances in a supersonic flow propagate along the Mach lines. The following relationship between the streamwise (α_r) and vertical (γ) wave numbers was obtained:

$$\frac{\gamma}{\sqrt{M_\infty^2 - 1}} = -\alpha_r + \frac{2\pi f}{U_\infty} \cdot \frac{M_\infty^2}{M_\infty^2 - 1} \cdot \qquad (1)$$

From here, we can obtain the wave vector inclination angle in the XY plane:

$$tg(\varphi) = \sqrt{M_\infty^2 - 1} \times \left(-1 + \frac{C_x}{U_\infty} \cdot \frac{M_\infty^2}{M_\infty^2 - 1}\right) \cdot \qquad (2)$$

Free stream fluctuations. The measured amplitude and phase distributions pulsations along the streamwise coordinate X (Fig.2) are very similar to data obtained in [3,4]. The main difference in the source of disturbances used in these investigations and in the present work is that the disturbances are simultaneously introduced by a spark discharge through an orifice in the model and by a glow discharge on the model surface because of the low static pressure. The size of the source of disturbances exceeds considerably the size of the orifice. This is especially noticeable at high voltages on the electrodes. Following [4], we can suggest a simplified model of the source of disturbances. Two periodic electric discharges generate two toroid vortices, their axes being perpendicular to the XZ plane. These vortices interact with each other and generate disturbances propagating upstream and downstream.
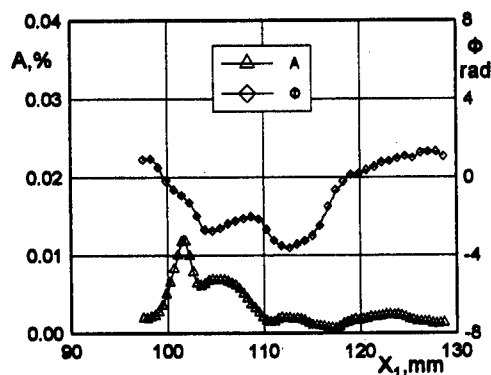
164

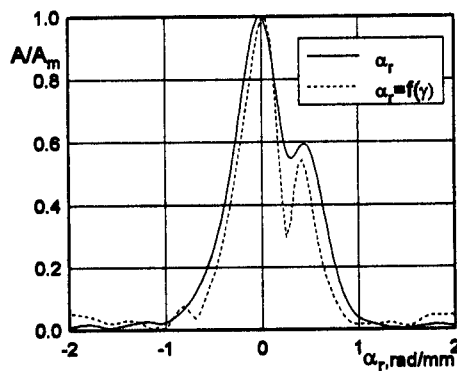Fig.2 Amplitude A and phase Φ of pulsations in the free stream along the streamwise coordinate X

Fig. 3 Comparison of α_r spectra, obtained from pulsation distribution along X, and α_r spectra, evaluated from γ spectra

Tollmien-Schlichting waves propagating downstream are also excited in the boundary layer of the model P. These processes are accompanied by emission of acoustic oscillations into the external flow. The field of emission should be complicated and consists of several zones where the disturbances propagate with different phase velocities. In phase distributions, using the linear regions of phase variation with respect to X as a criterion, one can roughly reveal characteristic zones of disturbances with a constant phase velocity.

Amplitude and phase distributions pulsations along the vertical coordinate Y were also measured. The wave number spectra along X and Y (α_r, γ - spectra) were obtained after the discrete Fourier transform of distributions along X, Z. The γ spectra can be used to estimate the α_r spectra from formula (1). The results of these estimates are presented in Fig.3. The results are in satisfactory agreement, which means that the pulsations really propagate in the flow along the Mach lines. In this case, the wave inclination angles φ in the free stream can be estimated using formula (2). The results of such an estimate showed that high-amplitude waves are introduced at $\varphi \cong 90°$, the waves with small inclination angles ($\varphi \cong 0°$ and $\varphi \cong 180°$) have appreciably smaller amplitudes.

Receptivity measurements. To obtain the maximum accuracy, it was decided to perform all the necessary measurements in one run. To do so, one had to measure during one run the X and Z distributions of pulsations in the free stream upstream of the leading edge of model T (as close to it as possible) and the same distributions in the layer of maximum pulsation in boundary layer of model T to obtain the α_r and β spectra of pulsations of external acoustic disturbances and proper disturbances of the boundary layer. However, the time of one run (≈20 min) was sometimes insufficient to obtain all the information. Therefore, the X distributions in the boundary layer of model T were measured only once for each frequency of pulsations (50 and 31.6 kHz). Some Z distributions in the boundary layer of model T were not completely measured either. A total of four measurements of this type were performed at difference distances between plates and at two frequencies (31.6, 50 kHz).

From the inclination of the pulsation phase curves, one can estimate the streamwise wave number of external acoustic disturbances α_r near the leading edge. To obtain the phase derivative with respect to X, a polynomial approximation was used. Then we estimated the inclination angle of an acoustic wave in the XY plane using formula (2) and
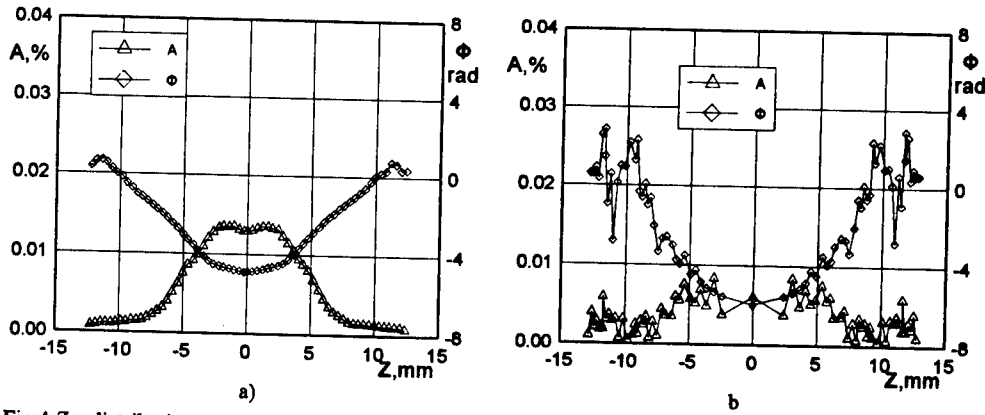
165

Fig.4 Z – distributions of amplitude A and phase Φ of external acoustic disturbances (a) and boundary layer pulsation (b).

obtained that in all cases φ-angle was close to 90^0.

Distributions of phase in the center of wave packet in the boundary layer was measured. The wave numbers and phase velocities were obtained: $\alpha_r=0.46$ and 0.31, $C_x/U=0.83$ and 0.78 for $f=50$ and 31.6 kHz, respectively. The values of phase velocity are close to $1-1/M_\infty=0.83$; hence, the acoustic waves generate mainly the Tollmien-Schlichting waves in the boundary layer.

The measured spanwise pulsations distributions in the boundary layer (Fig.4b) are in qualitative agreement with the profiles of external disturbances (Fig.4a), contrary to spanwise distributions obtained at M=3.5 [4].

After the discrete Fourier transform of the Z distributions, the transversal wave spectra (β spectra) were obtained (Fig.5). Plot shows the β spectra of pulsations in the free stream and in the boundary layer. It is seen that the maximum of pulsations in the free stream is at $\beta=0$, the amplitude of pulsations decreases rapidly as β increases. The amplitude of pulsations in the boundary layer at $\beta<1$ rad/mm is smaller than in the free stream. At $\beta>1$ rad/mm the pulsation amplitude in the boundary layer becomes larger (at $f=50$ kHz) than in the free stream.

<u>Receptivity coefficients.</u> Since the amplitudes of controlled disturbances of the mass flow in the experiments were very small (<0.04%), the process of receptivity of the boundary layer on the leading edge of the model to external acoustic disturbances can be assumed linear. The receptivity coefficient were determined using the following formula: $K(\beta) = \dfrac{A(\beta)_{X=X'}}{A(\beta)_{X=0}}$

The receptivity coefficients calculated are shown in Fig.6 as functions of the wave inclination angle χ. Besides, data for all experiments are shown in the figure. Receptivity coefficients were calculated for both positive and negative χ (dashed lines) whereas solid lines indicate averaged coefficients. The receptivity coefficients were obtained for different values of the streamwise coordinate X in the boundary layer; therefore, they should be compared taking into account the linear development of disturbances in the boundary layer. For the wave inclination angle $\chi=0°$, the receptivity coefficients ($K\cong0.48\div0.65$) are higher than the coefficients obtained at M=2 $K\cong0.25\div0.35$ [3]. Comparison with bigger receptivity coefficients ($K=2.7\div3$) obtained in [5] at M=6 shows that boundary layer is more sensitive to acoustic waves with small inclination angle φ, which is in agreement with results [8].
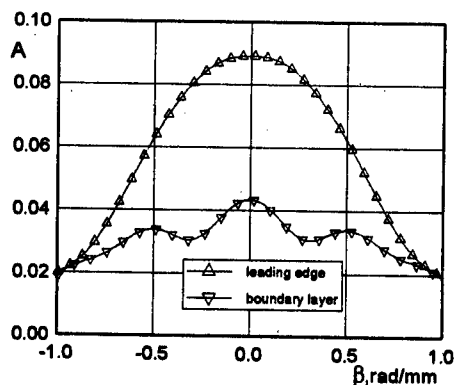
Fig.5 β spectra
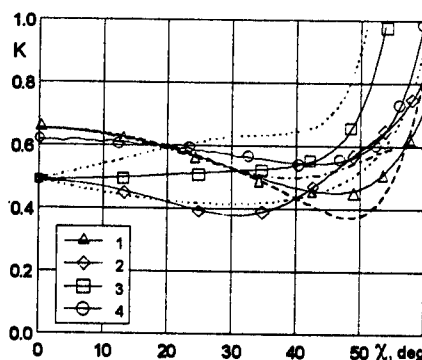
Fig.6 Receptivity coefficients versus wave inclination angle χ. 1-3 - f=50 kHz, 4 - f=31.6 kHz

When increasing χ, the coefficients slightly decrease down to $K \cong 0.38 \div 0.57$ for $\chi = 35 \div 48°$ and then increase rapidly up to $K \cong 1.0 \div 0.7$ at $\chi \cong 55 \div 60°$. This result agrees with [8] where was shown that incline acoustic waves induce biggest excitation of boundary layer. Because of small amplitude of pulsations at high β (see Fig.5) the error of determining the receptivity coefficients becomes large already at $\chi > 60°$.

Conclusions. Experimental investigations of the leading edge receptivity of a boundary layer on a flat plate to controlled acoustic disturbances with frequencies 50 and 31.6 kHz ($F = 0.19 \cdot 10^{-4}$ and $0.30 \cdot 10^{-4}$, respectively) induced by point source of disturbances have been performed for a free stream Mach number $M \cong 6$. A field of the free stream disturbances from a point source has been studied. The resultant spatial distributions of pulsations were similar to the results of measurements taken at M=2 and 3.5. It was shown that the propagating disturbances follow the Mach lines. The waves with inclination angles $\varphi \approx 90°$ prevailed in emission of a point source. The disturbances excited in the boundary layer have been measured. It was shown that disturbances with streamwise phase velocities close to $1-1/M_\infty$ were excited. The maximum resultant receptivity coefficients have been obtained for wave inclination angles $\chi \approx 60°$.

References

1. Kendall J.M. Wind tunnel experiments relating to supersonic and hypersonic boundary-layer transition // AIAA J. 13, N 3, 1975, pp 290–299.

2. Maslov A.A., Kosinov A.D., Shevelkov S.G. Development of spatial wave packets in the supersonic boundary layer. Preprint/ RAS SB, ITAM N 17–18, 1985, Novosibirsk.

3. Semionov N.V., Kosinov A.D., Maslov A.A. Experimental investigation of supersonic boundary layer receptivity // Proc. of colloquium «Transitional boundary layer in aeronautics». Noth-Holland, Amsterdam, 1996, pp. 413–420

4. Kosinov A.D., Maslov A.A., Semionov N.V. Modified method of experimental study of supersonic boundary layer receptivity// Int.Conf. on the Methods of Aerophys.Research: Proc.Pt 3, Novosibirsk, pp. 161–166.

5. Maslov A.A., Shiplyuk A.N., Sidorenko A.A., D.Arnal Leading edge receptivity of the hypersonic boundary layer on a flat plate. Preprint/ RAS SB, ITAM N 1-98. Novosibirsk. 1998.

6. Smits A.J., Hayakawa K., Muck K.C. Constant temperature hot-wire anemometer practice in supersonic flows // Experiments in fluids, Vol.1, 1983, pp. 83–92.

7. Kosinov A.D., Semionov N.V., Ermolaev Yu.G. Automated measuring method of noise level in T-325 test section // Int.Conf. on the Methods of Aerophys.Research: Proc.Pt 2, Novosibirsk, 1996, pp. 131–136.

8. Fedorov A.V., Khohlov A.P. Supersonic boundary layer receptivity to the acoustic disturbances // Izv. Akad. Nauk USSR. Zh. Mech. Zhidk. G. 1, 1992, pp. 40–47 (in Russian).

A NEW TYPE OF HYPERSONIC WIND TUNNELS

G.E.A. Meier and M. Rein

DLR, Institute of Fluid Mechanics
Bunsenstr. 10, 37073 Göttingen

A free piston driven Ludwieg tube is introduced that enables the simulation of flows of high Reynolds and Mach numbers at high stagnation temperatures. The test time is longer than in other hypersonic facilities operating under similar test conditions as, for example, in shock tunnels. The test gas is unsteadily compressed and heated thus reducing the thermal loads to the walls. It is shown that the free piston driven shock tunnel HEG of the DLR at Göttingen can also be run in a free piston driven blowdown tunnel mode.

1. Introduction

In order to fully duplicate high Reynolds and Mach numbers as well as high stagnation temperatures that are characteristic of hypersonic flights in the atmosphere, it is necessary to develop new types of wind tunnels. At ITAM, for example, the concept of adiabatic compression by using pressure multipliers is applied at the facility AT-303 that is presently under development (Kharitonov *et al.*, 1996). Here, we will describe a different approach that can easily be implemented in existing free piston driven high enthalpy tunnels such as the HEG of the DLR at Göttingen. In this manner, hypersonic flows at high static pressures, temperatures and densities can be reproduced during a relatively long test time as compared with, for example, shock tunnels.

At Göttingen the idea of using free piston driven Ludwieg tubes was proposed several years ago (Meier *et al.*, 1991). A piston is used to unsteadily compress and heat the gas in the charge tube of the Ludwieg tube. Because of the short unsteady compression only the gas is heated up while the heat transfer to the tunnel walls remains small. In the following we will discuss the principles of a piston driven Ludwieg tube for the example of a geometry as being present at the HEG (cf. Fig. 1). The charge tube of the Ludwieg tube is formed by the driven section of the HEG. Initially, the test gas fills both, the compression tube and the driven section of the HEG that are no longer separated by a diaphragm. The piston is accelerated into the driven section by pressurized air behind the piston as usual, compressing the test gas ahead of the piston. In this manner both, high pressures and temperatures are obtained thus allowing for a simulation of hypersonic flows with high stagnation temperatures. On principle, such flows can also be produced with the HEG being run in its shock tunnel mode. There, the test time of about $1ms$, however, is one to two orders of magnitudes smaller than in the Ludwieg tube mode. A free piston driven Ludwieg tube is, hence, also well suited for scramjet investigations.

pressure   driver   tube   driven   tube   nozzle   dump tank
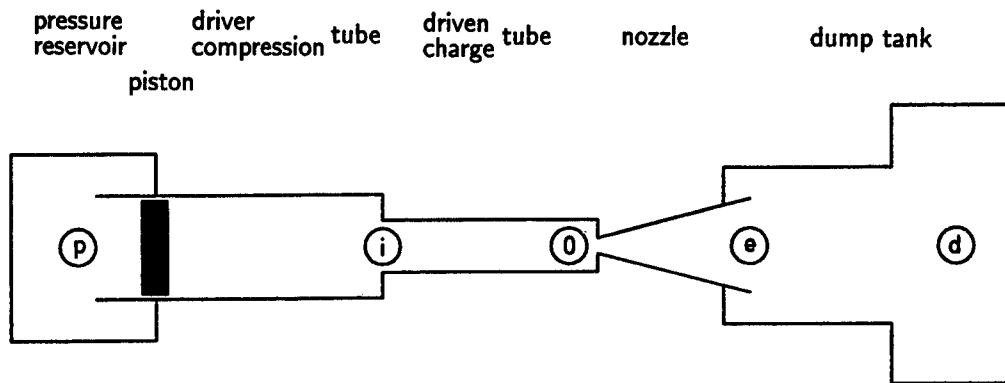reservoir   compression   charge
        piston

Fig. 1: Sketch of the high enthalpy tunnel HEG.

The two operation modes of the HEG are compared in Fig. 2. The compression tube which also contains the piston, the driven and charge tube, respectively, and the nozzle are shown (for more details see McIntyre *et al.*, 1997). One diaphragm is always located directly ahead of the nozzle. In the shock tunnel mode the driver and driven sections are separated by another diaphragm, and the driver and test gas are normally different. The test gas is finally compressed and heated by a shock wave. In the Ludwieg tube mode compression and driven tube that are no longer separated by a diaphragm, are both filled with the test gas. Here, the test gas is directly compressed by the piston which is pushed into the compression tube by pressurized air. The acceleration of the piston needs to be adjusted so that the piston will stop at the end of the compression tube. The strength of the diaphragm ahead of the nozzle needs to be chosen accordingly so that it bursts at the required reservoir pressure. The maximum test time is given by the travelling time of expansion waves through the charge tube as usual.

2. Free piston driven Ludwieg tubes

In free piston driven Ludwieg tubes the test gas is isentropically compressed by a piston. (An entropy production by weak shock waves that may be caused by the steepening of waves will be neglected.) The total duration of the compression phase is so small that a heat transfer from the gas to the tunnel wall will also be neglected. The state of the compressed gas is then directly given by its initial state and the compression ratio α which is defined as

$$\alpha = \frac{V_s}{V_c + V_s} \quad .$$

V_s and V_c are the volumes of the charge and compression tube, respectively. In the case of the HEG, $V_s = 0.30 m^3$ and $V_c = 7.84 m^3$, thus $\alpha = 1 : 27.13 = 3.69 \cdot 10^{-2}$. The length of the charge tube is given by $L_s = 17m$. On principle, the ideal test time is given by the time that an expansion wave needs for propagating back and forth through the charge tube. Disturbances caused by piston motions (such as a rebound) and the finite burst time of the
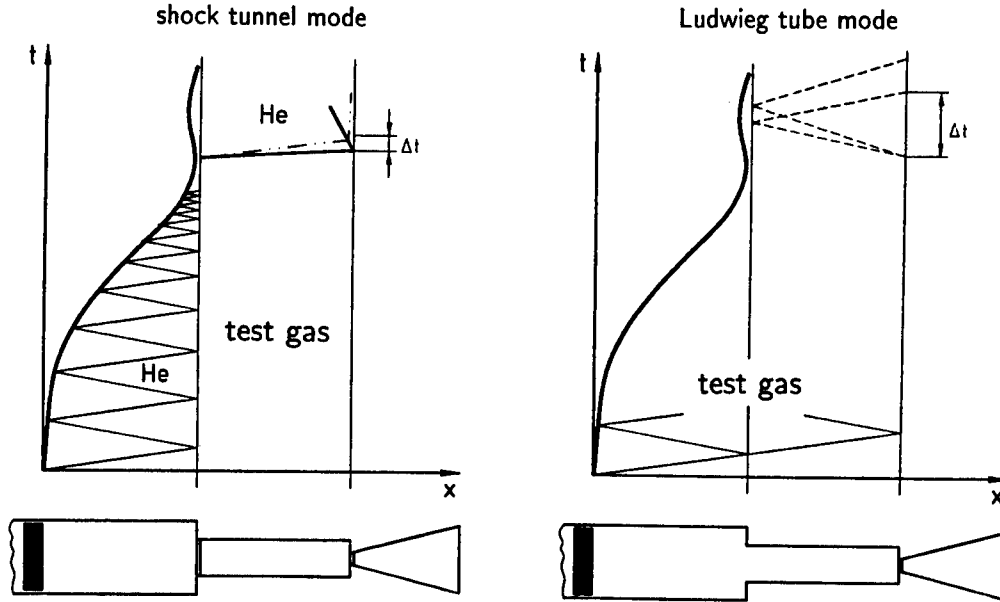
Fig. 2: Comparison of the HEG in the free piston driven shock tunnel mode and in the free piston driven Ludwieg tube mode: wave diagrams and facilities.

diaphragm, as well as the growth of the boundary layer will reduce the test time to smaller values.

In the following, the initial state of the test gas which initially fills both, the compression and charge tube, is denoted by the subscript i. At the end of the compression phase the piston sits at the end of the compression tube right ahead of the charge tube in which the state now equals the reservoir state (subscript 0) of the succeeding nozzle expansion. The test conditions at the nozzle exit are denoted by subscript e (cf. Fig. 1). The mass of the gas is not changed during the isentropic compression. Hence, the reservoir state (pressure p, density ρ and temperature T) is given by:

$$\frac{p_0}{p_i} = \left(\frac{\rho_0}{\rho_i}\right)^\gamma = \left(\frac{T_0}{T_i}\right)^{\frac{\gamma}{\gamma-1}} = \alpha^{-\gamma}$$

where γ is the ratio of the specific heats. In the case of air ($\gamma = 7/5$) and with $\alpha \approx 1 : 27$ this yields $p_0 \approx 100\ p_i$ and $T_0 \approx 3.7\ T_i$. Normally, T_i equals the ambient temperature while the initial pressure can be chosen within wide bounds. Hence, with $T_i = 293K$ a stagnation temperature of $T_0 \approx 1100K$ is obtained. The initial pressure needs to be smaller than the pressure p_p driving the piston. At the HEG the maximum value of the driving pressure is given by $(p_p)_{max} \approx 22MPa$. If we assume that $p_i \leq 0.1 p_p$ in order to accelerate the piston appropiately, the maximum value of the reservoir pressure is given by $(p_0)_{max} \approx 220MPa$.

With reservoir conditions as cited in the last paragraph the nozzle expansion is ideal and, thus, $p_0/p_e = \alpha^{-\gamma} p_i/p_e$. The static pressure in the test section, p_e, can be chosen within certain bounds by adjusting the initial pressure p_i. In the following, the pressure ratio p_0/p_e is assumed to be given. The test conditons at the nozzle exit are then readily obtained. In Fig. 3 the Mach number M_e, the temperature T_e and the Reynolds number per unit length, Re_m, at the nozzle exit are plotted versus the pressure ratio. The Reynolds number per unit length is defined by $Re_m = u_e/\nu(T_e)$ where u_e denotes the flow velocity at the nozzle exit. The kinematic viscosity ν that is a function of temperature, has been fitted to data by Schwier (1984), $\nu(T) = 1.824 \cdot 10^{-3} m^2/sK \quad T + 1.775 \cdot 10^{-4} m^2/sK^2 \quad T^2$ ($100K < T < 350K$). The diameter of the nozzle throat should not be bigger than about one third of the diameter of the charge tube. At the HEG, the diameter of the test section is then $0.25 - 0.35m$ when the exit Mach number lies between $5 - 6$.

In Fig. 3 the dependence on the pressure ratio of M_e, T_e and Re_m has been plotted for different initial temperatures T_i of the test gas (air, $\gamma = 7/5$). This corresponds with different stagnation temperatures ($T_0 = \alpha^{-(\gamma-1)}T_i$). In order to increase the stagnation temperature the test gas needs to be preheated before the compression starts. The stagnation temperature also defines the ideal test time since the sound speed is a function only of the temperature. Under conditions of the HEG the ideal test time lies within $30 - 50ms$. The stagnation temperature not only increases with the initial temperature but also with the compression ratio α. An increase in the compression ratio can be achieved by reducing the radius of the charge tube, e.g., by inserting a liner. A radius reduction of 20% results in $\alpha = 1 : 40$. The temperature increase comes along with a higher density, but occurs at the expense of a decreasing Reynolds number as can be seen in Fig. 3 where the Reynolds number per unit length decreases with increasing initial temperature, i.e., with increasing stagnation temperature. Here, Re_m is of the order of 10^8 $1/m$.

A main difference between the shock tunnel and Ludwieg tube mode is the much higher initial pressure of the gas ahead of the piston in the latter case. This is due to the much higher pressures desired in the test section. We have simulated the piston path using the program PaCT developed at DLR (McIntyre and Atcitty, 1991). The program is based on the classical approach of Hornung (1988). A chocking of the flow at the transition between compression and charge tube where a change in the cross sectional area occurs, has not yet been considered. In our example the initial state is given by $p_i = 1.58MPa$, $T_i = 300K$ and $\gamma = 7/5$. The strength of the diaphragm has been chosen so that it bursts at $p = 150MPa$. In order to accelerate the piston so that it actually reaches the end of the compression tube and does not stop ahead of it, a piston of a high mass needs to be chosen. With the driving pressure behind the piston being $p_p = 22MPa$ it turned out that a piston mass of about $m_p \approx 2200kg$ is required. This is about three times the mass of the most heavy piston in use at the HEG shock tunnel. The maximum piston velocity was about $200m/s$ which is well within the range normally observed at HEG. However, due to the high mass of the piston and the slow pressure reduction ahead of it, a strong rebound can occur. In order to avoid the rebound the piston needs to be stopped at its return point. This is already performed, e.g., at T5, Galcit (Hornung and Belanger, 1990).
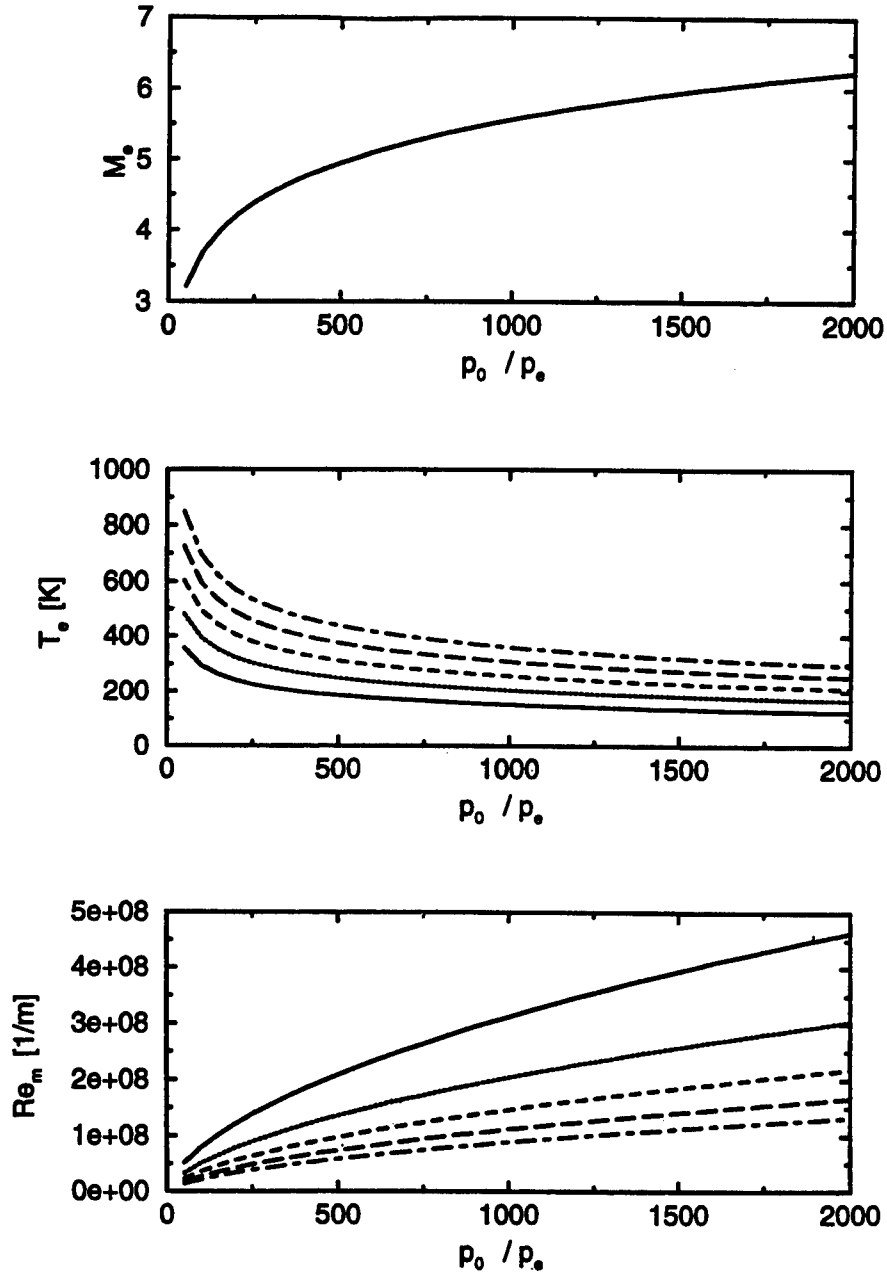
Fig. 3: Conditions in the test section as a function of the ratio between the reservoir and exit pressure, p_0/p_e, at different initial temperatures T_i: (a) Mach number, (b) temperature, (c) Reynolds number per unit length. The test gas is air. (Solid line: $T_i = 293K$, dotted line: $T_i = 393K$, short-dashed line: $T_i = 493K$, long-dashed line: $T_i = 593K$, dash-dotted line: $T_i = 693K$)

3. Conclusions

We have shown that a free piston driven Ludwieg tube is a usefull means of producing hypersonic flows of high static pressures, stagnation temperatures and Reynolds numbers. In particular, the Reynolds number is of the order of $Re_m = O(10^8\ 1/m)$. Static pressures of up to $0.1MPa$ can be obtained in the test section. The stagnation temperature ($T_0 \approx 1100K$) characteristic of the HEG geometry can be increased either by preheating the test gas prior to its compression or by reducing the diameter of the charge tube. In the latter case, however, the diameter of the test section (which is normally in the range of $0.25 - 0.35m$ for $M = 5 - 6$) will also be reduced. In the ideal case the test time is $30 - 50ms$. Free piston driven shock tunnels such as the HEG can be remodelled into free piston driven Ludwieg tubes thus increasing the test time appreciably. In this manner, for example, scramjet investigations become feasible.

4. References

Meier, G.E.A., Eitelberg, G., Krogmann, and McIntyre, T.J., Instationär aufgeheizter Rohrwindkanal, 5. STAB-Workshop, *13.-15. Nov. 1991, Göttingen*, 223-224 (1991)

Hornung, H.G., The piston motion in a free-piston driver for shock tubes and tunnels, *GALCIT, California Institute of Technology, FM 88-1*, Pasadena (1988)

Hornung, H.G., and Belanger, J., Role and Techniques of Ground Testing for Simulation of Flows Up to Orbital Speeds, *AIAA paper no. 90-1377* (1990)

Kharitonov *et al.*, Wind tunnel AT-303, *ITAM, SB RAS* (1996)

McIntyre, T.J. and Atcitty, C., Piston and Compression Tubes - Piston Motion in the High Enthalpy Shock Tunnel (HEG), *DLR IB 222-90 A 20* (1991)

McIntyre, T.J., Krek, R.M., Hannemann, K., Eitelberg, G., Beck, W.H., Kortz, S., Kastell, D. and Wollenhaupt, M., Calibration of the High Enthalpy Shock Tunnel in Göttingen, HEG, *Shock Waves* (accepted for publication, 1997)

Schwier, K., Stoffwerte von Luft, in: VDI-Wärmeatlas, Düsseldorf, Db8 (1994)

INVESTIGATION OF HEAT MASS TRANSFER PROCESSES
IN A BOUNDARY LAYER WITH INJECTION

L.N. Perepechko

Institute of Thermophysics SB RAS,
630090, Novosibirsk, Russia

INTRODUCTION

A Reynolds analogy is wide used for problems of heat and mass transfer, from which follows that equations of motion, energy and diffusion are brought to an identical form at Pr=Sc=1. The use of similarity hypothesises as well as simplifications connected with distribution of transfer coefficients in a flow require justification both for laminar and for turbulent flows.

To calculate the turbulent flows in many cases a molecular heat conductivity and molecular diffusion are considered as negligible quantities in a comparison with a turbulent transfer [1]. An assumption that Pr=Sc=1 is used even in some problems to calculate laminar flows with the heat and mass transfer, for example, in [2] for a modeling of a flow with combustion. Calculations in simplified mathematical statement require less of a time and bring into a satisfactory agreement with experimental data in many cases.

On the other hand, diffusion coefficients of individual substances can differ from each other several times in multicomponent media (for comparison, Schmidt numbers in dilute mixtures with air of hydrogen and ethanol are 0,2 and 1,3 respectively). The Prandtl number depending weakly on a temperature can depend on a composition (for mixture of hydrogen and air the Prandtl number varies from 0,7 to 0,45 versus a hydrogen concentration). A distinction of the Le number from unity can influence essentially on calculating results. For example, in [3] calculating combustion a considerable influence of the Lewis number on a flame temperature is marked.

Therefore the problem on admissibility of the use of the approximation Pr=Sc=1 should be solved for each case individually. In previous studies the authors of the work have considered the problem of burning of ethanol, evaporating from plate into a turbulent boundary layer of air. In [4] Lewis numbers are taken to be equal to unity for calculation of the turbulent boundary layer. Such an assumption should not exert profound influence on results, if molecular transfer coefficients are negligibly small in a comparison with turbulent ones. However an influence of a dissimilarity of heat and mass transfer processes for the laminar boundary layer should be more significant than for the turbulent one, because for many substances laminar Lewis numbers differ from unity greater than turbulent ones.

Apart from the problem on acceptability of the use of a triple Reynolds analogy at modeling of multicomponent mixture flows, studies on a similarity of physical processes of the heat and mass transfer under actual conditions are of interest. The similarity of physical processes of the heat and mass transfer is wide used, for example, for experimental determination of convective heat transfer coefficients, in studies of an efficiency of film cooling and etc. [5]. In these cases the heat and mass transfer coefficients are related : $St_h = St_d (Le)^{-n}$, where n is the empirical

constant depending on a surface geometry and flow characteristics. Processes of the heat and mass transfer are interrelated in flows of a boundary layer type with evaporation or injection of a foreign substance from a porous plate. In this case a heat flux is determined not only by a heat conduction, but a diffusion of the foreign substance as well [6]. Therefore in this work apart from the problem on admissibility of the use of the approximation $Pr=Sc=1$, the problem on similarity of the heat and mass transfer ($Le=1$) is being studied.

MATHEMATICAL STATEMENT OF THE PROBLEM
AND THE METHOD OF SOLUTION

The turbulence k-ε model considering the laminarization effects [7] was used in this work. The equation for each variable: the longitudinal velocity u, enthalpy of the mixture h, mass components' concentrations c_i, kinetic energy of turbulence k, and ε (dissipation rate of turbulence) can be presented in the generalized form:

$$\frac{\partial(\rho u \Phi)}{\partial x} + \frac{\partial(\rho v \Phi)}{\partial y} = \frac{\partial}{\partial y}\left(\Gamma_\Phi \frac{\partial \Phi}{\partial y}\right) + S_\Phi \qquad (1)$$

Values Φ, diffusion coefficients Γ_Φ and source terms S_Φ are presented in tab. 1.

Table 1. Values of diffusion coefficients and source terms in eq. (1).

Φ	Γ_Φ	S_Φ
1	0	0
u	$\mu + \mu_t$	0
k	$\mu + \mu_t / \sigma_k$	$G_k - \rho \varepsilon$
ε	$\mu + \mu_t / \sigma_\varepsilon$	$\frac{\varepsilon}{k}\left(C_{1\varepsilon} f_1 G_k - C_{2\varepsilon} f_2 \rho \varepsilon\right)$
h	$\mu / Pr + \mu_t / Pr_t$	$\frac{\partial}{\partial y}\frac{\mu}{Pr}\sum_{i=1}^{N}\left(\frac{Pr}{Sc_i} - 1\right)h_i \frac{\partial c_i}{\partial y}$
c_i	$\mu / Sc_i + \mu_t / Sc_t$	0

Here

$$\mu_t = \rho C_\mu f_\mu \frac{k^2}{\varepsilon} \text{ - turbulent viscosity,}$$

$C_1=1,44$, $C_2=1,92$, $C_\mu=0,09$, $\sigma_k=1,0$, $\sigma_\varepsilon=1,3$, - turbulence model constants,

$$Pr_t = Sc_t = 0,9, \ G_k = \mu_t\left(\frac{\partial u}{\partial y}\right)^2,$$

$$f_1 = 1 + (0.05 / f_\mu)^3, \quad f_2 = 1 - \exp(-R_t^2)$$

$$f_\mu = (1 - \exp(-0.0165 R_y))^2 (1 + 20.5 / R_t)$$

$$R_t = k^2 / \nu\varepsilon, \quad R_y = \sqrt{k} y / \nu$$

where y - distance from the wall, index t means turbulent value, ρ and μ are density and molecular viscosity respectively, R_t and R_y are turbulent Reynolds numbers. The viscosity of the mixture was determined according to Wilke's formula [6] which is widely used in practical calculations.

The system of equations (1) is added by the state equation for ideal gas:

$$\rho = \frac{P}{RT \sum\limits_{i=1}^{N} c_i / M_i},$$

where M_i is the molecular mass of the i-species. This system is also added by supplementary thermodynamic ratios which connects the enthalpy of each component with its temperature:

$$h = \sum_{i=1}^{N} h_i c_i, \quad h_i = \int_{T_0}^{T} c_{pi}(T) dT + h_{0i},$$

h_{0i} is the enthalpy of the i-species formation at temperature T_0.

The boundary conditions

The temperature, velocity, and composition of the main stream were assigned at the entrance to the calculated area. Air flow at the temperature of 300 K was calculated. Velocity of main flow - $u_0 = 10$ m/s. The temperature and composition were assigned for the injected substance before the injection into a porous wall. The mass flow rate J_w on the wall for evaporation was determined according to the condition

$$J_w = (\rho v)_w = \frac{q_w}{(h_w - h')},$$

where h' is the enthalpy of the injected gas, h_w is the enthalpy of the mixture on a wall, q_w is the total heat flux. Index w means the near wall value, index 0 means the value in main stream. In a case of blowing on a wall the constant mass flow rate $J_w = (\rho v)_w = (\rho u)_0 \cdot 10^{-4}$ was set.

Temperature on a porous wall in case of evaporation was determined under the Antoine's formula on concentration of evaporating substance in the assumption of phase equilibrium between vapor and liquids [8]. For injection the enthalpy and temperature at the wall were calculated from the condition of the heat equilibrium balance

$$h_w = \frac{q_w}{(\rho v)_w} + h'.$$

The mass concentration of each component of mixture was determined from the condition of the substance's balance on the wall:

$$c_{iw} = c_i' + \frac{\mu}{J_w Sc_i}\left(\frac{\partial c_i}{\partial y}\right)_w.$$

The equation system (1) was solved by means of the control volume method [9]. In a non-uniform grid amount of cells in a direction x and y was equal to 40. It is necessary to tell, that when the grid 22 on 22 was used, the results differed insignificantly.

RESULTS

For investigations three substances - ethanol, water and hydrogen were chosen. At evaporation or weak blowing the concentrations of injected gas in air are small and it is possible to consider Prandtl number to be constant, and for air it is equal 0,73. The Schmidt numbers for diffusion of ethanol, water or hydrogen in air are equal accordingly 1,3 and 0,6 and 0,22 and they can be considered to be constant too. The appropriate Lewis numbers (Le=Pr/Sc) of these substances are placed in tab. 2.

Table 2. Lewis numbers of substances.

H_2	H_2O	C_2H_5OH
3,32	1,22	0,562

For flows with injection of ethanol, water and hydrogen with the help of the above mentioned equations (1) in numerical predictions were received fields of velocity, temperature and concentrations, that has allowed to calculate heat and mass transfer coefficients determined as follows:

$$St_h = \frac{q_w}{\rho_0 u_0 (h_0 - h_w)}, \quad St_d = \frac{\left(\frac{\mu}{Sc}\frac{\partial c}{\partial y}\right)_w}{\rho_0 u_0 (c_0 - c_w)} = \overline{J}_w \frac{(c'-c_w)}{(c_w - c_0)}.$$

Here heat flux q_w is determined as follows:

$$q_w = \left(\frac{\mu}{Pr}\frac{\partial h}{\partial y} + \frac{\mu}{Pr}\sum_{i=1}^{NS}\left(\frac{Pr}{Sc_i} - 1\right)h_i\frac{\partial c_i}{\partial y}\right)_w$$

In a case Le = 1 the heat flux is determined by enthalpy gradient only. In flows with evaporation of substance the diffusive part of a heat flux is very important. On fig.1 it is shown, that the

relation of heat fluxes in a case Le = 1 and Le≠1, received in predictions, depends on Lewis's number: the more Le number differs from unit, the more their values differ. In turbulent flows this difference is less significant.
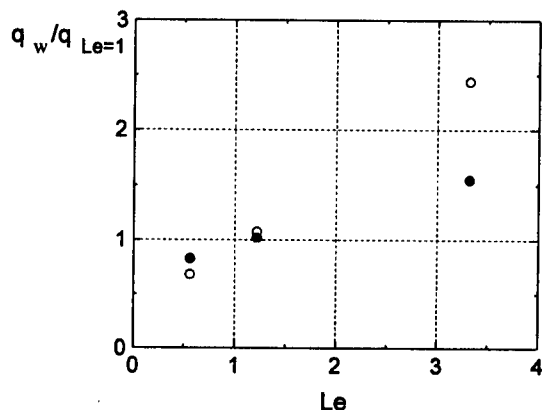
Fig. 1. The ratio of heat fluxes in dependence on Le number, open circles - laminar flow, dark circles - turbulent flow.

Under the conditions, realized in predictions, processes of heat mass transfer are interconnected, therefore it is interesting to define the relation of heat mass transfer coefficients at various Lewis's numbers. On fig.2 is shown, that their relation is close to unit in the large range of changes of Le numbers.
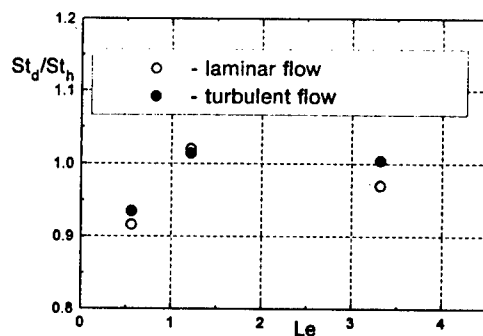
Fig.2. The relation of heat transfer coefficients and mass transfer coefficients in dependence on Le number.

In a fig. 3 the comparison of predicted results at Le≠1 with experimental data [10] on heat transfer coefficients is given. Conditions, at which the experiment was carried out, are as follows: u = 20m/s, T_0 = 300 K, Tu_0 = 2%. The standard dependence gives overestimate of heat transfer coefficients approximately on 20%.

St_h

4.0×10^{-3}

• - experimental data

- - - - - prediction

- - - - - - $St = 0.0288 Re_x^{(-0.2)} Pr^{(-0.6)}$

2.0×10^{-3}

0.0 2.0×10^5 4.0×10^5 6.0×10^5 8.0×10^5

Re_x
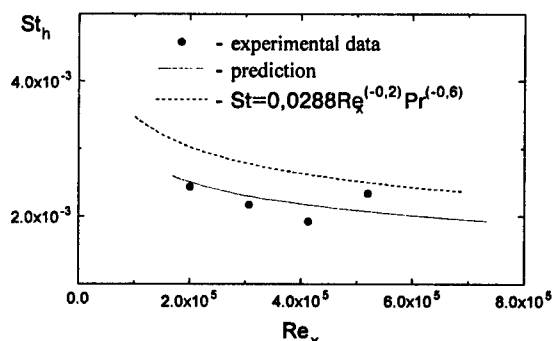
Fig. 3. Heat transfer coefficients in comparison with experimental data
and standard distribution in a turbulent boundary layer.

CONCLUSION

Thus, at research of heat mass transfer processes in a boundary layer, when the heat flux except for heat conductivity, is determined also by diffusion of substances, use of Reynolds's analogy (Pr=Sc=1) can result in significant errors in definition of heat flux values. However coefficients of heat and mass transfer are interconnected also their relation close to unit. It means that diffusive part of heat flux plays the determining role in heat transfer at the investigated level of substance injection.

The work is executed at support of the Russian fund of fundamental researches (code of the project 97-02-18520).

REFERENCES

1. Hutchinson, P., Khalil, E.E., Whitelaw, J.H., Wigley, G. The Calculation of Furnace-flow Properties and Their Experimental Verification // Trans. of the ASME, J. of Heat Transfer - 1976, V. 98, P. 276-283.

2. Kono, M., Tsukamoto, T., Iinuma, K. Numerical Simulation of Laminar Flame Propagation in Constant Volume Vessels // Laser Diagnostics and Modeling of Combustion. - Berlin : Springer-Verlag, 1987. P.319-328.

3. Katta V.R., Goss L.P., Roquemore W.M. Effect of Nonunity Lewis Number and Finite-Rate Chemistry on the Dynamics of a Hydrogen-Air Jet Diffusion Flame // Combustion and Flame. - 1994. V. 96. P. 60-74.

4. Volchkov E.P., Dvornikov N.A., Perepechko L.N. Comparison of various methods of modeling turbulent combustion in a boundary layer // Combustion, Explosion and Shock Waves. - 1996. V.32, N 4. P. 340-344.

5. Sun Y., Gartshore I.S., Salcudean M.E. An Experimental Investigation of Film Cooling Heat Transfer Coefficients Using the Mass/Heat Analogy // Journal of Heat Transfer. - 1995. V. 117. P. 851-858.

6. Lyapin Yu.V. and Streletz M.Kh. The internal flow of gas mixtures. - Moscow: Nauka, 1989.

7. Lam C.K.G., Bremhorst K.A. Modified form of the (k-ε)-model predicting wall turbulence// J.Fluids Eng. - 1981. V.103. P.456-460.

8. Reid R.C., Prausnitz J.M., Sherwood T.K. The Properties of Gases and Liquids. - McGraw-Hill Book Company, 1978.

9. Patancar, S. Numerical Heat Transfer and Fluid Flow. - New York : Hemisphere Publishing Corporation, 1980.

10. Boyarshinov B.F. Heat mass transfer in a boundary layer with evaporation and combustion of ethanol: Ph.D. Thesis. - Novosibirsk: Institute of Thermophysics, 1988.

THE VON NEUMANN CRITERION AND THE CONDITIONS FOR ITS SUFFICIENCY

B.Yu. Scobelev, E.V. Vorozhtsov

Institute of Theoretical and Applied Mechanics SB RAS,
630090, Novosibirsk, Russia

INTRODUCTION

The Fourier method is the most popular practical method for stability investigation of difference schemes in quadratic norm. It is known that a widely accepted von Neumann criterion is only a necessary condition and does not ensure the difference scheme stability. The available sufficient stability criteria of difference schemes [1,2] use the estimates of the norms of the amplification matrix G of difference scheme. On the other hand, it is well known that the finite powers of a matrix can have the properties, which the original matrix does not possess. We prove in the present paper three new sufficient stability criteria of difference schemes in quadratic norm, which use the properties of the finite powers of the amplification matrix G. An investigation of the satisfaction of the obtained stability criteria for a number of well-known difference schemes for the numerical solution of aerohydrodynamics problems is carried out.

BASIC RESULTS

It is known that the von Neumann criterion [1,2] is the necessary stability condition of a difference scheme:

$$\max_{\vec{\xi},i} |\lambda_i(\vec{\kappa},\vec{\xi})| \leq 1 + O(\tau), \tag{1}$$

where τ is the time step, $\vec{\xi} = \vec{k} \cdot \vec{h}$ is the wave vector, $\vec{k} = (k_1,\dots,k_L)$ are the real wavenumbers, $L \geq 1$ is the number of spatial variables, $\vec{h} = (h_1,\dots,h_L)$, h_j is a step of a uniform rectangular grid along the spatial coordinate x_j, $j = 1,\dots,L$; $\vec{\kappa} = (\kappa_1,\dots,\kappa_M)$, where κ_m, $m = 1,\dots,M$ $(M \geq 1)$ are the nondimensional similarity parameters in the space of the variation of which the stability region of a difference scheme is determined; $\lambda_i(\vec{\kappa},\vec{\xi})$ are the eigenvalues of the amplification matrix G, which is the Fourier transformation of the step operator S entering the difference scheme $\vec{u}^{n+1} = S\vec{u}^n$ (n is the number of time level, $n = 0,1,2,\dots$; $\vec{u}^n$ is the difference solution vector).

It is also well known that the von Neumann condition yields not only a necessary but also sufficient stability criterion of scheme if the amplification matrix G is a normal matrix (or, which is the same, the step operator S is a normal operator):

$$G^*G = GG^* \quad (S^*S = SS^*).$$

The following equality is valid for a normal matrix:

$$\| G(\vec{\kappa},\vec{\xi}) \| = \max_i |\lambda_i(\vec{\kappa},\vec{\xi})|. \tag{2}$$

Since

$$\| S \| = \max_{\vec{\xi}} \| G(\vec{\kappa}, \vec{\xi}) \| = \max_{\vec{\xi}, i} |\lambda_i(\vec{\kappa}, \vec{\xi})|,$$

the condition (1) ensures the difference scheme stability.

A more general condition for the sufficiency of the von Neumann criterion was obtained in the work [3]. It was proved that the von Neumann criterion is sufficient for the stability of difference scheme if some finite power of the matrix G is a normal matrix. The basic result of the work [3] is the following theorem:

Theorem 1 [3]. Let the following conditions be satisfied.

1. The estimate

$$\| C_{n,k} \| \leq \| S^{n-k} \|$$

takes place for the norm of the transition operator $C_{n,k}$ of a difference scheme, where S is some majorant step operator with constant coefficients.

2. The operator S is uniformly bounded at a sufficiently small time step τ:

$$\| S \| \leq M_1 \quad 0 < \tau < \tau.$$

3. For the Fourier transformation $G(\vec{\kappa}, \vec{\xi})$ of the operator S there exists certain integer $N \geq 1$ such that G^N is a normal matrix.

Then the von Neumann condition for the matrix $G(\vec{\kappa}, \vec{\xi})$ is a necessary and sufficient stability condition of difference scheme.

Proof. Consider the stability definition of difference scheme [4]. The difference scheme is called stable if there is such a number $M(\bar{t}) > 0$ that

$$\| C_{n,k} \| \leq M(\bar{t}) \tag{3}$$

for all $0 \leq k \leq n - 1$ and $n\tau \leq \bar{t}$. It follows from condition 1 and inequality (3) that the difference scheme will be stable if the inequality

$$\| S^{n-k} \| \leq M \tag{4}$$

is satisfied for all n and $0 \leq k \leq n - 1$.

Denote by $\zeta_i(\vec{\kappa}, \vec{\xi})$ the eigenvalues of the matrix $G^N(\vec{\kappa}, \vec{\xi})$. It is well known that

$$\zeta_i(\vec{\kappa}, \vec{\xi}) = \lambda_i^N(\vec{\kappa}, \vec{\xi}), \tag{5}$$

where λ_i are the eigenvalues of the matrix G. Let the von Neumann condition be satisfied:

$$\max_{\vec{\xi}, i} |\lambda_i(\vec{\kappa}, \vec{\xi})| \leq 1 \tag{6}$$

(the proof can easily be extended for the case where $O(\tau) \neq 0$ in the condition (1)). Then the following estimate is valid:

$$\| S^N \| = \max_{\vec{\xi}} \| G^N(\vec{\kappa}, \vec{\xi}) \| = \max_{\vec{\xi}, i} |\zeta_i(\vec{\kappa}, \vec{\xi})| = \max_{\vec{\xi}, i} |\lambda_i(\vec{\kappa}, \vec{\xi})|^N \leq 1. \tag{7}$$

Consider $\| S^{n-k} \|$. It is easy to prove that

$$\| S^{n-k} \| \leq \| S^{Np+\delta} \| \leq \| S^N \|^p \| S \|^\delta \leq \| S \|^\delta, \tag{8}$$

where $p = [\frac{n-k}{N}]$ and $\delta = (n-k) - N[\frac{n-k}{N}]$. It is easy to show that

$$\| S \|^{\delta} \leq M_2, \tag{9}$$

where $M_2 = \max\{1, \| S \|^{N-1}\}$. It follows from condition 2 that M_2 is uniformly bounded:

$$M_2 \leq \max\{1, M_1^{N-1}\}. \tag{10}$$

It follows from inequalities (8)–(10) that the condition (4) is satisfied. Hence the difference scheme is stable. The theorem is proved.

Example 1. A two-cycle MacCormack scheme was considered in [3] for the two-dimensional convection equation

$$\frac{\partial u}{\partial t} + A\frac{\partial u}{\partial x_1} + B\frac{\partial u}{\partial x_2} = 0,$$

where A and B are the scalar constants. It was shown that the two-cycle MacCormack scheme satisfies the conditions of Theorem 1 at $N = 2$. That is the squared amplification matrix is a normal matrix. Therefore, the von Neumann condition is a sufficient condition, and the scheme is stable in the overall region of the parameters $\kappa_1 = A\tau/h_1$, $\kappa_2 = B\tau/h_2$ found in [5].

It turns out that there exist fairly many difference schemes whose amplification matrix is a normal operator.

Theorem 2. Let the following conditions be satisfied.
1. The estimate

$$\| C_{n,k} \| \leq \| S^{n-k} \|$$

takes place for the norm of the transition operator $C_{n,k}$ of difference scheme, where S is some majorant step operator with constant coefficients,
2. At sufficiently small values of the time step τ the operator S is uniformly bounded.

$$\| S \| \leq M_1 \quad \text{at} \quad 0 < \tau \leq \bar{\tau}.$$

3. For the Fourier transformation $G(\vec{\kappa}, \vec{\xi})$ of the operator S there exists a positive integer $N \geq 1$ such that $G^N(\vec{\kappa}, \vec{\xi})$ is a diagonalizable matrix.

Then the von Neumann condition for the amplification matrix $G(\vec{\kappa}, \vec{\xi})$ is the necessary and sufficient condition for the stability of difference scheme.

The proof of this theorem is similar to a large extent to the proof of Theorem 1.

Now consider the difference schemes for which it is impossible to find an integer $N > 0$ such that G^N is a normal matrix. It turns out that the stability condition for such schemes may be formulated in a form similar to the fon Neumann criterion but under a more severe constraint for the eigenvalues of the amplification matrix.

Theorem 3. Let the following conditions be satisfied.
1. The estimate

$$\| C_{n,k} \| \leq \| S^{n-k} \|$$

is valid for the norm of the transition operator $C_{n,k}$ of difference scheme, where S is some majorant step operator with constant coefficients.

2. The operator S is uniformly bounded at a sufficiently small time step τ:

$$\| S \| \leq M_1 \quad \text{at} \quad 0 < \tau < \bar{\tau}.$$

3. All the eigenvalues of the Fourier transformation of the operator S are strictly less that unity in their moduli at any $\vec{\xi}$ in some region D of κ points:

$$\max_{\vec{\xi},i} |\lambda_i(\vec{\kappa}, \vec{\xi})| < 1, \quad \kappa \in D.$$

Then the difference scheme is stable in D.

<u>Proof</u>. According to condition 1, $\| C_{n,k} \| \leq \| S^{n-k} \|$. Therefore, as in the proof of Theorem 1, one must prove that the condition (4) is satisfied.

Consider the amplification matrix $G(\vec{\kappa}, \vec{\xi})$ and make use of the theorem on a spectral decomposition of an operator [6] and the theorem on the Jordan form of a matrix. It follows from these theorems that there exists a similarity transformation $V(\vec{\kappa}, \vec{\zeta})$, which transforms the matrix $G(\vec{\kappa}, \vec{\xi})$ to the Jordan form:

$$V(\vec{\kappa}, \vec{\xi})G(\vec{\kappa}, \vec{\xi})V(\vec{\kappa}, \vec{\xi})^{-1} = T(\vec{\kappa}, \vec{\xi}) + D(\vec{\kappa}, \vec{\xi}), \tag{11}$$

where $T(\vec{\kappa}, \vec{\xi})$ is a diagonal matrix, and $D(\vec{\kappa}, \vec{\xi})$ is a nilpotent matrix. The matrix $T(\vec{\kappa}, \vec{\xi})$ diagonal is occupied by the eigenvalues of the matrix G (each eigenvalue λ_i is repeated m_i times, where m_i is the multiplicity of λ_i). We note the fact that the matrices $T(\vec{\kappa}, \vec{\xi})$ and $D(\vec{\kappa}, \vec{\xi})$ commute. This property of transformation (11) plays a significant role in our proof.

It is well known that the columns of the transformation matrix $V(\vec{\kappa}, \vec{\xi})$ are the generalized eigenvectors of the amplification matrix $G(\vec{\kappa}, \vec{\zeta})$. Therefore, it is always possible to choose $G(\vec{\kappa}, \vec{\xi})$ in such a way that the estimates

$$\| V(\vec{\kappa}, \vec{\xi}) \| \leq C_1 \quad \text{and} \quad \| V^{-1}(\vec{\kappa}, \vec{\xi}) \| \leq C_1 \tag{12}$$

will be valid uniformly in $\vec{\xi}$. Since the diagonal matrix $T(\vec{\kappa}, \vec{\xi})$ is a normal operator, then

$$\| T(\vec{\kappa}, \vec{\xi}) \| = \max_i |\lambda_i(\vec{\kappa}, \vec{\xi})|.$$

Therefore, the estimate

$$\max_{\vec{\xi}} \| T(\vec{\kappa}, \vec{\xi}) \| < 1. \tag{13}$$

follows from condition 3. Consider the quantity $\max_{\vec{\xi}} \| D(\vec{\kappa}, \vec{\xi}) \|$. We obtain with regard for formulas (11),(12),(13) and condition 2:

$$\max_{\vec{\xi}} \| D(\vec{\kappa}, \vec{\xi}) \| \leq \max_{\vec{\xi}} [\| T(\vec{\kappa}, \vec{\xi}) \| + \| V(\vec{\kappa}, \vec{\xi}) \| \| G(\vec{\kappa}, \vec{\xi}) \| \| V^{-1}(\vec{\kappa}, \vec{\xi}) \|]$$

$$\leq 1 + C_1^2 M_1 \equiv M_2. \tag{14}$$

Introduce the notation $p = n - k$ and consider the quantity

$$\| S^p \| = \max_{\vec{\xi}} \| G^p(\vec{\kappa}, \vec{\xi}) \| . \tag{15}$$

183

In order to prove the theorem one must show that the right-hand side of equality (15) is uniformly bounded at any p.

$$\max_{\vec{\xi}} \| G^p(\vec{\kappa}, \vec{\xi}) \| = \max_{\vec{\xi}} \| V^{-1}(\vec{\kappa}, \vec{\xi}) V(\vec{\kappa}, \vec{\xi}) G^p(\vec{\kappa}, \vec{\xi}) V^{-1}(\vec{\kappa}, \vec{\xi}) V(\vec{\kappa}, \vec{\xi}) \|$$

$$\leq C_1^2 \max_{\vec{\xi}} \| V(\vec{\kappa}, \vec{\xi}) G^p(\vec{\kappa}, \vec{\xi}) V^{-1}(\vec{\kappa}, \vec{\xi}) \| = C_1^2 \max_{\vec{\xi}} \| (T(\vec{\kappa}, \vec{\xi}) + D(\vec{\kappa}, \vec{\xi}))^p \| . \qquad (16)$$

For further estimations we take into account the fact that D is a nilpotent operator. That is $D^l = 0$ at certain natural $1 < l \leq N$, where N is the dimension of the amplification matrix G. In addition, we use the commutativity of the operators T and D. Then at sufficiently large values of p ($p \geq N$) we obtain that

$$\| (T + D)^p \| = \left\| \sum_{m=0}^{N-1} \binom{p}{m} T^{p-m} D^m \right\| = p^{N-1} \left\| T^{p-N+1} \left[\sum_{m=0}^{N-1} \frac{1}{p^{N-1}} \binom{p}{m} T^{N-1-m} D^m \right] \right\|$$

$$\leq p^{N-1} \| T \|^{p-N+1} \left[\sum_{m=0}^{N-1} \frac{1}{p^{N-1}} \binom{p}{m} \| T \|^{N-1-m} \| D \|^m \right], \qquad (17)$$

where $\binom{p}{m}$ are the binomial coefficients. Introduce the notation

$$\max_{\vec{\xi}} \| T(\vec{\kappa}, \vec{\xi}) \| = \bar{\lambda} \qquad (18)$$

and take the inequalities (13),(14) into account. Then the substitution of inequality (17) in formula (16) yields

$$\max_{\vec{\xi}} \| G^p(\vec{\kappa}, \vec{\xi}) \| \leq C_1^2 p^{N-1} \bar{\lambda}^{p-N+1} \left[\sum_{m=0}^{N-1} \frac{1}{p^{N-1}} \binom{p}{m} M_2^m \right] . \qquad (19)$$

It is easy to see that the expression in the square brackets is uniformly bounded at any $p \geq N$. Therefore,

$$\max_{\vec{\xi}} \| G^p(\vec{\kappa}, \vec{\xi}) \| \leq M_3 p^{N-1} \bar{\lambda}^{p-N+1}. \qquad (20)$$

Since $\bar{\lambda} < 1$ then at $p \to \infty$ the right-hand side of inequality (20) tends to zero. Therefore, the quantity on the left-hand side of inequality (20) is uniformly bounded at all $p \geq N$. It is easy to prove the boundedness of this quantity at $p < N$ by using condition 2 of the theorem. Summarizing the above we obtain that

$$\| C_{n,k} \| \leq \| S^{n-k} \| = \max_{\vec{\xi}} \| G^{n-k}(\vec{\kappa}, \vec{\xi}) \| \leq M_4 \qquad (21)$$

at any n and $0 \leq k \leq n-1$. Hence the difference scheme is stable. The theorem is proved.

Consider a difference in'the stability character of a difference scheme satisfying the conditions of Theorems 1 or 2 and a difference scheme for which the conditions of Theorems 1 or 2 are not satisfied, but the conditions of Theorem 3 are satisfied. Denote by Δ_0 a closed region in the space of the parameters $(\kappa_1, \ldots, \kappa_M)$, for which the von Neumann criterion is satisfied:

$$\max_{i,\vec{\xi}} |\lambda_i(\vec{\kappa}, \vec{\xi})| \leq 1 \text{ at } \vec{\kappa} \in \Delta_0.$$

Let the conditions of Theorems 1 or 2 be satisfied for a difference scheme. Then the difference scheme is stable in the overall region Δ_0, including its boundary Γ. The transition operator is uniformly bounded for all $\vec{\kappa} \in \Delta_0$.

If the conditions of Theorems 1 and 2 are not satisfied, but the conditions of Theorem 3 are satisfied then the difference scheme is stable in any internal subregion Δ_1 of region Δ_0, which does not contain its boundary Γ: $\Delta_1 \subset \Delta_0 \backslash \Gamma$. In this case, the stability is generally nonuniform. As the boundary Γ is approached the quantity $\bar{\lambda}$ in inequality (20) tends to unity, and the norm of the transition operator can increase unboundedly.

Example 2. Approximate the wave equation $u_{tt} = c^2 u_{xx}$, where $c^2 = \text{const} > 0$, by the scheme [1]

$$\frac{v_j^{n+1} - v_j^n}{\tau} = c\frac{w_{j+1/2}^n - w_{j-1/2}^n}{h}; \quad \frac{w_{j-1/2}^{n+1} - w_{j-1/2}^n}{\tau} = c\frac{v_j^{n+1} - v_{j-1}^{n+1}}{h}. \tag{22}$$

Here $w = cu_x$, $v = u_t$. Introducing the vector $\vec{U} = (v_j^n, w_j^n)^T$ we obtain the amplification matrix G in the form [1]

$$G = \begin{pmatrix} 1 & ia \\ ia & 1 - a^2 \end{pmatrix}, \tag{23}$$

where $a = 2\kappa \sin(\xi_1/2)$, $\kappa = c\tau/h$. Consider at first the case where $|\lambda_i| < 1$. Then it is easy to find the matrix V, which diagonalizes the matrix G, so that one can set $D = 0$ in the Jordan representation (11). It then follows from Theorem 2 that scheme (22) is stable under the satisfaction of the inequalities $|\lambda_{1,2}| < 1$ from which the inequality $\kappa < 1$ follows.

At $\kappa = 1$, $\xi_1 = \pi$ we have that

$$G = \begin{pmatrix} 1 & 2i \\ 2i & -3 \end{pmatrix},$$

and $VGV^{-1} = T + D$, where

$$V = \begin{pmatrix} 0 & 1 \\ 2i & -2 \end{pmatrix}, \quad T = \begin{pmatrix} -1 & 0 \\ 0 & -1 \end{pmatrix}, \quad D = \begin{pmatrix} 0 & 1 \\ 0 & 0 \end{pmatrix}. \tag{24}$$

It follows from (24) that $|\lambda_{1,2}| = 1$, that is condition 3 of Theorem 3 is violated. Thus, the sufficient stability condition of scheme (22) has the form $c\tau/h < 1$.

REFERENCES

1. Richtmyer R.D., Morton K.W. Difference methods for initial-value problems. – New York: Wiley-Interscience, 1967.
2. Strikwerda J.C. Finite difference schemes and partial differential equations. – Pacific Grove, CA: Wadsworth & Brooks/Cole Advanced Books & Software, 1989.
3. Scobelev B. Yu. On the question about the sufficiency of the von Neumann criterion for stability of difference schemes// J. Comput. Phys. – 1998. – In press.
4. Roždestvenskiĭ B.L., Janenko N.N. Systems of quasilinear equations and their applications to gas dynamics. – Providence: American Mathematical Society, 1983.
5. Vorozhtsov E.V., Scobelev B.Yu., and Ganzha V.G. Symbolic-numerical method for the stability analysis of difference schemes on the basis of the catastrophe theory// J. Comput. Phys. – 1995. – Vol. 116. – P. 26–38.
6. Kato T. Perturbation theory for linear operators. – New York: Springer-Verlag, 1966.

COLLOCATION-GRID METHOD FOR SOLVING BOUNDARY PROBLEMS FOR NAVIER-STOKES EQUATIONS

L.G. Semin, V.P. Shapeev
Institute of Theoretical and Applied Mechanics
630090, Novosibirsk, Russia

Introduction

The present work is aimed at constructing a grid method of collocation and least squares (CLS) for solving the boundary problems of Navier — Stokes equations. It is one of the variants of the finite-element method. Being used originally for solving the ordinary differential equations, it was used later for solving the elliptic and parabolic partial differential equations [1] and turned out to be attractive for solving the elliptical problems on adaptive grids with the small parameter at the highest derivative, where boundary and/or inner layers may occur [2]. For sets of equations, we pioneered in applying this method to boundary problems for Stokes equations [3].

In the finite-element approximation of the boundary problem for a set of Navier — Stokes equations, one of difficulties consists in proper account for the continuity equation div $\vec{v} = 0$ and realization of the boundary conditions. In the method proposed here the continuity equation is rigorously satisfied in each cell of the grid due to specific choice of basis and the boundary conditions are simply accounted. To find the coefficients of solution decomposition with respect to basis, the least squares method is used, yielding a better conditioned matrix of resulting linear system, as compared with other methods.

The present method was used for solving the problem of the viscous incompressible liquid flow within the rectangular lid-driven cavity. The lid-driven cavity problem is interesting because it is a model to test and compare numerical methods. That is why a number of researches [4] – [10] compare their results using this problem as a test one.

Problem formulation

A boundary problem for Navier—Stokes equations is considered:

$$\begin{cases} \mathrm{Re}^{-1} \, \Delta \, v_j - v_1 \frac{\partial v_j}{\partial x_1} - v_2 \frac{\partial v_j}{\partial x_2} - \frac{\partial p}{\partial x_j} = f_j, & (x_1, x_2) \in \Omega, \quad j = 1, 2, \\ \mathrm{div} \, \vec{v} = 0, \\ \vec{v}|_{\partial \Omega} = \vec{V}. \end{cases} \tag{1}$$

An approximate solution is sought as a piecewise polynomial function on a regular grid. The following designations are introduced: h is the half-width of a cell; (x_{1m}, x_{2m}) are the coordinates of m-th cell center; $y_1 = (x_1 - x_{1m})/h$, $y_2 = (x_2 - x_{2m})/h$ are the local coordinates within the cell; $\vec{u}(y_1, y_2) = \vec{v}(x_1, x_2)$, $q(y_1, y_2) = hp(x_1, x_2)$. Then, in local variables, equations (1) become:

$$\Delta u_j - \mathrm{Re}\Big(h\big(u_1 \frac{\partial u_j}{\partial y_1} + u_2 \frac{\partial u_j}{\partial y_2}\big) + \frac{\partial q}{\partial y_j}\Big) = \mathrm{Re}h^2 f_j, \quad j = 1, 2, \tag{2}$$

$$\mathrm{div} \, \vec{u} = 0, \tag{3}$$

$$\vec{u}|_{\partial \Omega} = \vec{U}. \tag{4}$$

Let some approximate solution $(\breve{u}_1, \breve{u}_2, \breve{q})$ be known. Let the desired refined solution be represented as $u_1 = \breve{u}_1 + \widehat{u}_1$, $u_2 = \breve{u}_2 + \widehat{u}_2$, $q = \breve{q} + \widehat{q}$. Substituting this representation into equations (2) and neglecting terms with second order of smallness, we obtain Oseen equations:

$$\triangle \widehat{u}_j - \mathrm{Re}h(\breve{u}_1\widehat{u}_{j,y1} + \breve{u}_2\widehat{u}_{j,y2} + \widehat{u}_1\breve{u}_{j,y1} + \widehat{u}_2\breve{u}_{j,y2}) - \mathrm{Re}\widehat{q}_{y_j} = F_j, \quad j = 1, 2, \quad (5)$$

where $F_j = \mathrm{Re}(h^2 f_j + h(\breve{u}_1\breve{u}_{j,y1} + \breve{u}_2\breve{u}_{j,y2}) + \breve{q}_{y_j}) - \triangle\breve{u}_j$.

Approximate solution in each cell is searched for in the form:

$$\begin{pmatrix} \widehat{u}_1 \\ \widehat{u}_2 \\ \widehat{q} \end{pmatrix} = \sum_j a_{jm}\varphi_j, \quad (6)$$

where φ_j are the basic functions (three-component vectors), m is the cell number.

Coefficients a_{jm} are to be determined from the collocation equations together with matching conditions at the boundaries of adjacent cells or the boundary conditions on $\partial\Omega$.

Approximate equations

Basic functions are chosen so that to represent the velocity vector components as second order polynomials, and the pressure — as a linear function, with the solution (6) being required to satisfy the continuity equation (3) $\mathrm{div}\,\vec{u} = 0$.

In order to obtain a unique piecewise polynomial solution, matching conditions are to be specified at the inter-cell boundaries. As a matching condition we have chosen the continuity conditions for the relations:

$$\frac{\partial U_n}{\partial n} - p + \eta U_n, \quad \frac{\partial U_t}{\partial n} + \eta U_t. \quad (7)$$

Here U_n and U_t are the normal and tangential (to the cell boundary) velocity components, n is the unit vector of external normal to the cell, η is some positive parameter. The latter may control the conditionality of the resulting set of linear algebraic equations and may affect the rate of convergence of iterations.

To find a_{jm} coefficients in representation (6), method of iterations over subdomains was used, each grid cell being considered as the subdomain. When refining the solution for an m-th cell, conditions (7) were used. Generally, these conditions can not be satisfied along the entire inter-cell boundary. We satisfy these conditions requiring them to be valid in terms of the least squares method at eight points of the cell boundary.

If the cell boundary coincides with the domain boundary then velocity vector is specified at two points of the boundary. Besides, the pressure is prescribed at the lower left corner of the domain.

Collocation conditions for equations (5) at four points inside the cell are added to the matching conditions (boundary conditions). As a result, we derive the following set of linear algebraic equations:

$$\sum_{k=1}^{12} B_{lk}a_{km} = F_l, \quad l = 1, \ldots, 24. \quad (8)$$

The system (8) is overdetermined as it involves 24 equations for 12 unknowns. To specify what is recognized as a solution of this set, let us consider two functionals:

$$\Phi_1 = \sum_{l=1}^{16}(\sum_{j=1}^{12} B_{lj}a_{jm} - F_l)^2, \qquad \Phi_2 = \sum_{l=17}^{24}(\sum_{j=1}^{12} B_{lj}a_{jm} - F_l)^2. \qquad (9)$$

The first functional corresponds to the sum of residual squares for the equations derived from the matching or boundary conditions. The second one corresponds to the sum of residual squares for collocation equations. A solution of (8) is found by minimizing these functionals, the minimum of Φ_1 is taken with respect to the coefficients a_{jm}, j=1,...,10 under fixed a_{11m} and a_{12m}, while the minimum of Φ_2 is taken with respect to a_{jm}, j=11,12 under fixed a_{jm}, j=1,...,10.

Thus, to find the coefficients a_{jm}, j=1,...,12, we obtain a set of equations of the form:

$$\sum_{j=1}^{12} D_{lj}a_{jm} = \tilde{F}_l, \quad l=1,\ldots,12, \qquad (10)$$

and the solution is found by the method of direct elimination.

To find the solution of the problem, an iterative method is used where the desired solution is refined for each individual cell of the domain. When refining the solution in the m-th cell during each iteration, the solution for adjacent cells either have been already refined, or is taken from the previous iteration.

Validity of obtained formulas, convergence and workingability of the method were tested on a number of problems with exact solution being known.

Calculation of the flow in a rectangular lid-driven cavity

Using the CLS method, calculations of the flow in a rectangular lid-driven cavity were performed for Reynolds numbers Re = 1, Re = 10, Re = 100, Re = 400, Re = 1000, Re = 2000. Let A be the depth-to-width ratio for the cavity. For A = 1 (square cavity) and A = 0.5, an increase in the Reynolds number leads to an increase in near-bottom corner vortices. Maximum and minimum values of the velocity profiles along vertical and horizontal centerlines of the cavity for various Reynolds numbers with A = 1 on the 80x80 cell grid are shown in table 1. These values obtained by present method are in good agreement with those obtained by [7] – [10] (see table 2).

For A = 2, unlike the cases A = 1 and A = 0.5, the second vortex is developed, occupying the overall cavity bottom even at low Reynolds numbers and increasing with the latter. For all A, increase in Reynolds number results in the shift of the main vortex center at first in the direction of lid motion and then to the center of the cavity. Similar results were observed in the physical experiment [5] and computations [4], [6] – [10].

Fig. 1 - 3 show the flow patterns for Re = 1 and Re = 1000 at A = 0.5 and A = 1, and for Re = 1, Re = 1000 and Re = 2000 at A = 2. The vortex centers are denoted by '+' mark.

Conclusion

A grid method of collocation and least squares (CLS) has been developed for the set of steady Navier — Stokes equations. The method is implemented on a regular square grid. Using this method, the flow in a rectangular lid-driven cavity at various Reynolds numbers has been computed. A comparison of the values for horizontal velocity component v_1 along

Table 1: Distinctive values of the velocity profiles, obtained by CLS method

Re	$v_{1\ min}$	$v_{2\ min}$	$v_{2\ max}$
1	-0.2074	-0.1846	0.1839
100	-0.2125	-0.2497	0.1756
400	-0.3222	-0.4443	0.2970
1000	-0.3590	-0.4901	0.3463

Table 2: Distinctive values of the velocity profiles, obtained from literature

Re	Method	$v_{1\ min}$	$v_{2\ min}$	$v_{2\ max}$
100	Ref. [7], grid 128x128	-0.2106	-0.2521	0.1786
	Ref. [8], grid 129x129	-0.21090	-0.24533	0.17527
400	Ref. [8], grid 129x129	-0.32726	-0.44993	0.30203
	Ref. [9], grid 128x128	-0.32751	-0.45274	0.30271
	Ref. [10], grid 49x49	-0.2960	-0.4051	0.2662
1000	Ref. [7], grid 256x256	-0.3764	-0.5208	0.3665
	Ref. [8], grid 129x129	-0.38289	-0.51550	0.37095
	Ref. [9], grid 128x128	-0.38511	-0.52280	0.37369
	Ref. [10], grid 129x129	-0.3689	-0.5037	0.3553

the vertical centerline and values for vertical component v_2 along the horizontal centerline of the cavity with those from the previous papers [4] – [10] demonstrates close agreement between the present calculations and the literature data. The best agreement of the velocity values is observed at low Reynolds numbers. For higher Reynolds numbers, our results agree best with the data of [10]. The discrepancy is less then 3%, with 80x80 grid being used in present computations and 129x129 grid being used in [10].

The flow patterns for various Reynolds numbers are identical with those obtained in numerical [4] – [10] and physical [5] experiments.
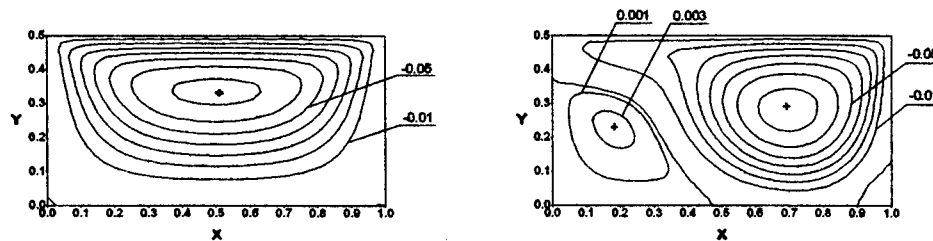
Figure 1: A = 0.5, grid 80x40 cells. On the left: Re = 1, on the right: Re = 1000.
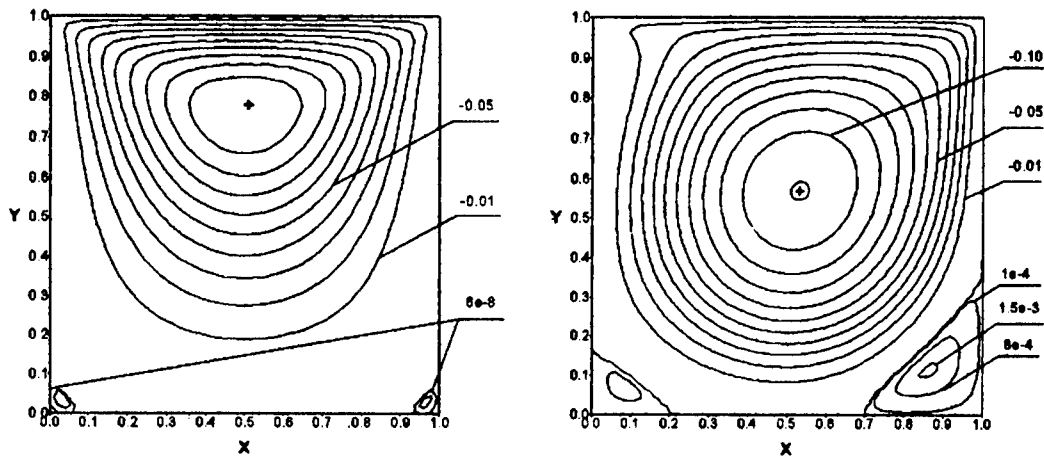
Figure 2: A = 1, grid 80x80 cells. On the left: Re = 1, on the right: Re = 1000.
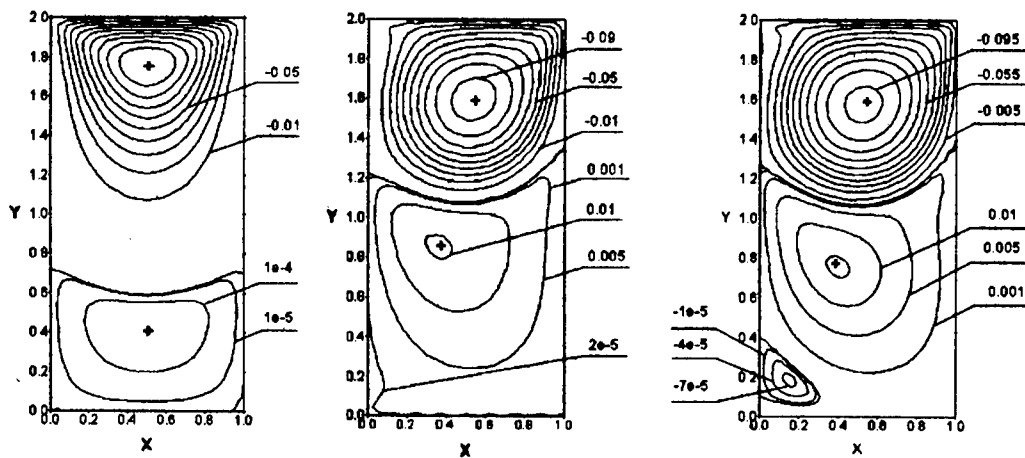
Figure 3: A = 2. On the left: Re = 1, in the middle: Re = 1000 (grid 40x80 cells), on the right: Re = 2000 (grid 80x160).

REFERENCES

1. Sleptsov A.G. Grid - projection solution of elliptic problem for a irregular grid // Rus. J. Numer. Analys. and Math. Modelling. — 1993. — Vol. 8, № 6. — P. 501 – 525.

2. Sleptsov A.G., Shokin Yu.I. Adaptive grid-projection method for elliptical problems. // Zhurnal vichislitel'noi matematiki i matemeticheskoi phiziki. — 1997. — Vol.37, № 5. — P. 572 – 586. (in Russian)

3. Semin L.G., Sleptsov A.G., Shapeev V.P. Collocation and least squares method for Stokes equations // Vichislitel'nie Technologii. — 1996. — Vol. 1, № 2. — P. 90 – 98. (in Russian)

4. Burggraf O.R. Analytical and numerical studies of the structure of steady separated flows // J. Fluid Mech. — 1966. — Vol. 24, part 1. — P. 113 – 151.

5. Pan F., Acrivos A. Steady flows in rectangular cavities // J. Fluid Mech. — 1967. — Vol. 28, part 4. — Pp. 643 – 655.

6. Bozeman J.D., Dalton C. Numerical study of viscous flow in a cavity // J. Comput. Phys. — 1973. — Vol. 12, № 3. — P. 348 – 363.

7. Bruneau C.H., Jouron C. An efficient scheme for solving steady incompressible Navier—Stokes equations // J. Comput. Phys. — 1990. — Vol. 89, № 2. — P. 389 – 413.

8. Ghia U., Ghia K.N., Shin C.T. High–Re solutions for incompressible flow using the Navier—Stokes equations and a multigrid method // J. Comput. Phys. — 1982. — Vol. 48, № 4. — P. 387 – 411.

9. Deng G.B., Piquet J., Queutey P., Visonneau M. A new fully coupled solution of the Navier—Stokes equations // Int. J. for Numer. Meth. in Fluids. — 1994. — Vol. 19, № 7. — P. 605 – 639.

10. Chen C.J., Chen H.J. Finite analytic numerical method for unsteady two-dimensional Navier—Stokes equations // J. Comput. Phys. — 1984. — Vol. 53, № 2. — P. 209 – 226.

AN EXPERIMENTAL STUDY OF INSTABILITY DISTURBANCES EXCITATION BY EXTERNAL SOURCE IN SUPERSONIC BOUNDARY LAYER OF A BLUNTED PLATE

N.V. Semionov, A.D. Kosinov, A.A. Maslov
Institute of Theoretical and Applied Mechanics SB RAS,
630090, Novosibirsk, Russia

INTRODUCTION

Very few experimental investigations of supersonic receptivity phenomena were fulfillment up to date. Note Kendall's experiments [1], where the development of natural disturbances in the boundary layer was studied, and the correlation factor between the free-stream and boundary layer oscillations was measured at Mach number M=1.6-8.5. A high intensity of disturbances was found in the boundary layer close to the leading edge. It was induced by an external acoustic field. The receptivity problem was solved at the Institute of Theoretical and Applied Mechanics with the help of external controlled disturbances, which generate eigen oscillations in the boundary layer [2-5]. The areas of the maximum boundary layer receptivity on a flat plate to acoustic disturbances were established experimentally in [2]. They are: a) the plate leading edge; b) the area corresponding to the acoustical branch of the neutral curve; c) the area corresponding to the lower branch of the neutral stability curve.

Experimental investigations of the supersonic boundary layer receptivity on leading edge of the plate to the external controlled disturbances were carried out at Mach number M=2 in [3,4] and at M=3.5 in [5,6]. The transformation coefficients K (the ratio of the amplitude of disturbances generated in the boundary layer to the amplitude of acoustic waves falling onto the leading edge) were experimentally obtained in [4,6] for the first time.

All our previous investigations of receptivity problem were carried when the models were flat plates with sharp leading edge [2-6]. The experiments, presented in this article, were fulfilled on a blunted plate.

EXPERIMENTAL CONDITIONS

The experiments were performed in the supersonic wind tunnel T-325 of the Institute of Theoretical and Applied Mechanics of the Russian Academy of Sciences with the test section dimensions 600×200×200 mm, at Mach number M=2, unit Reynolds number $Re_1 = 10 \times 10^6$ 1/m. The model was described in [4]. It consists of two flat plates, mounted at zero angle to the flow. External controlled disturbances were generated by using discharge with frequency f=20 kHz. Plate 1 contains the discharge in chamber and can be moved in normal direction. Artificial disturbances were entered into supersonic flow through an aperture with diameter of 0.5 mm in working surface of the flat plate as described in [5,7]. Coordinates of the source are: x=18±0.25 mm and z=0, where x is the longitudinal coordinate from the leading edge of plate 1. Spanwise coordinate z was counted from the hole in the plate plane. The distance of the plate 1 from the wall of the test section was equal a=76 mm. Plate 1 was placed below the plate 2. In this case generation of disturbances in the boundary layer by the external controlled acoustic field taken place near the leading edge of plate 2. The plate 2 was fastened to pylon at a distance 116 mm from the wall of the test section T-325. The sizes of plate 2 are 280 mm

length, 160 mm width at top and 80 mm at basis, 7 mm thickness. The radius of the leading edge bluntness was equal r=2.5 mm.

Disturbances were registered by the constant temperature hot-wire anemometer. A probe with tungsten wire of 5 μm diameter and 0.76 mm length was used. The probe could be moved along three coordinates with the help of a traversing device with an accuracy 0.1 mm for the longitudinal x and spanwise z coordinates and 0.01 mm for the normal coordinate y. The hot-wire signal was put in the computer with the help of 12-bit 0.75 MHz A/D converter. For these measurements the selective amplifier with bandwidth of 1% was used, output of which was connected with ADC. A synchronous summation was used for improving the signal to noise ratio in the experiments. The technique of experiment and procedure of data processing was described in [5] in detail.

RESULTS

The initial field of controlled fluctuation in free stream was measured in a plane of the plate 2 on distance y_l=40 mm from a surface of the plate 1 (plate 2 was established downstream). In this case the plate 2 was used as a support for the traversing gear. The initial amplitude of controlled disturbances from the local source was fixed during all measurements. At the analysis of the experimental data in [4,5] simplified physical model of disturbances generation near to the source was used. The artificial disturbances penetrate through the aperture of the plate 1 into the boundary layer. Thus in result of braking of a flow in the near field of upstream and downstream of the discharge, possibly the vortices were formatted with different directions of rotation in the plane yx. Further downstream, the generated disturbances induce to origin of Tollmien-Schlichting (TS) waves in the boundary layer of plate 1. All this process was accompanied by radiation of various types of controlled disturbances into the free stream. The radiation propagates inside the Mach cone from the discharge. On the basis of this model, typical regions corresponding to various types of controlled disturbances were identified from the functions $A_0(x)$ and $\Phi_0(x)$. The acoustic nature of the radiation was obtained in [5]

Such physical model was based on distributions, similar adduced on fig.1, where relations of amplitude and phase of controlled disturbances $A_0(x)$ and $\Phi_0(x)$ over the longitudinal coordinate in section z=0 are shown. The first zone corresponds to acoustic waves, radiated by
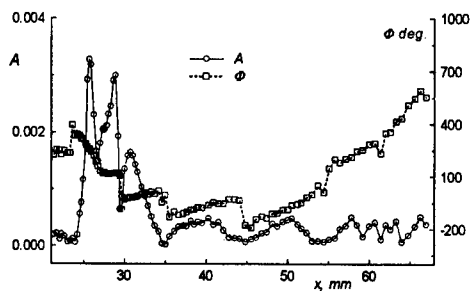
Fig.1 Dependence $A(x)$, $\Phi(x)$ of controlled initial
disturbances at the position of plate 2
(plate 2 removed)
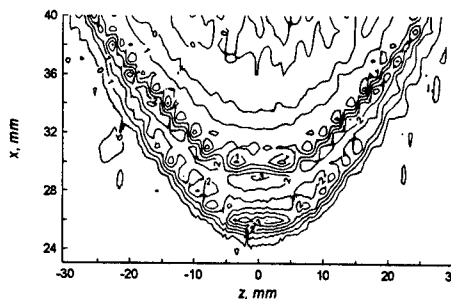
Fig.2 Lines of equal amplitude of initial artificial
disturbances at the position of plate 2

disturbances from the source, propagated upstream in the boundary layer of the plate *1* (in fig.1 this zone about corresponds to area of the first maximum at 24 mm $< x <$ 27 mm, where phase reduction with increasing of the coordinate x was observed). The second zone (disturbances radiation directly from the aperture of the source) corresponds to the area of the second maximum in fig.1. The third zone corresponds to radiation from the vortex behind of the aperture (on fig.1 this zone about corresponds to area of the third maximum at x from 30 mm up to 35 mm). The fourth zone is observed for $x>35$ mm as radiation from TS waves. The similar analysis of amplitude and phase distributions over x was made in [4-6].

Measurements of $A_0(x)$ and $\Phi_0(x)$ in free stream had allowed to define border on the coordinate x of area of excited disturbances and to began more in-depth researches of initial disturbances. For this purpose measurements of transversal distributions of amplitude and phase $A_0(z)$, $\Phi_0(z)$ of controlled disturbances in the plane of the plate *2* were made for values of the longitudinal coordinate from $x=24$ mm (the border of excited disturbances) up to $x=40$ mm with a step 1 mm. Lines of equal amplitude of artificial disturbances, obtained after the processing of the distributions $A_0(z)$, $\Phi_0(z)$ with the help of spline, are shown in fig.2. The border of perturbed area for the radiation is good observed in the plot.

The distributions $A_0(z)$ and $\Phi_0(z)$ of initial controlled disturbances were measured for cross-sections $x=$const in four different regions of radiation ($x=26$, 29, 31 and 38 mm) in free stream. These values of the coordinate x were chosen from distributions $A(x)$ and $\Phi(x)$ presented in fig.1. At study of a field of boundary layer disturbances induced by the external controlled waves, the plate *2* was established so that its leading edge consistently placed precisely in those sections, where external disturbances, belonging to various areas of radiation, were investigated (i.e. coordinate of the leading edge was $x=26$, 29, 31 and 38 mm). The distributions $A(z)$, $\Phi(z)$ of disturbances were measured in the boundary layer of the plate *2* at x^* equal to 40 and 50 mm (here x^* is the distance from the leading edge). The measurements were carried out in an unstable region of disturbances development in the supersonic boundary layer. In this way the structure of external disturbances and the waves generated by them in the boundary layer were defined.

Only the data correspond to the leading edge coordinate $x=31$ mm are presented in the paper. The amplitude and phase spectra of external acoustic disturbances and eigen oscillations generated by them are compared in fig.3 as functions of transversal coordinate. Here distributions at $x^*=0$ correspond to the initial controlled disturbances in free stream at $x=31$ mm. Though distributions $A(z)$, $\Phi(z)$ for oscillations in the boundary layer shows, that
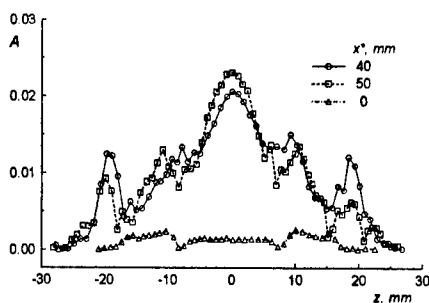
Fig.3a. Distribution of $A(z)$ over transversal
coordinate for leading edge coordinate $x=31$ mm.
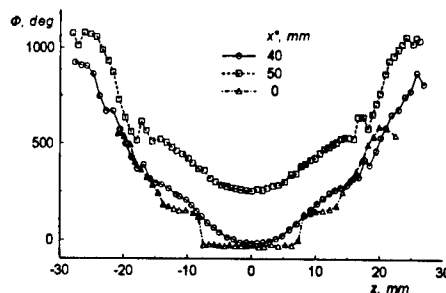
Fig.3b. Distribution of $\Phi(z)$ over transversal coordinate
for leading edge coordinate $x=31$ mm.
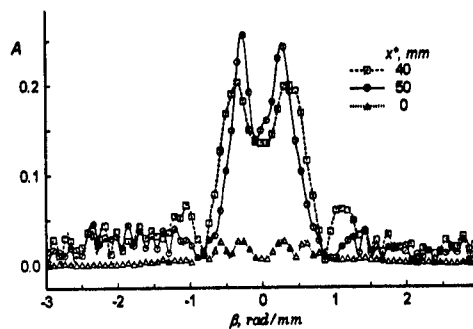
Fig.4a. Distribution of $A(\beta)$ over wave number β for leading edge coordinate $x=31$ mm.
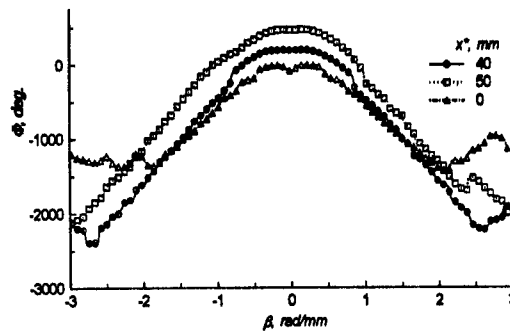
Fig.4b. Distribution of $\Phi(\beta)$ over wave number β for leading edge coordinate $x=31$ mm.

the generation of eigen oscillations by the external controlled disturbances takes place. The amplitude of excited disturbances in the boundary layer exceeds amplitude of initial controlled disturbances in several times.

The β-spectra were determined with the help of discrete Fourier - transformation under the data, presented in fig.3. The amplitude and phase spectra of external acoustic disturbances and eigen oscillations generated by them are compared in fig.4 as functions of the wave number β. Significant amplification of the external disturbances in the boundary layer is observed too. Using obtained data the transformation coefficients of disturbances (coefficient of generation) can be found from the relation

$$K(\beta) = \frac{A(\beta)\big|_{x^*=x_i^*}}{A(\beta)\big|_{x^*=x_i^*}} .$$
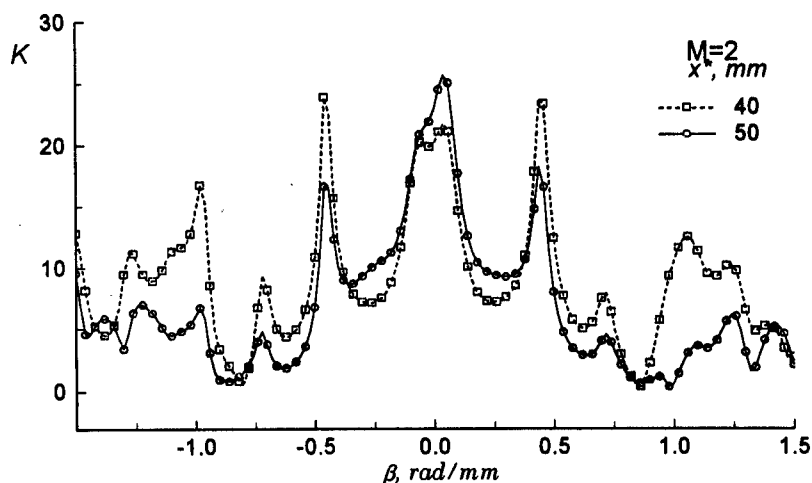
Fig.5. Transformation coefficients $K(\beta)$ over wave number β at leading edge coordinate $x=31$mm.

195

Figure 5 shows the transfer functions of disturbances $K(\beta)$ obtained for the blunted leading edge. In the case of plate with the sharp leading edge the integrated transformation coefficient was close to the unit. Two typical regions of disturbances generation were found, namely, the region ±10° with the minimum transformation coefficients K ($K<1$) and the region ±(20°-40°) with the maximum coefficients ($K>1$) [4]. It was obtained, that for the case of blunted leading edge the transformation coefficient greater the ones for the case of sharp leading edge more than an order. The maxima at $\beta=\pm0.5$ show that the inclined waves are excited in the boundary layer of the blunted plate. The existence of maximum in the distribution $K(\beta)$ in a vicinity of $\beta=0$ shows that acoustic are generated in the boundary layer too. Bluntness is the reason of such difference in our opinion. The excitation occurs in the small location at the leading edge, but this location is greater for the case of blunted leading edge. Furthermore a shock wave is formed near the leading edge. External controlled disturbances interact with the shock wave. The shock waves become an additional source of disturbances by itself and excites oscillations in the boundary layer too. Confirmation of this conclusion may be obtained from fig.6, where distributions of $A(x)$ and $\Phi(x)$ are presented in dependence of the longitudinal coordinate in free stream over the surface of the plate 2. At the same measurement in the case of sharp leading edge the initial controlled disturbances were observed up to maximum, corresponded to the Mach line from the leading edge. The disturbances, correlated with the source, were close to zero in free stream after the Mach line [4,6]. Another picture can be seen in fig.6, where disturbances in free stream under the surface of the plate 2 exceed initial controlled disturbances.

Analogous measurements were carried out and analogous results were obtained for the other radiation zones.
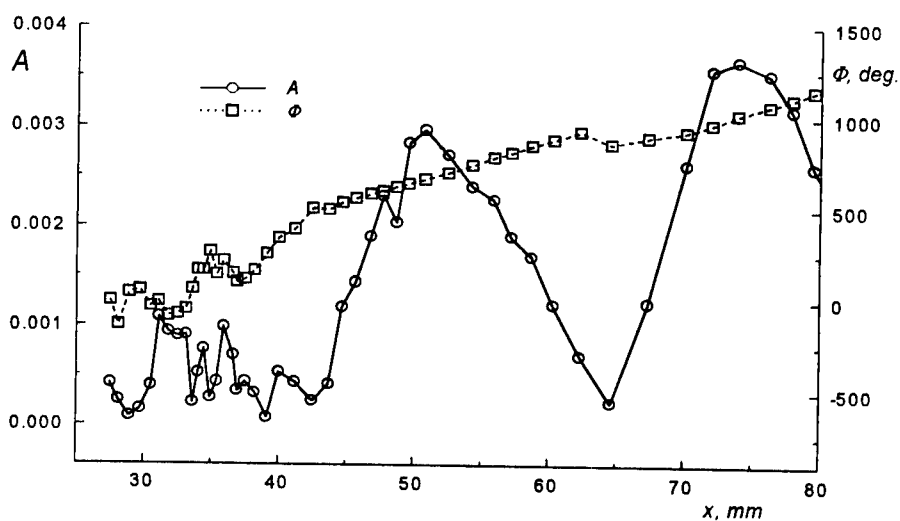
Fig.6. Distributions of $A(x)$ and $\Phi(x)$ over longitudinal coordinate in free stream at the distance $y=1.5$ mm under the surface of the plate 2.

CONCLUSIONS

Experimental study of the controlled disturbances field, introduced into free stream with the help of the local source of disturbances, was carried out. Disturbances in the flat plate boundary layer, excited by the external controlled acoustic oscillations in the vicinity of the blunted leading edge, were measured.

Quantitative comparison of levels of initial acoustic disturbances in free stream and fluctuations of the supersonic boundary layer, caused by them, was made. The transformation coefficients of acoustic disturbances into oscillations of the supersonic boundary layer were obtained.

It was found, that the excitation of disturbances in the boundary layer by the external disturbances at the case of blunted leading edge occurs considerably more heavily than at the case of sharp leading edge.

ACKNOWLEDGMENT

REFERENCES

1. Kendall J.M. Wind tunnel experiments relating to supersonic and hypersonic boundary-layer transition // AIAA J. - 1975. - V.3. - P.290-299.
2. Maslov A.A., Semionov N.V. Excitation of eigen boundary layer oscillation by external acoustic field // Izv. Akad. Sci. USSR. Zh. Mech. Zhid. G. - 1986. - V.3. - P.74-78 (in Russian).
3. Kosinov A.D., Maslov A.A., Semionov N.V. Methods of controlled disturbances generation for experimental investigation of supersonic boundary layer receptivity // Int. Conf. on the Methods of Aerophys. Research: Proc. Pt 1. - Novosibirsk, 1994. - P.138-144.
4. Semionov N.V., Kosinov A.D., Maslov A.A. Experimental investigation of supersonic boundary layer receptivity // Transitional Boundary Layers in Aeronautics: Amsterdam, North-Holland, 1996. - P.413-420.
5. Kosinov A.D., Maslov A.A., Semionov N.V. Modified method of experimental study of supersonic boundary layer receptivity // Int. Conf. on the Methods of Aerophys. Research: Proc. Pt.3. - Novosibirsk, 1996. - P.161-166.
6. Semionov N.V., Kosinov A.D., Maslov A.A. Experimental study of boundary layer receptivity at M=3.5 // Stability and Transition of Boundary Layer Flows. Abstracts, EUROMECH Colloquium 359: Stuttgart, 1997.
7. Kosinov A.D., Maslov A.A., Shevelkov S.G. Experiments on the stability of supersonic laminar boundary layers // J. Fluid Mech. - 1990. - Vol.219. - P.621-633.

MODELING OF PROCESS OF VAPOUR CONDENSATION
ON A ROTATING DISK

V.N. Shepelenko

Institute of Theoretical and Applied Mechanics, SB RAN,
630090 Novosibirsk, Russia

In the paper a model of vapour condensation on a rotating disk is described. A Nusselt model [1–3] has been taken as the basis for investingation of the phenomena. An algorithm and results of compartive calculations are presented. The model permits to obtain preliminary characteristics of a process of condensation in disk ventilators used for draining and cleaning of air in premises.

1. We use the following denotations: x – radial coordinate of a disk, m; θ – polar coordinate of a disk, rad; y – axial coordinate, m; $R1$ – inner radius of a disk, m; $R2$ – external radius of a disk, m; ω – angular velocity of a disk, 1/s; U – radial velocity of a condensate, m/h; Pr – Prandtl number; t_r – temperature of air in premises, °C; t_s – temperature of a saturated vapour, °C; t_w – temperature of a disk, °C; C_p – specific heat of air, kcal/kG·°C; Δt – difference $\Delta t = t_s - t_w$, °C; α – heat transfer coefficient kcal/m·°C·h; q – density of a heat flow, kcal/m²·h; r – latent heat of condensation, kcal/kG; μ – viscosity of cndensate, kG·s/m²; ν – kinematic viscosity of condensate, m²/h; λ – thermal condactivity of condensate kcal/m·°C·h; γ – specific gravity of condensate, kG/m³; δ – condensate film thickness, m; τ – force of internal friction of condensate, kG/m²; ρ – density of condensate, kg/m³; g – gravity acceleration, m/s².

In the future we shall consider only the stationery flow and assume that condensation take place only on boundary vapour–liquid, condansate is incompressible viscous liquid, pressure in condensate film is constant and equal to the vapour pressure, the flow of the film is laminar, inertial forces are small in comparison with the forces of viscosity, the surface tension on a boundery vapour–liquid is absent, temperature of film is linear along a normal to surface of a disk, parametrs μ, λ, γ are constant and equal to that of at temperature $t = 0.5(t_w + t_s)$, motion of condensate along coordinate y can be neglected.

The equation for the thickness of condensate film is derived from the general equations of movement of viscous incompressible liquid. In

---

the cilindrical system of coordinates with account of assumed above suppositions those equation can be witten in the form [4]

$$\mu \Delta \vec{W} = \rho \vec{f}, \quad div \vec{W} = 0, \tag{1.1}$$

where $\vec{W}$ – vector of velosity of the condansate particals, $\vec{f}$ – vector of voluem forces. As in our case

$$W_\theta = 0, \quad W_y = 0, \quad W_x = U(x, y),$$

equations (1.1) takes the form

$$\mu \left[\frac{\partial}{\partial x} \left(\frac{\partial U}{\partial x} + \frac{U}{x} \right) + \frac{\partial^2 U}{\partial y^2} \right] = -\rho x \omega^2, \qquad \frac{\partial U}{\partial x} + \frac{U}{x} = 0, \tag{1.2}$$

whence it follows

$$\mu \frac{\partial^2 U}{\partial y^2} = -\rho x \omega^2. \tag{1.3}$$

Let us consider x as parameter, then

$$U(x, y) = -\frac{\rho x \omega^2}{\mu} \frac{y^2}{2} + Cy + C'. \tag{1.4}$$

The constants of integration C and C' can be found from the followig two conditions

$$U(x, 0) = 0, \quad U'_y(x, \delta(x)) = 0,$$

stipulated with viscosity of condensate and stationary film flow. So we have

$$U(x, y) = -\frac{\gamma}{\mu} \frac{x \omega^2}{g} \left(\frac{y^2}{2} - \delta(x) \right) y. \tag{1.5}$$

Average film velocity can be written as follows

$$U_{cp}(x) = \frac{1}{\delta(x)} \int_0^{\delta(x)} U(x, y) dy = \frac{\gamma}{3\mu} \frac{x \omega^2}{g} \delta^2(x). \tag{1.6}$$

Now let us write the influx of condensate dG on the part dx of a radius over the density of heat flux q:

$$dG = \frac{2\pi x q(x) dx}{r'} = \frac{2\pi x}{r'} \frac{\lambda}{\delta(x)} (t_s - t_w) dx$$

where $r' = r + C_p(t_r - t_s)$, and compere it to the increment of expenditure on the same part dx

$$dG = d \Big(2\pi x \delta(x) U_{cp}(x) \gamma \Big) = \frac{\gamma^2 \omega^2}{3\mu g} 2\pi d \Big(x^2 \delta^3(x) \Big).$$

We have

$$2\delta^4 + \frac{3x}{4}\frac{d\delta^4}{dx} = \frac{3\mu\lambda g}{r\gamma^2\omega^2}(t_s - t_w). \qquad (1.7)$$

Let

$$A(x) = \frac{3\mu\lambda g}{r\gamma^2\omega^2}(t_s - t_w), \quad D(x) = \delta^4, \qquad (1.8)$$

then equation (1.10) can be written in the form

$$\frac{dD}{dx} = \frac{4}{3x}\Big(A(x) - 2D\Big). \qquad (1.9)$$

Boundery condition for equation (1.12) is obvious

$$D(R1) = 0. \qquad (1.10)$$

In general case the solution of the problem (1.9), (1.10) is calculated with one of the Runge–Kutt method [5]. For the case $A(x) = $ const the solution has the form

$$D(x) = \frac{A}{2}\Big(1 - \Big(\frac{R1}{x}\Big)^{8/3}\Big), \qquad (1.11)$$

and, consequently,

$$\alpha(x) = \frac{\lambda}{\delta(x)} = \sqrt[4]{\frac{2}{A}}\frac{\lambda x^{2/3}}{\sqrt[4]{x^{8/3} - R1^{8/3}}}. \qquad (1.12)$$

For $R1 = 0$ we have from (1.12)

$$\alpha(x) = \sqrt[4]{\frac{2\lambda^4}{A}} = \sqrt[4]{\frac{2r\lambda^3\gamma^2\omega^2}{3\mu g\Delta t}} = \text{const}.$$

Thes formula can be rewritten as [6, 7]

$$\alpha\frac{(\nu/\omega)^{1/2}}{\lambda} = 0.904\Big(\frac{r\cdot Pr}{C_p\Delta t}\Big)^{1/4}, \qquad (1.13)$$

where $\nu = \mu/\rho$, $\ Pr = \mu C_p/\lambda$.

2.Consider numerical exampel: define amaunt of drain saturated vapour, condensating at atmosphere pressure in an hour on one side of the rotating disk with $\omega = 200$ rev/s, $t_w = 60°C$ and $R1 = 0.05$ m, $R2 = 0.10$ m.

Values of parametrs μ, λ, γ are taken at average temperature $t_m = 0.5(60 + 100) = 80°C$ [2]:

$\mu = 36.6 \cdot 10^{-6}$ kG·s/m^2 = $1.008 \cdot 10^{-8}$ kG·h/m^2,

$\lambda = 0.580$ kcal/m·°C·h.

$\gamma = 971.8$ kG/m^3.

Latent heat of condensation of the water at atmosphere pressure is equal $r = 539$ kcal/kG. So we have:

$$A = 3\mu\lambda g\Delta t/r\gamma^2\omega^2 = 33.8015 \cdot 10^{-20} \text{ m}^4;$$

$$\delta(R2) = \left[\tfrac{A}{2}\left(1 - \left(R1/R2\right)^{8/3}\right)\right]^{1/4} = 1.9425 \cdot 10^{-5} \text{ m};$$

$$U_{cp} = \gamma R2\omega^2\delta^2(R2)/3\mu g = 4944.5493 \text{ m/h} = 13.7349 \text{ m/s};$$

$$G = 2\pi R2\delta(R2)U_{cp}\gamma = 58.6481 \text{ kG/h}.$$

The same result can be obtained by virtue of average heat trasfer coefficient

$$\alpha_{cp} = \frac{1}{F}\int_{R1}^{R2}\int_{0}^{2\pi}\alpha(x)x d\theta\, dx = \frac{2\pi\lambda}{F\sqrt[4]{A/2}}\int_{R1}^{R2}\frac{x^{5/3}dx}{\sqrt[4]{x^{8/3} - R1^{8/3}}} = \quad (2.1)$$

$$= frac\lambda\sqrt[4]{A/2}\frac{\left(R2^{8/3}-R1^{8/3}\right)^{3/4}}{R2^2-R1^2} = 33540.6364 \text{ kcal/m}^2\cdot°\text{C}\cdot\text{h}$$

$$G = Q/r = \alpha_{cp}\Delta t \cdot F/r = 58.6481 \text{ kG/h}.$$

Using above discribed algorithm many calculations have been made at constant and variable temperature t_w. On the results the following conclusions can be made:

1. the thickness of condensate film very strong depends on difference $\Delta t = t_s - t_w$, and almost independs on values itself temperatures t_s and t_w,

2. for increasing temperature t_w the thickness of condensate film at first icrease and then begins decrease and can quit vanish, so we have no condensation,

3. with growing angular velosity ω the boundary between condansate and dry surface move to the rim of the disk.

REFERENCES

1. Nusselt W. Die Oberflachen Kondensation des Wasserdampfes // *Zeitschrift des Vereines Deutqscher Ingenieure.*- 1916. - Bd 60.- S.541, 569.

2. Михеев М.А. Основы теплопередачи.- М.: Гос. энерг. изд-во, 1949.

3. Исаченко В.П., Осипова В.А., Сукомел А.С. Теплопередача.- М.- Л.: Энергия, 1965.

4. Кочин Н.Е., Кибель И.А., Розе Н.В. Теоретическая гидромеханика. Т.2.- М., 1963.

5. Березин И.С., Жидков Н.П. Методы вычислений. Т.2.- М.: Физматгиз, 1962.

6. Sparrow E.M. A theory of rotating condensation // *Trans. ASME, Series C, Journal of Heat Transfer.*- 1959.- Vol. 81.- No 2.- P.113-120.

7. Yanniotis S., Kolokosta D. Experimental study of water vapour condensation on a rotating disc //*Int. Comm. Heat Mass Transfer.*- 1996.- Vol. 23.- No 5.- P.721-729.

RECONSTRUCTION PROBLEM OF ADAPTED AIRFOIL WITH GIVEN ELECTROMAGNETIC SCATTERING

M.S. Soppa

Novosibirsk State Architecture Civil Engineering University
630008, Leningradskaya, 113, Novosibirsk, Russia

PROBLEM STATEMENT

The scattering of a plane H - polarized electromagnetic wave on a profile with ideally conducting (metallic) surface S is stadied. For the nonzero component of the magnetic field $u = H_z$ we have the Helmholtz equation:

$$\frac{\partial^2 u}{\partial x^2} + \frac{\partial^2 u}{\partial y^2} + k^2 u = 0 \qquad \text{outside S}$$

with the boundary condition :

$$\frac{\partial u}{\partial n} = 0 \qquad \text{on S ,}$$

here $k = 2\pi / \lambda$, λ — wave length, $\dfrac{\partial}{\partial n}$ - derivative along outward normal .

The noncompressed potentional flow over profile is described with Laplas equation for the velocity potential :

$$\frac{\partial^2 \Phi}{\partial x^2} + \frac{\partial^2 \Phi}{\partial y^2} = 0 \qquad \text{outside S}$$

with the boundary condition :

$$\frac{\partial \Phi}{\partial n} = 0 \qquad \text{on S ,} \qquad (1)$$

and with the Joukowsky - Kutta condition at the trailing edge.

The inverse problem of the unknown surface part $S_0 \subseteq S$ reconstruction is considered in the following statement. Find the set of values $\{ \rho_i \}$, $i = 1,..,L$, which parametricaly describe desired surfase S_0, and which ensure:

    a) a sufficiently accurate approximation to a given scattering diagram (SD);
    b) unshocked, smooth flow over profile.

The scattering diagram is given at a finite number of far field points: $h_1(\varphi)$, $\varphi \in \{ \varphi_j, j = 1,...m \}$, φ — is the polar angle, m = L - 1. The criterion of approximation

to a given SD is understood in a root-mean-square sense :

$$J_1 \equiv \sum_{j=1}^{m} \left| h(\varphi_j) - h_1(\varphi_j) \right|^2 \to \min .$$ (2)

The smooth flow over airfoil nose part corresponds to close to zero load of the leading edge. In case of thin airfoil it ensures the essential decreasing of drag and increasing of aerodynamic efficiency. We assume the airfoil to be thin, its middle line to be weakly deformed and we will suggest, that boundary condition (1) is realized at the airfoil base surface (chord). The unshocking condition (in terms of pressure coefficient) then will be written down as $C_P(0) = 0$. While using the panel method [1] for calculation of the flow around airfoil this is equivalent to zero vortex strength at the leading edge, or

$$J_2 \equiv \left| \gamma(0) \right| \to \min .$$ (3)

This condition, following from aerodynamic consideration , will be added to the indefinite (m < L) electrodynamic problem of the airfoil form identification..

NUMERICAL SOLUTION METHOD

Assume, that desired parameters $\{ \rho_i \}$ are equal to absolute values of unknown surface S_0 radius - vectors at the supporting sections with polar angles ψ_i , $i = 1,..,L$.

In order to obtain the numerical solution of electrodynamic problem we will use scattering field integral representation :

$$h = \sqrt{r} \exp(-ikr) \frac{ik}{2\pi W_0} \int_{S(\rho)} ((\frac{\partial g}{\partial n} D^{-1} B + g) \, W - \frac{\partial g}{\partial n}) u_0 ds ,$$ (4)

where $r = \sqrt{x^2 + y^2} \to \infty, y / x = tg\varphi$, g - is a fundamental solution of the Helmholtz equation, B, D - operators of direct problem inversion. Here we use the method of artificial «immersion» in a more general problem, when the surface impedance W at the part S_0 is
accounted to be unknown.

Aerodynamic problem is solved using panel method [1] with the «plane» boundary condition and piece - linear vortex density function along the airfoil chord. Using the inversion of the aerodynamic influence matrix A , obtain expression for vortex density by means of panel local angles of attack. Thus , the relationship (3) can be rewritten as

$$\gamma_l = \sum_{p=1}^{NW} (A^{-1})_{p,l} (\delta_p - \alpha + \delta_p^0) = 0,$$ (5)

where α - angle of attack, δ_p^0 - panel deflexion angle, corresponding to initial airfoil middle line deformation, δ_p - variable deflexion angle, NW - node points number along the chord.

In paper [2] effective method of surface impedance reconstruction, in case of fixed geometry S_0 , is suggested. Thereby operator can be defined:

$$\vec{W} = \vec{Y}(\vec{\rho}) ,$$

here vector objects are discrete analogs for an according continuous functions.

The relationship (5) permits to express the airfoil nose loading by means of vector $\vec{\rho}$:

$$\gamma_1 = G(\vec{\rho}).$$

Note, desired inverse problem solution corresponds to zero values of parameters $\vec{W}$ and γ_1. Therefore, instead of extremal problem (2,3) we obtain the nonlinear operator equation :

$$\vec{Z}(\vec{\rho}) = 0,$$

where $\vec{Z} = \{ \vec{Y}, G \}$. This equation can be solved by means of, for example, Newton's method. As a result we will have airfoil nose contour, which ensures given scattering diagram together with unshocking airflow regime.

REFERENCES

1. Lipatnikova T.P., Silantiev V.A., Soppa M.S. Lifting system optimization for subsonic flow using Woodward panel method // Simulation in Mechanics. Novosibirsk, 1989, v. 3 (20), N 1, p. 107-115.
2. Soppa M.S.,Ershova E.E. Numerical Solution of Inverse Scattering Problem on Impedance Bodies for E- and H-polarizations // Optoelectronics, Instrumentatin and Data Processing. No. 2, 1997, p.51-55, Allerton Press, Inc.

DEVELOPEMENT OF THE LASER SHEET IMAGING METHOD FOR SUPERSONIC WIND TUNNELS

L.G.Vasenev, S.B.Nikiforov, A.A.Pavlov, A.M.Shevchenko

Institute of Theoretical and Applied Mechanics SB RAS,
630090, Novosibirsk, Russia

INTRODUCTION

Laser sheet technique is one of the most powerful means to investigate 3D flows. Flow field seeded with particles is visualised due to the scattering of a plane laser beam light, with the distribution of brightness of the scattered light depending on the particles concentration inside the plane of interest. Recently, at ITAM laser sheet technique has been widely used grabbing the data using originally designed photo camera mounted inside the wind tunnel, which allows one to obtain one frame per wind tunnel run. This way has a number of restrictions such as limited amount of information obtained, inability to correct a quality of images at the rate of experiment.

A progress achieved in microelectronics allowed one to modify the described technique to increase the amount of data per wind tunnel run and to allow one to correct the quality of images adjusting either electronic system parameters or seeding system parameters. Possibilities of digital image processing and displaying can also be applied to the data collected.

1. HARD- AND SOFTWARE

Hardware used includes the optical scheme forming the plane laser beam (laser sheet), the seeding system and the registration system collecting images of the flow field formed in the plane of interest. An optical scheme is shown in figure 1. A light source 1 is the argon laser of continues operation rate with the radiation power of approx. 1 W. The light beam is extended, if needed, by a pair of diverging lenses 2, 3. Then the light beam passes through the spherical convergent lens 4. Its focal plane is to coincide with a centre of the plane of interest thus providing a width of the laser sheet less than 1 mm.
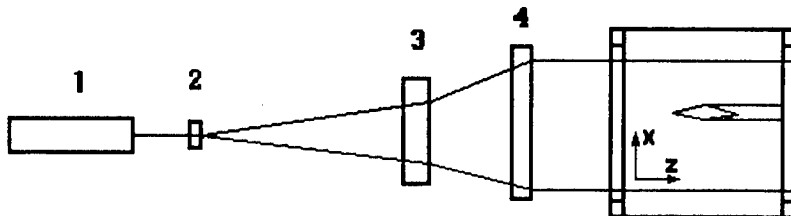
Fig. 1. Optical scheme forming the laser sheet.

When using this technique at ITAM T-313 supersonic wind tunnel water was used for flow seeding. Works [1-3] shows the results of investigations of influence of water particles present inside the wind tunnel tract on flow parameters. It was shown that the amount of water needed for the flow field visualisation does not affect the flow parameters.
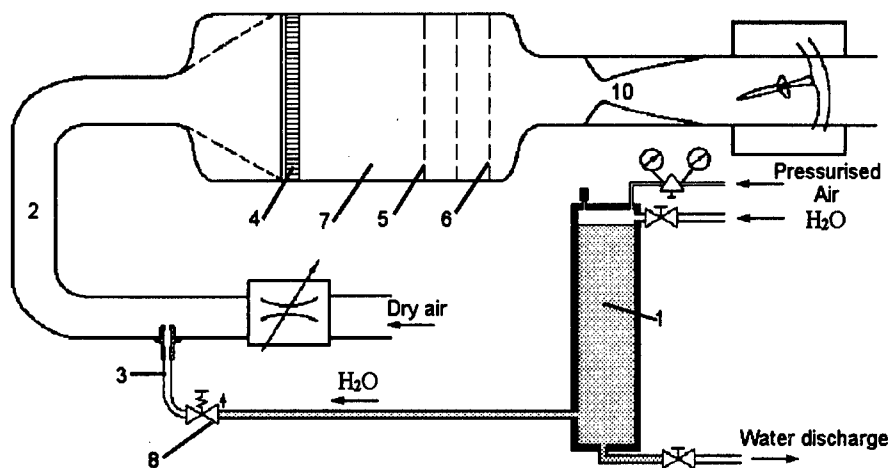
Fig. 2. Scheme of the seeding system.

The seeding system is shown in figure 2. The water from tank 1 is charged into the wind tunnel tract 2 through sprayer 3. Flowing out through the sprayer, the water medium is atomised in small drops which intensively vaporise in dry air. These particles flowing through filter 4, honeycomb 5 and grids 6 mounted in the settling chamber 7 uniformly fill the tract. The use of remote controlled electromagnetic valve 8 allows one to seed the flow only at the moment of data grabbing thus neglecting the influence of the moist air on the wind tunnel components, investigated models and registration devices. The water flow rate can be adjusted at the rate of experiment by means of an air reducer 9 providing the air pressure in the water tank 1. While extending in the supersonic nozzle 10 water vapour transforms in a fog which particles provide the laser light scattering. Water mass flow should provide the beginning of water condensation. An additional amount of water should also be added to provide light scattering particles. The water mass flow needed for water condensation is less than 10^{-6} Kg/sec which is a negligible value and may not be taken into account. Thus the needed water mass flow rate is defined by the amount of water needed for the light scattering particles to arise. Tests have shown that the water mass flow mentioned above does not exceed 150 g/sec.

The most significant improvements of the method were made by replacing the photo-camera by a CCD camera connected to the frame grabber mounted in PC. PC allows one to grab images into its memory, to store them on a hard disk, to display on a PC screen, to adjust and control registration system parameters at the rate of the experiment. In our case JAI CV-M10 progressive scan, 30Hz, 659x494 pixels CCD camera was used. This camera has a high light sensitivity, remote electronic control of amplification coefficient and expose time, and small sizes.

The registration system scheme is presented in figure 3. A CCD camera is placed in the shielding box mounted on the dummy strut directly in the wind tunnel test section. The box was designed to provide the possibility to mount it on either side of the dummy strut higher or lower the wind tunnel axis. It is also possible to adjust the box angle of deflection in both vertical and horizontal directions. To protect the camera lens, the protecting glass is mounted ahead the lens, the glass is also protected
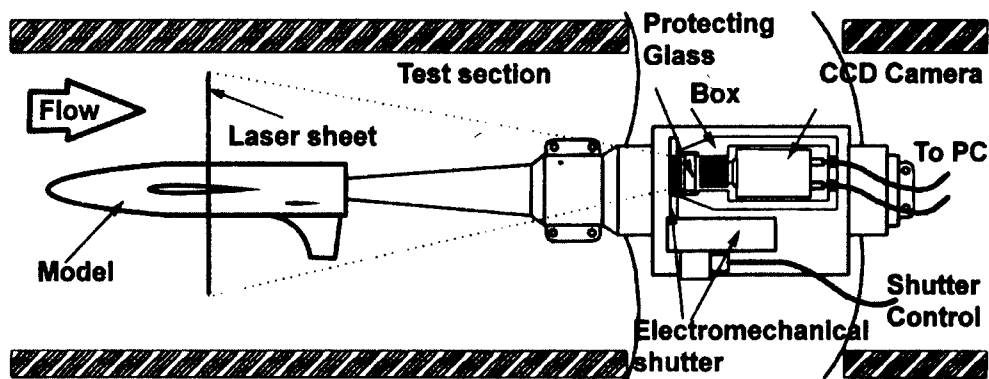
Fig. 3. The CCD camera and the protecting box mounted inside the work section of T-313 wind tunnel.

by the electromechanical shutter. The shutter is opened only at the time of expose and controlled by the wire remote control. Eltec PC-EYE1 frame grabber mounted in PC allows one to grab both single frames and the sequence of frames with a predefined period. The control software includes two Win32 applications. The primary one (CAMERA.EXE) allows one to adjust CCD camera parameters. The later one (GRABBER.EXE) controls the frame grabber. In some cases it is needed to simultaneously register additional parameters such as time, temperature, incident angle, etc. Originally designed ISA card also mounted in PC allows one to do this providing a 16-bit input interface. The time delay between the end of the frame and the registration of additional parameter does not exceed 1 micro-second. The software also allows for processing and displaying the data collected.

2. CALIBRATION TESTS AND RESULTS DISCCUSSION

To demonstrate the functionality of the system described calibration tests on visualisation of the flow field formed by a thin delta wing with a symmetrical profile and a sharp leading edge were performed. The wing scheme and parameters are shown in fig. 4.

$$\chi=78°$$

$$b_0=526\text{mm}$$

$$\overline{c}=c/b(z)=0.03$$
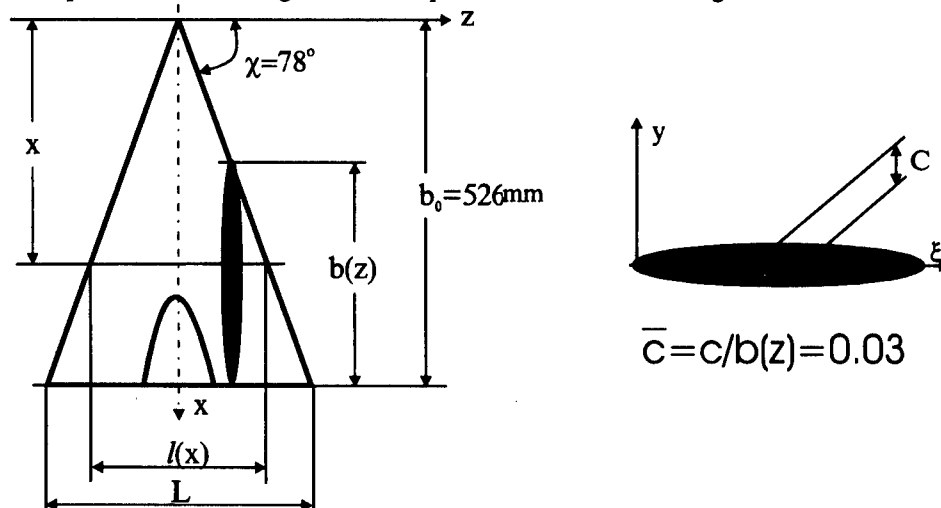
Fig. 4. Scheme of the wing used.

p_{H2O}=4 atm 0.26 s, (8 fields)
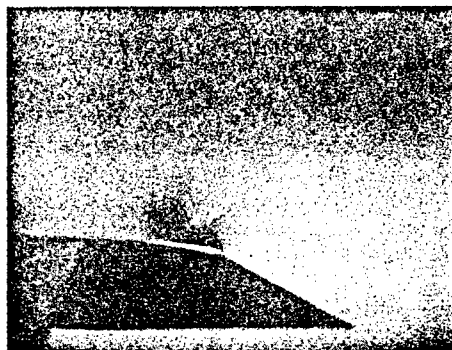
p_{H2O}=4 atm, 1/30 s

p_{H2O}=8 atm, 1/30 s

p_{H2O}=12 atm, 1/60 s
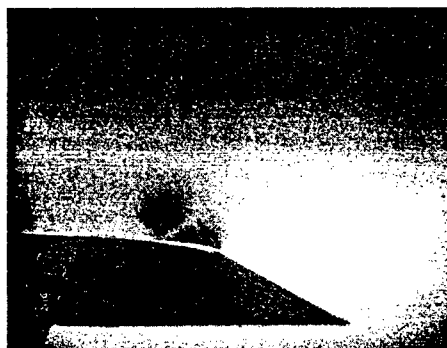
p_{H2O}=12 atm, 1/30 s

Fig.5. M=2, Re_1=27.05·10^6, p=4 atm, α=10°

209

p_{H2O}=1.5 atm, 0.13 s (4 fields)

p_{H20}=1.5 atm, 0.26 s (8 fields)
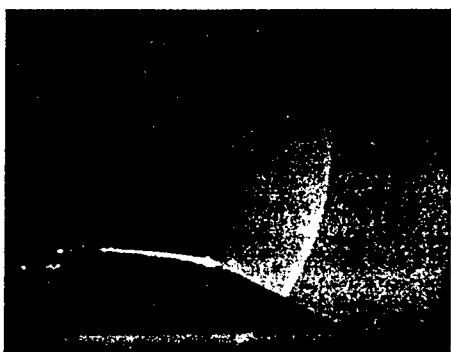
p_{H20}=3.5 atm, 0.13 s (4 fields)

p_{H20}=3.5 atm, 0.26 s (8 fields)

p_{H20}=5.5 atm, 0.13 s (4 fields)

p_{H20}=5.5 atm, 0.26 s (8 fields)

Fig. 6. M=3, Re_1=8.38·10^6, p=1atm, α=15°

The visualisation was performed for Mach numbers $M_x=2$ и $M_x=3$ in the range of angle of incidence 0° - 18°. The Reynolds number were: $Re_1=27.05 \cdot 10^6$ and $Re_1=13.53 \cdot 10^6$ for $M_x=2$ and $Re_1=35.12 \cdot 10^6$ and $Re_1=8.38 \cdot 10^6$ for $M_x=3$. The laser sheet plane coincides with the plane perpendicular to the wind tunnel axis at the relative length $X' = X / b_0 = 0.65$ from the nose of the model. While changing the angle of incidence, the laser sheet plane was rotated by the corresponding angle.

The main task of the tests was to clarify the possibility of obtaining the images of good quality at different regimes of the flow, adjusting the grabber and camera parameters and changing the water flow rate at the rate of the experiment. For each regime and system parameters three frames were grabbed. This allowed one to control the image quality and excluded the probability of losing data in case of a system failure.

Further, figures 5, 6 show some images grabbed. It should be noted that adjustment of the electronic system parameters and the water mass flow rate allowed one to obtain good quality images for all flow regimes. The quality of the printed images is worse than original ones and depends on the printer used (HP Laser Jet 5L in our case). For example, in fig.6, the λ-structure looks less clear, than in the original image.

REFERENCES

1. Maksimov A.I., Pavlov A.A. Development of a laser sheet technique of flow visualisation for supersonic wind tunnels // Uchen. Zap. TSAGI. 1986. Vol.17, N 5. P. 5 -18. (In Russian)

2. Vasenev L.G., Maksimov A.I., Pavlov A.A., Shevchenko A.M. Development of a laser sheet technique of flow visualisation for generic supersonic wind tunnels // Proc. of IV All-Union Conference on Methods of Aerophysical Research. Novosibirsk: ITAM, 1986. (In Russian)

3. Maksimov A.I. Oblique shock wave diffraction in a vicinity of a expansion right corner // PMTF, 1987, № 4. (In Russian)

4. Brodetsky M.D., Shevchenko A.M. Some features of a separated flow and supersonic vortex structure at the leeside of a delta wing // Separated Flows and Jets: Proc. of IUTAM Symp. Berlin-Heidelberg: Springer-Verlag, 1991. P.341-344.

COMPARATIVE RESEARCH OF HYPERSONIC RAREFIED AIR FLOW AROUND BLUNT BODIES USING MODELS OF VISCOUS SHOCK LAYER AND FULL NAVIER-STOKES EQUATIONS

V.I. Vlasov, A.B. Gorshkov

TSNIIMASH, Korolev, Moscow region, Russia

INTRODUCTION

For calculating external hypersonic flows in a continuous approach a model of the viscous shock-layer (VSL) and less often, in view of rather large computing costs, the full Navier-Stokes equations (NS) are frequently used. The equations in the VSL model are received from the set of NS equations, in which the terms up to the first order inclusively on the small parameter $\varepsilon = 1 / \sqrt{Re_s}$ (Re_s - Reynolds number defined with parameters in a shock layer) are saved and contain terms of both the Euler and boundary layer equations. The shock wave in the VSL model is considered as an indefinitely thin front, on which the so-called generalized Rankine-Hugoniot conditions are satisfied, which are obtained by an integration of the one-dimensional NS equations across a shock wave, neglecting longitudinal gradients of parameters along the shock. The VSL model well predicts flows at large Re, when the approximation of a boundary layer is true, and the shock wave is thin. However, at approximately $Re_s \leq 1000$ (Re_γ defined with parameters in the free stream) the thicknesses of a boundary layer and a shock become comparable with the size of a shock layer. For hypersonic flow of thermo-chemical nonequilibrium gas the approximation of a thin shock in the VSL model leads to omitting an upstream part of a shock wave, where chemical reactions can begin. Therefore, the determination of applicability bounds of the VSL model is of interest by comparing its results with that of the full NS equations. It is necessary to note, that the validity of the NS equations at small Re requires a research, however this problem is beyond the frame of the present work.

NUMERICAL METHODS AND RESULTS

In the literature there are some varieties of the VSL model, distinguishing by terms of the second order of the parameter ε. In this work the set of VSL equations presented, for example, in [1] is used. For solving the NS equations, cast in conservative form, an implicit iterative scheme described in [2] was used. For numerical stability the artificial dissipation was added in the finite difference equations at $Re_\gamma \geq 1000$ [see e.g. 3].

The computational region is bounded by a body surface (hereafter only a sphere is considered), a symmetry axis, inward (external) and outward boundaries (for a sphere - ray of 90 degrees). At solution of the NS equations a shock wave was captured, therefore external boundary was put far enough from a body, so that the condition of undisturbed free stream was valid. For the VSL equations the generalized Rankine-Hugoniot conditions were used on a shock wave. The velocity and temperature wall slip conditions, which are necessary to take into account at low Re, are as follows (for perfect gas):

$$U_s = \frac{2-\vartheta}{\vartheta}\sqrt{\frac{\pi}{2}}\frac{\mu_s}{\sqrt{P_s\rho_s}}\left[\left(\frac{\partial U}{\partial n}\right)_s - kU_s\right]$$

$$T_s = T_w + \frac{2-0,83\alpha}{\alpha}\frac{2\gamma}{\gamma+1}\sqrt{\frac{\pi}{2}}\frac{\mu_s}{\sqrt{P_s\rho_s}}\frac{1}{\Pr}\left(\frac{\partial T}{\partial n}\right)_s$$

Where the index s means the value of a parameter on the external boundary of the Knudsen layer, k - curvature, ϑ, α - accommodation coefficients, which in all presented calculations were equal 1.

In Fig.1 the experimental data on heat flux in terms of the dependence of Stanton number $St=q_w/[\rho_\infty U_\infty c_p(T_0-T_w)]$ from Reynolds number $Re_0=\rho_\infty U_\infty R/\mu_0$ are represented, where ρ_∞, U_∞ - density and velocity of a free stream, R - radius of a sphere, (μ_0 - viscosity calculated at the total temperature T_0). In an experiment [4], carried out in TSAGI, heat flux was measured at the stagnation point of a sphere on two models in a range of Re_0 from 0.36 ($Re_\infty=20$) to 606 ($Re_\infty= 5\times10^4$). The value of heat flux q_w was obtained with the help of semiconductor calorimetric gauge. The accuracy of experimental results was approximately 10%. The Mach number M_∞ varied from 20 to 30 at constant value of the temperature factor $T_w/T_0 = 0.18$. The tests were conducted in an air at total temperature $T_0=1600K$, therefore it is possible to consider gas perfect in experimental conditions. In the same figure the numerical data obtained with both theoretical models (VSL and NS) at Mach number $M_\infty=20$ are also represented. It is visible, that there is a rather good agreement between experimental and numerical data down to value $Re_0=3$ ($Re_\infty=170$, $Kn_\infty = \sqrt{\pi\gamma/2}\,M_\infty/Re_\infty = 0.174$).

Fig.1 Stagnation heat flux for sphere,
M=20, T_0=1621K, T_w/T_0=0.18, γ=1.4

To compare solutions of the full Navier-Stokes equations and the viscous shock layer model for thermo-chemical nonequilibrium flows calculations were made for a front part of a sphere of a radius R = 0,1524m at the conditions of flight experiment RAM-C [5]. Three points of trajectory in a transient regime were selected, their parameters are listed in Table 1. The Reynolds and Knudsen numbers in the table are calculated using the radius of a sphere. It was supposed, that the ionized chemically reacting air consists of eight components: N_2, O_2, NO, N, O, N_2^+, NO^+ and e^-. At calculation of vibrational temperatures of molecules of nitrogen $T_{v,N2}$ and oxygen $T_{v,O2}$ only the excitation of vibrations by impacts of heavy particles (V-T exchange) was considered, the exchange of vibrational energy between N_2 and O_2 (V-V exchange) was not taken into account.

213

Table 1

H, km	Re∞	Kn∞	Velocity, km/sec	T_w, K
84	1000	0.042	7.65	400
88	470	0.089	7.65	300
92	230	0.183	7.65	300

It was supposed, that the molecules N_2 and O arise and disappear in chemical reactions with their mean vibrational energies. The Schmidt numbers were considered constant and equal $Sc=0.75$ for neutral particles and $Sc=0.375$ for charged ones. The Prandtl number was assumed constant $Pr=0.71$ at Navier-Stokes computations, but it was calculated at computations using the viscous shock layer model. However, calculations have shown, that at these conditions the Prandtl number does not vary considerably. The wall is considered noncatalytic for neutral particles - $(\partial C_i/\partial n)_{wall} = 0$, and for charged particles the condition $C_{i,wall} = 0$ was specified. For a tangential velocity and translational temperature on a body surface the slip condition and temperature jump were used. At the definition of vibrational temperatures at the wall the absence of an accommodation of vibrational energy was assumed, which is equivalent to a condition $(\partial T_{V,k}/\partial n)_{wall} = 0$. The system of chemical reactions is presented in Table 2:

Rate constants of chemical reactions

Table 2

$$k_f(T) = A_f T^{B_f} \exp(-C_f/T), \quad k_r(T) = A_r T^{B_r} \exp(-C_r/T)$$

	Reactions	A_f	B_f	C_f	A_r	B_r	C_r
1	$O_2 + M_1 = O + O + M_1$	3.6×10^{19}	-1.0	59400	3.1×10^{15}	-0.5	0
2	$N_2 + M_2 = N + N + M_2$	5.8×10^{17}	-0.5	113200	3.1×10^{16}	-0.5	0
3	$NO + M_3 = N + O + M_3$	1.2×10^{19}	-1.0	75500	2.9×10^{8}	-1.0	0
4	$O + N_2 = N + NO$	2.0×10^{12}	0.5	38000	4.4×10^{11}	0.5	0
5	$O + NO = N + O_2$	2.8×10^{9}	1.0	20000	1.1×10^{10}	1.0	4000
6	$O + N = NO^+ + e^-$	2.6×10^{12}	0.0	32200	6.7×10^{21}	-1.5	0
7	$N + N = N_2^+ + e^-$	4.4×10^{10}	0.7	67500	1.5×10^{22}	-1.5	0

Matrix of catalytic activities

	O	O2	N	N2	NO
M1	2.5	1	0.25	0.25	0.25
M2	0.5	0.5	4	1	0.5
M3	20	1	20	1	20

The results of calculations using the Navier-Stokes equations (NS, solid lines) and the viscous shock layer model (VSL, markers) for altitude of 84 km (Re_∞ =1000) along a symmetry axis are shown in Fig.2a. Here the comparison of the profiles of translational and vibrational temperatures of nitrogen and oxygen molecules for the two theoretical models is given. In the same figure the profiles of mass concentrations of neutral (O, NO) and charged (NO^+) particles are also depicted. The concentration profiles of other chemical species have a similar type and therefore are not shown. From the presented figure it is seen that the size of a perturbed region, predicted by the NS equations, is more than two times larger than the shock layer thickness in the calculation with the VSL model. However, in the shock layer limited by a shock wave in the VSL model, there is a rather good (to within several percents) agreement of results for all compared parameters. This similarity of profiles holds along the whole windward
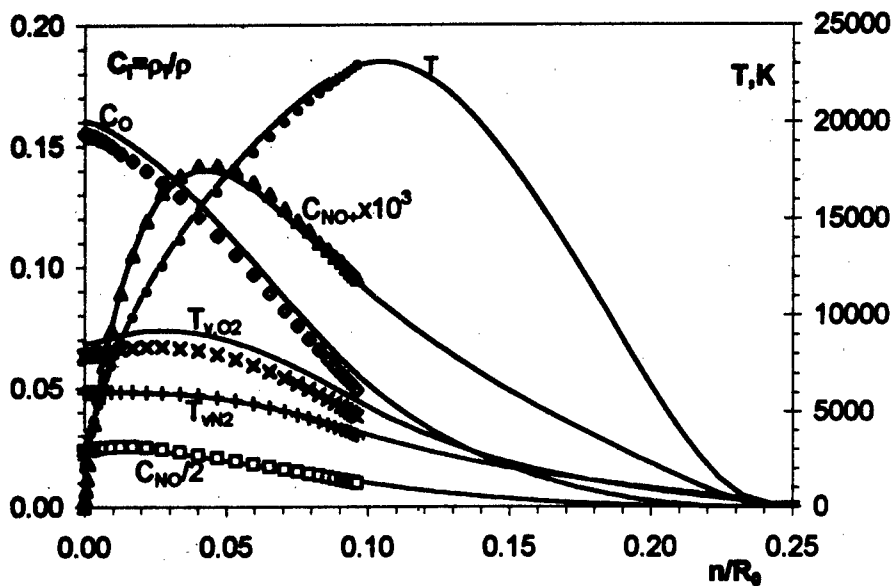
Fig.2a. Flow parameters along symmetry axis of sphere
obtained using NS equations (lines) and VSL model (markers)
at conditions of experiment RAM-C H=84km, V=7650м/c,
R=0.1524м, Re=1000
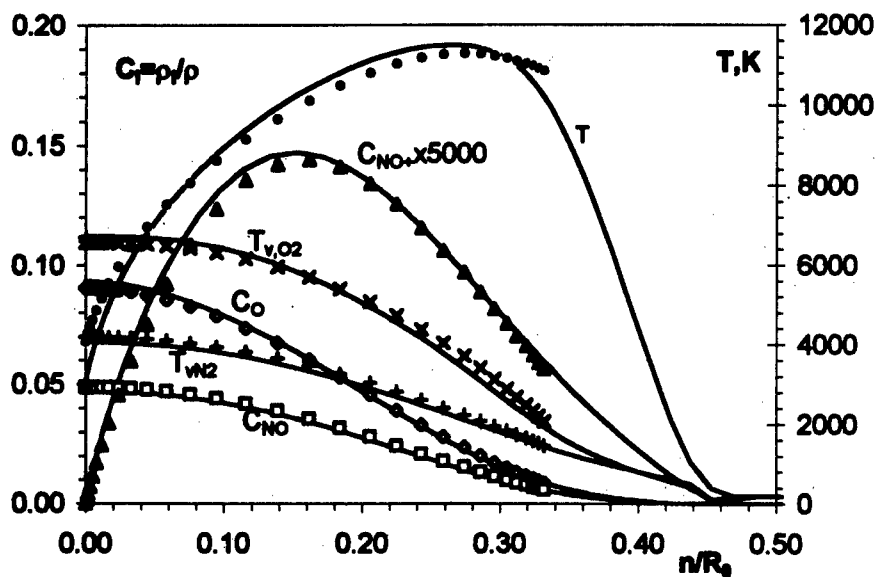
Fig.2b. Flow parameters at 75° angle on sphere obtained
using NS equations (lines) and VSL model (markers) at
conditions of experiment RAM-C H=84km, V=7650м/c,
R=0.1524м, Re=1000
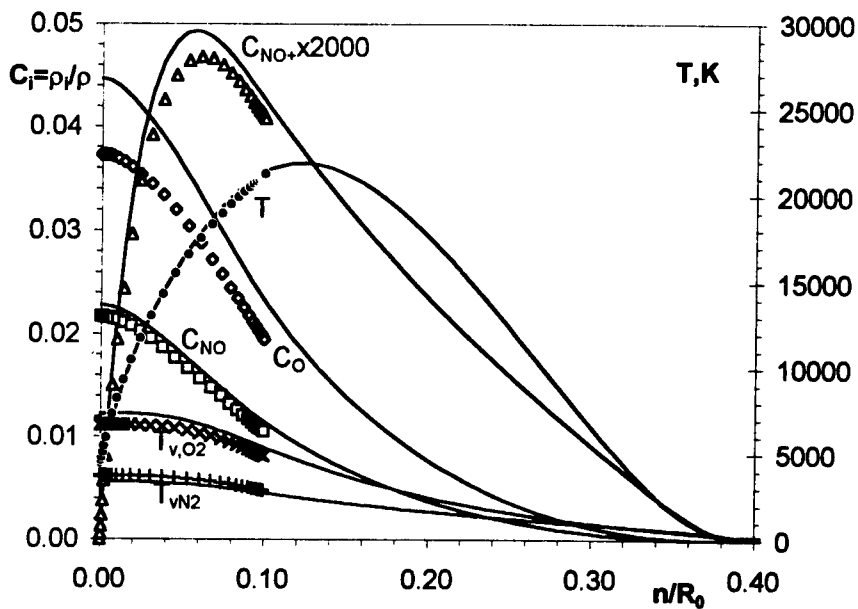
Fig.3. Flow parameters along symmetry axis of sphere at
conditions of experiment RAM-C H=88км, Re=470
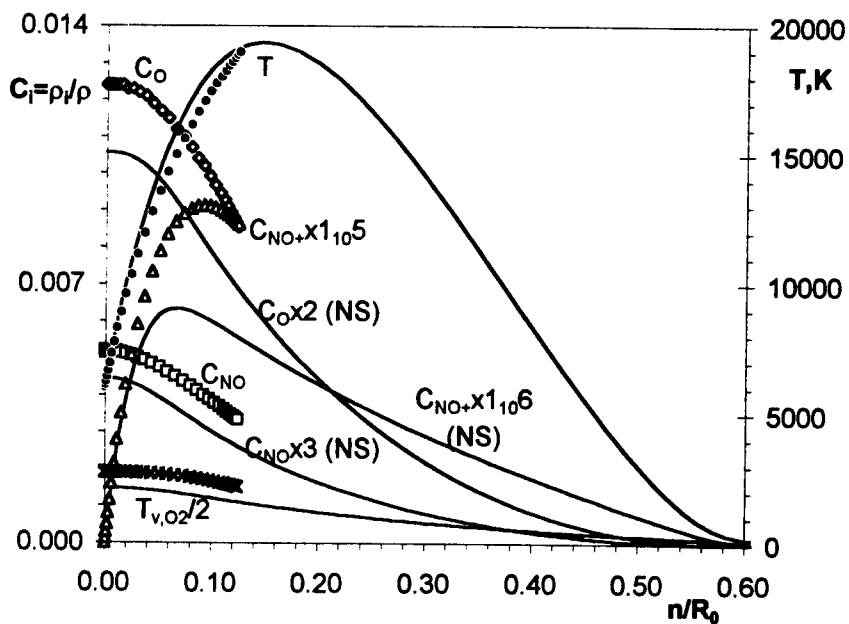
Fig.4. Flow parameters along symmetry axis of sphere at
conditions of experiment RAM-C H=92км, Re=230

part of a sphere, which is illustrated in Fig.2b, where the profiles of the same flow parameters on a corner 75 degrees are presented.

The comparison of the profiles of temperatures and concentration calculated with the NS equations and the VSL model, at the altitude of 88 km (Re_∞=470) along the symmetry axis is presented in Fig.3. As can be seen, at his altitude the results of calculations with the two models also rather well coincide with each other. The greatest discrepancy, approximately 15 %, is observed for mass concentration of atomic oxygen, the values obtained with the use of the NS equations exceeding that of the VSL model. It can be explained by the fact that at calculations with the Navier-Stokes equations a dissociation, as well as other chemical and relaxation processes, in a shock wave begin earlier, than in the VSL model, where the thermo-chemical processes at the obtaining of the generalized Rankine-Hugoniot conditions are assumed frozen. Higher values of parameters at calculation with the NS equations, though not so noticeable, are observed also for the concentrations of NO, NO^+ and the vibrational temperature of O_2 (the latter results in additional increase in a dissociation of oxygen). The similar coincidence of results obtained with the two models, is observed along all windward side of a sphere (not shown for brevity).

Absolutely other situation takes place at the altitude of 92 km (Re_∞=230) - Fig.4 (symmetry axis). Unlike the two previous altitudes, 84 and 88 km, in this case the calculation with the NS equations gives considerably smaller values in comparison with the VSL model of both vibrational temperatures and concentrations of chemical species. The difference between parameters calculated with the two models, is increasing from temperatures to concentrations, which is connected to the step character of thermo-chemical processes in a shock layer. The underestimation of vibrational temperatures leads to smaller values of dissociation rates of O_2, N_2 and accordingly of concentrations of N, O and NO. This in turn results in the decrease of concentrations of ions NO^+ and N_2^+, formed in the reaction of associative ionization.

From the presented results it is seen, that for the heat flux at stagnation piont of a sphere (perfect gas) the VSL model gives values consistent with that of the NS equations down to the Reynolds number $Re_\infty \approx 200$. For the calculation of main flow parameters (static and vibrational temperatures, concentrations of neutral and ionized species) in a shock layer on a windward side of a sphere at hypersonic flow of a chemically reacting air it is possible to use the VSL model down to $Re_\infty \approx 500$.

REFERANCES

1. R.T.Davis. Numerical solution of the hypersonic viscous shock layer equations //AIAA J. 1970. v.8, N5. p. 843-851
2. A.Jameson and S.Yoon. An LU-SSOR scheme for the Euler and Navier-Stokes equations. AIAA Paper 87-0600
3. T.H.Pulliam and J.L.Steger. Recent improvements in efficiency, accuracy, and convergence for implicit approximate factorization algorithms. AIAA Paper 85-0360
4. Гусев В.Н., Никольский Ю.В. An Experimental research of heat transfer in a critical point of an sphere in hypersonic stream of rarefied gas // Уч. Зап. ЦАГИ, 1970. т. II, N1. p. 122-125
5. The Entry Plasma Sheath and its Effect on Space Vehicle Electromagnetic Systems. Vol. I, NASA SP-252, 1970.

ON INVERSE PROBLEM OF WING AERODYNAMICS IN SUBSONIC FLOW

N.F.Vorob'ev

Institute of Theoretical and Applied Mechanics SB RAS,
Novosibirsk, Russia

The problems of potential incompressible flow over a thin weakly curved finite-span wing can be considered as problems of the flow over a lifting vortex surface rigidly bound with the wing and a free vortex surface simulating tangential discontinuities outside the wing. The velocity potential $\Phi(x, y, z)$ of the flow disturbed by these surfaces satisfies the Laplace equation. In the linear formulation, the conditions on the wing surface and on the free vortex surface are shifted to the basic plane $\eta = 0$ slightly different from the wing surface (Fig. 1). For the Laplace equation we have the Neumann problem when the governing function in the plane $\eta = 0$ is a normal derivative of velocity potential $\partial\Phi/\partial y$. The solution can be represented as a simple layer potential

$$\Phi_1(x, y, z) = -\frac{1}{2\pi} \iint\limits_{\eta=0} \frac{\partial\Phi}{\partial y}\phi\,ds, \quad \phi = \frac{1}{r}, \ r = \sqrt{(x-\xi)^2 + (z-\zeta)^2 + y^2}, \ ds = d\zeta\,d\xi.$$

Another possibility is a Dirichlet problem when the governing function is a potential of Φ in the plane $\eta = 0$

$$\Phi_2(x, y, z) = \frac{1}{2\pi} \iint\limits_{\eta=0} \Phi\frac{\partial\phi}{\partial y}\,ds, \quad \left(\frac{\partial\phi}{\partial y}\right)_{\eta=0} = -y\left[(x-\xi)^2 + (z-\zeta)^2 + y^2\right]^{-3/2}. \quad (1)$$

One more variant is a mixed problem when the governing function is $\partial\Phi/\partial y$ on one part of the plane $\eta = 0$ and Φ on the other part.

In the problems of the finite-span wing theory for a subsonic flow, when the regions of formulation of the boundary conditions is the entire plane $\eta = 0$, possible formulations of the boundary conditions are considered when the problem is stated.

The use of a double-layer potential (1), where the solution is written in terms of the function $(\Phi)_{\eta=0}$ makes it possible within the framework of the linear theory to formulate the problem of the flow over a wing in terms of the loads acting upon the wing. The problems of finding the wing surface shape from a given load were called inverse problems of wing aerodynamics.

After term-by-term integrating the double layer potential (1) with respect to the variable ξ, taking into account that $(\Phi)_{\eta=0} = 0$ at infinity and that, according to the linearized Bernoulli equation, on the wing surface S

$$\Delta p = 2\rho u_\infty \Phi'_\xi, \quad (\xi, \zeta) \in S,$$

where Δp is the pressure difference on the wing surface and $\Delta p = 0$ on the remaining part of the plane $\eta = 0$ outside the projection on wing S onto this plane, we can transform this potential into [1]

$$\Phi_3 = \frac{1}{4\pi\rho u_\infty} \iint\limits_{S(\eta=0)} \Delta p \int\limits_\infty^\xi \frac{\partial\phi}{\partial y}\, d\xi\, ds, \quad \left(\int\limits_\infty^\xi \frac{\partial\phi}{\partial y}\, d\xi\right)_{\eta=0} = \frac{y}{[(z-\zeta)^2 + y^2]}\left\{1 + \frac{(x-\xi)}{r}\right\},$$

when the integration is performed only over the region of wing projection S onto the plane $\eta = 0$. The derivative of the potential Φ_3 with respect to the parameter y is

$$\Phi'_{3y} = \frac{1}{4\pi\rho u_\infty} \iint\limits_{S(\eta=0)} \Delta p \int\limits_\infty^\xi \frac{\partial^2\phi}{\partial y^2}\, d\xi\, ds. \tag{2}$$

For $y = 0$ the derivative $(\Phi'_{3y})_{y=0}$ is a normal velocity component on the basic plane $\eta = 0$, and for points $(x,z) \in S$ it describes the wing surface shape [1, 2]

$$(\Phi'_{3y})_{y=0} = \frac{1}{4\pi\rho u_\infty} \iint\limits_{S(\eta=0)} \Delta p\left(\int\limits_\infty^\xi \frac{\partial^2\phi}{\partial y^2}\, d\xi\right)_{y=0} ds, \tag{3}$$

$$\left(\int\limits_\infty^\xi \frac{\partial^2\phi}{\partial y^2}\, d\xi\right)_{\eta=0,y=0} = \frac{1}{(z-\zeta)^2}\left\{1 + \frac{(x-\xi)}{\sqrt{(x-\xi)^2 + (z-\zeta)^2}}\right\}, \quad (x,z) \in S.$$

The gas dynamic source $\left(\int\limits_\infty^\xi \frac{\partial^2\phi}{\partial y^2}\, d\xi\right)_{\eta=0,y=0}$ has a strong singularity $(z-\zeta)^{-2}$. For points $(x,z) \in S$ the singular integral in the right-hand side of formula (3) exists only in the sense of Hadamard. To obtain the solution in the class of bounded functions, it is necessary to decrease the power of singularity of the integral operator in (3) by posing additional conditions onto the smoothness of the specified load $\Delta p(\xi,\zeta)$ on the wing. The order of singularity of the integral operator of the derivative $(\Phi'_{3y})_{y=0}$ can be decreased by term-by-term integration of the operator in (2) with respect to the variable ζ:

$$\Phi'_{3y} = \frac{1}{4\pi\rho u_\infty}\left\{\oint\limits_{L(\eta=0)} \left[\Delta p \iint\limits_\infty \frac{\partial^2\phi}{\partial y^2}\, d\xi d\zeta\right]_{\zeta=f(\xi)} d\xi - \iint\limits_{S(\eta=0)} \Delta p'_\zeta \iint\limits_\infty^\xi \frac{\partial^2\phi}{\partial y^2}\, d\xi d\zeta\, ds\right\},$$

where $\Delta p'_\zeta$ is the derivative of the wing loads in the crossflow direction, and $\zeta = f(\xi)$ is the equation of the wing contour L in the plane $\eta = 0$. For $y = 0$

$$(\Phi'_{3y})_{y=0} = \frac{1}{4\pi\rho u_\infty}\left\{\oint\limits_{L(\eta=0)} \left[\Delta p \iint\limits_\infty^\xi \frac{\partial^2\phi}{\partial y^2}\, d\xi d\zeta\right]_{\zeta=f(\xi),y=0} d\xi -\right.$$

$$-\iint\limits_{S(\eta=0)} \Delta p'_\zeta \left(\iint\limits_\infty^\xi \frac{\partial^2 \phi}{\partial y^2} d\xi d\zeta \right)_{y=0} ds \Bigg\}, \qquad (4)$$

$$\left(\iint\limits_\infty^\xi \frac{\partial^2 \phi}{\partial y^2} d\xi d\zeta \right)_{y=0} = \frac{(x-\xi) + \sqrt{(x-\xi)^2 + (z-\zeta)^2}}{(x-\xi)(z-\zeta)}, \qquad (x,z) \in S.$$

The gas dynamic source $\left(\iint\limits_\infty^\xi \frac{\partial^2 \phi}{\partial y^2} d\xi d\zeta \right)_{y=0}$ entering into integral operators of formula (4) has a Cauchy kernel singularity in two directions: $((x-\xi)(z-\zeta))^{-1}$. Integrals with kernels of this type exist in the sense of the main value in the class of bounded functions under the conditions of continuity of the weight functions Δp, $\Delta p'_\zeta$ in the region of their determination.

Let us consider some examples of constructing the finite-span wing surfaces according to formula (4). Apart from the requirement that the pattern of prescribed loads should be physical, it is necessary that the analytical description of these loads and the wing contour be so simple that all integrals are "taken" up to the end, and the solution is written analytically in terms of elementary functions. This is a complex and labor-consuming process. The solutions are not written in this paper, only their principal properties are discussed, and examples of the terms of solution corresponding to integrand singularities are presented.

The solution of the problem of the perfect fluid flow over a lifting surface leads us to a flow regime with infinite velocities of some sections of the contour L, where the shock-free condition is not set. In a real flow, high gradients of flow parameters lead to flow stall on these edges and vortex sheet formation. The appearance of vortex sheet involves an increase in drag and, finally, a decrease in the lift-to-drag ratio of the wing. Designing of a wing surface with shock-free edges makes it possible to decrease the inductive drag of the wing. The conditions of zero load on the edges $(\Delta p)_L = 0$, which is the condition of shock-free edges, can be satisfied assuming that the vortex surface of the wing S is extended as a free vortex sheet shed from the edges of the wing L. The condition of shock-free edges can be fulfilled without vortex sheet shed from the edges, if a smooth incoming and outgoing flow is organized at the edges by means of surface deformation (Fig. 2).

Thus, equation (4), which describes the wing surface under the condition of shock-free edges $(\Delta p)_L = 0$, can be written as

$$(\Phi'_{3y})_{y=0} = -\frac{1}{4\pi\rho u_\infty} \iint\limits_{S(\eta=0)} \frac{\Delta p'_\zeta \left[(x-\xi) + \sqrt{(x-\xi)^2 + (z-\zeta)^2} \right]}{(x-\xi)(z-\zeta)} d\zeta d\xi, \qquad (5)$$

$$(x,z) \in S + L.$$

In the region of wing projection S onto the plane $\eta = 0$ we specify the load on the wing $\Delta p(\xi,\zeta)$, $(\xi,\zeta) \in S + L$. Outside the wing projection S onto the plane $\eta = 0$, we obtain $\Delta p = \Delta p'_\zeta = 0$.
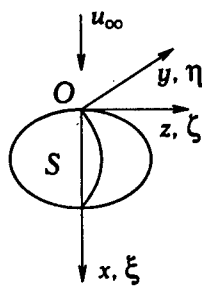
Fig.1
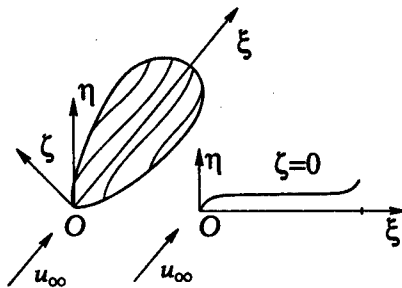
Fig. 2
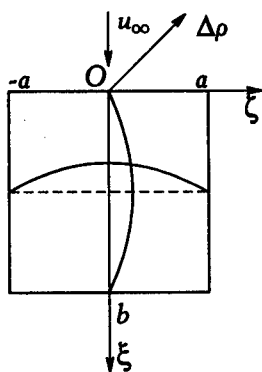
Fig. 3
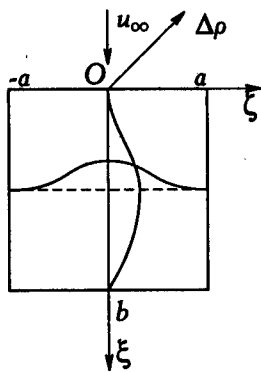
Fig. 4
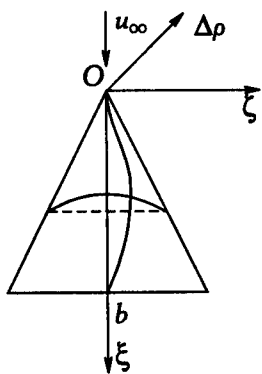
Fig. 5

Wing with rectangular planform

Wing 1: $0 \leq \xi \leq b$, $-a \leq \zeta \leq a$, $\Delta p = (a^2 - \zeta^2)\xi(b - \xi)$, $\Delta p'_\zeta = -2\zeta\xi(b - \xi)$ (Fig. 3). The condition $(\Delta p)_L = 0$ is valid for the entire contour L. The condition of continuous junction of the quantity $\Delta p'_\zeta$ on the wing S with its value $\Delta p'_\zeta = 0$ outside the projection S is fulfilled on the leading and trailing edges $(\Delta p'_\zeta)_{\xi=0,\xi=b} = 0$, while on the side edges $(\Delta p'_\zeta)_{\zeta=\pm a} = \mp 2a\xi(b - \xi)$. This discontinuity in initial data leads, after "taking" all integrals according to (5), to appearance of terms with logarithmic singularity of the quantity $(\Phi'_{3y})_{y=0} \sim z \ln \frac{a+z}{a-z}$.

Wing 2: $0 \leq \xi \leq b$, $-a \leq \zeta \leq a$, $\Delta p = (a^2 - \zeta^2)^2 \xi(b-\xi)$, $\Delta p'_\zeta = -4\zeta(a^2 - \zeta^2)\xi(b-\xi)$ (Fig. 4). The conditions $(\Delta p)_L = 0$, $(\Delta p'_\zeta)_L = 0$ are valid for the entire contour L, which ensures the condition of continuous junction of initial data in the region $S + L$ with initial data of the remaining portion of the plane $\eta = 0$. The wing geometry is described in the class of bounded functions, according to (5). The integrand singularities in the solution after "taking" all integrals correspond to the terms of the form $z(a^2 - z^2)\ln \frac{a+z}{a-z}$, which take finite values both on the side edges and on the leading and trailing edges.

Delta wing: $0 \leq \xi \leq b$, $-k\xi \leq \zeta \leq k\xi$, $\Delta p = (k^2\xi^2 - \zeta^2)(b - \xi)$, $\Delta p'_\zeta = -2\zeta(b - \xi)$ (Fig. 5). The condition $(\Delta p)_L = 0$ is valid for the entire contour L. The condition $(\Delta p'_\zeta)_L = 0$ is fulfilled on the trailing edge, and $(\Delta p'_\zeta)_{\zeta=\pm k\xi} = \mp 2k\xi(b - \xi)$ on the side edges. This discontinuity in initial data, contrary to the same discontinuity on the side edges of the rectangular wing 1, does not lead to the appearance of singularities of the quantity $(\Phi'_{3y})_{y=0}$ after all integrals are "taken". This is explained by the fact that for a rectangular wing the limits of integral (5) are constants, and one integration with respect to ζ does not eliminate the Cauchy singularity, but reduces it to a logarithmic one. In the case of delta wing, the integration limits of the internal integral are variable, which leads to additional smoothness of the singularity under external integration. The integrand singularities in the solution correspond to the terms of the form $z(kb \pm z)^2 \ln(kb \pm z)$, $z^2 \ln z$.

REFERENCES

1. Vorob'ev N.F. Lifting Surface Aerodynamics in a Stable Flow. Novosibirsk: Nauka, 1985

2. Multhopp H. Methods of calculating the lift distribution of wings (subsonic lifting – surface theory). ARC R. and M., 1950, N 2884.

HYDROGEN JET COMBUSTION IN CONFINED AND UNCONFINED SUPERSONIC AIR FLOW

V.A.Zabaikin, P.K.Tretyakov, C.Bruno*

Institute of Theoretical and Applied Mechanics SB RAS,
630090, Novosibirsk, Russia
*Roma University, Italy

The efficiency of diffusion combustion of H_2 in an unconfined high-temperature supersonic flow is compared with pseudo-shock combustion regime in a constant-area duct.

It is shown that the control of combustion characteristic (ignition delay, flame length, combustion process evolution) of diffusion flame is possible with the use of various actions (chemically active and inert additions, enhancement of mixing etc.). Nevertheless, under the conditions of constant flow parameters (Mach number, temperature) the combustion process in the duct develops more intensively (on a smaller length) with the realization of a pseudo-shock mechanism of combustion, which can be explained by mixing improvement owing to gas dynamic effects.

It is known [1] that the length of a turbulent diffusion flame of combustible gas in a co-current oxidizer flow depends on numerous factors: relative speed of the co-flow, relative density of the co-flow, gas type, turbulence intensity, thickness of injector nozzle thickness, etc. Yu.A. Annushkin and his collaborators recommended criterial dependences for determining the flame length, which were obtained on the basis of experimental study of the diffusion characteristics of combustion of various fuels. Recommendations are given in his papers for the calculation of combustion chambers for rocket ramjets with multinozzle injection of combustible gas on the basis of using an appropriate diffusion mechanism of combustion. It is possible to note one important feature of this methodology, which is based on an experimental fact. The complete combustion of fuel requires the amount of oxidizer (air) higher than the stoichiometric ratio by more than 2.5-2.8 times. The combustion efficiency in the combustion chamber of rocket ramjet (completeness of combustion) is determined by the ratio of it length to the length of diffusion flame in the duct (providing an equal "access" of the air to each nozzle of the fuel block) and the total air-to-fuel equivalence ratio. The correctness of this approach is proved by good accordance between the completeness of combustion calculated by that method with experimental data for axisymmetric ramjets for flow parameters: $T_{0air}=1000 \div 1200$ K; $T_{0H2}=600 \div 1500$ K; free-stream Mach number $M=3.0 \div 5.0$ [2,3].

The study of diffusion combustion in the free stream is more accessible in comparison with the investigation in the duct from the viewpoint of application of a larger number of diagnostic methods. In particular, the optical method of radiation registration, as was shown in many works (for example, [4]) can be used to analyze the combustion efficiency.

The objective of the present work is to compare the efficiency of control of the hydrogen diffusion flame with combustion in a co-current high-enthalpy supersonic air stream with combustion in the duct under the conditions of pseudo-shock regime.

The experiments were conducted in a facility with an arc heater [5] at constant flow parameters: $M=2.2$, $T_0=2000 \div 2200$ K, air nozzle diameter 50 mm. Hydrogen was
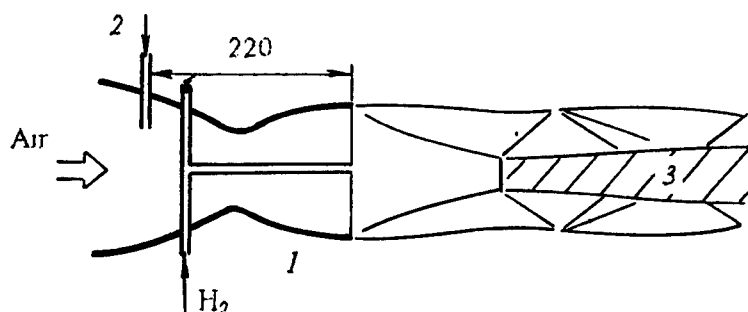
Fig.1. Scheme of experiments. *1* – supersonic air nozzle, *2* – additions, *3* – flame.

injected coaxially to the air stream through the nozzle with diameter of 10 mm (Fig.1). Both active (H_2, H_2O_2) and passive (CO_2, H_2O) additions were injected usually in the plenum chamber at a distance of 220 mm from the hydrogen injector.

A regime with hydrogen mass flow rate 3 g/s and stagnation temperature T_0=2000 K of the air stream was chosen as a basic one. In this regime there exists a steady ignition delay on the shock waves in a supersonic air stream [6]. In accordance with that, any effect on the flame is well observed (by changing of the ignition point).

An optical-mechanical scanner used in experiments recorded the distribution of radiation of OH-radicals along the flame length, which yielded information about the heat release. The use of the technique suggested in [4] allowed one to obtain the combustion efficiency. Figure 2 (curve *1*) shows the H_2 combustion curve behavior on the basic regime. In this case the ignition takes place at 150 mm from the nozzle exit (injection of H_2 into the stream), and the flame length reaches 325 mm.

An addition of chemically active agents (for example H_2O_2) to the fuel can have an effect on the ignition delay and the time of chemical reactions. It is shown numerically
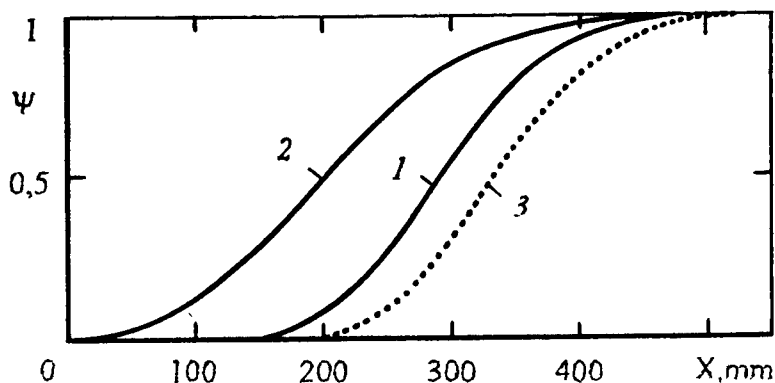
Fig.2. Completeness of combustion (combustion efficiency). *1* – main regime, *2* – +H_2 injected into plenum, *3*–+CO_2 injected into plenum.

224

in [7, 8] that an addition of H_2O_2 in amounts less than 10 vol.% to a methane-air mixture with initial temperature of $1200 \div 2025$ K decreases considerably the ignition delay. The ignition of H_2 in a co-current supersonic air flow (M=2, $T<1400$ K) can be achieved by burning part of hydrogen in the plenum chamber or by introduction of 10% hydrogen peroxide to the fuel. Pure hydrogen did not ignite under these conditions. It is noted that OH and H radicals have a strong effect on the acceleration of chemical reactions.

Experiments with active additions injected to the plenum chamber really showed a significant decreasing of ignition delay. Figure 2 (curve *2*) shows the combustion curve for the case of injection of a small amount of H_2 to the plenum chamber (H_2O_2 has a similar effect). The ignition delay is practically absent here, beginning with H_2 addition ≥ 0.1 g/s. But the flame length increases, i.e., the speed of heat release is lower here. This is explained by the mixing factor effect. The mixing of H_2 with the air under parallel coaxial injection occurs very slowly [8]. Active additions affect only the kinetic aspect of the process, but not the mixing speed.

The injection of passive additions does not change the character of heat release. It is seen from Fig. 2 (curve *3*) that the addition of CO_2 (mass flow rate ≈ 15 g/s) leads only to flame displacement and does not change its length. The influence of CO_2 (or H_2O) injection was analogous to decreasing the temperature of the air stream [9].

The analysis of duct flow was made for identical conditions for H_2 and air stream parameters, like in the case of unconfined flow. The calculations were based on the technique described in [10]. The calculations are performed without taking into account the heat transfer to the wall, which (as was shown by the estimates) does not lead to principle changing of the result.

The highest possible heat amount which can be brought to a constant-area duct is defined by the flow crisis ("thermal" choking). In this case, the flow velocity (mean mass flow rate) equal to the speed of sound is established in a certain cross-section of the duct. It is easy to show (see [10]) that the static pressure in this section equals (with accuracy to friction losses) a half of pressure difference in the constant total temperature pseudo-shock $p_{M=1}=(p_i+p_e)/2$. (It follows from momentum and continuity equations applied to one-dimensional examination of the flow with heat supply.) On the basis of literature data on the length of constant total temperature pseudo-shock it is possible to construct the dependence of the fraction of supersonic deceleration portion of the flow (to M=1) from the free-stream Mach number. This dependence can be described as [10]

$$\frac{\Delta l}{L} = -0.02\,M_i^2 + 0.24\,M_i - 0.22 \tag{1}$$

where $1.0 < M_i \leq 4.0$, L is the total length of the constant total temperature pseudo-shock which can be found from

$$\bar{L} = \frac{L}{D} = \frac{\Delta W}{cW^*} \tag{2}$$

(see [11]), where W^* is the maximum dimensionless speed (Crocco number), ΔW is the difference of dimensionless speeds at the beginning and end of the pseudo-shock, c is a constant.

Otherwise, $\bar{L}$ can be found from the empirical relationship ([12], here St=L):

$$\frac{St(M_i^2 - 1)\,\mathrm{Re}_\Theta^{1/4}}{D^{1/2}\Theta^{1/2}} = 50(\frac{p_f}{p_a} - 1) + 170(\frac{p_f}{p_a} - 1)^2 \tag{3}$$

225

D is the duct diameter; Θ is the momentum thickness; Re is the Reynolds number calculated by the momentum thickness; $p_a=p_i$; $p_f=p_e$ are the pressures in the beginning and in the end of the flow deceleration zone.

The functions (1) and (2 or 3) can be used to find the flame length in the duct with the maximum heat supply, assuming the speed of chemical reactions is high and corresponds to the speed of changing gas dynamic parameters in a decelerated flow due to heat supply. It is shown in [13] that this assumption holds true for hydrogen combustion with initial parameters $M_i=2.4$ and $T_{0i}\approx 1700$ K. Another experimental confirmation [14] is the universality of relative variation of static pressure in the pseudo-shock $(p-p_i)/(p_e-p_i)$ against the relative pseudo-shock length $\bar{X}=(X-X_i)/(X_e-X_i)$, where (X_e-X_i) is the pseudo-shock length, $(X-X_i)$ is the length from pseudo-shock beginning to the cross-section with a current value of pressure. Experiments [14] testify that the relative change of pressure increment along the pseudo-shock is the same both for hydrogen combustion with different ways of injection (transverse injection jets or annular jet) and without combustion. An curve is proposed, which approximate the experimental data:

$$\frac{p-p_i}{p_e-p_i}=3\,\bar{X}-4.2\,\bar{X}^2+3.4\,\bar{X}^3-1.2\,\bar{X}^4 \tag{4}$$

A similar dependence is suggested in [15]

$$\frac{p-p_i}{p_e-p_i}=3\,\bar{X}-3\,\bar{X}^2+3\,\bar{X}^3 \tag{5}$$

It is valid for the entire Mach number range and independent of the duct expansion degree.

Using any of those dependences (4, 5) and assuming the flame length equal to the length of the supersonic portion of constant total temperature pseudo-shock, it is possible (using the technique for determining the heat supply under pseudo-shock conditions [10]) to find the heat-release function or the curve of hydrogen combustion in the constant-area duct for given initial flow conditions and air-to-fuel equivalence ratio (α). Certainly, α must be smaller than α^*, where α^* corresponds to the flow rate of H_2, whose combustion is sufficient to produce heat for realization of "thermal chocking".

The above procedure was used to find the combustion length zone in the duct with diameter 50 mm (equal to the air stream diameter in experiments) and heat-release rate (for hydrogen combustion on the basic regime with diffusion combustion in an unconfined flow ($M=2.2$, $T_0=2000$ K).

A comparative relative change of the heat-release function is shown in Fig. 3. The longitudinal coordinate of combustion beginning in the duct coincides with the beginning of diffusion combustion of hydrogen on the basic regime. As it follows from the figure, the combustion in the duct terminates on a smaller length and, thus, is more intensive. This can be explained by the influence of gas dynamic structure taking place in the pseudo-shock, which promotes a rapid mixing of H_2 with the air.

In conclusion it should be noted that control methods of mixing and combustion for fuel jets injected into an unconfined flow can turn to be less effective for combustion control in ducts. We will also emphasize that in the pseudo-shock combustion regime the method of fuel injection is not important for the development of combustion
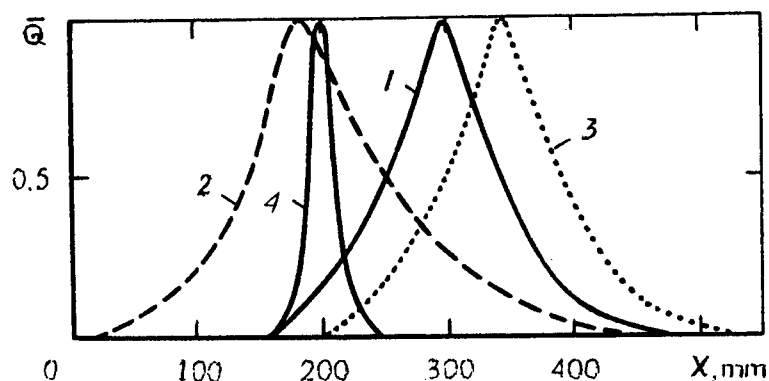
Fig.3. Relative heat-release. *1* – main regime, *2* – +H_2, *3* – +CO_2, *4* – combustion in pseudo-shock.

process. It is necessary, however, that this regime developed from the initial part of the combustion chamber.

REFERENCES

1. Annushkin Yu.M. Diffusion combustion of gaseous fuels in unconfined flow // Trudy CIAM. 1979. N 857.
2. Annushkin Yu.M. Basic regularities of burning out of hydrogen turbulent jets in air canals // Fizika Goreniya i Vzriva. 1981. Vol.17, N4. P.59-71.
3. Annushkin Yu.M., Sverdlov E.D. Regularities of the change of diffusion flame length of high-energetic gaseuos fuels in cocurrent air flow // Ibide. 1984. Vol.20, N3. P.46-51.
4. Zabaikin V.A., Tretyakov P.K. OH-radicals radiation used to study the combustion efficiency of H_2 in high speed flow // Proc. of the Fourth Asian Symposium on Visualization. Int. Academic Publishers / Ed. by Q.D.Wei. Beijing, 1996. P.495-497.
5. Zabaikin V.A., Lazarev A.M. Influence of different injection methods on hydrogen combustion in supersonic air flow // Izvestiya Sibirskogo Otdeleniya AN SSSR, Ser. Tech.Nauk. 1986. Issue 1, N 4. P.44-49.
6. Zabaikin V.A., Lazarev A.M., Tretyakov P.K. The use of gasdynamic structure of a free jet to control the hydrogen flame combustion // Proc. of Workshop on the Gas Flame Structure. Novosibirsk, ITAM, 1988. Pt 1. P.145-148.
7. Golovitchev V.I., Pilia M.L., Bruno C. Autoignition of methane mixtures: The effect of hydrogen peroxide // J.Propulsion and Power. 1996. Vol.12, N4. P.699-707.
8. Golovitchev V.I., Bruno C. Modeling of parallel injection supersonic combustion // ISTS 94-a-08. Yokohama, Japan, 1994.
9. Zabaikin V.A., Tretyakov P.K. The control of H_2 combustion in supersonic flow under influence of inert and chemically active addtions // Int. Conf. on the Methods of Aerophys. Research: Proc. Pt 2. Novosibirsk, 1996. P.227-230.
10. Tretyakov P.K. Pseudoshock Regime of Combustion // Fizika Goreniya i Vzriva, 1993. Vol.29, N6. P.33-38.
11. Takefumi Ikui, Kazuyasu Matsuo, Minory Nagai. The mechanism of pseudo-shock waves. Bulletin of the JSME, Vol.17, N108, June, 1974.
12. Billig F.S., Waltrup P.J. Structure of shock waves in cylindrical ductes // AIAA J., 1973, Vol.11, N10, P.1404-1408.
13. Tretyakov P.K. Length definition of combustion zone in the duct with supersonic flow speed // 6 Int. Workshop: Modern problems of fluid and gas mechanics. Samarkand – Tashkent, 1992. P.82-84.
14. Rozhitsky S.I., Strokin V.N. On supersonic flow deceleration by combustion in the duct // Pioneers of Space Development and Contemporaneity: Proc.of Vsesouz. Conf. Moscow, Nauka. 1988. P.57-61.
15. Gimranov E.G. Tarasov F.F. About pseudoshock length // Trudy Ufim. Aviatsion. Inst. 1975. Vol.96. P.87-94.

CONTENTS